Low Frequency Seismic Isolation for Gravitational Wave Detectors

Thesis by

Akiteru Takamori

Department of Physics
School of Science
University of Tokyo

2002

Contents

Preface

Gravitional waves (GW) are perturbation of spacetime, which propagate at the speed of light. They were predicted by A. Einstein as one of the consequences of the theory of general relativity in 1916. So far, their existence has been only indirectly proven by Taylor and Hulse's observation on the decay of the orbital period in the binary pulsar PSR1913+16.

Direct detection of GW is one of the most exciting subjects in physics and in modern astronomy. Several large-scale laser interferometric GW detectors have been constructed for this purpose and are progressively achieving their design sensitivity.

Following these successful evolutions in the field, various R&D programs study the next generation of the interferometric gravitational wave detectors. To achieve the goal of the superior sensitivity desired for refined astronomical observations, even more sophisticated technologies and detail are required for the advanced detector components. One of the major obstacles for an advanced ground-based interferometer is the seismic disturbance. In order to obtain a wide observation band, especially at low frequencies ($\sim$10 Hz), the residual seismic noise acting on the optics needs to be further attenuated. We have developed SAS (Seismic Attenuation System) with the specific objective of achieving sufficient low frequency seismic attenuation. The system, not only suppresses the seismic noise well below the required noise levels even at very low frequency (around a few Hz), but it also reduces the residual motion of the optics to well below 1 μm, which is a condition necessary for maintaining lock indefinitely and a stable operation of the interferometer. The SAS, is basically a multi-layer passive mechanical filter, composed by an inverted pendulum, MGAS (Monolithic Geometric Anti-Spring) filters for vertical and horizontal attenuation, and the mirror suspension system. SAS is instrumented with an active damping on the

primary stages to damp the body resonances of the mechanical filters and a passive damping technique on the mirror suspension for stable operation. We have developed and successfully validated the SAS prototypes designed to meet the requirements of the coming upgrade of TAMA300 interferometer, by performing the independent test of each component, and by operating a 3m Fabry-Perot cavity implemented with the SAS prototypes. By doing so we also validated the SAS technologies for future use in more demanding, kilometer class, advanced gravitational wave interferometric detectors. In this thesis we discuss the basic principles of SAS technologies, and report the results of the validations.

This thesis work is part of larger effort to develop advanced seismic isolation for gravitational wave interferometric detectors. The job is larger what could be tackled by a single person, and in fact it is the results of a team effort. I am very grateful to the other team members that entrusted me with the responsibility of leading and organizing it, and for all the support that they all provided. I could not have done it without them. I hope that the results of this thesis will reassure them that they made the right choice.

Chapter 1

Introduction[1]

1.1 Gravitational Waves

Gravitational Waves (GW) are the perturbations of the spacetime, which propagates at the speed of light. They were predicted by Einstein as one of the consequences of the theory of general relativity in 1916 [1]. Their existence has been only indirectly proven by the observation of the decay of the orbital period in the binary pulsar PSR1913+16 by Taylor and Hulse [4, 5]. Direct detection of the GW has been attempted as the final validation of the theory of general relativity. The detection of GW is also one of the frontiers in the modern astronomy, because it is supposed to open a new window for astronomical observations. As the interaction between the GW and matter is so small, detectable GWs are expected to be generated only by dynamical and relativistic acceleration of compact massive stars, the most interesting subjects in astronomy.

In the general relativity theory, the interval between two points in the spacetime (x^μ and $x^\mu + \mathrm{d}x^\mu$) is expressed as

$$\mathrm{d}s^2 = g_{\mu\nu}\mathrm{d}x^\mu \mathrm{d}x^\nu \ (\mu, \nu = 1, 2, 3, 4). \tag{1.1}$$

Here $x^\mu = (-ct, x, y, z)$ (c is the speed of light) and $g_{\mu\nu}$ represents the metric tensor which describes the geometry of spacetime [2, 3]. The metric tensor satisfies the Einstein's equation

[1] As the formulations of the gravitational waves have already been repeatedly presented in many theses and papers, in this chapter we only describe a few, very basic, facts on GWs, and their possible detection with the interferometric devices. We also present a catalog of possible GW sources.

$$R_{\mu\nu} - \frac{1}{2} g_{\mu\nu} R = \frac{8\pi G}{c^4} T_{\mu\nu}. \tag{1.2}$$

G is the Newton's gravity constant and $T_{\mu\nu}, R_{\mu\nu}, R$ are the energy-momentum tensor, the Ricci tensor, and the Ricci scalar, respectively. In vacuum ($T_{\mu\nu} = 0$), the Einstein's equation is simplified as

$$R_{\mu\nu} - \frac{1}{2} g_{\mu\nu} R = 0. \tag{1.3}$$

As the general relativity theory contains the special relativity, the Minkowski metric $\eta_{\mu\nu}$ is a solution of the above equation.

As GWs are extremely weak, they can be approximated as small perturbations to the Minkowski flat background metric as:

$$g_{\mu\nu} = \eta_{\mu\nu} + h_{\mu\nu} \ (|h_{\mu\nu}| \ll 1). \tag{1.4}$$

By linearizing the equation (1.2), one obtains

$$\frac{\partial}{\partial x^\nu} \frac{\partial h^\rho_\mu}{\partial x^\rho} + \frac{\partial}{\partial x^\mu} \frac{\partial h^\rho_\nu}{\partial x^\rho} = \left(\nabla^2 - \frac{\partial^2}{c^2 \partial t^2} \right) h_{\mu\nu} - \frac{\partial^2 h^\rho_\rho}{\partial x^\mu \partial x^\nu}. \tag{1.5}$$

After applying the following transformation

$$\overline{h}_{\mu\nu} = h_{\mu\nu} - \frac{1}{2} \eta_{\mu\nu} h^\mu_\mu, \tag{1.6}$$

the equation (1.5) is written as

$$\left(\nabla^2 - \frac{\partial^2}{c^2 \partial t^2} \right) \overline{h}_{\mu\nu} = 0. \tag{1.7}$$

Thus the perturbation metric is that of a wave propagating at the speed of light. The GW which propagates along the z axis is expressed in the following form in the an appropriately chosen gauge[2]:

$$\overline{h}_{\mu\nu} = \begin{bmatrix} 0 & 0 & 0 & 0 \\ 0 & \overline{h}_+ & \overline{h}_\times & 0 \\ 0 & \overline{h}_\times & -\overline{h}_+ & 0 \\ 0 & 0 & 0 & 0 \end{bmatrix}. \tag{1.8}$$

Here $\overline{h}_+$ and $\overline{h}_\times$ correspond to two polarizations of the GW with relative

[2]so-called Transverse-Traceless gauge.

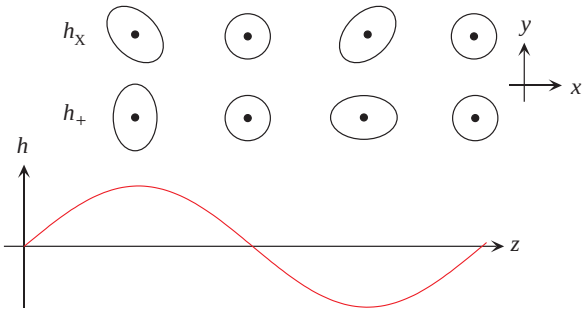

Figure 1.1: Propagation of gravitational wave along z axis.

angle of 45 degrees. The GW causes the tidal distortion of the spacetime, as illustrated in figure 1.1.

Sources of Gravitational Waves[16] There are various astronomical sources expected to radiate GWs with sizeable amplitudes. They are classified into three types according to the wave form:

- Periodic GW sources: Spinning neutron stars (pulsars), Binary systems of massive compact objects.
- Burst GW sources: Supernova explosion, Final coalescence of compact binary systems.
- Stochastic GW sources: Cosmological source related to the Big-Bang, White dwarf binaries.

Black holes are supposed to generate GWs with large amplitude. Larger mass black holes emit in a frequency band of these events too low (below 1 Hz) to detect with the ground based detectors due to their limited scale and to the environmental noises. Intermediate mass Black holes recently observed by Chandra are turning out to be some of the most promising sources of strong and frequent sources of GW signal in the 5 to 100 Hz frequency range for the ground based interferometers [74]. The previously accepter, most promising sources for the ground-based detectors are the neutron star binaries, and supernova explosions. These events are expected to release GWs with typical strain amplitude of $h \sim 10^{-21}$, which corresponds to 10^{-18} m of stretch (or shrink) over distances of ~1 km. The frequency band of these events are expected to be between few Hz to few kHz.

1.2 Interferometric Detection of Gravitational Waves

The description and some formulations for the optical systems used to detect GWs are presented in this section.[6]

1.2.1 Michelson Interferometer

The Michelson interferometer is a optical configuration used to detect the phase difference accumulated in different optical paths. It is applied in various fields as metrology, solid state physics etc.. Laser interferometric GW detection is a very direct application of this optical system. The mirrors that form a Michelson interferometer must be allowed to follow the distorted spacetime: i.e. the mirrors must "float" in an inertial frame. In practice this fundamental requirement is achieved in the distortion direction by suspending each optical component of the interferometer from a pendulum.

Figure 1.2 is the sketch of a Michelson interferometer. The laser beam is emitted from the light source and split at the surface of the beam splitter (BS) into two orthogonal directions. At the end of each arm, there is a mirror which reflects the beam back to the BS. The the beams reflected from the arms recombine on the BS surface. A fraction of the recombined beam transmits through the BS and the rest is reflected from it. The intensity of each recombined beam is determined by the interferometer conditions and is detected by a photo detector (PD) that gives the signal from the apparatus.

Differential Michelson Interferometer

The electric field of the input beam at the surface of the BS is described as

$$E = E_0 \exp\left[i\Omega t\right]. \tag{1.9}$$

Here E_0 is the amplitude of the electric field and Ω is the optical angular frequency (the initial phase is set to zero for simplicity). The electric fields of the beams returning from the interferometer are written as

$$E_1 = E_0 \exp\left(i\Omega t\right)\left[r_{bs}^2 r_1 \exp\left(-i\theta_1\right) + r_2 t_{bs}^2 \exp\left(-i\theta_2\right)\right], \tag{1.10}$$

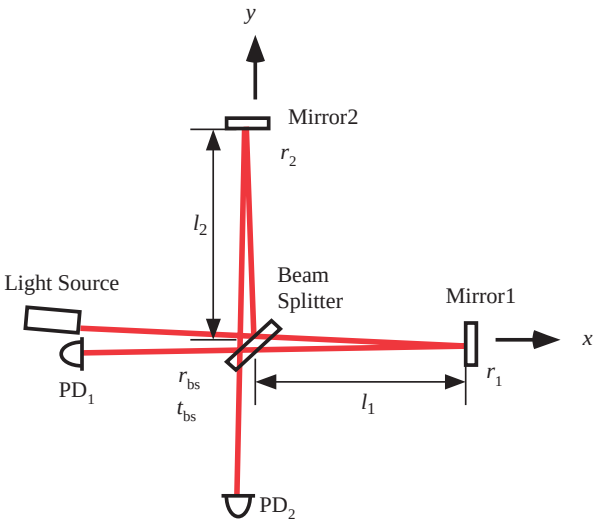

Figure 1.2: Frequency response of simple Michelson interferometer. The baseline length of 150 km is optimized for the GW at 1 kHz.

$$E_2 = E_0 r_{bs} t_{bs} \exp(i\Omega t) \left[r_1 \exp(-i\theta_1) - r_2 \exp(-i\theta_2) \right]. \tag{1.11}$$

Here r_{bs}, r_1, r_2 are the amplitude reflectance of the BS, that of the mirror1, and one for the mirror2. t_{bs} is the amplitude transmittance of the BS. θ_1 and θ_2 are the phase delay caused by the round trip in each the arm. The returning beams are detected by the PDs in each port, and the current in each PD is obtained from the above equations, as

$$I_1 = \alpha_1 |E_1|^2 = E_0^2 \left[\left(r_{bs}^2 r_1 \right)^2 + \left(t_{bs}^2 r_2 \right)^2 + 2 t_{bs}^2 r_{bs}^2 r_1 r_2 \cos(\Delta\theta) \right], \tag{1.12}$$

$$I_2 = \alpha_2 |E_2|^2 = E_0^2 \left(r_{bs} t_{bs} \right)^2 \left[r_1^2 + r_2^2 - 2 r_1 r_2 \cos(\Delta\theta) \right], \tag{1.13}$$

where $\Delta\theta = \theta_1 - \theta_2$ is the difference of the round trip phase in the arms, and α_1, α_2 are the efficiencies of the PDs. The visibility of the interferometer is defined as

$$v = \frac{I_{max} - I_{min}}{I_{max} + I_{min}} = \frac{(r_1 + r_2)^2 - (r_1 - r_2)^2}{(r_1 + r_2)^2 + (r_1 - r_2)^2}, \tag{1.14}$$

where I_{max} and I_{min} correspond to the maximum and to the minimum intensity of the light in either PD. The visibility is a measure of symmetry of the reflectivity of the mirrors. When they are fully symmetric ($r_1 = r_2$), the visibility takes the maximum value, 1.

In the differential operation of the interferometer, the signal which gives the differential phase is the difference of the signal from the PD $I = I_1 - I_2$.

When the system is fully symmetric, i.e. under the conditions of $t_{bs}^2 = 1/2$, $r_{bs}^2 = 1/2$, and $\alpha_1 = \alpha_2 = \alpha$, the output signal is simplified as

$$I = \alpha E_0^2 r_1 r_2 \cos(\Delta\theta). \tag{1.15}$$

Therefore, the interferometer has linear response to the phase difference, around the points where $\Delta\theta = n \times \pi/2$ (n is any integer).

Response to the Gravitational Waves

We define the frequency response of the optical system $H^x(\omega)$ as follows:

$$\Delta\theta = \theta_0 + \int_{-\infty}^{+\infty} x(\omega) H^x(\omega) e^{i\omega t} \mathrm{d}\omega. \tag{1.16}$$

Here θ is the phase shift detectable by the optical system, and θ_0 is the offset in phase. The second term in the right hand of the above equation is the dynamic phase shift caused by a physical input to the optical system $x(\omega)$, expressed by its inverse Fourier transformation.

The frequency response of a simple Michelson interferometer to the GW is derived by computing the dynamic phase shift during the propagation of the laser beams in the arms of the interferometer. It is formulated as [13]:

$$H_{\mathrm{MI}}^{\mathrm{GW}}(\omega) = \frac{2\Omega}{\omega} \sin\left(\frac{\omega l}{c}\right) \exp\left(-i\frac{\omega l}{c}\right). \tag{1.17}$$

Here l is the average arm length. For simplicity we assumed that the GW is propagating along the z axis and that the direction of the two orthogonal oscillation of one of the polarization is parallel to the arms of the interferometer. The frequency response of the interferometer is plotted in figure 1.3. The corner frequency is given as

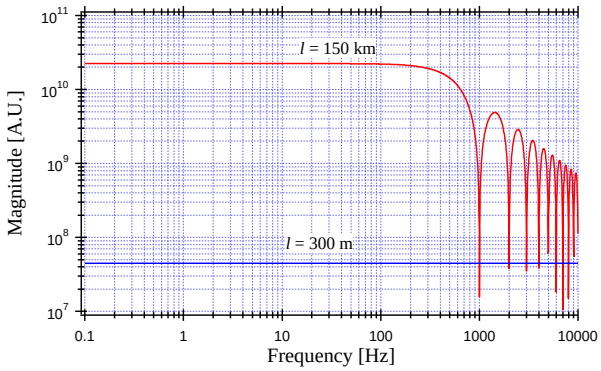

Figure 1.3: Frequency response of simple Michelson interferometer. The baseline length of 150 km is optimized for the GW at 1 kHz.

$$f_0 = \frac{c}{2l}, \tag{1.18}$$

below that frequency, the interferometer response is constant.

Response to the Vibration of the Mirrors

When the mirrors in the interferometer moves along the optical axes around their nominal position, they causes a phase shift detectable by the interferometer. The frequency response of a Michelson interferometer to the mirror motion is obtained in a similar way to the one used to derive the response to the GW. Instead of using the geodesic equation, we simply compute the propagation time of the beam to calculate the dynamic phase shift.

The frequency response to the mirror motion is written as:

$$\begin{aligned} H_{\mathrm{MI}}^{L-}(\omega) &= \frac{2\Omega}{c}\cos\left(\frac{\omega l_-}{c}\right)\exp\left(-i\frac{\omega l}{c}\right), \\ H_{\mathrm{MI}}^{L+}(\omega) &= \frac{2\Omega}{c}\sin\left(\frac{\omega l_-}{c}\right)\exp\left(-i\frac{\omega l}{c}\right). \end{aligned} \tag{1.19}$$

Here l_- and l are defined as $l_- = l_1 - l_2$. H_{MI}^{L-} and H_{MI}^{L+} are the response to the common and differential motion of the mirrors, respectively. When the interferometer has equal length for both arms, it is insensitive to the common motion and the response to the differential motion is simplified as

$$H_{\mathrm{MI}}^{L-}(\omega) \sim \frac{2\Omega}{c}\exp\left(-i\frac{\omega l}{c}\right), \tag{1.20}$$

under the conditions that $\omega l/c \ll 1$. Also the response to the GW is

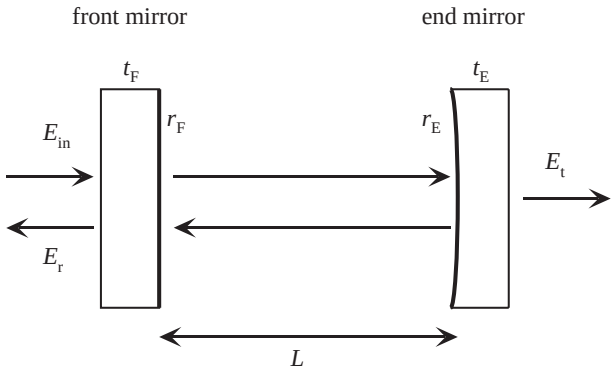

Figure 1.4: Schematic view of a Fabry-Perot cavity.

related to the response to the mirror motion as

$$H_{\mathrm{MI}}^{\mathrm{GW}}(\omega) \sim \frac{2\Omega}{\omega}\frac{\omega l}{c}\exp\left(-i\frac{\omega l}{c}\right) = lH_{\mathrm{MI}}^{L-}(\omega), \tag{1.21}$$

in this approximation.

1.2.2 Fabry-Perot Cavity

A Fabry-Perot resonator is a standard optical component in the GW experiments. It works as an integrator of the dynamic phase shift due to GW or mirrors' motion. Here we review the frequency response of a single Fabry-Perot cavity.

A Fabry-Perot cavity is formed by two mirrors facing each other as shown in figure 1.4. r_{F} and t_{F} are the amplitude reflectivity and the amplitude transmissivity of the front mirror. r_{E} and t_{E} are those of the end mirror. L is the distance of the surface of the two mirrors.

The cavity is illuminated by a laser beam with an amplitude of the electric field of

$$E_{\mathrm{in}} = E_0 e^{i\Omega t}. \tag{1.22}$$

The amplitude of the light reflected by the cavity and the one transmitted through it is written as

$$E_{\mathrm{r}} = \left(\frac{t_{\mathrm{F}}^2 r_{\mathrm{E}} \mathrm{e}^{-i\Phi}}{1 - r_{\mathrm{F}} \mathrm{r}_{\mathrm{E}} \mathrm{e}^{-\Phi}} - r_{\mathrm{F}}\right) E_{\mathrm{in}} \equiv r_{\mathrm{cav}} E_{\mathrm{in}} \tag{1.23}$$

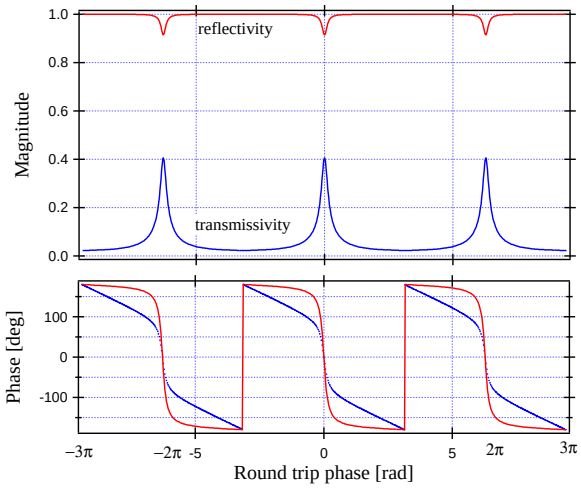

Figure 1.5: Response of a Fabry-Perot cavity. The optical parameters of the mirror were chosen arbitrarily to obtain clear view.

$$E_{\rm t} = \frac{t_{\rm F}^2 r_{\rm E} {\rm e}^{-i\Phi}}{1 - r_{\rm F} {\rm r}_{\rm E} {\rm e}^{-\Phi}} E_{\rm in} \equiv t_{\rm cav} E_{\rm in}, \tag{1.24}$$

where $\Phi = 2L\Omega/c$ is the round trip phase advance of the cavity, and $r_{\rm cav}$, $t_{\rm cav}$ are the amplitude reflectivity and transmissivity of the cavity. They are plotted in figure 1.5 as a periodic functions of the round trip phase Φ. The transmitted light has maximum amplitude when the cavity resonates to the input beam: i.e. the round trip phase satisfies

$$\Phi = 2n\pi, \tag{1.25}$$

therefore

$$L = n\pi \frac{c}{\Omega} = n\lambda, \tag{1.26}$$

or

$$\Omega_0 = n\pi \frac{c}{L}, \tag{1.27}$$

where λ is the wavelength of the input laser, and n is an integer. Ω_0 is the period of the functions and $\nu_0 = \Omega_0/(2\pi)$ is called free spectral range.

From the equation (1.24), we can compute the intensity of the transmitted light, and using the full-width half-maximum (FWHM) of its peak, we

define the finesse of the cavity as

$$F \equiv \frac{\pi}{\mathrm{FWHM}} = \frac{\pi\sqrt{r_{\mathrm{F}} r_{\mathrm{E}}}}{1 - r_{\mathrm{F}} r_{\mathrm{E}}}, \tag{1.28}$$

and it is related to the storage time τ and the average number of round trip N in the cavity as

$$\begin{array}{rcl} \tau & = & \frac{2L}{\pi c} F \\ N & = & \frac{2}{\pi} F. \end{array} \tag{1.29}$$

Response to the Gravitational Waves

The frequency response of a Fabry-Perot cavity to the GW is written as

$$H_{\mathrm{FP}}^{\mathrm{GW}}(\omega) = \alpha \frac{\Omega}{\omega} \frac{\sin\gamma}{1 - r_{\mathrm{E}} r_{\mathrm{F}} \mathrm{e}^{-2i\gamma}} e^{-i\gamma}. \tag{1.30}$$

For simplicity, we assume that the cavity is locked to the resonance. Then α and γ are defined as

$$\begin{array}{rcl} \alpha & \equiv & \frac{t_{\mathrm{F}}^2 r_{\mathrm{E}}}{-r_{\mathrm{F}} + r_{\mathrm{E}}\left(r_{\mathrm{F}}^2 + t_{\mathrm{F}}^2\right)}, \\ \gamma & \equiv & \frac{\omega L}{c}. \end{array} \tag{1.31}$$

When the GW is dominated by low frequency component, which satisfies $\gamma \ll 1$, the amplitude of the frequency response function is approximated as

$$\left| H_{\mathrm{FP}}^{\mathrm{GW}}(\omega) \right| \sim \frac{\alpha \Omega L}{c\left(1 - r_{\mathrm{E}} r_{\mathrm{F}}\right)} \frac{1}{\sqrt{1 + (\omega\tau)^2}},$$

where τ is the storage time of the cavity defined in equation (1.29). Here we regard a Fabry-Perot cavity as a single optical pole with the corner frequency of

$$f_0 = \frac{1}{2\pi\tau}. \tag{1.32}$$

In the low frequency limit ($\omega\tau \ll 1$), the response of the cavity becomes constant.

Response to the Vibration of the Mirrors

The frequency response of a Fabry-Perot cavity to its length fluctuation is written as

$$H_{\mathrm{FP}}^{L}(\omega) = 2\alpha \frac{\Omega}{\omega} \frac{e^{-i\gamma}}{1 - r_{\mathrm{E}} r_{\mathrm{F}} \mathrm{e}^{-2i\gamma}}, \tag{1.33}$$

when it is in resonance. It is simply related to the the response to the GW:

$$H_{\mathrm{FP}}^{L}(\omega) \sim \frac{2}{L} H_{\mathrm{FP}}^{\mathrm{GW}}(\omega). \tag{1.34}$$

Pound-Drever-Hall Technique

The Pound-Drever-Hall (PDH) technique is commonly used to detect the cavity length fluctuation of the interferometer [17]. In this method, the cavity is illuminated by the laser which comprises three components: the carrier and two sidebands generated by an Electro-Magnetic Modulator (EOM) driven at a radio modulation frequency. The sideband frequency differs from the laser frequency by the modulation frequency in opposite direction, and two sidebands have opposite phase.

When the carrier resonates with the the Fabry-Perot cavity, the sidebands are rejected by it if the modulation frequency is not equal to a FSR. The phase of the carrier leaked back from the cavity is strongly shifted by the cavity length fluctuation according to the frequency response of the Fabry-Perot cavity. The idea of the PDH is to use the sidebands as a phase reference. As the PD located at the reflection port detects the interference of the phase-shifted carrier and the sidebands, the output signal of the PD consists of the RF modulation frequency component that corresponds the difference between the carrier frequency and the resonant frequency of the cavity. By demodulating this signal, one can extract a signal proportional to the phase shift: i.e. the length fluctuation of the cavity (see figure 1.5).

1.2.3 Fabry-Perot Michelson Interferometer (FPMI)

A Fabry-Perot Michelson interferometer (FPMI) is a Michelson Interferometer instrumented with a Fabry-Perot cavity instead of a single mirror in each arm. The frequency response of an FPMI to GW is (see figure figure 1.6)

written as:

$$H_{\mathrm{FPMI}}^{\mathrm{GW}} = 2\alpha \frac{\Omega}{\omega} \frac{\sin\gamma \times e^{-i\gamma}}{1 - r_{\mathrm{E}} r_{\mathrm{F}} \mathrm{e}^{-2i\gamma}}. \tag{1.35}$$

The cut off frequency of the FPMI is defined by the FP cavity pole and the interferometer can be regarded as a Michelson interferometer with the effective arm length of $l_{\mathrm{eff}} = 2LF$. In the low frequency limit ($\omega L/c$), the Fabry-Perot cavity works as an amplifier of the phase delay in the arm.

1.2.4 Noise Sources in GW Detectors

Because of extremely small interaction of GW with matters, gravitational wave signals can be easily covered by various noises. In this section we list the main expected sources of noise in gravitational wave detectors. As the seismic noise relates to the main subject of this thesis, it will be described independently in the next section.

Thermal Noise

The test masses of GW detectors are immersed in the thermal bath and exchange energy with it through dissipation mechanisms. The energy exchange causes the thermal motion of the test masses and their surfaces, which is a fundamental noise for GW detection. In the fluctuation-dissipation theorem [19], the dissipated energy is re-injected into the mechanical system as a fluctuation force F_{th} which is related to the dissipation of the system as

$$F_{\mathrm{th}}^2 = 4k_{\mathrm{B}}T\mathrm{Re}\left(Z\left(\omega\right)\right). \tag{1.36}$$

Here k_{B} is the Boltzmann constant, T is the temperature of the system, and $Z\left(\omega\right)$ is the mechanical impedance of the object defined as

$$Z\left(\omega\right) = \frac{f_{\mathrm{ex}}\left(\omega\right)}{\mathrm{v}\left(\omega\right)}, \tag{1.37}$$

where f_{ex} is the force exerted onto the object whose thermal motion is of interest, and $v\left(\omega\right)$ is its velocity response to the external force. From equation (1.36) and (1.37), the thermal motion of the object is written as

$$x_{\mathrm{th}} = \sqrt{\frac{-4k_{\mathrm{B}}T}{\omega}\mathrm{Im}\left(H_f\left(\omega\right)\right)}, \tag{1.38}$$

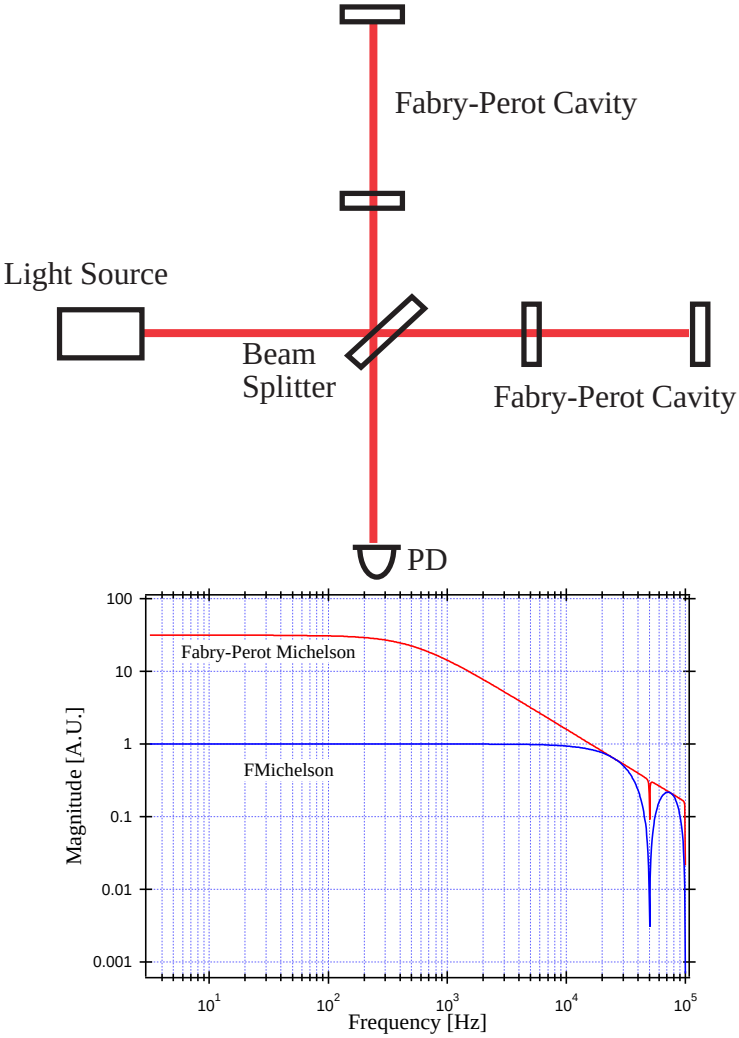

Figure 1.6: Fabry-Perot Michelson interferometer (above), and its frequency response to gravitational waves. The arm length of the FPMI and the Michelson interferometer is 3 km. The reflectivity of the mirrors used in the FPMI is chosen to realize finesse of 50.

where $H_f \equiv x/f_{\rm ex}$ is the frequency response of the object to the external force. In the case of a harmonic oscillator with frequency-independent dissipation (structural damping), its thermal motion is expressed as

$$x_{\rm th}^2 = \frac{4k_{\rm B}T}{m\omega\omega_0^2}\frac{\phi}{\left(1-\frac{\omega^2}{\omega_0^2}\right)^2+\phi^2}, \tag{1.39}$$

Here ω_0 is the resonant frequency of the oscillator, and ϕ is a constant loss angle related to the quality factor of the oscillator as $Q = 1/\phi$. To reduce the thermal motion, one needs to use high quality material, or to lower the temperature. The thermal noise is a thermal motion of the test masses in GW detectors, and comprises the contributions from different modes.

Pendulum Mode As the test masses are suspended by a pendulum to realize GW detection, the pendulum causes some thermal motion. From the fundamental requirement, the resonant frequency of the pendulum must be much lower than the GW detection frequency band, therefore its thermal motion in the band is approximated as [6]

$$x_{\rm th,pend}^2 \sim \frac{4k_{\rm B}T\omega_0^2}{m\omega^5 Q_{\rm pend}}. \tag{1.40}$$

Here the quality factor of the pendulum is defined by the intrinsic loss of the wire material, and the dilution factor γ. The energy of the pendulum is mostly stored as the lossless gravitational potential energy, while the suspension wire contributes only little. The dilution factor of 100 has been reported [20]. Typical quality factors of metallic suspension are measured to be of the order of 10^6, while higher values have been reported for fused silica fibers suspensions [21].

Internal Mode The wires used in the suspension for test masses, and test masses themselves have limited rigidity. Consequently they have elastic internal modes: i.e. violin modes for the wires, and drum modes for the masses. These modes can be thermally excited as well. In the modal expansion approach, these internal modes are expressed as independent harmonic oscillators and contribute to the thermal noise with no correlation as

$$x^2_{\rm th,int} \sim \frac{4k_{\rm B}T}{\omega} \sum_j \frac{\omega_j^2 \phi_j}{m_j \left[\left(\omega_j^2 - \omega^2 \right)^2 + \omega_j^4 \phi_j^2 \right]}. \tag{1.41}$$

Here ω_j and ϕ_j are the natural frequency and the loss angle of the j-th mode, and m_j is the effective mass of the mode. While the fundamental internal resonant frequency of the test masses tends be of the order of 10 kHz, much higher than the GW detection band, the first violin mode frequency is usually of the order of 100 Hz. Thence some violin modes may be located in the GW detection band. Their thermal motion disturbs the measurements only at the resonant frequencies and will not be a serious problem for GW detection.

Quantum Noise

Photon Shot Noise A Michelson interferometer is a device which converts the phase difference accumulated in its arms to the power variations of the recombined beam, and the number of photons in the return beam is counted by a photo diode to obtain the electric signals. The accuracy of photon counting is limited by the quantum nature of photons. The number of photon is proportional to the power of incident light $P_{\rm in}$, and it fluctuates following the Poisson distribution $\sqrt{P_{\rm in}}$. As a result, the accuracy of photon counting is proportional to $\sqrt{1/P_{\rm in}}$. This is called shot noise. To reduce the shot noise, one needs to increase the input beam power to the interferometer. The most straightforward approach is to implement high power laser as a light source of the detector. There is also a technique, the so-called power recycling, used to re-inject the beam reflected by an interferometer operated on its dark hinge by interposing a mirror between the interferometer and the light source.

Radiation Pressure Noise The photons in the beam resonating in the Fabry-Perot arm cavities of an FPMI impinge on the surface of the mirrors, and yield momentum onto them. Thence the statistic distribution of the number of photons causes non-stationary pressure on the mirrors and causes fluctuation of the mirror position, proportional to $\sqrt{P_{\rm in}}$. If one increases the power of light in the cavities to reduce the shot noise, the radiation pressure noise increases correspondingly. Therefore, there is an optimal laser power

with which the sum of the shot noise and the radiation pressure noise is minimized at a given frequency. The strain sensitivity corresponding to the minimum noise as a function of frequency is called *standard quantum limit*. However, the radiation pressure noise caused by currently available lasers (with output power of the order of 10 to 100 W) is negligible with respect to the contribution of the shot noise.

Noise of the Laser

Intensity Fluctuation As an interferometric GW detector is operated at the *dark fringe* of the Michelson, where the beams reflected by two arms cancels each other at the output port, the intensity fluctuation of its light source in principle does not affect the noise of the detector. In principle. But in practice, the dark fringe condition is realized only within a limited precision, due to the finite control gain, the residual length fluctuation of the interferometer arms δx. etc.. In such conditions, the power fluctuation of the input beam couples to the output signal of the interferometer as $\delta x_{\rm int} = \delta P_{\rm in}/P_{\rm in}\delta x$. However, usually the output signal of the interferometer is obtained at the phase modulation frequency for the PDH technique, which is of the order of 10 MHz, where the laser intensity fluctuations are negligible with respect to the shot noise.

Frequency Fluctuation As the interferometer is sensitive to the phase difference in the two arms, the fluctuation of the frequency of the laser will be detected if the optical path length of the two arms is not perfectly equal. The asymmetry of the optical path can be easily imposed by the difference of the arm length, or finesse of the arm cavities, residual gas density and etc.. Usually GW detectors require extremely high stability for the laser frequency, and which is realized by using a suspended triangular ring cavity[3], so-called a *mode cleaner,* and one of the arms of the FPMI is used, as a reference for the frequency stabilization.

The mode cleaner consists of three mirrors suspended like the test masses of the main interferometer, to form a ring cavity, with typical arm length of the order of 10 m. The laser frequency is locked to it by the appropriate control system. The mode cleaner is locked to the $\rm TEM_{00}$ mode of the laser and is used also to reject higher spatial modes of the laser.

[3]In some GW projects, a rigid cavity is used for pre-stabilization as well.

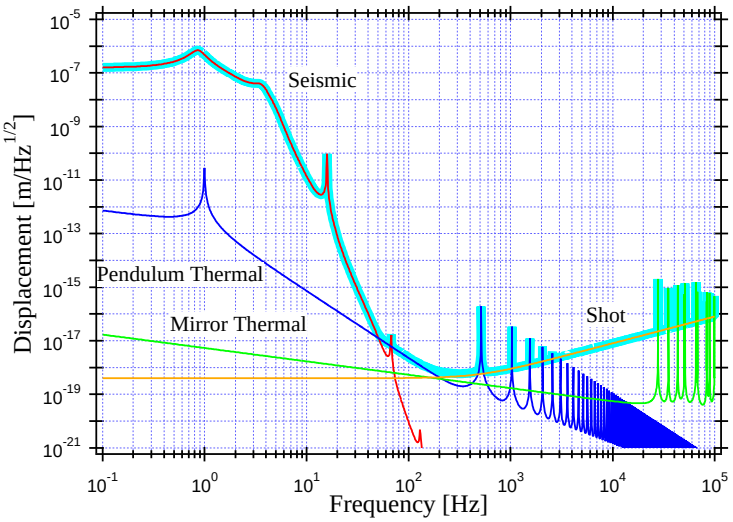

Figure 1.7: Typical noise budget of an interferometric gravitational wave detector, taken from the design of TAMA300.

1.3 Seismic Noise

1.3.1 Overview

Seismic motion is an inevitable noise source for interferometers built on the Earth's crust. The signal of an interferometer caused by the continuous and random ground motion is named *seismic noise*. The ground motion transmitted through the mechanical connection between the ground and the test masses results in perturbations the test masses separation. Seismic motion is excited by the natural phenomena like macro-seismic, oceanic, and atmospheric activities, as well as by the human activities.

The ground motion transmits to the motion of the test masses through different paths. The most straightforward path is that the horizontal ground motion at the suspension point of the test mass causes the longitudinal motion of the test mass. Since the ground motion is of the order of 10^{-6} m and the expected GW signal is 10^{-18} m, we need attenuation factors of the order of 10^{-12}. The ground motion in the other degrees of freedom can also cause noise in the interferometer. As the GW interferometer with long arm length is constructed on the Earth, which has finite curvature, the direction of verticality (local gravity) at the test different locations of the masses converge to the center of Earth and therefore are not parallel (figure 1.8).

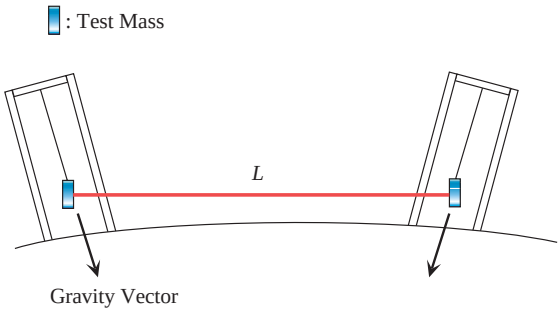

Figure 1.8: Vertical-Horizontal coupling of the mirror motion caused by misalignment of gravity vectors.

Thence the *local* vertical motion of the test mass Δz appears in the *global* horizontal motion Δx detectable with the interferometer, with the relation of $\Delta x = \alpha \Delta z$, where $\alpha = L/r_0$ (r_0 is the radius of Earth) and this trivial coupling factor (less than 10^{-3}) is negligible with respect to the much larger other couplings ($\sim< 1\%$) imposed by practical reasons. Comparing these $\sim$percent horizontal to vertical couplings with the required 10^{-12} attenuation factors, one easily see the necessity of the seismic attenuation also in the vertical direction, and in the angular d.o.f. as well.

The spectra of the horizontal ground motion at various sites are shown in figure 1.9. As the amplitude of the ground motion in general is larger at lower frequencies, the seismic motion will primarily limit the sensitivity of an interferometer in the low frequency band, usually below several tens of Hz (see figure 1.7). This is the most difficult frequency band to be attenuated by an appropriate seismic isolation system. Often, the typical amplitude of the ground motion is expressed in the form of

$$x = a/f^2 \quad [\mathrm{m}/\sqrt{\mathrm{Hz}}] \quad (f > 0.1\,\mathrm{Hz}), \tag{1.42}$$

where f is the frequency and a is a constant varying from 10^{-9} to 10^{-7} depending on the sites. However, by comparing with the spectra shown in figure 1.9, the above equation seems an oversimplification, omitting the obvious structures visible in the measured spectra. Below 100 Hz, typically the ground motion in Hongo and TAMA300 (Tokyo, Japan) is 10 to 1000 times noisier than that of Kamioka mine or of LIGO Hanford observatory. The broad peak commonly observed in Tokyo and at the LIGO site between 100 mHz to 300 mHz is the microseicmc motion induced by oceanic wave

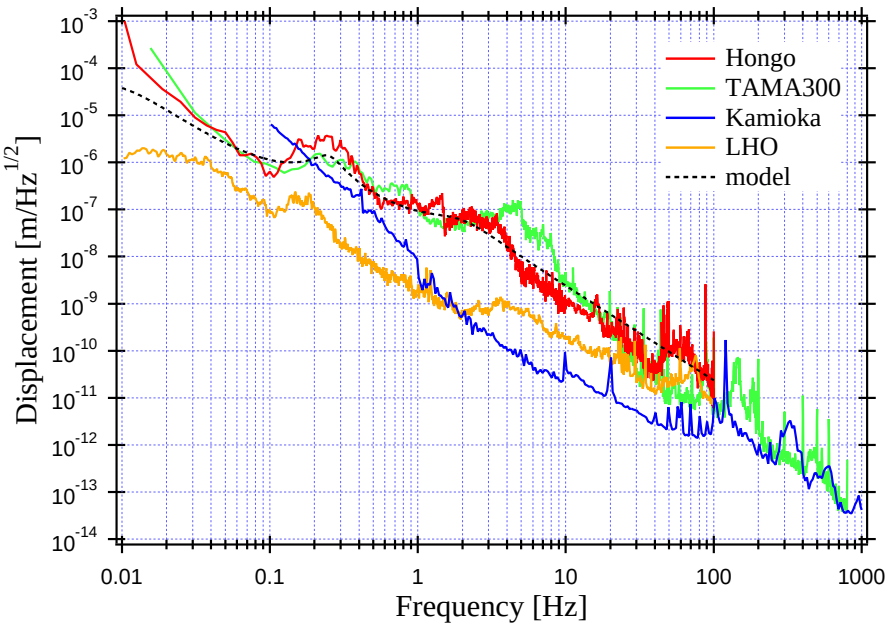

Figure 1.9: Seismic activities at the sites related to GW detectors. The dotted line shows the model of equation (1.43).

activities [18]. Also there is a flattened region between 1 Hz to several Hz in the Tokyo spectra. The structure is thought to be related to a characteristic crustal layer in the region, although a similar structure is observed at the LIGO site as well. At frequencies higher than 10 Hz, all the measurements imply the common asymptotic trend inversely proportional to the square of the frequency. Generally the ground vibrates isotropically, thence we assume the same amplitude of spectrum in the transversal and vertical direction. We constructed a more appropriated model of the ground motion in Tokyo, using a few double poles as follows.

$$\begin{aligned} x\left(f\right) \quad = \quad & \left[\left|\mathrm{LP}\left(f,0.01,0.75\right)\right| + 0.01 \times \left|\mathrm{LP}\left(f,0.25,2.5\right)\right| \right. \\ & \left. +0.001 \times \left|\mathrm{LP}\left(f,0.01,0.75\right)\right|\right] \times 5 \times 10^{-5}\ [\mathrm{m}/\sqrt{\mathrm{Hz}}], \end{aligned} \tag{1.43}$$

where

$$\mathrm{LP}\left(f,f_0,Q\right) \equiv \frac{f_0^2}{f_0^2 - f^2 + i\frac{f_0 f}{Q}}. \tag{1.44}$$

The spectrum computed with this model is also shown in figure 1.9. We

will use the above model as a standard to evaluate ground motion for Hongo and TAMA300 in the following discussion.

1.3.2 Ground Tilt

The ground motion is also excited in the rotational directions by the propagation of the seismic waves on the Earth's surface. The surface seismic waves is composed of Rayleigh waves (a mixture of longitudinal waves and transverse waves which produce the vertical ground motion) and Love waves (transverse wave associated to the horizontal ground motion). Although, there have been some attempts to observe the local rotation of ground, there no 'typical' amplitude established as for the translational motion. Therefore we apply a simple theory to estimate the rotation of the ground. In this model, the ground tilt is related to the vertical component of Rayleigh waves:

$$\theta = \frac{2\pi f}{c} S_{\mathrm{v}}. \tag{1.45}$$

Here θ and S_{v} are the power spectra of the ground tilt (in rad/$\sqrt{\mathrm{Hz}}$) and the vertical seismic motion (in m/$\sqrt{\mathrm{Hz}}$), and c is the local speed of the seismic waves. The propagation speed of the seismic waves depends on the properties of crust and it is also a function of frequency. However, from the past measurements of the speed of seismic waves, one can obtain nominal numbers for different frequency band as listed below [68]. Using these values and interpolating them with straight lines in the log plot, we can make models of the speed of seismic waves, shown in figure 1.10, for a typical surface location. From equation (1.45), lower speeds correspond to larger amplitude of the ground tilt, thus we use the low speed model to evaluate the upper limit of the ground tilt. The ground tilt estimated from the low speed model and equation (1.45) is shown in figure 1.11, which corresponds to the upper limit of the ground tilt. The coupling factor $2\pi f/c$ is also plotted in the figure. We assume isotropy and use this model for the ground rotation around all three axes.

1.3.3 Passive Mechanical Filters

Passive mechanical filtering is realized by utilizing the elasticity of mechanics. The simplest example is the bob suspended by a spring as illustrated in

freq. range	speed	main source
$f > 0.5$ Hz	$c \geq 10$ km/s	localized. human activities
0.5 Hz $> f >$ 0.05 Hz	$c \sim 3$ km/s	microseismic (oceanic activities)
0.05 Hz $> f >$ 1 mHz	$c = 5$ -30 m/s	atmospheric activities, windy
	$c = 300$ m/s	infrasound waves, when not windy

Table 1.1: Nominal speed of surface seismic waves. It depends on wind in the lowest frequency band.

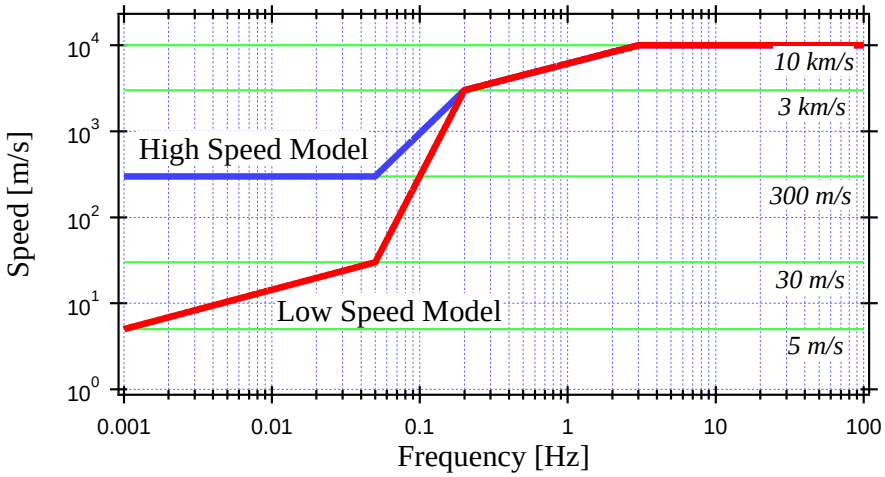

Figure 1.10: Assumed model for the speed of surface seismic waves.

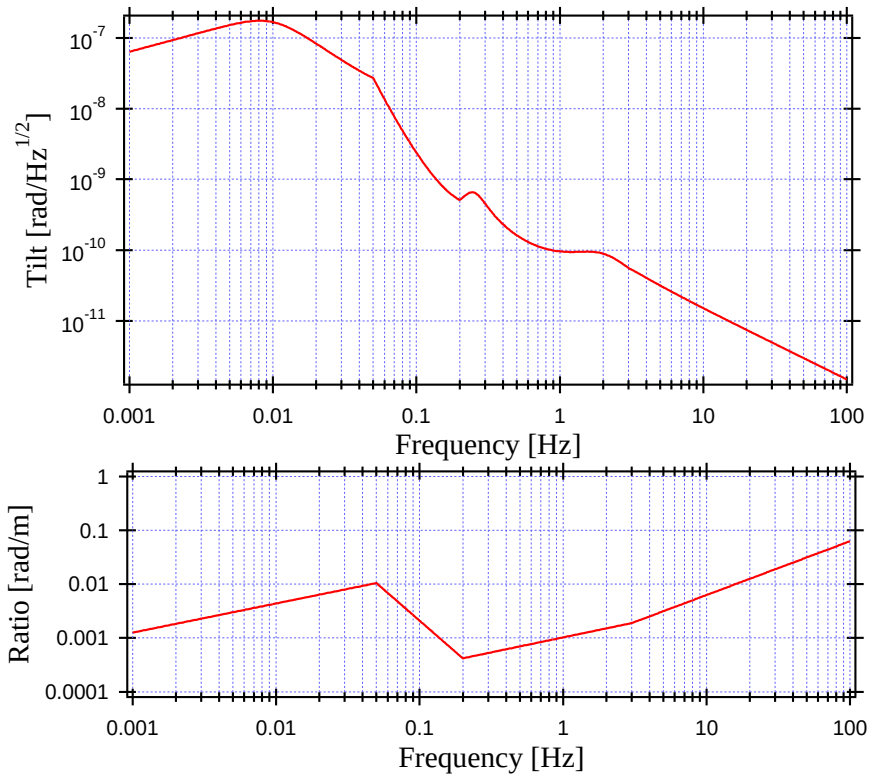

Figure 1.11: Standard model of ground rotation (above), with its coupling factor to the translational motion (below).

figure 1.12. Assuming that the bob can move only along x axis, its equation of motion in the frequency domain is written as:

$$-m\omega^2 x - M\omega^2 x_0 = -k\,(1+i\phi)\,(x-x_0) - i\gamma\omega x + f. \tag{1.46}$$

Here x and x_0 are the position of the bob and of the suspension point. m is the mass of the bob, while M is the parameter determined by the mass distribution in the spring. k is the stiffness of the spring. γ and ϕ represents the coefficient of the damping due to the viscosity of medium around the bob and the internal energy dissipation due to the spring. f is the external force applied on the bob. From the above equation, the motion of the bob is related to the motion of the suspension point and the external force as:

$$x = H_{\rm x}{\rm x}_0 + H_{\rm F} f, \tag{1.47}$$

where the motion transfer functions from the suspension point and from the external force to the bob are defined as:

$$\begin{aligned} H_{\rm x} &\equiv \frac{\omega_0^2(1+i\phi)+\frac{M}{m}\omega^2}{\omega_0^2(1+i\phi)-\omega^2+i\frac{\gamma}{m}\omega} \\ H_{\rm F} &\equiv \frac{1}{\omega_0^2(1+i\phi)-\omega^2+i\frac{\gamma}{m}\omega}. \end{aligned} \tag{1.48}$$

$\omega_0 = k/m$ is the angular resonant frequency of the system. Figure 1.13 shows the motion transfer function $H_{\rm x}$. One can see general behavior of mechanical filters:

1. The motion of the bob is equal to that of the suspension point at low frequencies ($\omega \ll \omega_0$).

2. The motion of the bob increases around the resonant frequency ω_0 and the phase rotates -90 degrees at the resonant frequency, and -180 degrees above it.

3. Above the critical frequency defined by $\omega_c = \sqrt{m/M}\omega_0$, the magnitude of the transfer function saturates at the level of M/m.

4. Between the resonant frequency and the critical frequency, the amplitude of the transfer function reduces proportionally to ω^{-2}. This corresponds to the suppressed transmission of the ground motion to the suspended object.

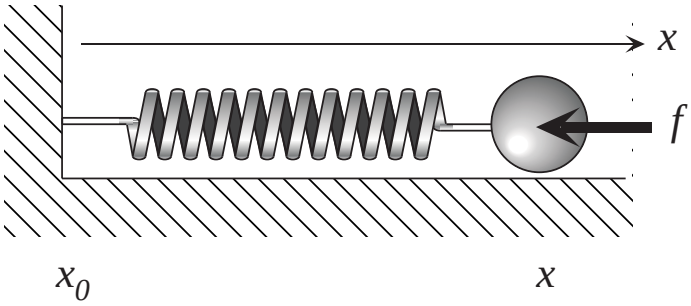

Figure 1.12: Simple example of a mechanical filter.

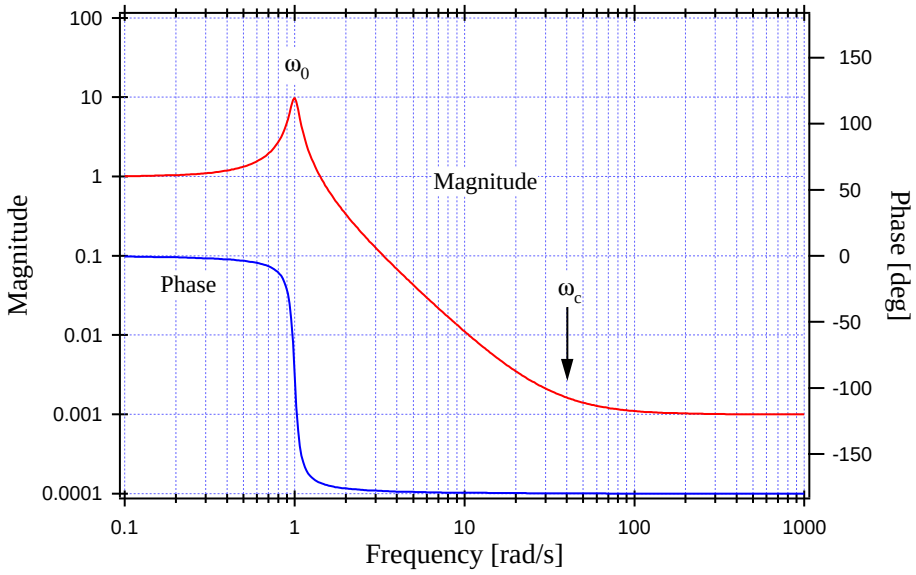

Figure 1.13: Standard transfer function of passive mechanical filters. The parameters are assumed as $\omega_0 = 1$ rad/s, $M = 10^{-3}$ kg, $m = 1$ kg, $\phi = 10^{-3}$, $\gamma = 0.1$ kg/s.

Some other remarks are needed. If there is no viscous damping ($\gamma = 0$), there is relatively small energy dissipation in the spring alone, we also define the *quality factor* of the mechanical system as the peak height at the resonant frequency. Under such a condition $Q = 1/\phi$. In the above calculation, we described the system as a combination of lumped elements, and assumed infinite rigidity. However, in the realistic case, mechanics have continuous mass distribution and limited rigidity, which result into internal resonances of the mechanical elements and energy transfers through the components' momentums of inertia. The realistic transfer function of a single pendulum will be discussed later in this article.

In the gravitational wave detectors, every test mass is suspended by a pendulum to behave as a free particle in the sensitive direction of the interferometer. This pendulum works as a seismic isolator as well. The typical resonant frequency of the pendulum is 1 Hz, and the mass ratio between the suspension wires and the test mass is very large thence we can very safely neglect the saturation of the attenuation performance at high frequencies. In such a case, at 100 Hz, the lowest frequency of the GW detection band, the attenuation factor provided by the pendulum is about 10^{-4}. From the simple model of the seismic motion (equation (1.42)), neglecting the vertical to horizontal cross-couplings, and assuming a quiet site $a = 10^{-9}$, the motion of the test mass induced by the seismic motion reaches of the order of 10^{-13} m/$\sqrt{\text{Hz}}$, corresponding to the strain $h \sim 10^{-16}$ to 10^{-15} depending on the scale of the detector. This is far above the required level (typically at least 10^{-21} in strain), and the attenuation performance needs to be improved. This improvement can be easily achieved by connecting the mechanical filters in series. In the high frequency approximation, the asymptotic trend of the attenuation factor improves to $1/f^{2n}$ where n is the number of the cascaded filters[4]. Thence by adding a few more stages above the mirror suspension, one can realize the required attenuation performance only by simply using the passive mechanics. An example of this strategy are the stack system composed by layers of rubbers and heavy stainless steel blocks interposed between the mirror suspension system and the ground in TAMA300, LIGO detectors, and GEO600. While LIGO is instrumented with a single pendulum for the mirror suspension, TAMA300 and GEO600 implemented more

[4]In reality, the cascaded filters interact with each other and result into complicated frequency response around their resonant frequencies.

project	detector type	arm length	location
LIGO	FPMI	4 km, 2 km	Hanford, US
		4 km	Livingston, US
Virgo	FPMI	3 km	Cacsina, Italy
GEO600	Delay-Line	600 m	Hannover, Germany
TAMA	FPMI	300 m	Tokyo, Japan

Table 1.2: First generation ground-based GW interferometers [7, 8, 9, 10].

efficient multi-stage suspension systems[5] [40, 30].

Another way to improve the isolation performance is to lower the resonant frequency of the mechanics. By shifting lower the resonant frequencies, one can greatly improve the attenuation performance at higher frequency. Virgo utilized this approach and realized extremely high attenuation performance starting at low frequency (4 to 6 Hz) with the low frequency isolation system coupled to a multi-stage suspension system, called Super Attenuator (SA) [46].

1.4 Current Circumstances and Purpose of this Work

There have been several interferometric GW detectors proposed and developed for direct detection of GW as listed in table 1.2. Particularly in the last couple of years, they made significant progress. LIGO and GEO600 were in commissioning stage, and Virgo proved extremely stable operation of their central Michelson interferometer thanks to the SA and implementing the arm FP cavities. TAMA is the most advanced one at present. They operated the detector over long duration, and acquired sufficient amount of data in reasonable quality for GW event search analysis[11, 12]. All these interferometers are expected to achieve the operation in the designed configuration and to start the GW observation in the next few years.

Following these successful results in these years, there are some programs proposed for the future with the aim to realize *GW astronomy* by the observation with refined sensitivity and reliability. LIGO is planning to upgrade the current interferometers with new technologies (Advanced LIGO), and the Japanese group proposed the construction of new detector with 3 km arm length. The key points for these next generation detectors:

[5] The detail of the TAMA vibration isolation system will be presented in the next chapters.

- Improvement of detector sensitivity in wide band starting from 10 Hz to several 100 Hz, to increase the event rate, and to detect GW from various sources.

- Improvement of duty cycle of the operation of the detectors, for continuous observation.

These goals require advanced technologies in all directions: higher laser power, lower thermal noise, and superior seismic attenuation at low frequencies. The seismic attenuation is particularly instrumental for the second goal.

The construction of the next generation detectors are scheduled after year 2005. The Japanese GW group also has a plan to install some of these advanced technologies into TAMA300. This 5 year intermediate mission, starting in 2002, has two main aims:

- To test the new technologies in the large scale interferometer.

- To upgrade TAMA300 and to run observations for GW detection with the refined performance.

The R&D of the advanced technologies are running at present for the coming installation. The Seismic Attenuation System (SAS) was initially designed for the Advanced LIGO, and then downgraded and reduced to adapt to the requirements of TAMA300. It was desired to design a simpler, more compact, more efficient than the Virgo SA, while maintaining its strong points, which are the completely passive attenuation (for reliability), the inertial damping of the resonances (to reduce the residual test mass motion), and the hierarchical controls (to reduce the control requirements). It was also desired to introduce the successful TAMA's magnetic passive damping (for added simplicity and reliability). To achieve these aims, we developed the MGAS filter technology described in chapter 3. Two MGAS filters have the attenuation performance to replace three Virgo filters and much more stable. As a result we could fulfill the TAMA requirements with a less than 2 meter tall tower and could replace with advantage the seven meter tall Virgo SA towers with four meter tall SAS ones.

It was a central part of this work to verify the operation soundness and attenuation performance of the towers before implementation in TAMA300.

The development was so promising that the SAS towers have been adopted "as is" to instrument a test Michelson interferometer in the University of Napoli, as a test facility for accelerometers in the University of Firenze, and Pisa. The SAS have also been tentatively baselined for the future LCGT.

1.5 Concept of the Seismic Attenuation System (SAS)

1.5.1 General Consideration

A typical GW event is supposed to generates the strain of 10^{-21} between few tens of Hz to few kHz, corresponding to the displacement of the test masses in 100 m to 1 km arm, of the order of 10^{-19}m to 10^{-18} m. This sets the *in-band* requirement of the displacement of the test masses. Therefore, every parameters of the interferometer must be optimized to be able to detect such small signals. Of course the seismic isolation system must be designed to suppress the seismic noise well below this level. There is also the *off-band* requirement to the residual motion of test masses. As the interferometer must be kept in the dark fringe condition, the motion of the test masses has to be suppressed at all frequencies to allow the control system to maintain the operation of the interferometer with the limited dynamic range. Figure 1.14 shows the spectrum of ground motion computed by the standard seismic model and its r.m.s. amplitude. When an r.m.s. amplitude is plotted as a function of frequency in this form, we define it as:

$$x_{\mathrm{rms}}(f) = \sqrt{\int_f^{f_{\max}} x_{\mathrm{psd}}^2(f)\,\mathrm{d}f}, \tag{1.49}$$

where x_{psd} is the power spectrum of the signal, and $f_{\max}$ is the highest frequency of a measurement or of a model. As one sees from the plot, the integrated displacement of the ground reaches values of the order of 1 μm. This is far above the residual motion required from the length control of the interferometer[6]. As the main contribution to the ground motion is concentrated in the low frequency band (below 10 Hz), this problem has to be solved by the seismic isolation system.

It is useful to summarize the general consideration for the design of a seismic isolation system at this point.

[6]Typically, the residual motion of the test masses need to be less than 10^{-12} m, and the dynamic range of the length control does not exceed 140 dB (10^7).

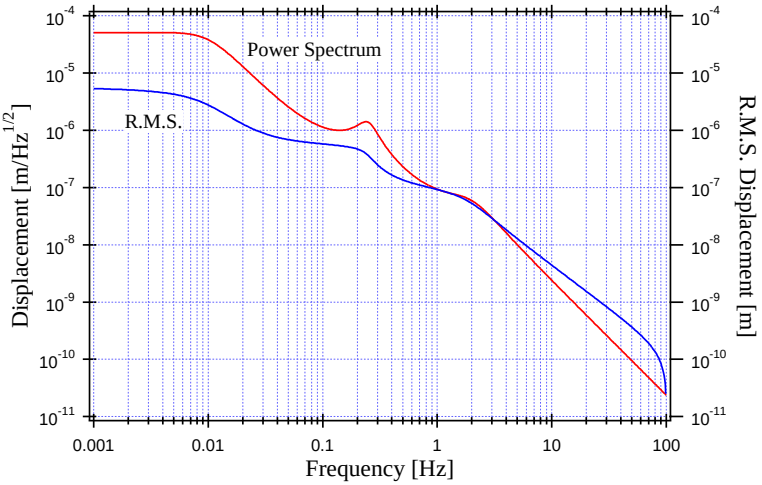

Figure 1.14: Standard seismic model.

1. *In-band requirement*: Typical mechanical filters have resonant frequency (f_0) of the order of 0.1 Hz to 1 Hz. As we saw in the previous chapter, the isolation performance of an ideal filter has the asymptotic behavior of $(f_0/f)^2$, and by using a chain of passive isolators one can obtain a suitable performance. The in-band requirement (the test mass motion has to be less than 10^{-19} m at the lowest frequency of interest) sets the minimum number of the filters and/or their resonant frequencies.

2. Filters are realized by pendulum in the horizontal direction and elastic elements like springs in the vertical direction. As their moving elements have finite mass (and momentum of inertia), their attenuation performance will meet a saturation level above a critical frequency. This limitation requires filters in addition to the minimum defined by the in-band requirement.

3. The motion of the test masses in every degree of freedom must be attenuated as well as in the longitudinal direction, because of the cross-couplings imposed by asymmetries of the mechanics and verticality considerations.

4. *Out-band requirement*: A mechanical filter with an ultra-low resonant frequency (below 100 mHz) works as a pre-isolation stage and suppresses the test mass motion at low frequencies which dominates its

the residual motion. The pre-isolation stage also can provide a way to position the test mass at low frequency.

5. Interferometers have extremely small range where they generate the linear signal proportional to the motion of the test masses. The lock of the detector must be acquired (and kept) while the masses are located within this linear range. This time to acquire lock is determined by the linear range of the detector and the residual velocity of the test masses. Thence, the test mass velocity must be suppressed as much as possible, to avoid the saturation of the interferometer control system. The pre-isolation stage is useful for this task as well.

6. The mechanical filters should have high quality to minimize the thermal noise. Particularly the final stage which suspends the test mass directly, must be composed by extremely high quality material like quartz or sapphire.

7. The high quality pendulums store large energy and move with large amplitude at their resonant frequency. This excessive motion may break the in and out-band requirements, and it may cause difficulties for the control of the interferometer. Therefore, the seismic isolation system needs to provide a way to damp these resonances without injecting unacceptable thermal (or control, depending on the damping method) noise. Also the seismic isolation system must not inject other noises like mechanical shot noise related to the internal friction of material beyond the requirement [22].

1.5.2 Baseline Design of SAS for TAMA300

The conceptual design of the SAS for TAMA300 is illustrated in figure 1.15. The SAS was designed to improve the low frequency sensitivity of TAMA300. In this upgrade, no improvement of thermal noise is planned. The most important in-band requirement is that the seismic noise must be substantially lower than the thermal noise above the lowest frequency of interest. We define this crossing frequency at 10 Hz, as a tentative, and aggressive, requirement. From the design of TAMA300, shown in figure 1.16, the thermal noise level at 10 Hz lays at 10^{-15} m/$\sqrt{\text{Hz}}$, while the expected ground motion at this frequency is 10^{-9} m/$\sqrt{\text{Hz}}$. Therefore the required minimum isolation

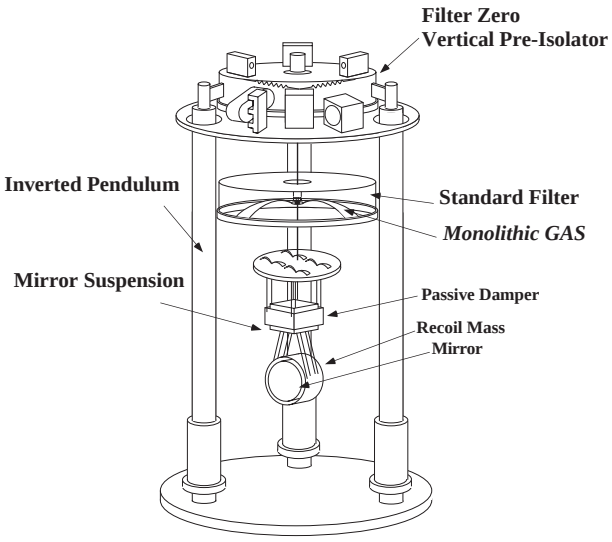

Figure 1.15: Conceptual design of SAS.

performance at 10 Hz is -120 dB. By assuming the resonant frequency of 1 Hz for each stage of the seismic attenuation system, at least three stages are needed. To have comfortable safety margin of 100, we decided to have five stages in our system. For the vertical attenuation, we used three stages of low frequency (few hundred mHz) springs described in chapter 4.

About the out-band requirements, it is a matter of control rather than just a passive attenuation. However, to attenuate the test mass motion at the frequency of the micro seismic peak (100 mHz to 300 mHz), and to provide an easy way to position the mirror at very low frequency, we implemented a pre-isolation stage with the resonant frequency of a few tens of mHz. This pre-isolation stage is realized with an inverted pendulum (IP) described in the next chapter.

The pre-isolator also provides earthquake protections for quakes of up to several mm of excitation, thanks to its dull response.

To suppress the residual motion of the system, we use the active damping scheme successfully demonstrated by Virgo [37, 42]. In this technique, explained in chapter 6, the motion of the IP is sensed by accelerometers and position sensors, and fed back to the IP itself through an appropriate servo system.

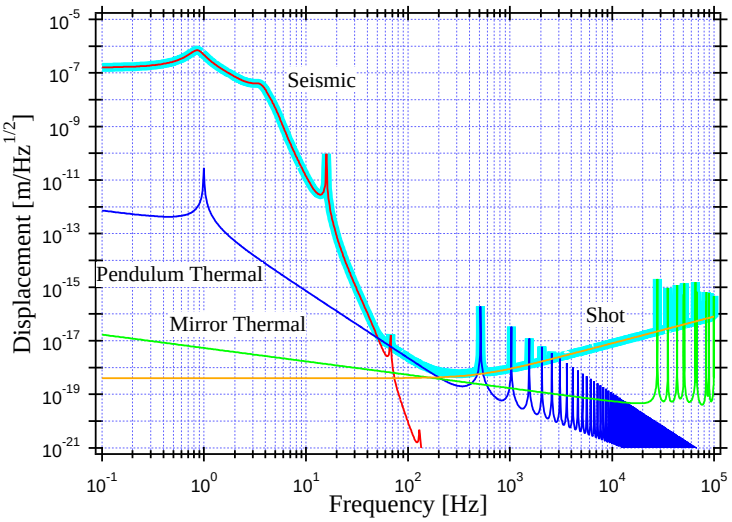

Figure 1.16: Noise budget of TAMA300 (Phase I, without the power recycling).

1.5.3 Scope and Outline of this Thesis

The works described in this thesis includes:

- Design of the new seismic isolation system for TAMA300: Mechanical components and control schemes.
- Prototype testing of the new seismic isolation system: Evaluation of the passive/ active isolation performance.
- Demonstration of operation of an interferometer with the prototype new seismic isolation system

This thesis is divided into 8 chapters.

- In this chapter 1,we explained the motivation of the work and some fundamental issues about the seismic isolation.
- From chapter 2 to 5, the individual passive mechanical components of the SAS are described along with their theoretical principles and experimental validations.
- Chapter 6 gives a description of the active damping used in the SAS.

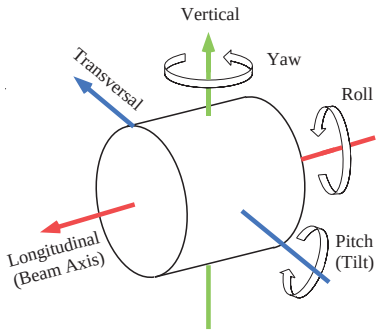

Figure 1.17: Definition of the coordinate system used in this article.

- In chapter 7, the demonstration of interferometer operation with SAS is presented.
- Chapter 8 contents the discussion and conclusions of this thesis.

Coordinate System

The coordinate system used in this article is defined in figure 1.17. The 'longitudinal direction' coincides with the axis of beam in interferometers. The names for the rotational degrees of freedom are taken from the customary aviation and nautical terminology.

Chapter 2

Inverted Pendulum

2.1 Design of Inverted Pendulum

2.1.1 Roles in Seismic Isolation

An inverted pendulum (IP) is a horizontal pre-isolation stage with ultra-low resonant frequency (below 100 mHz). The IP is implemented in the SAS, to achieve three main objectives:

- To provide sufficient attenuation at frequencies of the micro seismic peak (100 mHz to 300 mHz).
- To realize a mean to position the entire system, with a load of approximately 100 kg, without requiring large force (i.e. high power consumption).
- To provide a quasi-inertial stage on which to detect the recoil and actively damp the motion of the suspended chain. One can do this operation while taking advantage of the passive attenuation between the IP itself and the test mass at the bottom, to avoid actuation noise re-injection.

To achieve those aims, the IP is implemented using an elastic flex joint counteracted by a gravitational anti-spring. The principle and some practical problems are discussed in this section.

l	length of the IP leg
m	mass of the IP leg
I	momentum of inertia about the center of mass of the IP leg
M	mass of the payload
k_θ	rotatinal spring constant of the flex joint
(x, z)	position of the payload
(x_l, z_l)	position of the center of mass of the IP leg
(x_0, z_0)	position of the flex joint attachement to the ground
θ	angle of the IP leg with respect to the vertical axis

Table 2.1: Parameters for the simple IP model.

2.1.2 Working Principle of the IP

A simple model of the IP is illustrated in figure 2.1. The IP consists of a flex joint fixed to the ground, a rigid cylindrical leg connected onto it, and the payload on top of the leg. The payload, which is represented as a point mass in the model, is the object being isolated from the ground motion. Note that the IP leg is represented as a complete rigid body and its internal resonances are omitted in the models described in this section. The parameters for the mechanics in this model are defined as shown in a table 2.2.

In this model, the Lagrangian of the system L is expressed as

$$L = K - U, \tag{2.1}$$

$$K = \frac{1}{2}M\left(\dot{x}^2 + \dot{z}^2\right) + \frac{1}{2}m\left(\dot{x}_l^2 + \dot{z}_l^2\right) + \frac{1}{2}I\dot{\theta}^2 \qquad \text{(kinetic)}, \tag{2.2}$$

$$U = Mgz + mgz_l + \frac{1}{2}k_\theta\theta^2 \qquad \text{(potential)}, \tag{2.3}$$

with the geometrical constraints

$$\begin{aligned} x_l &= \tfrac{1}{2}(x + x_0) \\ z_l &= \tfrac{z}{2} \\ x &= l\sin\theta + x_0 \\ z &= l\cos\theta. \end{aligned} \tag{2.4}$$

Under these conditions, the Lagrangian of the system is simplified, by omitting the vertical component of the velocity:

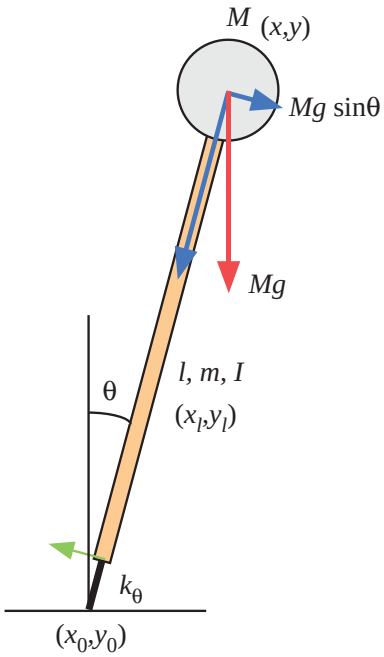

Figure 2.1: A schematic view of the IP, in the simple model.

$$K = \frac{1}{2}M\dot{x}^2 + \frac{1}{8}m\left(\dot{x} + \dot{x}_0\right)^2 + \frac{1}{2}I\left(\frac{\dot{x} - \dot{x}_0}{l}\right)^2 \tag{2.5}$$

$$U = Mgl\cos\left(\frac{x - x_0}{l}\right) + \frac{mgl}{2}\cos\left(\frac{x - x_0}{l}\right) + \frac{1}{2}k_\theta\left(\frac{x - x_0}{l}\right)^2. \tag{2.6}$$

The potential energy of the IP obtained from the above equation for the different payloads is shown in figure 2.2. When the IP is not loaded sufficiently, its potential energy can be approximated by a parabolic curve. The curve flattens out around the equilibrium point ($x = x_0$) as the system is loaded more. Beyond a certain level of load, the system will have bistability.

The Euler-Lagrange equation of motion is derived as:

$$\frac{\mathrm{d}}{\mathrm{d}t}\frac{\partial K}{\partial \dot{x}} = \frac{\partial U}{\partial x} \tag{2.7}$$

$$\left(M + \frac{m}{4} + \frac{I}{l^2}\right)\ddot{x} + \left(\frac{m}{4} - \frac{I}{l^2}\right)\ddot{x}_0 = -\left\{\frac{k_\theta}{l} - \left(\frac{m}{2} + M\right)g\right\}\frac{x - x_0}{l}, \tag{2.8}$$

in the first order, and it has the form of the equation of motion of a

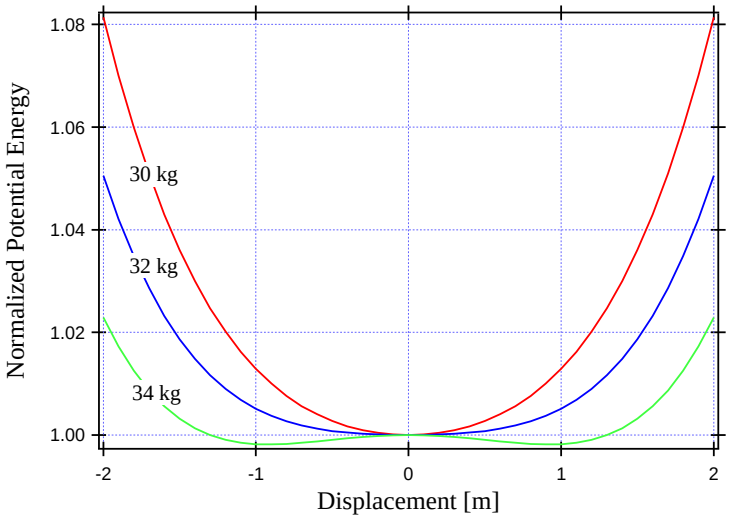

Figure 2.2: Potential Energy of the IP.

harmonic oscillator, with an effective spring constant,

$$k_{\text{eff}} = \frac{k_\theta}{l^2} - \left(\frac{m}{2} + M\right)\frac{g}{l}. \tag{2.9}$$

The first term of k_{eff} corresponds to the elastic restoring force of the flex joint, while the rest represents a repulsive force, so called *gravitational anti-spring* force. With the gravitational anti-spring effect, the cumulative spring constant of the joint is effectively reduced. Note that the effect of the anti-spring is proportional to the mass of the leg and the payload and it can be tuned by changing the payload. One can replace k_θ by a complex spring constant $k_\theta\,(1 + i\phi)$ to impose energy dissipation with the loss angle of ϕ in the flex joint.

A stable IP has only one equilibrium point, as both the flex joint and the gravitational anti-spring have quadric form of potential energy around it. From the equation (2.8), the resonant frequency of the IP will be determined as

$$f_0 = \frac{1}{2\pi}\sqrt{\frac{k_{\text{eff}}}{M + \frac{m}{4} + \frac{I}{l^2}}}. \tag{2.10}$$

Let's consider an example of an IP, with a set of parameters, shown in table 2.2. If the aspect ratio of the leg is small enough, its momentum of inertia satisfies the approximation, $I \sim \frac{ml^2}{12}$. From equation 2.9, the

m	3 kg
k_θ	700 N/rad
l	2 m

Table 2.2: typical parameters for the linear spring model.

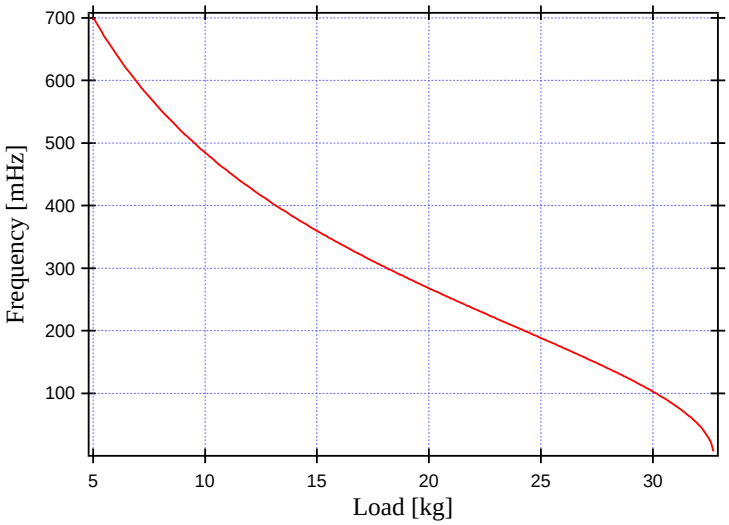

Figure 2.3: IP resonant frequency as a function of payload.

maximum allowed value for M to keep the system stable is $M_{\text{critical}} = 32.714$ kg. The dependency of the resonant frequency on the payload is shown in a figure 2.3.

By solving the equation (2.8) in the Fourier domain, one obtains the motion transfer function between the ground and the payload $H_{\text{IP}}(\omega)$.

$$H_{\text{IP}}(\omega) = \frac{x}{x_0} = \frac{k_{\text{eff}} + (\frac{m}{4} - \frac{I}{l^2})\omega^2}{k_{\text{eff}} - (M + \frac{m}{4} + \frac{I}{l^2})\omega^2} \tag{2.11}$$

The Bode plot of the transfer function of the sample IP is shown in figure 2.4, for varying payload. The transfer function of the ideal harmonic oscillator is also shown for comparison.

2.1.3 Center of Percussion Effect

In the figure 2.4, the transfer function of the IP behaves similarly to that of the harmonic oscillator up to somewhere above the resonant frequency. While the standard oscillator shows infinite capability of attenuation, the

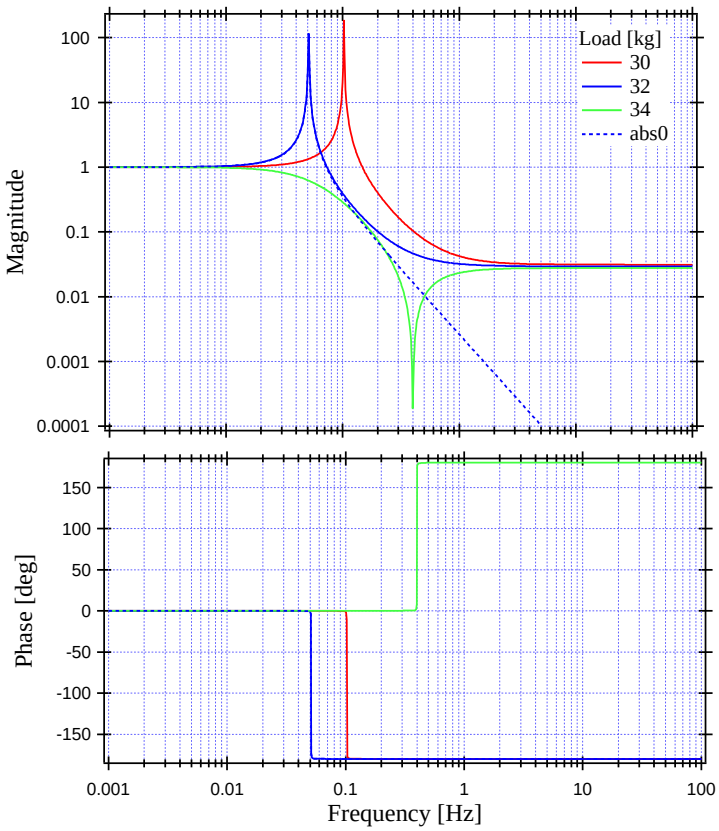

Figure 2.4: Transfer function of the IP for increasing loading levels (solid) and that of an ideal (massless) harmonic oscillator (dashed).

IP transfer function saturates at a certain level of attenuation, the 'plateau'. This behavior is physically related to the *'center of percussion (c.o.p.) effect'*. When an external force is applied onto a free rigid body, it accelerates both translaionally and rotationally around its center of mass. However a rigid body like the IP leg, is not allowed to rotate freely as it is connected to the payload at one end and to the ground by the flex joint at the other end at low frequencies. The flex joint is a negligible constraint at frequencies higher than the resonant frequency, and the leg will rotate around a well defined point. In this case the ratio of the translational motion of the payload and the ground is determined only by the geometry of the flex joint and the center of rotation. From the equation (2.11), the plateau level of the transfer function is defined as follows.

$$\lim_{\omega\to\infty} H_{\mathrm{IP}}(\omega) = -\frac{\frac{m}{4} - \frac{I}{l^2}}{M + \frac{m}{4} + \frac{I}{l^2}} \tag{2.12}$$

$$= -\frac{m\left(\frac{l}{2}\right)^2 - I}{Ml^2 + m\left(\frac{l}{2}\right)^2 + I} = -\frac{I_{cop}}{I_0} \tag{2.13}$$

Note that the plateau level is independent of the resonant frequency. The I_0 corresponds to the total momentum of inertia of the system with respect to the flexing point, where the seismic force is exerted. The I_{cop} is the difference of two components of the momentum of inertia of the IP leg: the first term corresponds to the momentum of inertia, with respect to the flex joint, of a lumped mass located at the CM of the leg (omitting its mass distribution), and the latter is the momentum of inertia of the leg around its center of mass. To eliminate the c.o.p. effect, one can change the mass distribution of the leg to move its center of rotation to coincide either to the payload suspension point, or to the flex joint on the ground. The first solution is not easy to realize in practice, because it requires a counter weight above the payload to balance the mass and the momentum of inertia of the leg. The second solution is achieved by extending the leg downwards below the flex joint and add a counter weight to null the I_{cop}. Figure 2.5 shows the model of the IP with the counter weight (CW).

The model is parameterized by the following variables.

In the model with the counter weight, the equation of motion and the motion transfer function of the IP is written as,

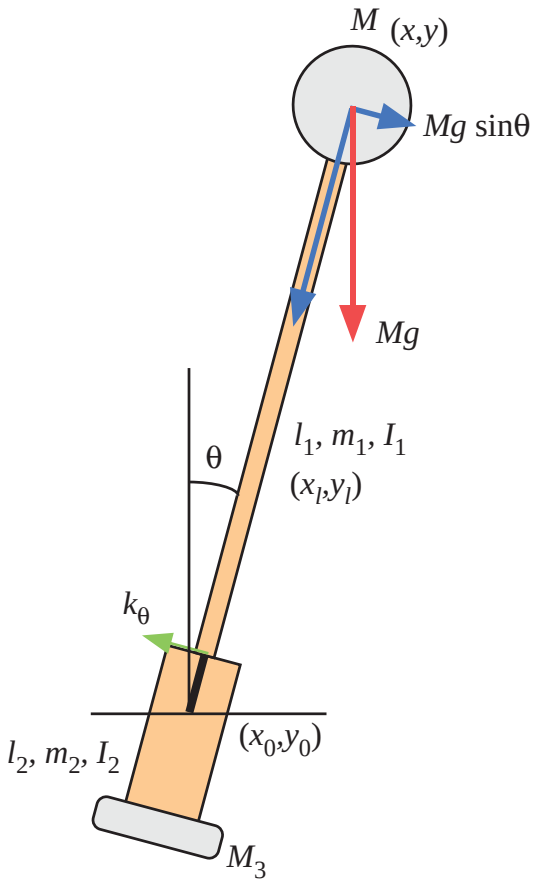

Figure 2.5: A schematic view of the IP with the CW mounted at the bottom of the leg. The counter weight is mounted at the bottom of a bell, coaxial with the leg.

l_1	length of the IP leg
m_1	mass of the IP leg
I_1	momentum of inertia about the center of mass of the IP leg
M	mass of the payload
l_2	length of the bell
m_2	mass of the bell
I_2	momentum of inertia about the center of mass of the bell
M_3	mass of the CW
k_θ	rotatinal spring constant of the flex joint
(x, z)	position of the payload
(x_0, z_0)	position of the flex joint attached to the ground
θ	angle of the IP leg with respect to the vertical axis

Table 2.3: Parameters for the simple IP model with the counter weight .

$$-C\omega^2 x - B\omega^2 x_0 = -A\left(x - x_0\right), \tag{2.14}$$

$$H_{IPCW}\left(\omega\right) = \frac{A + B\omega^2}{A - C\omega^2}, \tag{2.15}$$

where

$$A = \frac{k_\theta}{l_1^2} - \frac{g}{l_1}\left(M + \frac{m_1}{2} - \frac{m_2 l_2}{2l_1} - \frac{M_3 l_2}{l_1}\right) \tag{2.16}$$

$$B = -\frac{I_1 + I_2}{l_1^2} + \frac{m_1}{4} - \frac{l_2\left(2l_1 + l_2\right)m_2}{4l_1^2} - \frac{l_2\left(l_1 + l_2\right)M_3}{l_1^2} \tag{2.17}$$

$$C = M + \frac{m_1}{4} + \frac{l_2^2 m_2}{4l_1^2} + \frac{l_2^2 M_3}{l_1^2} + \frac{I_1 + I_2}{l_1^2}. \tag{2.18}$$

The plateau level in the transfer function is determined by B and C. The parameters related to the bell and the CW can be used to tune the maximum attenuation at high frequencies. Particularly the IP realizes ideal attenuation when the B is nulled with the optimal CW. Too much CW over-compensates the mass of the leg and brings the center of rotation point below the flex joint, then the IP leg rotates in differential mode to the translational motion, and a notch appears in the transfer function, as shown in figure 2.6[1].

2.1.4 Quality Factor of IP

Assuming that the energy dissipation of the IP is localized in the flex joint, and the origin of the loss is intrinsic of the material, one can introduce imaginary part with a loss angle ϕ_θ to the rotational spring constant. Thence from equation (2.9), the effective spring constant becomes

$$k'_{\text{eff}} = \frac{k_\theta}{l^2}\left(1 + i\phi_\theta\right) - \left(\frac{m}{2} + M\right)\frac{g}{l}, \tag{2.19}$$

and one can defines the equivalent loss angle of the effective spring constant as,

$$\phi_{\text{eff}} = \frac{k_\theta}{l^2 k_{\text{eff}}}\phi_\theta, \tag{2.20}$$

[1]Equation (2.15) holds true between the IP resonant frequency and the first internal mode resonant frequency of the IP leg. At higher frequencies, the IP leg acts like an elastic element and would provide additional isolation, while degrading the performance at its internal resonant frequencies.

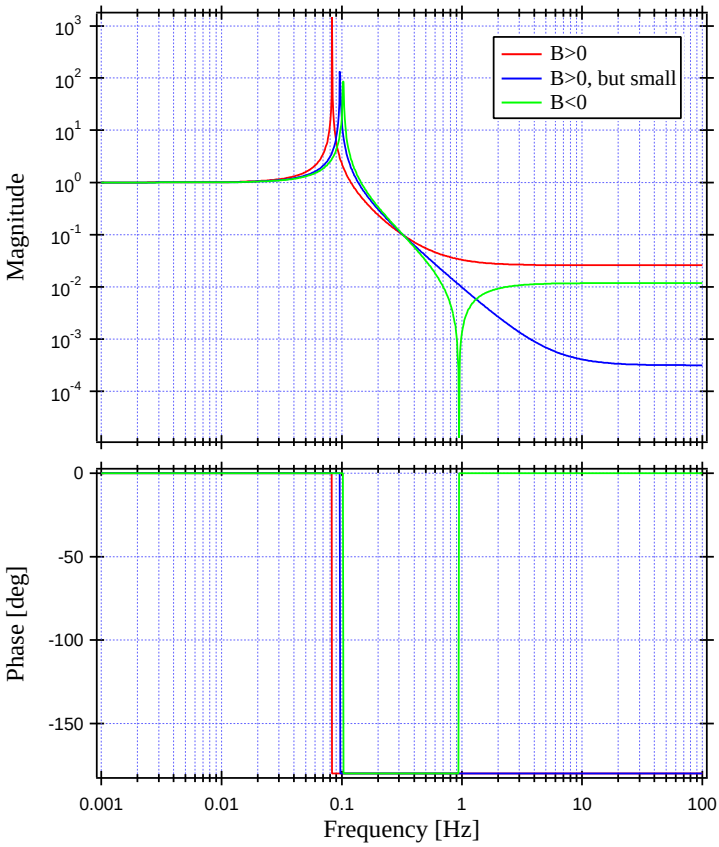

Figure 2.6: Transfer function of the IP with (blue and green), and without (red) the CW. The attenuation performance at high frequencies is substantially improved with an appropriate CW (blue).

and the quality factor of the IP reduces with the effective spring constant, proportionally to the resonant frequency as,

$$Q_{\mathrm{IP}} = \frac{l^2 k_{\mathrm{eff}}}{k_\theta} Q_{\mathrm{intrinsic}}. \tag{2.21}$$

2.1.5 Tilt and IP

Response to Ground Tilt

When the ground tilts by angle of Θ, with respect to the vertical axis, it simply introduces an additional external force $-k_\theta \Theta$ to the system. Thence from the equation of motion (2.14), the motion of the IP payload will be revised as,

$$x = \frac{A + B\omega^2}{A - C\omega^2} x_0 + \frac{k_\theta / l_1^2}{A - C\omega^2} \Theta. \tag{2.22}$$

k_θ / l_1^2 corresponds to equivalent spring constant for translational motion x[2] . Note that the ground tilt doesn't affect the c.o.p. effect, because it purely generates a torque at the flex joint.

As discussed in chapter 1, the coupling factor between the nominal ground tilt Θ and its translational motion x_0 varies from 10^{-3} to 10^{-1} rad/m. Then the effect of tilt is negligible when $10(A - B\omega^2) \gg k_\theta / l_1^2$. If the c.o.p. effect is perfectly eliminated ($B = 0$), and the stiffness of the elastic joint is extremely well neutralized, this condition can be broken. However, in practice, this condition is true at every frequency band due to the limitation of these tuning. Thus, we can practically neglect the horizontal motion of the IP caused by the ground tilt.

Drift due to Ground Tilt

Even if the ground tilt isn't a big problem from the view point of isolation in the GW detection band, it causes the long term drifts. The angular variation of the gravity caused by the ground tilt can be converted to a DC external force onto the payload of the IP following the relation $f_{external} = Mg \sin\Theta$, and the corresponding translational drift of the IP with respect to the inertial frame is,

[2]Obtained by comparing the elastic energy stored in the flex joint in term of θ and x, i.e. $\frac{1}{2} k_\theta \theta^2 = \frac{1}{2} k_x \left(\frac{x}{l_1}\right)^2$.

$$x_{drift} = \frac{Mg \sin\Theta}{k_{eff}} \sim \frac{Mg}{k_{eff}}\Theta. \tag{2.23}$$

In the sample IP, using the parameters in the table 2.2 and the typical payload of 30.0 kg, the conversion factor is about 36 m/rad. According to geophysical models, the typical ground drift in tilt is of the order of 10^{-6} rad [68]. Then the translational displacement of the IP due to the ground tilt becomes of the order tens of microns. Therefore it must be suppressed by an appropriate control system to keep the operation of an interferometer.

2.1.6 Vertical Isolation Performance

The IP is not intended to be soft in vertical direction. In each leg of the IP, there are two flex joints at the bottom and the top (see section 2.2), and these are where the compressional/expansional stress concentrates. Their stiffness is given as that of the bulk beam as

$$k_z = \frac{EA}{l}, \tag{2.24}$$

where l and A are the length and the cross section area of the beam. By using the geometry and the load of the actual IP legs, the vertical resonant frequencies of the bottom and the top flex joints are obtained as about 400 Hz and 700 Hz respectively. Thence we neglect the contribution of the IP to the vertical isolation.

2.1.7 Horizontal Normal Modes of the IP

By neglecting its vertical motion, the actual IP is regarded as a rigid body on the horizontal plane, supported by three soft springs. In principle, there are three 'normal' modes in such a system: two translational ones and a rotation around the vertical axis. The two translational modes are degenerated in the ideal case, i.e. equivalent stiffness in the three springs and perfect symmetry of the geometry. However, it is not obvious that how these modes are oriented when they are regenerated. Here we study a realistic case, with unequal spring constants, but with perfect symmetry.

The model is illustrated in figure 2.7. There is a round rigid body (vertical isolator) supported by three springs corresponding the IP legs, with spring constants k_1 , k_2 , and k_3, separated by angle of $\pi/3$ radians each other.

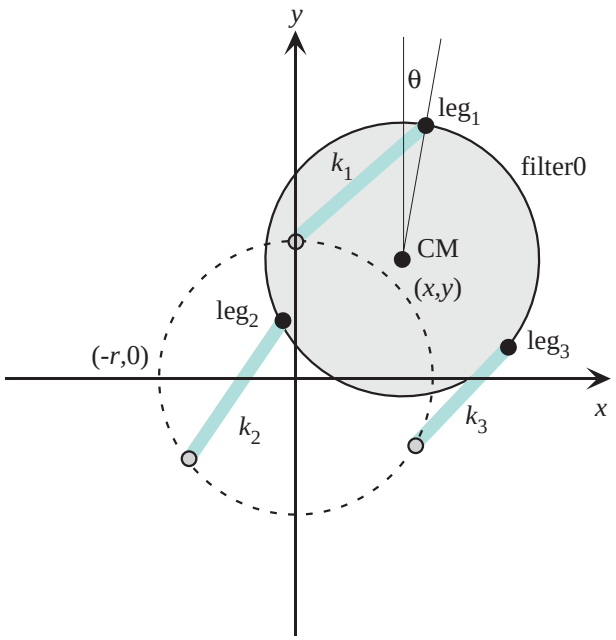

Figure 2.7: Model to study IP normal modes.

The motion of the rigid body is parameterized by a vector defined by its position and rotational angle (x, y, ϕ) in the Cartesian coordinate system. By giving a small perturbation in each degree of freedom, one obtains the stiffness matrix of the system as,

$$K = \begin{bmatrix} -k_1 - k_2 - k_3 & 0 & \frac{\sqrt{3}}{2}(k_2 - k_3) \\ 0 & -k_1 - k_2 - k_3 & \frac{1}{2}(-2k_1 + k_2 + k_3) \\ \frac{\sqrt{3}}{2}(k_2 - k_3) & \frac{1}{2}(-2k_1 + k_2 + k_3) & -k_1 - k_2 - k_3 \end{bmatrix}, \quad (2.25)$$

where the mass and momentum of inertia and the radius of the rigid body are assumed as unity for simplicity. By rotating eigen vectors of the above matrix, one obtains another set of vectors that determines the modes of the system as,

$$\begin{aligned}
\overrightarrow{v_1} &= \begin{pmatrix} \frac{2k_1-k_2-k_3}{\sqrt{3}(k_2-k_3)} \\ 1 \\ 0 \end{pmatrix}, \\
\overrightarrow{v_2} &= \begin{pmatrix} 1 \\ -\frac{2k_1-k_2-k_3}{\sqrt{3}(k_2-k_3)} \\ 0 \end{pmatrix}, \\
\overrightarrow{v_3} &= \begin{pmatrix} 0 \\ 0 \\ 1 \end{pmatrix},
\end{aligned} \tag{2.26}$$

after normalization. $\overrightarrow{v_1}$ and $\overrightarrow{v_2}$ correspond to purely translational modes, with relative angle of $\pi/2$, while $\overrightarrow{v_3}$ describes the rotation around the vertical axis: i.e. every IP has two *geometrically* normal translational modes and a yaw mode.

2.1.8 Translation - Tilt Coupling

Practical mechanical isolators have imperfection in general, given by limited precision of machining and assembly, and ununiform density distribution in material. Essentially all the normal modes of the mechanics are no longer normal and couples each other. These couplings tend to be a limiting factor of the isolation performance, and they are hard to predict, as the imperfection is given totally randomly. Here we consider a case of these imperfection in the IP, the cross-coupling between the horizontal and tilt motion of the IP top. This type of coupling may give some constraint to the local control design (discussed in section chapter 7).

As described earlier in this section, the IP for TAMA SAS has three legs supporting a vertical isolation stage via small flex joints. We simplify it by taking a projection to a vertical plane which includes two legs in our model, shown in figure 2.8 with geometrical parameters. Elasticity and rigidity of the flex joints are neglected and the legs are free to rotate, only with geometrical constraint. When the system consists of identical legs and they are parallel each other, there is no coupling between the horizontal motion of the IP and the tilt of the vertical isolator. However, the two motions linearly couples due to geometrical constraint around the equilibrium position when the legs are nonparallel, and the curvature of the trace of the vertical isolator

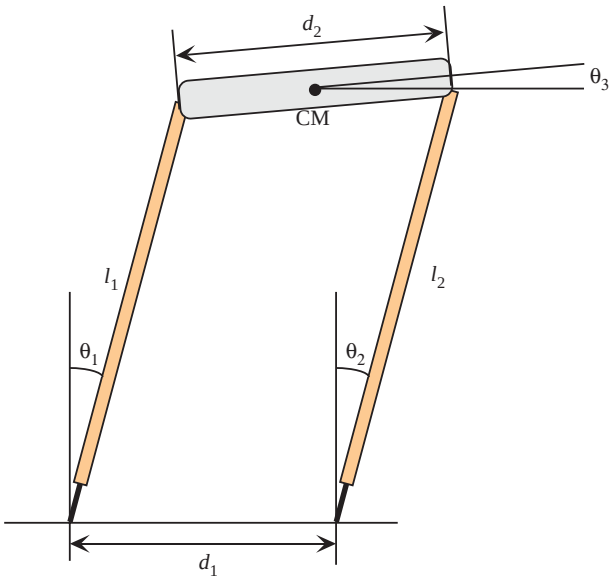

Figure 2.8: Geometry of the 2-dimensional model of the IP.

	l_1[mm]	l_2[mm]	d_1[mm]	d_2[mm]	θ_3/θ_1
CASE1 (legs converging at top)	3000	3000	1001	1000	+0.001
CASE2 (legs diverging at top)	3000	3000	999	1000	-0.001
CASE3 (mismatch in legs' length)	2999	3000	1000	1000	0

Table 2.4: Geometrical parameters of modeled IP. The coupling coefficients are defined at the equilibrium position of the IP.

can take either sign depending on the geometry. In the model, the tilt of the vertical isolator $\theta_3$can be solved analytically, as a function of θ_1 and the other parameters, however it is so complicated to write down and we present results of few examples (figure 2.9), computed with parameters in table 2.4.

When both the legs are identical, the vertical filter holds horizontal at the equilibrium position of the IP, but if they don't have equal length, the tilt of the filter never changes its sign. In practice, the error in assembly tends to be larger than that of machining, and the case1 and case2 are more realistic than the case3. By neglecting difference of the length of the legs, and changing the amount of the error in these realistic cases, one finds that the coupling coefficient is roughly equal to the ratio of the error and the

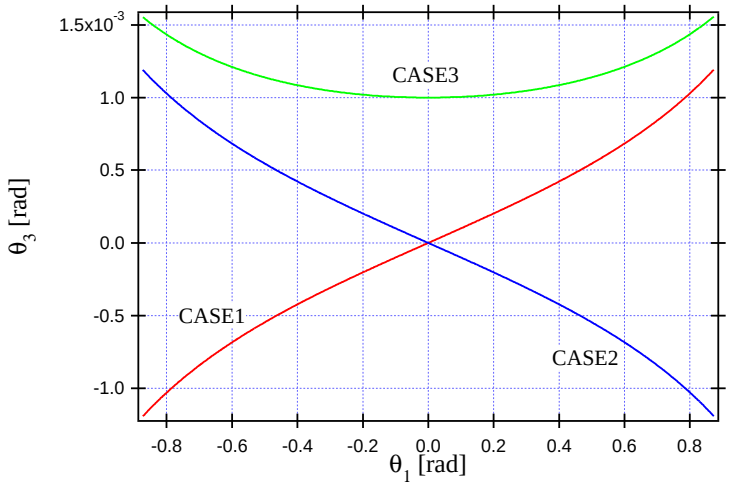

Figure 2.9: Relation between the tilt of the IP (θ_1) and that of the vertical filter (θ_3), with geometrical parameters in table 2.4.

nominal separation of the legs $(d_1 - d_2)/d_1$. Since θ_1 and the horizontal motion of the IP are approximately related as $x \sim l\theta_1$, where l is the length of the leg, cross-coupling ratio between the IP motion and the filter tilt holds linear relation.

Thence response of the accelerometers on the top of the IP to the ground motion is disturbed by the cross-coupling, as:

$$H_{acc}(\omega) = \left(-\omega^2 + \alpha\frac{g}{l}\right) H_{IPCW}(\omega), \tag{2.27}$$

where $\alpha = \mathrm{d}\theta_3/\mathrm{d}\theta_1$.

2.1.9 Thermal Stability of the IP

In general, low frequency mechanics tend to be sensitive to temperature, because their equilibrium position is determined by very small restoring force in the mechanics, neglecting the ground tilt and small change due to temperature variation can easily break the equilibrium. There are two possible paths how temperature affects the mechanics: i.e. thermal expansion and change of elasticity. In the case of the IP for TAMA SAS, the vertical isolation stage is supported by three equivalent soft springs corresponding to the IP legs, and the equilibrium position of the IP is determined only by the balance of restoring forces of these springs. The stiffness of the spring

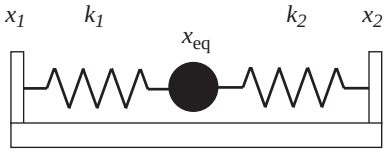

Figure 2.10: Uni-dimensional model to study thermal drift of the IP.

is a function of geometry of the leg and stiffness of the flex joint. Thence if the system is composed by perfectly symmetrical elements (identical stiffness, and legs' geometry), uniform temperature variation doesn't cause any drift. But if temperature drifts locally, it introduces asymmetry of mechanical parameters in the system and causes drift of equilibrium position. Also it is obvious that even uniform temperature drift can break an equilibrium if the system is originally asymmetric. From equation 2.9, the change of the stiffness of the effective spring due to temperature drift is,

$$\begin{aligned} \Delta k_{eff} &= \frac{\partial k_{eff}}{\partial k_\theta}\Delta k_\theta + \frac{\partial k_{eff}}{\partial l}\Delta l, \\ &= \frac{\Delta k_\theta}{l^2} - \left(\frac{2k_\theta}{l^3} - \frac{\frac{m}{2}+M}{l^2}g\right)\Delta l, \\ &= \frac{k_\theta}{l^2}\delta E \Delta T - \left(\frac{2k_\theta}{l^3} - \frac{\frac{m}{2}+M}{l^2}g\right) l \delta L \Delta T, \end{aligned} \tag{2.28}$$

where δE and δL are thermal coefficient of elasticity and thermal expansion coefficient, respectively. ΔT is the change of temperature.

In the case of TAMA SAS, the rotational stiffness $\delta E = 4 \times 10^{-4}$ for maraging steel, and $\delta L \sim 10^{-5}$ for stainless steel. Using the typical parameters of the TAMA SAS IP the change of the stiffness is,

$$\Delta k_{eff} = \left(1.8 \times 10^{-2}\Delta T\right)_{\text{elasticity}} - \left(1.7 \times 10^{-3}\Delta T\right)_{\text{expansion}} [\text{N/m}]. \tag{2.29}$$

Therefore the contribution from the change of elasticity is a dominant source of the change of spring constant, and we neglect the contribution from thermal expansion in the following discussion.

A real IP leg is equipped with a helical tension parasitic spring for positioning, with a stiffness comparable to that of the flex joint ($k \sim k_\theta/l^2$) and it contributes to the equilibrium. The variation fo the stiffness of the parasitic spring is equilvalent to the first term of Δk_{eff} calculated above.

Let's consider a uni-dimensional model shown in figure 2.10, to simplify the discussion. Although in an ideal IP, there is no restoring force in the flex

joint when the system is balanced, the parasitic spring is always in tension.

In the model, there is a rigid body supported by two springs, representing the combinations of the IP leg and the corresponding parasitic spring, and fixed to the ground at x_1 and x_2. Their spring constants are k_1 and k_2. The equilibrium position of the body is determined by these parameters as

$$x_{\mathrm{eq}} = \frac{k_1 x_1 + k_2 x_2}{k_1 + k_2}, \tag{2.30}$$

and the variation of the equilibrium position due to temperature drift becomes,

$$\Delta x_{\mathrm{eq}} = \frac{x_1}{k_1 + k_2}\Delta k_1 + \frac{x_2}{k_1 + k_2}\Delta k_2 - \frac{k_1 x_1 + k_2 x_2}{(k_1 + k_2)^2}\left(\Delta k_1 + \Delta k_2\right). \tag{2.31}$$

When the system is geometrically symmetric ($x_1 = -x_2$), but mechanically asymmetric ($k_1 \neq k_2$), Δx_{eq} will take a finite value. Using the typical parameters and assuming 1 % of difference between k_1 and k_2, one derives $|\Delta x_{\mathrm{eq}}| \sim 10^{-20}$ m/degree. In this case the thermal drift is practically negligible, however, if there is temperature gradient ($\Delta T_1 \neq \Delta T_2$), the drift becomes much larger $10^{-3}\,|\Delta T_1 - \Delta T_2|$ m/degree with the same parameter, and in a symmetrical system.

2.1.10 Non-Linear Effect in IP

Sine the motion of the IP is prescribed by the small restoring force of the effective spring, weak external force could make measurable influences. For instance, the residual friction in the mechanics is a possible source of the external force. Friction generally has non-linear nature, and the non-linearity mainly introduces harmonic oscillation and hysteresis into the mechanics. There are number of observations that imply the harmonic oscillations and hysteresis in the IP, when it is tuned to very low frequency. We will present an example of these measurements in section 2.3.

2.2 Prototype IP for TAMA SAS

2.2.1 Requirements

We set some requirements for the IP design, for the isolation performance and practical concerns. There are two critical issues at low frequency: r.m.s. displacement and velocity. In the case of SAS, the resonance of the IP and its tail are dominant components for the total r.m.s. displacement and velocity of the mirror, integrated from DC to uppermost frequency in the detection band. Thence choosing the right resonant frequency is crucial in the IP design. We required displacement fluctuation of one tenth of the wave length of the laser equipped in the interferometer, integrated in 10 seconds. Thence the goal r.m.s. displacement is 10^{-7} m in the interferometer with Nd:YAG laser ($\lambda = 1.064$ μm). Approximating the IP attenuation performance with that of the ideal harmonic oscillator, and assuming the standard seismic model, the isolation factor at 1 Hz must be below 1/1000, and the corresponding resonant frequency of the IP is about 30 mHz. Although the IP is not expected to provide isolation in the detection band, above 10 Hz, it is still useful to have an additional isolation out of it, and we minimized the plateau due to the c.o.p. effect in a practical level.

2.2.2 Design

The specific design of the IP leg developed for TAMA SAS is shown in figure 2.11. There are three legs like the one shown in the figure supporting a round shape table, a vertical isolation filter, described in the next chapter, via a small flex joint link. Every component of the leg is made of stainless steel 304, except for the flex joint, made of Marval 18 maraging steel to obtain high elasticity and high yielding strength [23]. The diameter of the flexing part is determined to realize the needed spring stiffness and to have enough safety margin in term of buckling. The mechanical properties of Marval 18 is shown in table 2.5. From the bulk strength of the material, even 1000 kg of weight on each leg is far below the critical load. The diameter is gradually widened at the both ends for reinforcement. The main part of the leg is made with a stainless steel tube, about 1.3 m long, with the thickness of 2 mm, for light weight without loosing stiffness. The counter weight for the c.o.p. tuning is bolted on the bell, surrounding the flex joint.

The tensile stress on the small link between the IP top and the first

Composition [%]	C$\leq$ 0.03 , Ni 18, Co 8, Mo 5, Ti 0.5, Fe
Density	7.9 g/cm^3
Poisson Ratio	0.3
Young's Modulus	186 GPa, with thermal coefficient 4.0×10^{-4} /K
Tensile/Yielding Strength	2 GPa
Bulk Strength	140 GPa
Shear Strength	73 GPa

Table 2.5: Mechanical properties of Marval 18 maraging steel.

vertical isolator is about 10 MPa and the yielding stress on the bottom flex joint is 3 MPa. These are less than 1 % of the maximum load for the joints.

It is particularly important to have the internal resonance of the IP leg well above the bandwidth of the active damping (typically below 10 Hz), discussed in chapter 6, to avoid saturation of the inertial sensors on the IP and for simplicity of the servo design [42]. Then, when we had designed a pre-prototype IP leg, longer than one for TAMA SAS, we ran finite element computations to define the dimensions and the mass distribution of the leg. So the first resonance was found at 60 Hz, and it is a significant improvement from the similarly designed IP in Virgo, which has the resonance at 9 Hz. For the TAMA SAS, we simply scaled down the design for the pre-prototype and obtained the resonance at 50 Hz.

2.3 Experiments on the Prototype IP

We had designed and fabricated two prototypes of the IP described in the next section. To tune and characterize them, we performed a series of experiments. This section contains the description and results of the experiments.

2.3.1 Frequency Tuning

To tune the IP prototype and to determine physical parameters such as leg length, and the stiffness of the flex joint and so on, we measured the resonant frequency varying payload on the top of the IP. The results are plotted in figure 2.12. The minimum resonant frequency measured through the tuning is about 25 mHz and the target frequency, 30 mHz is achieved with the payload of about 160 kg on three legs. Also by fitting the measured curve with the model described in the section 2.1.3, the parameters in the table

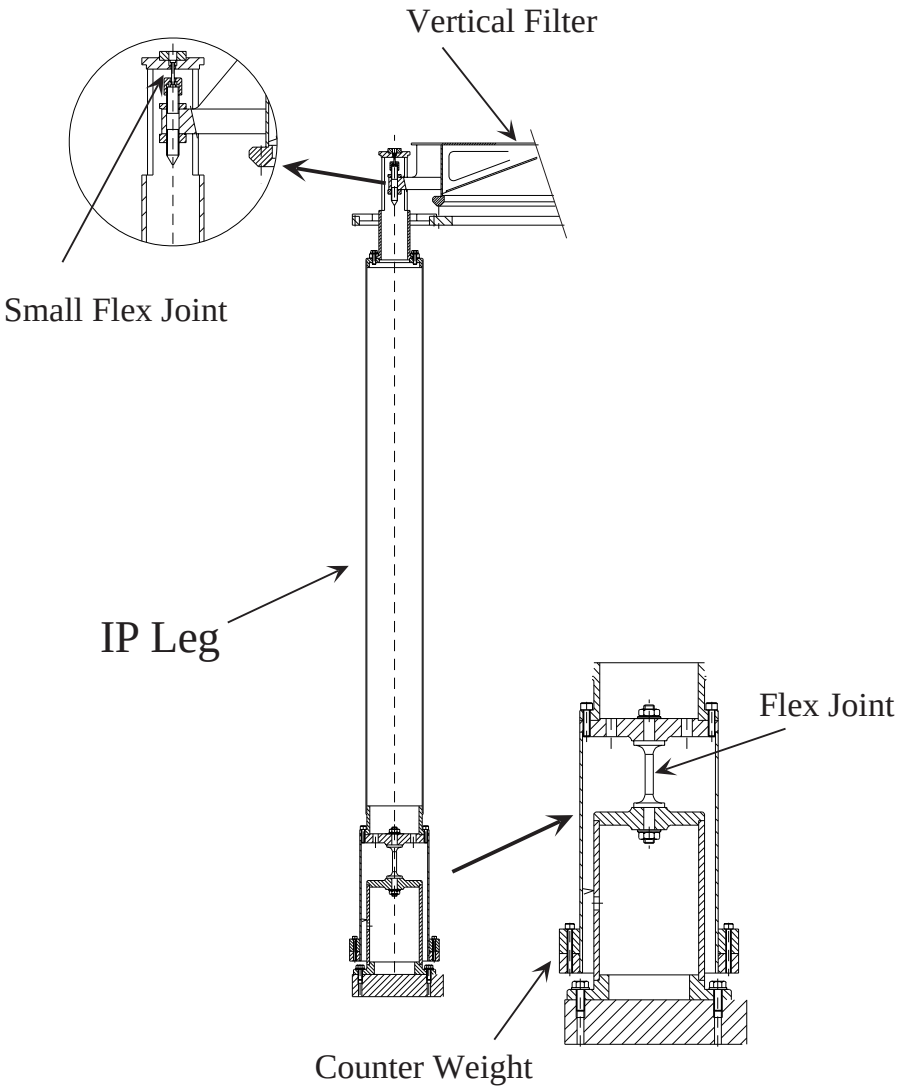

Figure 2.11: Prototype IP for TAMA SAS..

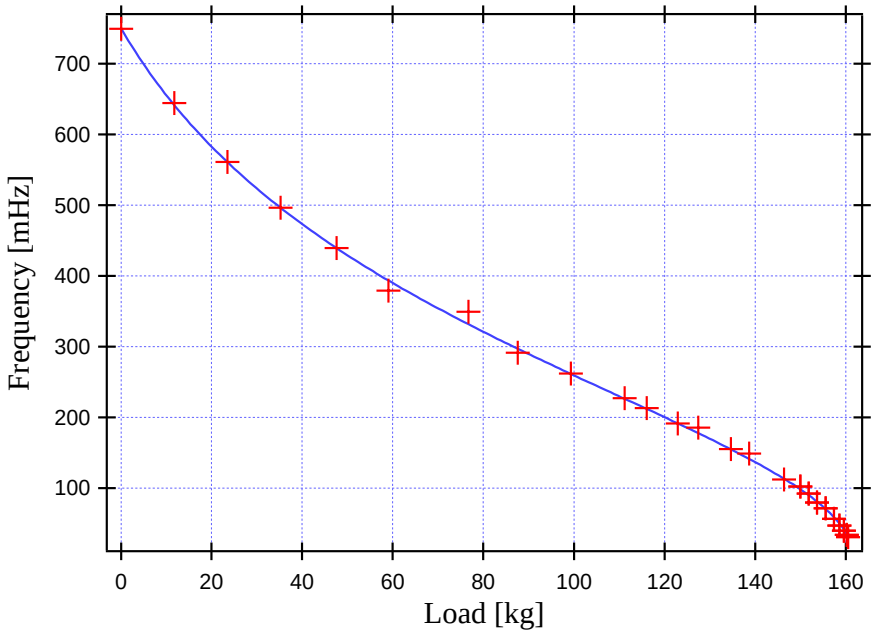

Figure 2.12: Load and the resonant frequency of the IP. Blue curve shows fitting using computed value from the equation (2.14). The load has uncertain offset.

2.3 can be determined, but they may be different from the actual dimensions in the drawings, because of simplification in the model.

2.3.2 Reduction of Quality Factor

Relation of the measured quality factor of the IP tuned at different frequencies is shown in figure 2.13. The quality factor reduces as a quadratic function of the resonant frequency as discussed in section 2.1.4.

2.3.3 Counter Weight Tuning: Isolation Performance Measurements

Since the c.o.p. effect is caused by the external force applied on the flex joint, it can be observed only when the ground where the IP stands on is shaken. To measure the isolation performance and the plateau level in it, we mounted the IP on a shaker, developed for this tuning.

The shaker consists of a voice coil exciter, and an oil bearing system connected to it. The bottom ring of the IP is mounted on three units of the oil bearing (figure 2.14), and it is connected to the ground by retainer

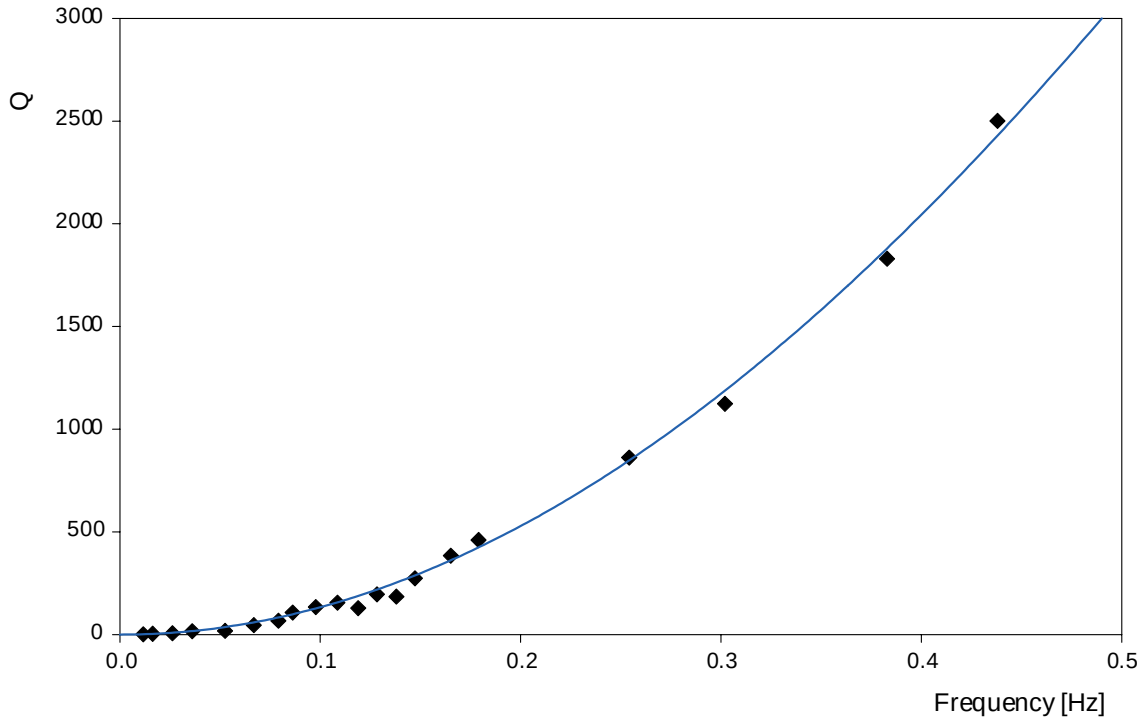

Figure 2.13: Measured relation between the quality factor and the resonant frequency of the IP. (measured by Sz. Marka).

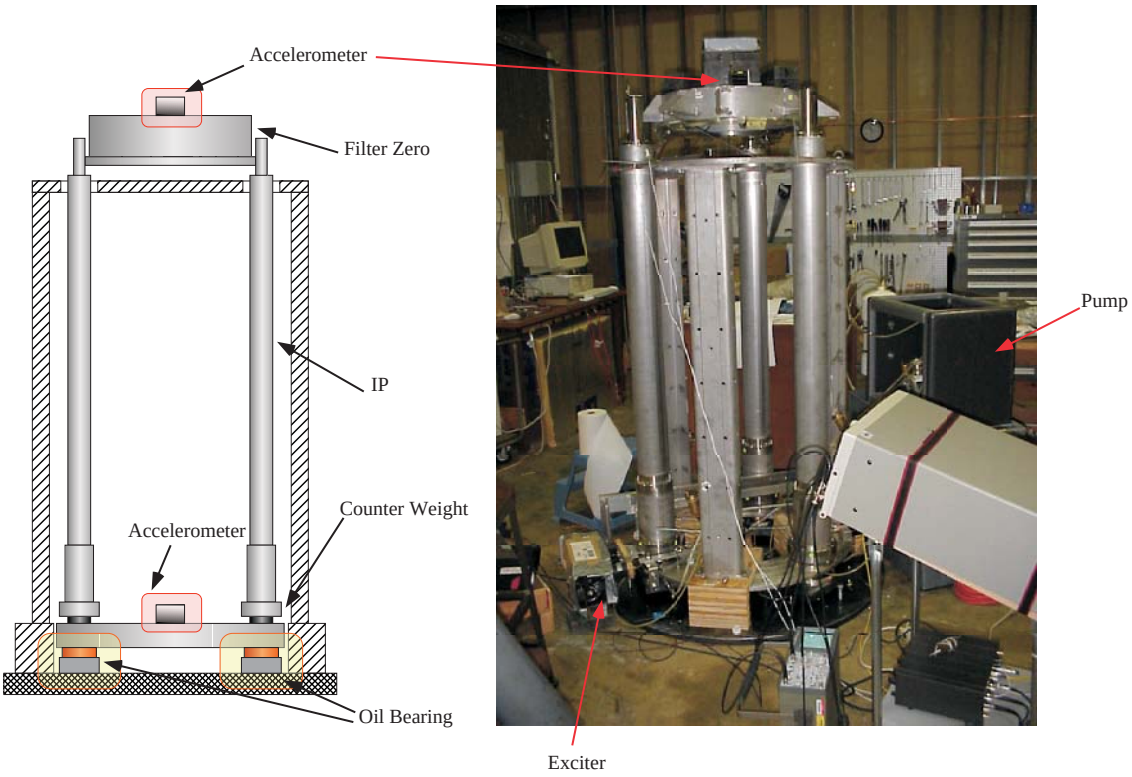

Figure 2.14: Setup for the isolation performance measurement.

springs to define equilibrium position. Also the motion of the bottom ring is constrained in one dimension by a linear slider mounted. The single unit oil bearing system is illustrated in figure 2.15. The motion of the IP top and the bottom ring is detected by commercial low frequency accelerometers (TEAC 710), and the transfer function of the IP is computed by an FFT analyzer (SR785 from Stanford Research Institution) in real time.

A history of the c.o.p tuning, the IP transfer functions around the plateau is shown in figure 2.16. B, the term in equation 2.15 is over-compensated to a negative value with the initial counter weight, and as reducing the weight, it eventually becomes positive. These measurements are taken with the IP tuned at 200 mHz, and the plateau level will be about 110 times smaller when the IP is tuned at 30 mHz, because the plateau level is proportional to square of the resonant frequency from equation (2.3) and (2.13). The transfer function of the final prototype IP is shown with the modeled function in figure 2.17. The IP is tuned at 220 mHz and the measured plateau level (-47 dB at 10 Hz) will improve to -81 dB when the IP is tuned at 30 mHz by

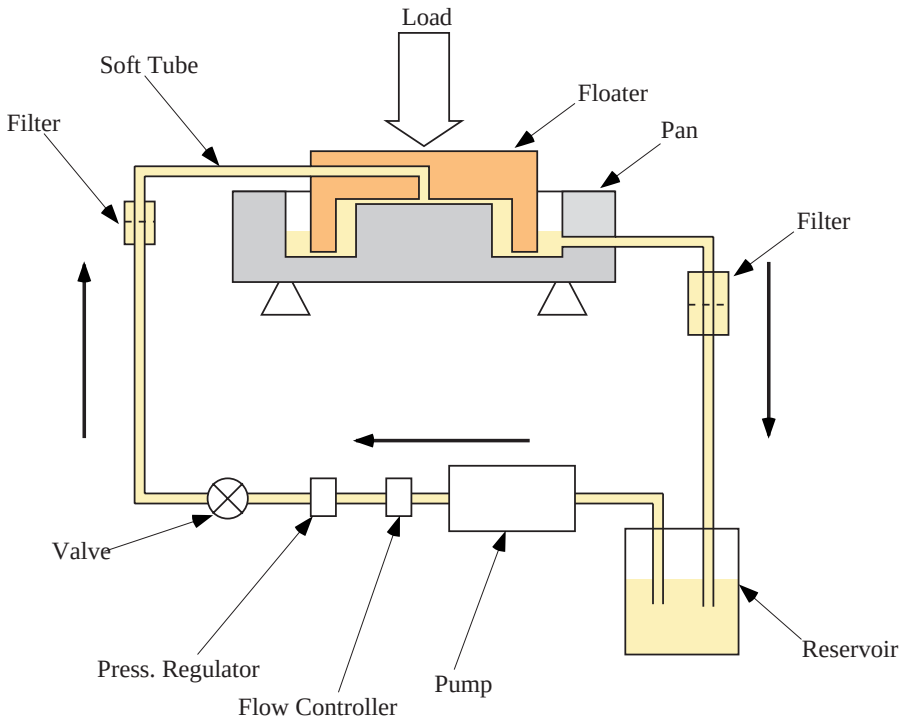

Figure 2.15: The oil bearing system. The oil is driven by a pump, and the flow and the pressure is controlled by regulators. Also there are two sieve filters in the path to remove residual dusts from the circulation. Tubes in the path is all made of flexible polyvinyl chloride that doesn't constrains free motion of moving parts. The load is applied on a floater made of brass, and there is an oil channel oil in the floater, opening downwards at the center. The oil flows through the channel into an oil pan, forming a thin film which greatly reduces the friction between the floater and the pan.

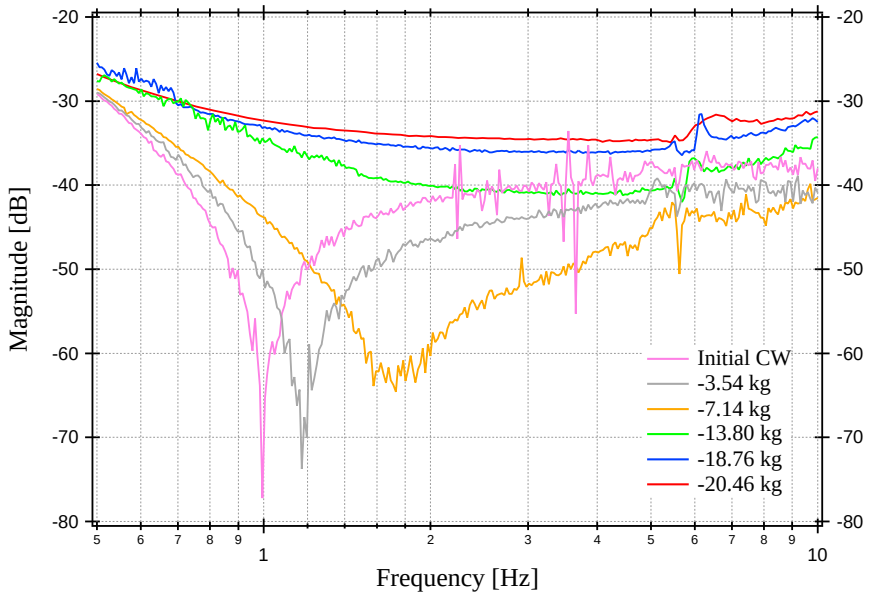

Figure 2.16: Plateau level in the IP transfer function, with various counter weight.

adding the payload. However, this improved attenuation performance may be degraded by the cross-coupling from the vertical degree of freedom.

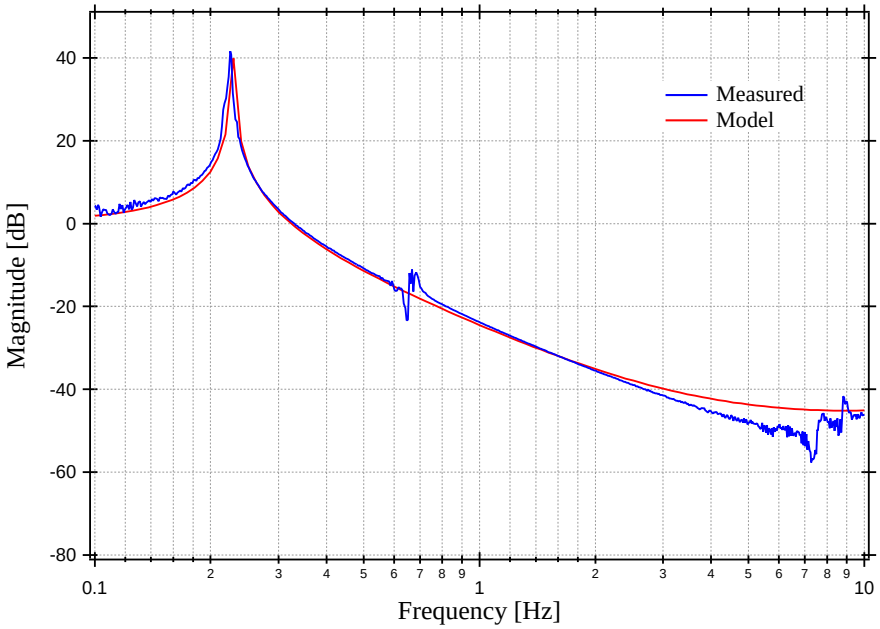

Figure 2.17: Horizontal transfer function of the prototype IP, tuned at 220 mHz. Structure around 650 mHz is caused by cross-coupling from the rotational mode of the IP. The plateau level given at 10 Hz is -47 dB.

Chapter 3

Monolithic Geometric Anti-Spring Filter (MGASF)

3.1 Design of Vertical Isolator

As discussed in chapter 1, cross-coupling between vertical and horizontal (longitudinal) modes potentially limits the performance of mechanical isolation systems. Thence the vertical isolation must be designed at least not to be the limiting factor of the overall performance. In a system like the SAS, equipped with the very low frequency horizontal isolator, the vertical isolation subsystem is also required to provide sufficient attenuation at low frequencies. It is not a simple task to design such a subsystem within a reasonable size. For instance, to realize a mechanical isolator with a resonance at 300 mHz by means of a linear spring, the elongation of the spring would have to be about 3 m. Several technical solutions have been attempted to overcome this practical problem, as utilizing magnetic repulsion force, or buckling effect[46, 24, 25, 26, 27].

Geometric Anti-Spring (GAS) is the solutions developed for SAS, and it realizes low frequency resonance, typically about a few hundreds of mHz, based on linear anti-spring effect. The design of GAS for SAS and its principle, as well as some other studies are described in this section.

3.1.1 Working Principle: A "Linear" Model

The GAS is essentially a set of cantilever springs mounted in a specific geometry to obtain a required amount of anti-spring effect. The anti-spring

Figure 3.1: View of the MGAS blade.

effect is realized by a totally passive technique to reduce the complexity and for high robustness. As shown in figure 3.1, the GAS is a set of radially arranged cantilever springs, mounted from a common retainer ring structure and opposing each other via a central disk. The payload to be isolated is connected to the central part. The blades are completely flat when manufactured and flex like a fishing rod under load. They are mounted on clamping devices with an appropriated initial angle to accommodate the bending. The clamping devices are positioned to introduce a suitable radial and horizontal compression of the blades. One needs a numerical computation, with a sophisticated non-linear finite element model to describe the macroscopic behavior of the GAS. However, a simple analytical model is quite useful to understand its working principle and is able to analyze the behavior of GAS around its equilibrium (working) position with good precision.

The model is illustrated in figure 3.2. A long cantilever spring can be represented as a simple vertical spring with a horizontal component. A set of two springs tied at their tips can be represented as a linear combination of vertical and horizontal linear springs. Due to the symmetry of the system, the model can be truncated to a single blade with the constraint that the tip of the blade can move only along the vertical axis. This constraint describes the compensation of the horizontal component of the spring forces in a real system. The cantilever spring system is best viewed as composed of two separate springs, one in the horizontal and one one in the vertical direction. Each spring is parameterized by k_z, k_x, l_{0z}, l_{0x}, representing the vertical and

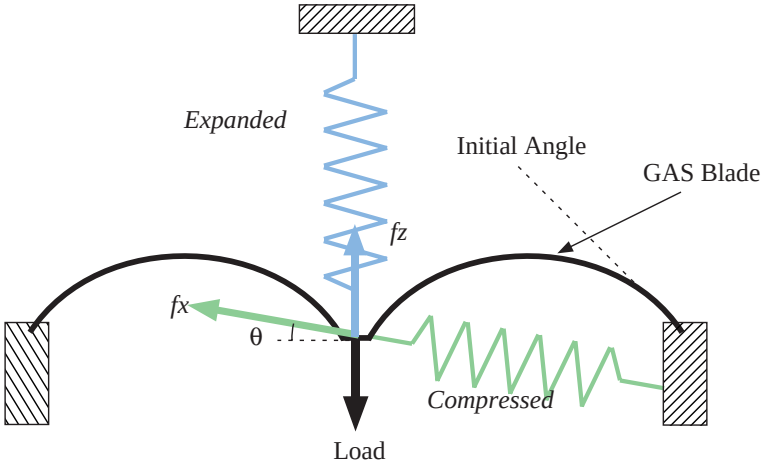

Figure 3.2: "Linear" Model for GAS.

horizontal spring constants and their natural lengths respectively. The blade is directly loaded at the tip with a mass of m, and the vertical spring alone supports its weight at the equilibrium point. The working (equilibrium) position of the tip is represented by z_{eq}, and z is defined as the difference between the actual tip height and the working position, while the horizontal position is fixed. The length of the horizontal spring is $l = \sqrt{x_0^2 + z^2}$, and its angle with respect to the vertical axis is θ.

The equation of motion in vertical axis is

$$m\ddot{z} = k_z(z_{eq} - z - l_{0z}) - k_x(l - l_{0x})\cos\theta - mg. \tag{3.1}$$

Removing the constant forces which correspond to the equilibrium, the net equation will be

$$m\ddot{z} = -k_z z - k_x(l - l_{0x})\frac{z}{l}. \tag{3.2}$$

At this point, we assume a set of typical parameter, as listed in the a table shown below, to analyze the characteristics of the system. The spring constants are chosen assuming a natural resonant frequency of an unconstrained but loaded cantilever blade of about 5 Hz [46, 47].

m	10 kg
k_z	10000 N/m
k_x	50000 - 150000 N/m
l_{0z}	0.2 m
l_{0x}	0.5 m

Table 3.1: typical parameters used for the linear GAS model.

Compression and Resonant Frequency

Expanding the equation of motion (3.2), around the working point ($z = 0$) to the first order on z, one obtains

$$m\ddot{z} = -\left\{k_z + k_x(1 - \frac{l_{0x}}{x_0})\right\} z, \tag{3.3}$$

and an effective vertical spring constant is defined as

$$k_{eff} \sim k_z + k_x(1 - \frac{l_{0x}}{x_0}). \tag{3.4}$$

When the horizontal spring is under compression ($x_0 < l_{0x}$), the latter terms of right side generates a reduction of the effective vertical spring constant ($keff < k_z$). This is the principle of the linear anti-spring effect, and the name of GAS stands from the fact that the anti-spring is realized taking advantage of a specific geometry of the cantilever blade assembly.

The effective stiffness and vertical resonant frequency of the GAS blades arrangement are shown in figure 3.3, and figure 3.4. Increasing the compression (i.e. decreasing x_0), one can, in principle, tune the resonant frequency arbitrarily low, in principle, and beyond a critical compression, at which k_{eff} is nulled and beyond which the system becomes unstable. The critical compression is given by the simple formula:

$$x_0 = \frac{k_x l_{0x}}{k_x + k_z}, \tag{3.5}$$

The GAS springs adopted in the TAMA SAS are called Monolithic GAS (MGAS) simply because the star of blades of a MGAS are obtained from a single piece of steel late. This arrangement has several advantages, in performance and simplicity of assembly, that will be discussed in the following section.

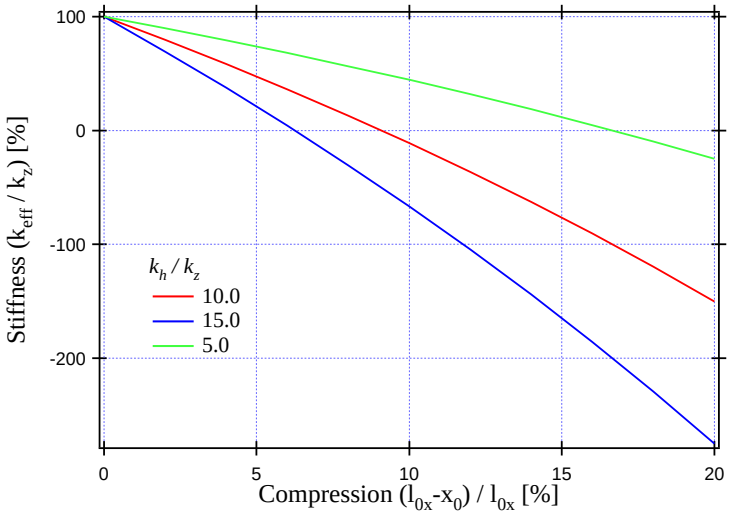

Figure 3.3: Compressional dependence of the effective stiffness of MGAS. The effective vertical spring constant reduces due to the radial compression of the cantilever blades.

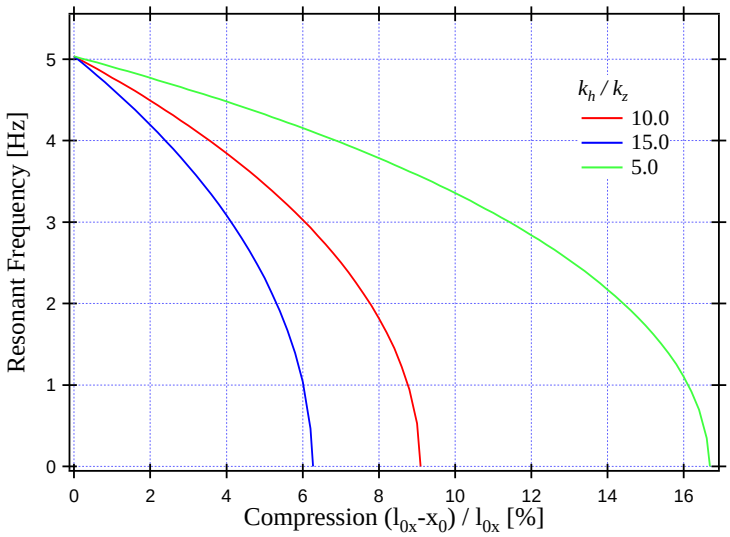

Figure 3.4: Compressional dependence of the vertical resonant frequency of MGAS around the working position.

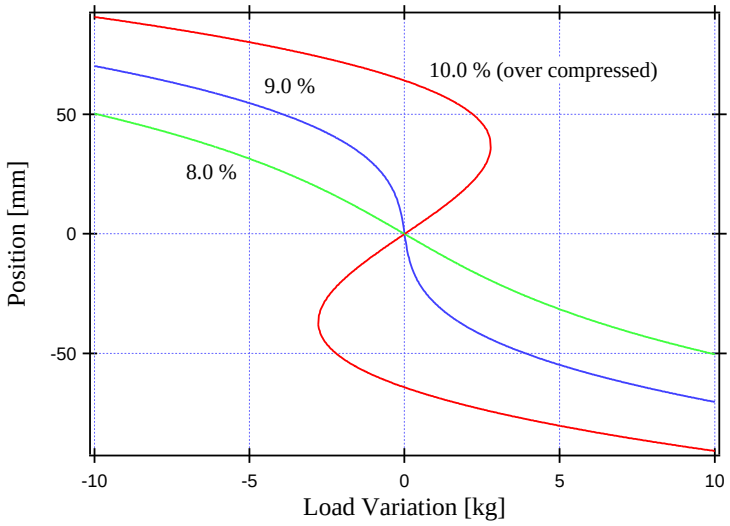

Figure 3.5: Change of the equilibrium position due to a variation of payload (center value 10 kg). This plot assumes $k_z = k_x$, for simplicity. The critical compression is 9.09 %. A red curve corresponds to over-compression, and the system has three points where the stiffness reduces to zero.

Mass Dependence

In general, the resonant frequency explicitly depends on the payload, but there is also an indirect dependence of the frequency on mass, as z is implicit function of load.

Solving equation of motion (3.1), after replacing m with $m + \delta m$, one is able to compute the change of the equilibrium position due to variation of the payload. The result is shown in figure 3.5. For simplicity, the ratio of the vertical and horizontal stiffness is fixed to one[1]. The system has single working point where resonant frequency takes its minimum value, i.e. when the horizontal spring is compressed less than the critical value. The system has two stable and one unstable working points if over-compressed. In this case there are two equilibrium points around the old stable working point. When there is a load variation, the equilibrium position changes rapidly, because of the anti-spring effect. The equilibrium position is more insensitive to load variation when the blade is less compressed and therefore effectively stiffer. The figure 3.5 can be construed as a relation between an external

[1] Although this calculation can be executed analytically, the result is a very complicated formula, and we avoid showing it here.

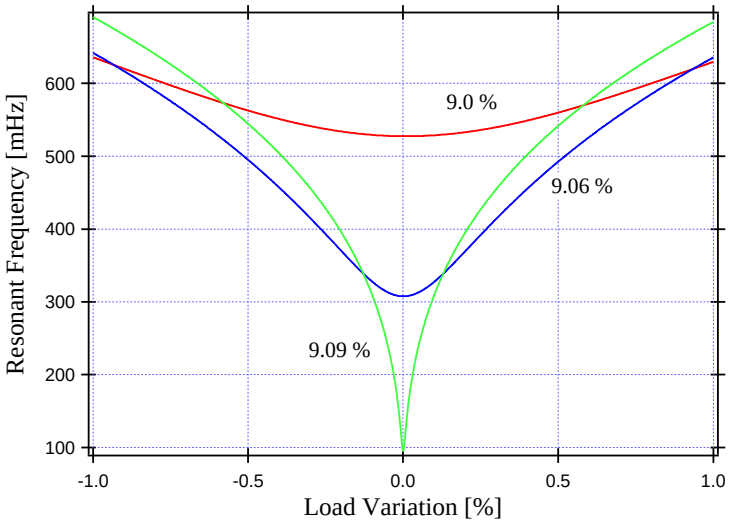

Figure 3.6: Resonant frequency around the optimal load, assuming $k_z = k_x$, for simplicity. The critical compression is 9.09 %.

force ($f_z = -mg$) and an equilibrium position. In this view, the blade works as a linear spring at the working position (null position), and the effective spring constant (equation (3.4)) could be obtained by locally linearizing the equation of motion. However, we redefine a general spring constant as a partial derivative of the vertical force with respect to the vertical position difference.

$$k(k_z, k_x, x_0, z, m) = \frac{\partial f_z}{\partial z}. \tag{3.6}$$

With the general spring constant, the resonant frequency of the blade for small oscillations is a simple function of several physical parameters. By using it, one can compute the dependency of the resonant frequency on load variation, as shown in figure 3.6. As the blade is compressed closer to its critical condition, the resonant frequency becomes much more sensitive to small load variation, and the curves are slightly asymmetric about zero load variation. This effect comes because the resonant frequency is defined by the spring constant and by the payload itself.

As shown in figure 3.5, once the load variation is set to a certain value, the equilibrium position will be determined uniquely in a stable (not over-compensated) system. With a spring constant defined as equation (3.6) and corresponding payload, the resonant frequency of the blade can be derived at

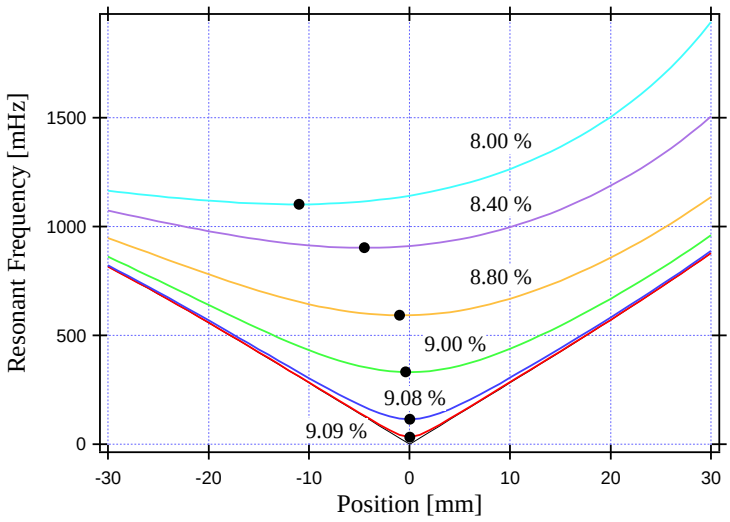

Figure 3.7: Resonant frequency of the blade with various compression factors. For each point on the curves, the payload is chosen to set the desired working position. Black dots mark the optimal working position with each compression factor.

each working position as shown in figure 3.7. The curve has an asymptotic shape with respect to the lines, under critical compression (50 % compression in this case) and no load variation. As the compression gets closer to the critical value, the minimum resonant frequency gets closer to zero.

3.1.2 Thermal Stability

Once the compression and the payload is fixed, the system can be regarded as a soft linear spring, which supports the payload. Here we consider the thermal stability of the GAS under this approximation, which is valid in a small range around the working position. In the GAS at equilibrium, the entire vertical force of the system comes from elasticity of the blade, and the working (equilibrium) position is determined by a balance of the stiffness and the payload weight, unlike the IP where the working point is independent from its load. From equation (3.4), the variation of the effective spring with a given perturbation of temperature $\triangle T$ is,

$$\Delta k_{\text{eff}} = \Delta k_z + \left(1 - \frac{l_{0x}}{x_0}\right)\Delta k_x - \frac{k_x}{x_0}\Delta l_0 + \frac{k_x l_{0x}}{x_0^2}\Delta x_{0,} \qquad (3.7)$$

$$\Delta k_{\text{eff}} = \left[\left\{k_z + \left(1 - \frac{l_{0x}}{x_0}\right) k_x\right\} \delta E_{\text{blade}} - \frac{k_x}{x_0} l_{0x} \left(\delta L_{\text{blade}} - \delta L_{\text{frame}}\right)\right] \Delta T. \tag{3.8}$$

The geometrical contribution depends on the differential thermal expansion coefficient of the blade and the frame (filter body). Assuming the use of maraging steel for the blade, and of the stainless steel for the frame, the difference of their expansion coefficients will be of order of 10^{-6}. By assuming 9.0 % of compression and substituting the typical parameters of table 3.1, and the properties of maraging steel, one obtains,

$$\Delta k_{\text{eff}} = \left(-4.4 \times 10^{-2}\right)_{\text{elasticity}} \Delta T - (0.11)_{\text{expansion}} \Delta T \text{ [N/m]}. \tag{3.9}$$

These values may differ depending on each implementation of GAS filter, but the differences of thermal expansion coefficients make a significant contribution to the resonant frequency variation, unlike as the case of the IP. This effect is implicit in the nature of the GAS, which utilizes the *geometric* anti-spring and is relatively small, comparing with the low frequency spring which employs magnetic anti-spring effect [45]. Also the above equation means the GAS spring tend to be softer under higher temperature, if the working point is somehow kept constant.

A much larger and important effect is due to the fact that the payload is supported by the vertical component of the naked cantilever blade stiffness. At constant mass load of the GAS, a percentage of change in elastic constant due to a temperature variation is equivalent to an equal percentage of load variation at fixed temperature. The resulting change in working position and resonant frequency can then be read out from the graphs of figure 3.5and 3.7. From the above equation and these figures, the expected drift is of the order of 1 mm/K, when the system is tuned to a few hundreds of mHz. Much larger drift has been observed with the GAS tuned to lower frequencies.

3.1.3 Vertical Isolation Performance

The GAS works as a normal harmonic oscillator in the vertical direction, which has a transfer function,

$$\begin{aligned} H_{z0}(\omega) &= \frac{z}{z_g} \\ &= \frac{\omega_0^2}{\omega_0^2-\omega^2}, \end{aligned} \tag{3.10}$$

derived by replacing z with $z - z_g$ in equation (3.2), where z_g represents the height from ground and $\omega_0^2 = k_{eff}/m$ is the local angular frequency of the vertical resonance. However, when mass and momentum of inertia of the blade is not negligible comparing with respect to the payload, a mass effect term must be imposed as the case of inverted pendulum. Thence a realistic transfer function will be:

$$H_z(\omega) = \frac{\omega_0^2 - \beta\omega^2}{\omega_0^2 - \omega^2}. \tag{3.11}$$

β in the above equation should be a function of the mass distribution in the blade and of the payload mass. As the origin of the mass term is an elastic support, the sign of the corresponding term must be negative, so the amplitude of the transfer function draws a continuous curve with no notch. In the linear spring model, we introduce β by using its measured value.

The MGAS geometry results in a better β factor than the first generation GAS filter described in the references [48, 49], resulting in a lower plateau of the MGAS attenuation transfer function.

The internal resonances of the blades need to be taken into account. This would require complicated numerical computations to precisely predict precisely a priori the frequencies of the internal modes as well as β. We performed the finite element computations to determine the geometry of the blade and to estimate its isolation performance (see figure 3.8), and obtain some approximate resonant frequency. However once measured, we simply imposed the resonant frequencies into equation (3.11).

An additional advantage of the choice of MGAS is that it is mechanically much simpler than the previous generation GAS, requiring no delicate link wires between the blades' tips and the load disks of the original GAS and no centering wires to impede buckling required in GAS and magnetic anti-spring system. The disadvantage of MGAS with respect to the original GAS is that the payload is fixed when cutting the blades' shape out of the original steel plate. Unlike in the original GAS, individual blades cannot be changed in situ tuning for payload tuning.

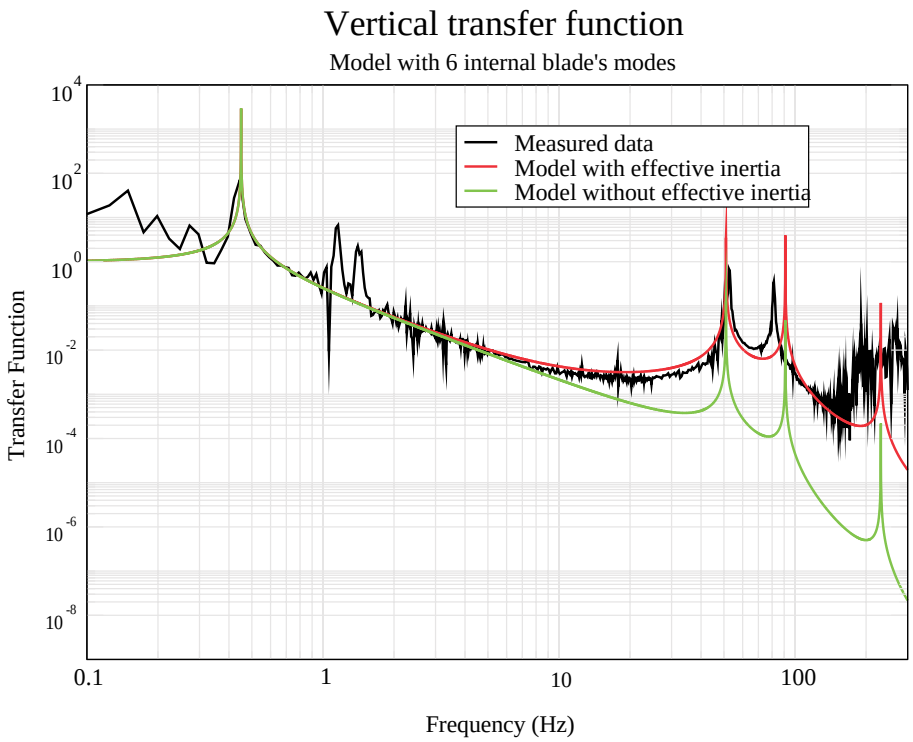

Figure 3.8: The example of the vertical transfer function of the GAS filter. The red curve was computed with finite element simulation, compared with the measurement (black). The effect of the internal modes of the blade appears at 50 Hz, 90 Hz, and 210 Hz. Note that these computation and simulation are based on the GAS filter similar to the MGASF for SAS, but not itself.

3.1.4 Horizontal Isolation Performance

Pendulum Mode

In a real suspension system, the wires have finite mass and elasticity. In such a case, the horizontal transfer function of the suspension neither matches that of the simple suspension with massless wires, nor that of the IP, equipped with a perfectly rigid support structure. Since the links between the MGASFs are relatively massive, comparing with the wires used in the mirror suspension (see section 3.9), the effect of the mass and the elasticity of the wire must be included to study the horizontal isolation performance of the passive attenuation chain.

Here we model the real single suspension. We consider a wire with the length l, and the diameter d clamped at both ends to a support structure and to a suspended mass, at the positions $(x_0, 0)$ and (x, l) respectively (figure 3.9). The rotation of the tips of the wire is restricted. The displacement of each point of the wire in the horizontal direction is $\eta(z)$.

When the external force f_{ex} is exerted onto the suspended load and it moved from the equilibrium ($x = x_0$) to x, the shear stress at each point of the wire satisfies:

$$\frac{1}{\rho} IE = (l - z)\, f_{\mathrm{ex}}. \tag{3.12}$$

Here ρ is the radius of curvature of the wire locally defined at the point $(\eta(z), z)$, and related to η as

$$\frac{1}{\rho} = \frac{\mathrm{d}^2\eta(z)}{\mathrm{d}z^2}. \tag{3.13}$$

Also $I = \frac{\pi d^4}{64}$ is the shear moment of the wire, and E is the Young's modulus of the wire material. Integrating equation (3.12) under the boundary conditions

$$\left.\frac{\mathrm{d}\eta}{\mathrm{dz}}\right|_{z=0,l} = 0, \tag{3.14}$$

and imposing

$$\eta(0) = x_0, \tag{3.15}$$

one obtains

$$\eta(z) = \left(\frac{l}{2}z^2 - \frac{z^3}{6}\right)\frac{f_{\rm ex}}{IE} + x_0. \tag{3.16}$$

Thence the horizontal displacement of the bottom of the wire is:

$$x = \eta(l) = \frac{l^3}{3}\frac{f_{\rm ex}}{IE} + x_0, \tag{3.17}$$

and the effective stiffness of the wire is[2]

$$k_{\rm wire} = \frac{f_{\rm ex}}{x - x_0} = \frac{3\pi d^4 E}{64 l^3}. \tag{3.18}$$

Using typical parameters of the MGASF chain[3], the stiffness of the wire will be about 3 % of that of the pendulum ($k_{\rm pend} = mg/l$). Therefore one can neglect the contribution of the wire stiffness to the resonant frequency of the pendulum. However the elasticity of the wire is the source of energy dissipation in the pendulum. Here we define the effective spring constant of the pendulum as

$$\begin{aligned} k_{\rm pendeff} &= k_{\rm wire}\left(1 + i\phi_{\rm wire}\right) + k_{\rm pend}, \\ &= \left(k_{\rm wire} + k_{\rm pend}\right)\left(1 + i\frac{k_{\rm wire}}{k_{\rm wire}+k_{\rm pend}}\phi_{\rm wire}\right), \end{aligned} \tag{3.19}$$

where $\phi_{\rm wire}$ is the loss angle of the wire material. As a result the quality factor of the pendulum is higher than that of the wire's material by the dilution factor of $\gamma = \frac{k_{\rm wire}+k_{\rm pend}}{k_{\rm wire}}$. In this simple calculation, the case of the MGASF pendulum the dilution factor is about 34. Much higher factor has been reported with the thinner wire suspensions [20].

Internal Resonances in Suspension Wire

By solving the wave equation on the suspension wire, the frequency of the n-th internal resonance is obtained as [34],

$$\omega_n \sim n\pi\omega_0\sqrt{\frac{m}{l\sigma}}, \tag{3.20}$$

where n is any integer. In the case of the MGASF suspension, the first

[2]Here we simply compare the bare stiffness of the elastic wire with the equivalent stiffness caused by gravity.

[3]$m = 30$ kg, $l = 500$ mm, $d = 3$ mm, $E = 186$ GPa for maraging steel

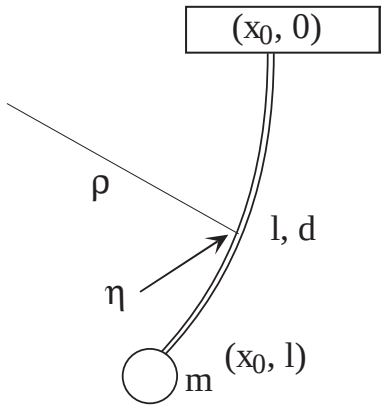

Figure 3.9: A simple suspension model.

resonant frequency is about 40 Hz.

Including the effect of the internal resonances, the horizontal transfer function is approximately obtained by modal expansion as [35],

$$H_{\mathrm{rp2}}(\omega) \sim H_{\mathrm{rp}}(\omega) + 2\sum_{n=1}^{\infty} \frac{(-1)^n \omega_0^2 \left(1 + i\phi_n(\omega)\right)}{\omega_n^2 \left(1 + i\phi_n(\omega)\right) - \omega^2}, \tag{3.21}$$

where $\phi_n(\omega)$ is the loss angle of the n-th mode, which is supposed to be constant for all the internal modes.

Horizontal Isolation Performance of the Actual MGASF

The horizontal motion transfer functions of a single MGASF computed using the equation (3.21) are shown in figure 3.10 together with that of the ideal pendulum. The amplitude of the transfer function disagrees from that of the ideal pendulum starting close to the first resonance (above few tens of Hz) and the asymptotic trend is degraded from $1/f^2$ to $1/f$ due to the harmonics of internal modes.

The nominal mechanical parameters of the MGASF and those of the suspension wire made of Marval18 maraging steel are shown in table 3.2 and 3.3, respectively. The wire diameters have not been optimized, thinner wires are possible resulting in higher violin mode resonant frequencies in lower torsional frequencies for the yaw movement of the payload.

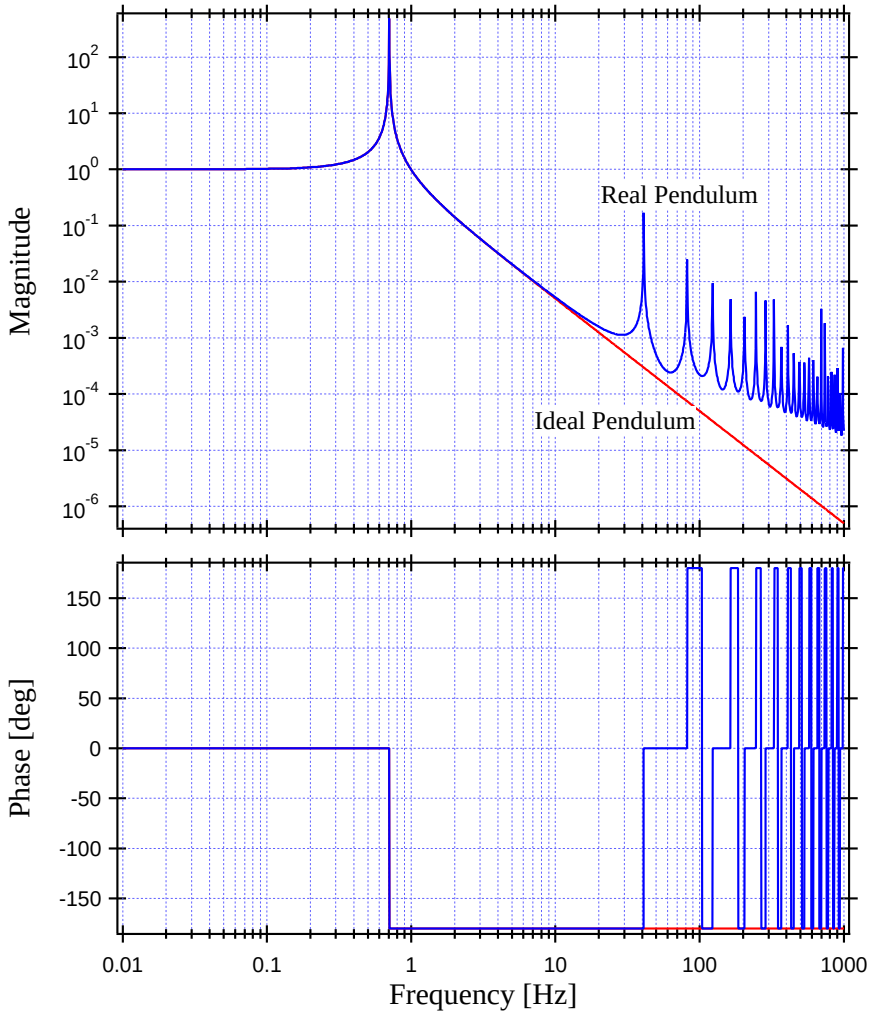

Figure 3.10: Horizontal motion transfer function of the single MGASF (blue). The phase of the real pendulum lags 180 degrees is wrapped at each internal resonances.

Radius	500 mm
Height	150 mm
Mass	30 kg
Momentum of Inertia	I_x,I_y: 0.95 kg $\cdot$ m^2
	I_z: 1.9 kg $\cdot$ m^2

Table 3.2: Nominal mechanical parameters of the standard MGASF. These parameters are a mixture of measured value and the computed values. In the actual system, the mass of the filter includes the MGAS inside, and it may be changed by adding ballast in different locations to correctly load and for frequency tuning of the filter0.

Radius	1.5 mm
Length	500 mm

Table 3.3: Dimensions of the suspension wire for the filter1. The wire is made of Marval18, whose properties of the material are described in the previous chapter.

3.1.5 Torsional Mode

As the MGASF is suspended by a single wire along its vertical axis, the restoring force in the yaw mode is only provided by the torsional stiffness of the wire. The torsional stiffness of the wire with the length l, and the shear modulus G is given as [73]

$$k_\phi = \frac{JG}{l}. \tag{3.22}$$

Here J the torsional moment of inertia of a circular cross section the wire with radius r is $J = \pi r^4/2$. Thence the equation of motion of the MGASF in the yaw direction is

$$I\ddot{\phi} = -k_\phi(\phi - \phi_0), \tag{3.23}$$

where I is the momentum of inertia of the filter around the vertical axis, and ϕ and ϕ_0 are the yaw angle of the filter and of the suspension point. This equation has the same form as that of the simple harmonic oscillator and the transfer function has the same the double pole formalism. Since the potential energy of the torsional pendulum is entirely stored in the elasticity of the wire, the dissipation is simply introduced by imposing an imaginary part to the stiffness equal to the loss angle of the material of the wire. From the equation (3.22) and (3.23), the resonant frequency of this mode is

$$f_{\phi 0} = \frac{1}{2\pi}\sqrt{\frac{k_\phi}{I}} = \frac{1}{2\pi}\sqrt{\frac{JG}{lI}}. \tag{3.24}$$

The yaw resonant frequency of the single standard MGASF suspension is obtained as about 120 mHz using the above equation.

3.1.6 Tilt Mode

The normal modes of the mechanics couple to each other, when the system has asymmetry. The asymmetry may come from the machining errors, or

from the design itself. In many occasions mechanical constraints introduce some asymmetries for practical reasons. For instance, to null the horizontal motion to tilt coupling, the wire end that suspends the filter body should ideally occupy the same position of the wire end attached to the MGAS inside the filter to suspend the lower stages. And both wire ends should coincide with the filter's CM. Thence both or at least one of them must be positioned above or below the CM of the filter, and the lever arms between the two wire end points and the CM will introduce torque onto the filter. To minimize the cross-coupling and to select the right frequency of the tilt mode, the distance between the two wire attachments and their relative distance from the CM of the filter must be determined carefully.

Let's consider the single pendulum of the MGASF illustrated in figure 3.11. The filter body hangs from the ceiling with a wire (assumed here no rigidity or mass for simplicity, approximation valid up to few tens of Hz, as discussed in the previous section). In a naive analysis, the equation of motion for the tilt angle ψ is given as,

$$md\ddot{\psi} + I_y\ddot{\psi} = -mgd\psi + \tau_{\mathrm{ex}}, \tag{3.25}$$

where m and I_y are the mass and the momentum of inertia around the y axis of the filter, and τ_{ex} is the external torque. From this, the resonant frequency in the tilt mode is

$$f_{\psi 0} = \frac{1}{2\pi}\sqrt{\frac{mgd}{md^2 + I_y}}. \tag{3.26}$$

The dependency of the resonant frequency as a function of the distance d between the wire attachment and the filter CM is plotted in figure 3.12. Below the critical distance $\sqrt{I_y/m}$, the resonant frequency monotonically increases defined only by d and the momentum of inertia of the filter.

We computed the cross-coupling between the pendulum mode and the tilt using the model in figure 3.11. The transfer functions between the suspension point and the CM of the filter are shown for different d values in figure 3.13 and 3.14. The resonant frequency and the amplitude of the tilt mode increase with the distance d. The cross-coupling appears significantly in the horizontal motion of the filter only at the resonant frequency of the tilt mode.

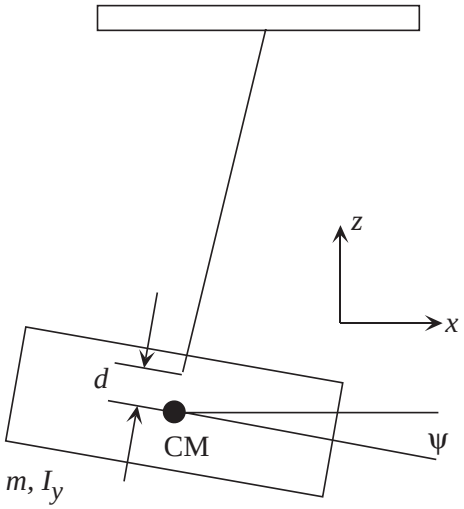

Figure 3.11: Suspended rigid body filter.

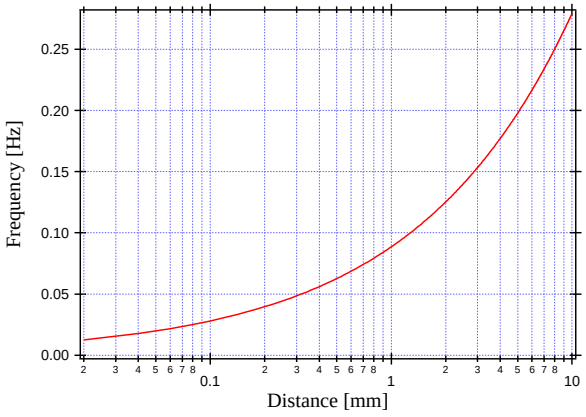

Figure 3.12: The resonant frequency of the tilt mode of the MGASF as a function of the distance d between the wire attachment and the CM of the filter. The critical distance is about 200 mm in this case.

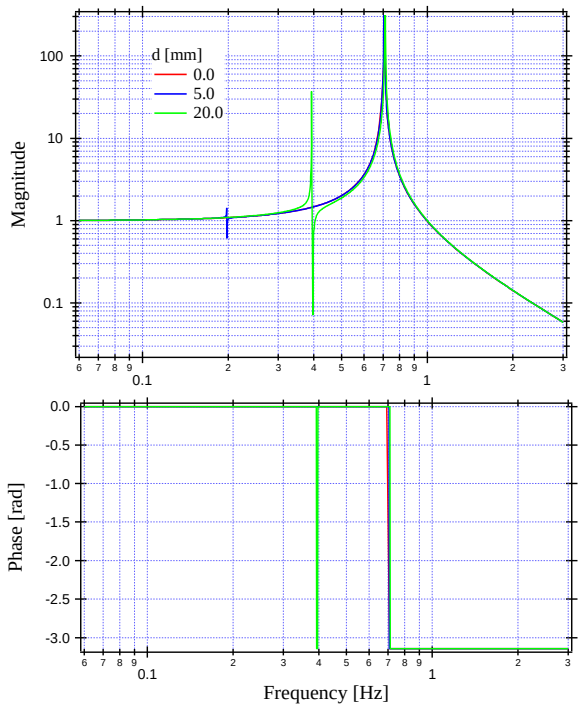

Figure 3.13: The horizontal transfer function of the CM of the single MGASF for varying d values. The peak at 700 mHz is the pendulum mode.

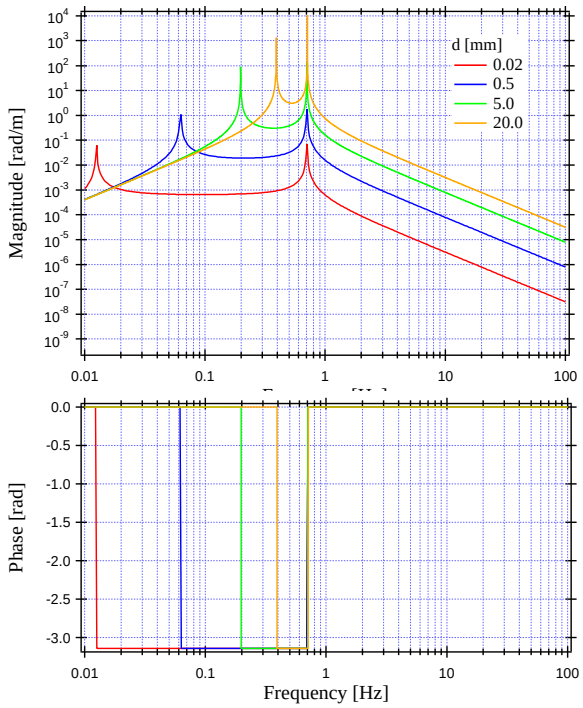

Figure 3.14: The cross-coupling transfer functions between the horizontal and the tilt mode of a single MGASF suspension for different d values The phase delays 180 π at each resonances corresponding to the two degrees of freedom.

3.1.7 Other Considerations on MGAS

Creep

Although the material in MGAS blades is not necessarily stresses more than any cantilever spring (the stress level is chosen when dimensioning the GAS blade), drift and acoustic emission (mechanical shot noise) due to micro creep in the blade material are an important concern in the system like MGAS. According to detailed studies [23, 50], there are some key points to minimize the creep and creak noise and drifts. MGAS is designed keeping into account these considerations.

- Choice of right material. The grains of precipitation hardened alloys (maraging steel) have an internal structure of inter-metallic precipitates that inhibit creep after an initial relatively short period of activity. The correct heat treatment makes uniformly distributed precipitates throughout the grains that work as 'blockers' against long range dislocation movements which causes stress concentration at the grain edges, acoustic emission and to result macroscopically observable creep.

- Stress distribution. It is well know that there is a close relation between the rate of creep and the stress applied on the material. An excess of stress can result in plasticity even in precipitation hardened metals. To minimize the creep, the concentration of stress should be avoided. The ideal condition is when the cantilever blades work under uniform stress throughout their surfaces.

Non-Linearity

Although, the MGAS blade is bent largely beyond a region where it is described as a linear system, it still can be treated as a linear spring in a small range around the equilibrium position. The geometrical anti-spring effect is fundamentally realized only by combination of linear springs, unlike the magnetic anti-spring system that essentially includes higher order effect [41]. From that point of view, the MGAS doesn't have non-linear nature, however there may be other practical sources of non-linearity, which are hard to model or identify in practice.

Any actual mechanical system is not immune from some form of friction. In the MGAS, apart from intrinsic internal friction in the material, the

contact between the blade and the supporting structure is likely source of friction and creak noise. The friction may result measurable non-linear effects as frequency up-conversion or hysteresis. We studied these effects with a prototype MGAS as described in section 3.3.4.

3.2 Prototype MGASF

3.2.1 Assembly

Figure 3.15 shows an assembly of the GAS filter for the TAMA SAS. There are three identical blades connected to the central disk. The payload is connected to the central disk via a single wire, also machined on a special lathe from a rod of maraging steel. The wire has monolithic"nail heads" at both ends. A pair of steel half cups will embrace each nail head, and settles either in a counter-bore machined in the central stainless steel column of the filter body or in a calibrated hole machined in the central disk connecting the tips of the blades of the preceding filter.(see the zoom in figure 3.15).

The bottom end of each blade is fixed to the filter body with a clamp mounted on a thick rim. The zoom in figure 3.15 shows the cross section of the clamp. The clamp consists of a U-channel and a wedge. The blade bottom end and the wedge are set into the U-channel slit and the wedge is force fit with a compressor tool to rigidly hold the blade. A small area (of 1 mm width) projection is machined on the rim of the filter body, in correspondence with the point of contact with the blade to concentrate the wedge pressure and eliminate play or sliding of the blade in the clamp. Any imperfect clamping in this area would cause non-linearity and degradation of the MGAS mechanical quality.

The filter body is a open cylinder made of stainless steel (figure 3.15). There are radial stiffeners attached inside of the top plate to avoid low frequency internal resonances.

3.2.2 The Blade

The shape of the blade shown in figure 3.16 is determined with finite element calculations to realize uniform stress in it [51, 49] (figure 3.17). Since the local stress on an elastically bent plate is inversely proportional to the local radius of curvature, the uniform stress is achieved if the blade has uniform

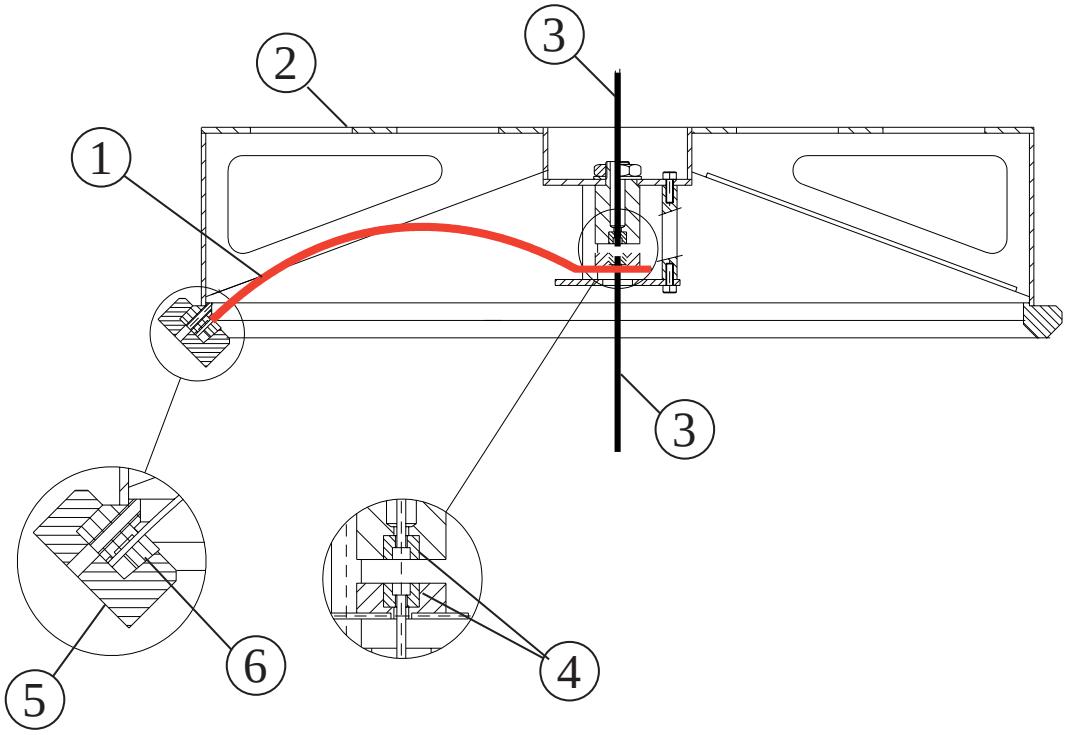

Figure 3.15: Assembly of MGASF. Only one blade is visible in this cross section.
1. Blade, 2. Filter body, 3. Suspension double "nail head" wire, 4. Half cups, 5. U-channel, 6. Wedge

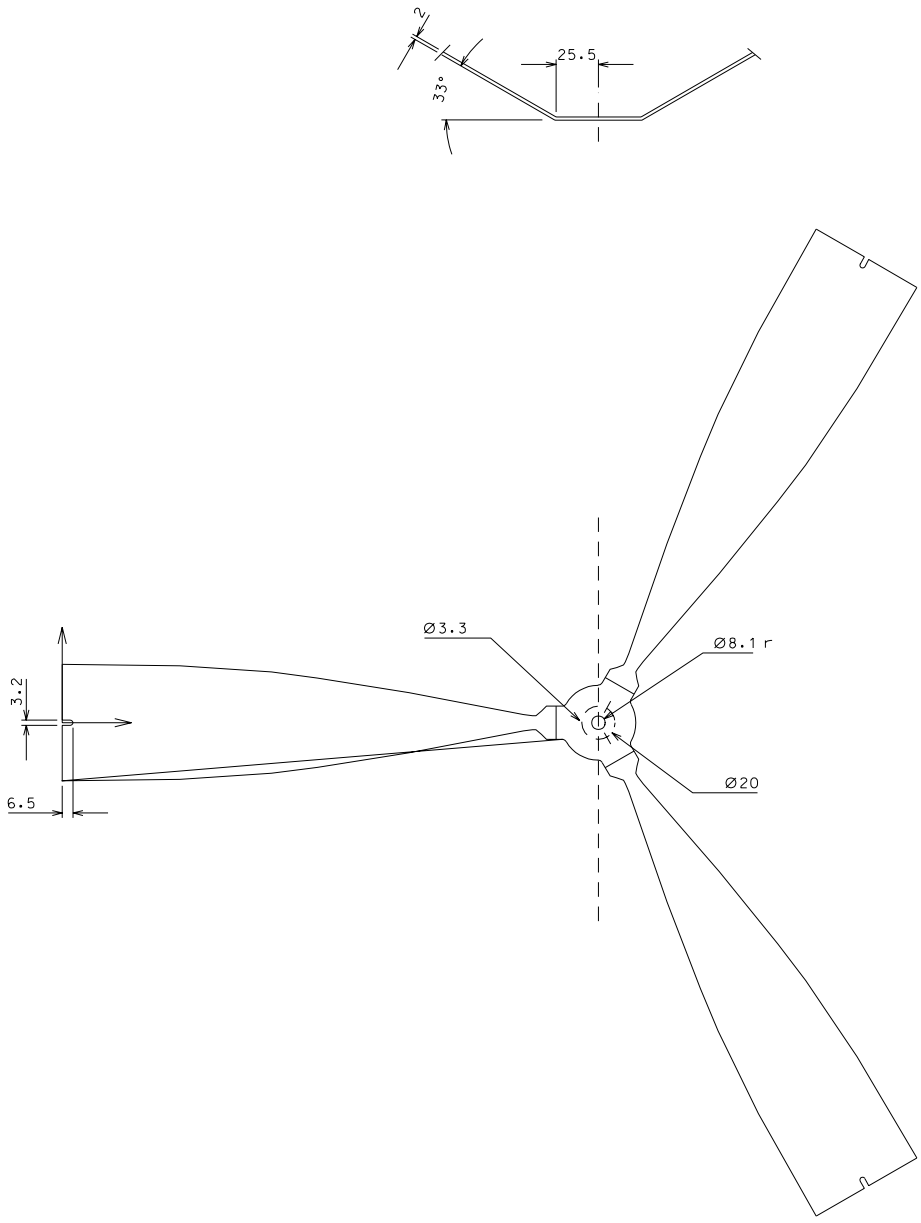

Figure 3.16: The design of the MGAS.

curvature. From the point of view of isolation performance, it is best if the overall stress is maximized (maximum payload with minimum blade's weight), but it remains smaller than the yielding stress of the material at every point along the blade. The best performance is then achieved with uniform stress.

The blades and the central disk are cut out of a single sheet of commercial maraging steel, the same material and applied the same heat precipitation as the flex joint of the IP. The disk connecting the blade is bent in a particular angle to obtain the desired coupling of the horizontal spring force to the vertical direction. The bent part is widened to increase rigidity.

3.3 Experiments on Prototype MGASF

3.3.1 Frequency Tuning

The vertical resonant frequency of each MGASF has been tuned independently. Once the blade is mounted with a certain compression, the resonant frequency and the working position were measured at various the load. The commercial low frequency accelerometer (TEAC 710) was mounted on the payload and the spectrum of its output signal was taken by the FFT analyzer (SR734) to measure the resonant frequency. The working position was simply measured by a caliper.

The results are shown in figure 3.18, 3.19, and 3.20. These measurements were taken with the filter0 GAS with the thickness of 2.0 mm. As foreseen by the model described in section 3, by compressing the blade more, the minimum resonant frequency decreases, and the resonant frequency becomes more sensitive to the load variation (corresponding to softer spring), while the sensitivity to the working position does not have clear correlation with the compression.

The tuning was performed for each filter and it was possible to tune all of them below 300 mHz. The optimal load for the filter0 (2.0 mm thick blade) is about 67 kg and that for the filter1 (1.5 mm thick blade) is about 30 kg.

3.3.2 Vertical Isolation Performance

We performed direct measurements of the vertical transfer function of the MGASF. Figure 3.21 illustrates the setup used for the measurement. The

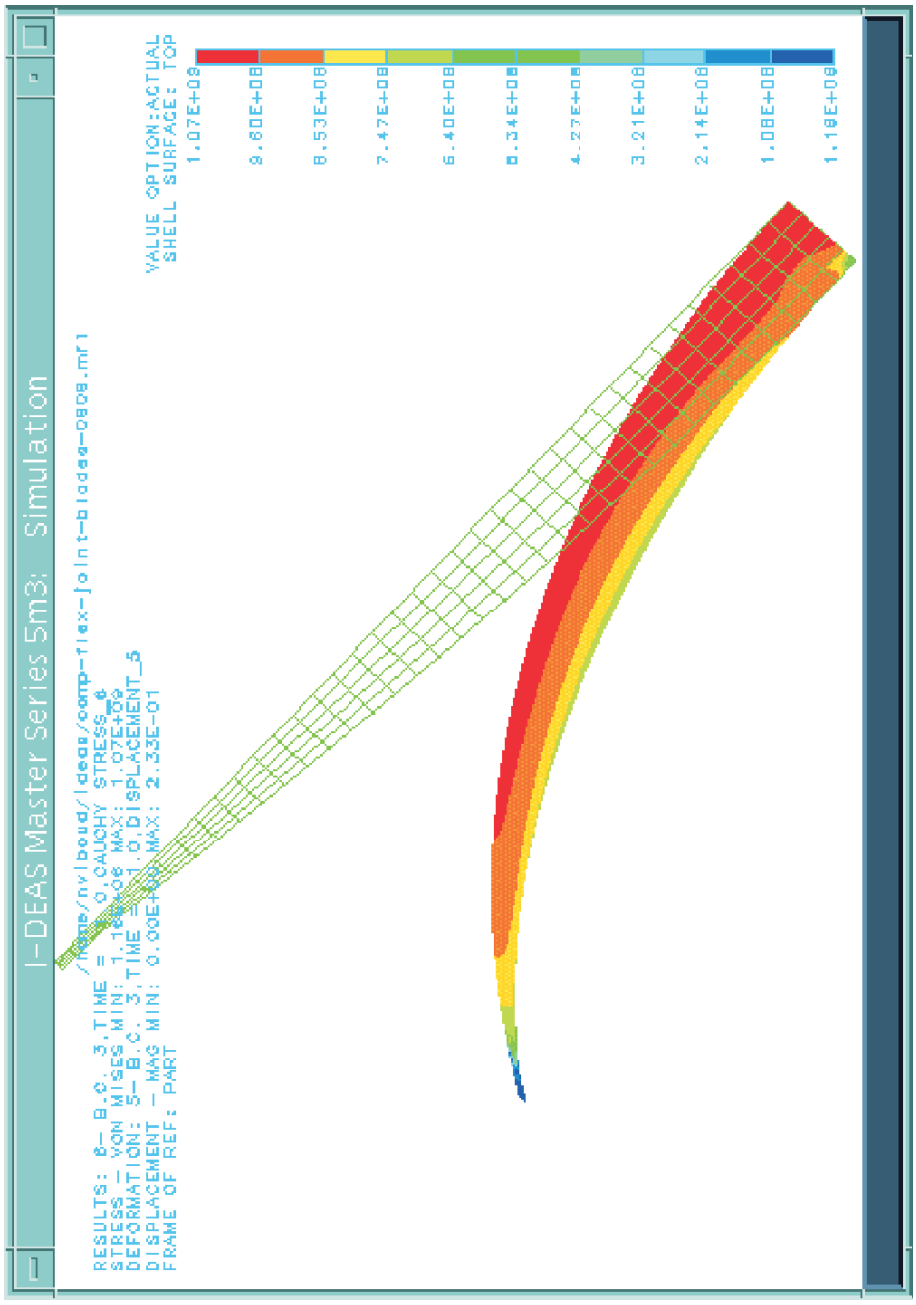

Figure 3.17: Stress distribution in the MGAS blade. Computed with the finite element simulator ANSYS. The stress distributes uniformly.

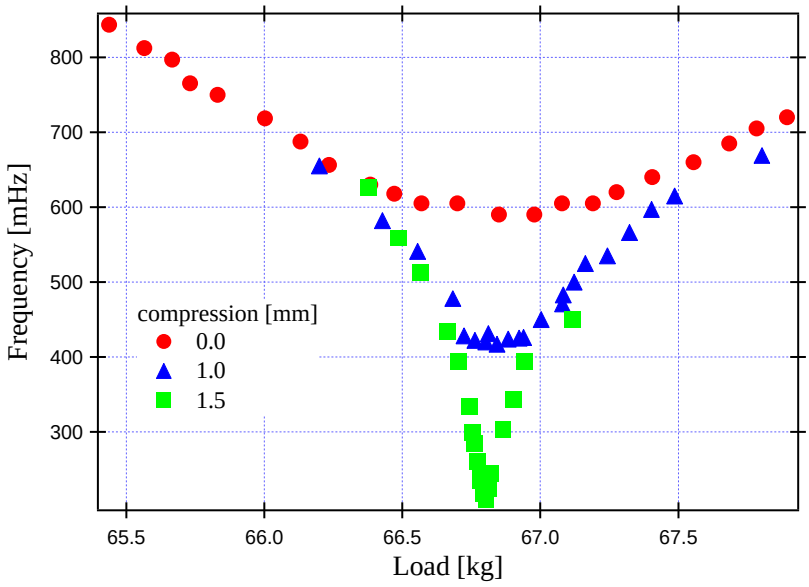

Figure 3.18: Load dependency of the vertical resonant frequency of the filter0. When the blade is compressed almost critically, the curve becomes sharper around the minimum and has negative curvature. The minimum resonant frequency was measured as 210 mHz.

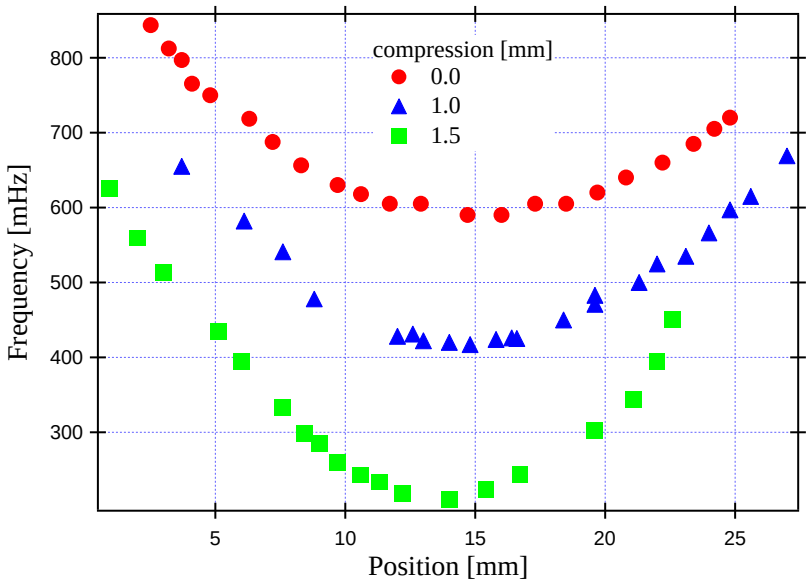

Figure 3.19: Position dependency of the vertical resonant frequency of the filter0. The curvature of the bottom part of each curve is not sensitive to the compression.

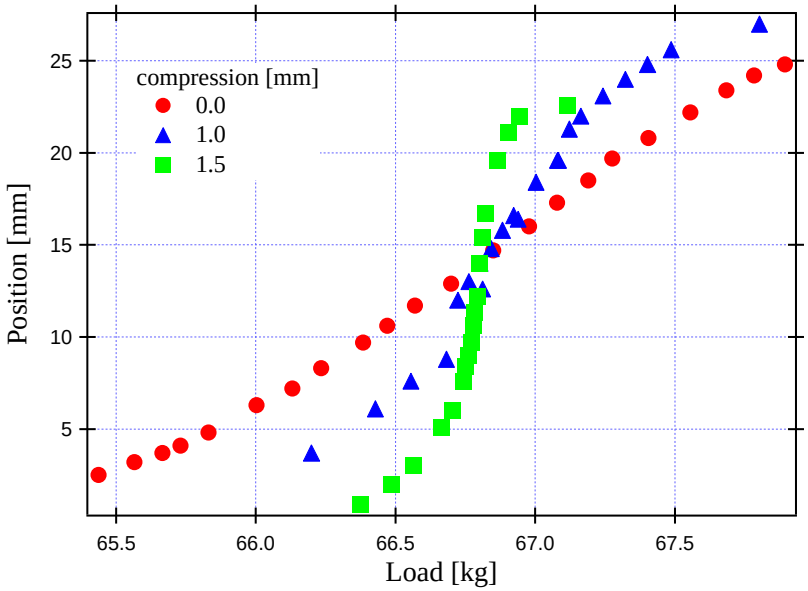

Figure 3.20: Load dependency of the working of the filter0.

filter body is suspended by four helical springs, with resonant frequency of a few Hz, and a loud speaker voice coil is connected to the body via rigid threaded rod to provide controlled mechanical excitation to the filter body. The motion of the body and of the payload is detected by commercial low frequency accelerometers (TEAC 710).

The results of the measurements are shown in figure 3.22. The saturation of attenuation appears above 10 Hz, and the plateau level -50 dB for the filter1 and -60 dB for the filter0 tuned at 350 mHz and 210 mHz respectively. The filter1 used in the measurement was tuned stiffer than the optimal condition (about 200 mHz). Since the plateau level is proportional to $\omega_0^{-1/2}$, with fixed compression of the blade, if the filter1 was tuned at the optimal frequency (about 220 mHz), the plateau level becomes about -58 dB. However, it is also true the plateau level gets worse when the filter is tuned far stiffer than the optimal condition. For instance, when it is tuned at 500 mHz, the level lays at -43 dB. The lowest blade internal mode observed was found at 130 Hz. Although its harmonics should appear as well, we did not manage to identify them because the measurement at higher frequencies was dominated by acoustic noise due to the excitation.

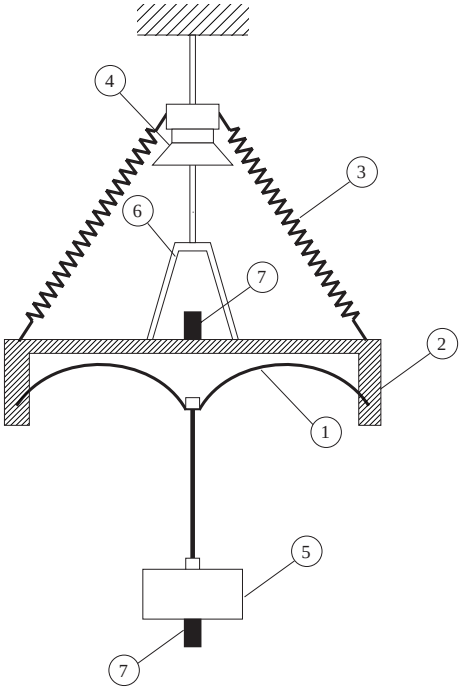

Figure 3.21: Setup for MGASF the vertical transfer function measurement. 1. GAS blade, 2. Filter body, 3. Support spring, 4. Voice coil, 5. Payload, 6. Rigid connector, 7. Accelerometer

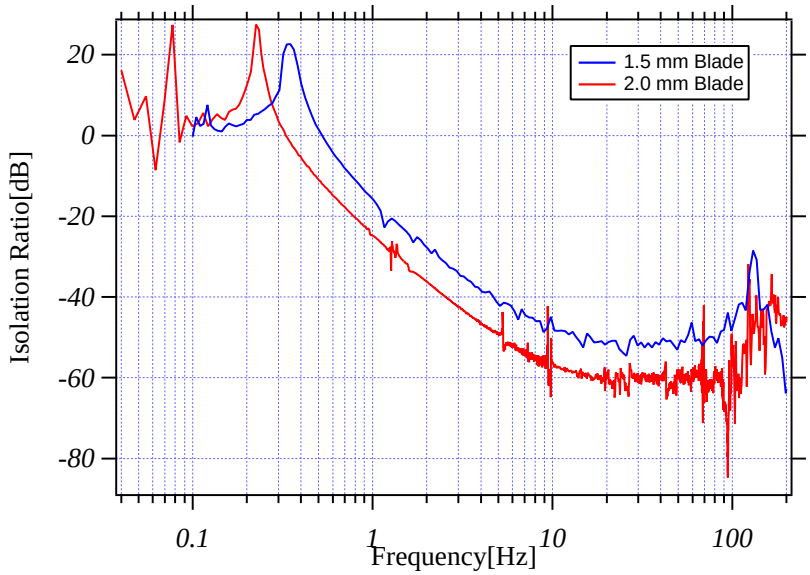

Figure 3.22: Vertical transfer function of the single MGAS.

3.3.3 Thermal Drift

To measure the thermal drift, we placed the filter in a box made of polyurethane insulator. There was a light bulb in the box as a heater, and the temperature of the blade, the filter body, and the air inside was measured by digital temperature sensor (DS1821 from Dallas Semiconductor). The small vertical LVDT was mounted on the blade center to detect the equilibrium position. The signal of the temperature sensors and the LVDT were monitored by a PC data acquisition system. The measured relation between the equilibrium position and the temperature of the blade is shown in figure 3.23. The filter was tuned at 210 mHz when the measurement was started. The equilibrium position dropped about 0.5 mm as the blade was heated about 1 degree in temperature. The thermal coefficient was obtained as -0.49 mm/K, and it was constant over 0.3 mm around the optimal working point. The effective stiffness of the blade was also constant within the range of several mm from the optimal position, therefore the attenuation performance of the filter was not affected by the temperature drift significantly.

3.3.4 Hysteresis

All mechanical setups have some level of friction, or other type of energy dissipation. These processes are more evident in non-linear, soft systems because the return forces are weak. As described in chapter 6, we observed non-linear effect of the IP when tuned to very low frequency. This happens because as the restoring force of the elastic element gets smaller, at some point it becomes comparable to the small residual friction in the system. We have observed the same trend in the MGAS.

The MGAS naturally has two equilibrium positions for a given load, as shown in figure 3.5, when it is over-compressed, and the system is unstable between these two positions. However even when the GAS is under-compensated and stable at every position, it had two slightly different working positions, typically apart from each other by less than 1 mm, and the blade is observed to stop at either point depending if it approaches the equilibrium position from above or from below. This phenomenon was clearly observed only when the GAS is tuned to have minimum frequency below 400 mHz [72], and one can draw two distinct parabolic curves tracing the two working position (figure 3.24). This is not a fundamental problem, as

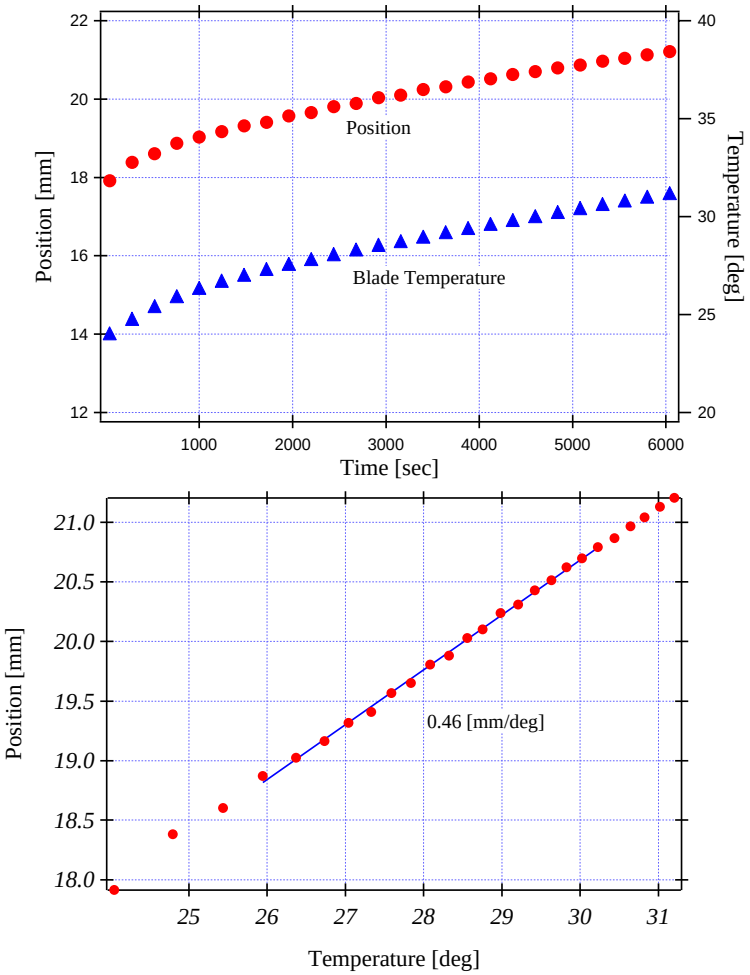

Figure 3.23: Measured thermal drift of the filter0.

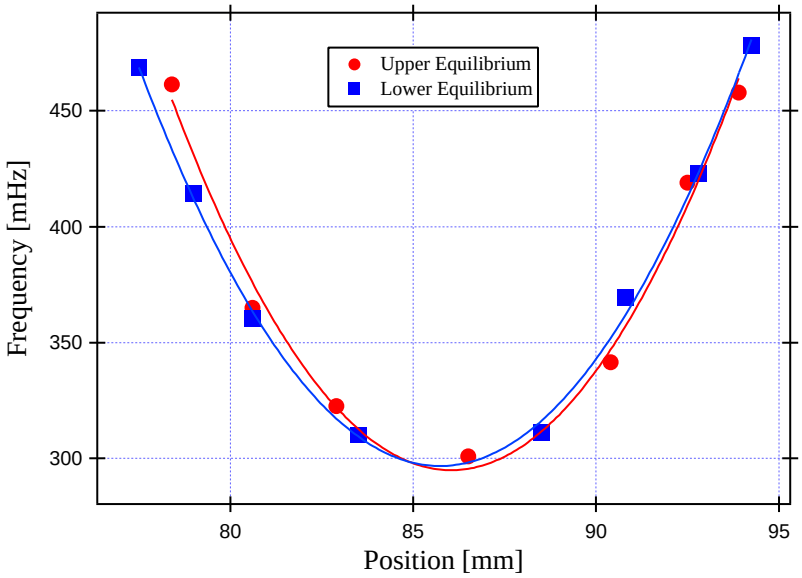

Figure 3.24: Frequency vs Position of the GAS with hysteresis. The red and blue curves correspond different working position.

the GAS just sits and effectively operate from one of the two bistable positions, but it is not good situation and it would be better to eliminate this bistability as much as possible.

We immediately suspected friction in the clamp of the blades. Checking the clamping components we obtained Rockwell hardness of 51 to 54 for the blades, while measured only 4 or 5 with the stainless steel of the clamp U-channels and of wedges. Very likely an excessive heat treatment of these wedges has softened the stainless steel. Less aggressive heat treatment and different wedge and clamp material are expected to solve this problem. Tests with harder clamps have not yet been performed to see if it helps avoiding the observed hysteresis.

3.3.5 Stress Distribution

Figure 3.25 shows measured radius of curvature at points along the MGAS blade. Deviation of the stress is within 0.2 %, corresponding to highly uniform stress distribution. The measured strain stress is slightly lower than the maximum elastic expansion, and much lower than the yielding stress of maraging steel.

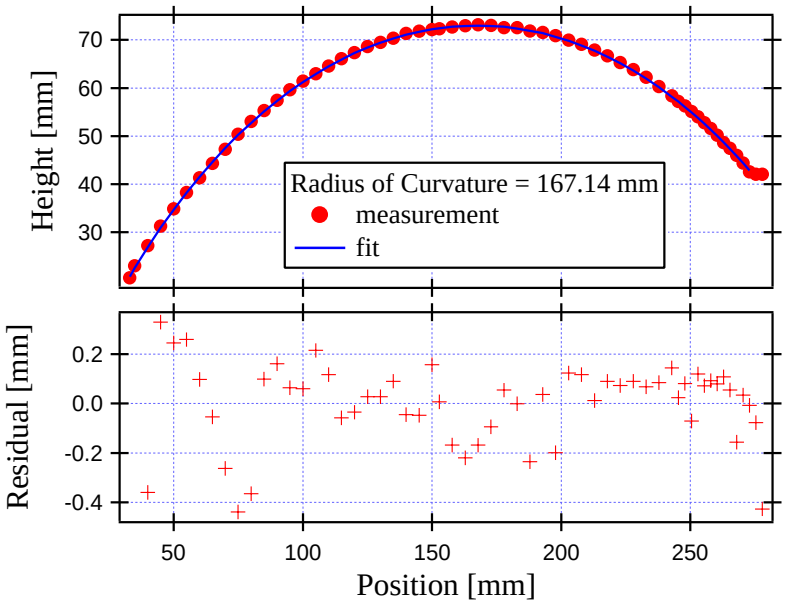

Figure 3.25: Measurement of the profile of a loaded MGAS blade, the blade's ogival shape achieves an uniform stress distribution.

Chapter 4

Mirror Suspension Subsystem (SUS)

4.1 Design of SUS

4.1.1 Roles of SUS

The mirror SUspension Subsystem (SUS) is an interface between the mechanical structures of the SAS and the core optics of the GW detector. It is located at the very bottom of the chain of the mechanical filters and holds directly the test mass of the GW detector. The SUS functions:

- Keep the mirror at rest in a quasi-inertial frame. It is fundamental that the test masses of the GW detector must float freely in an inertial frame. The simple pendulum isolating the mirror from the external forces approximates such condition in the horizontal plane at frequencies higher than the resonance of the pendulum. A pendulum's bob approaches the behavior of a free floating mass within $1/(f^2 - f_0^2)$.

- Provide a way to control the position of the test masses. To keep the interferometer in working conditions, it is necessary to position and/or orient the mirror using force actuators. The SUS houses the devices necessary for that purpose.

- Provide additional seismic attenuation. The SUS itself is regarded as the final segment of the seismic isolation chain. Particularly, suspending masses with light wires allows achieving high attenuation

performance at the frequencies where the main target GW sources exist. Also SUS will attenuate the noises internally generated in the upper stages of the seismic attenuation chain, such as thermal noise and acoustic emission noise. Of course the SUS must not generate these noises inside its own structure above the acceptable level.

- SLOW DOWN THE RESIDUAL LOW FREQUENCY MIRROR MOTION. SUS must be provided with sufficient damping, to suppress the pendular excursion and the velocity of the test mass for easy lock acquisition of the detector.

We define the "residual motion" the motion of the pendulum below the observational frequency band. In theory the residual motion could have arbitrary amplitude without spoiling the interferometer sensitivity. In practice, the interferometer must be kept in the dark fringe condition (within 10^{-12} m of precision). The residual motion must then be limited (damped) from above, or neutralized by the actuation on the test masses. Excessive force requirements from the mirror actuators would introduce control noise. To avoid this, small mirror residual motion is required.

4.1.2 Basics of the Suspension Design

Topology of the New Mirror Suspension: Baseline

The original seismic isolation system installed in the TAMA300 consists of a triple layer stack system carrying a structure containing a double pendulum mirror suspension as shown in figure 4.1 [39, 52, 53]. By replacing the original stack isolator with the IP and two stages of MGASFs, the isolation performance will be significantly improved in the low frequency band (below 100 Hz). The new SAS presents a large advantage from the original stack isolator. But the seismic attenuation provided by these stages reaches a saturated limit due to the c.o.p. effect in the observation band of the original TAMA 300 (from 150 Hz to 450 Hz) and needs to be complemented by efficient mirror suspensions. We preserved the same tested and successful topology of the mirror suspension system, the double pendulum with the Eddy current damping applied on the intermediate stage just above the mirror. The damper is suspended by flexible rods to avoid seismic noise re-injection in the GW detection band.

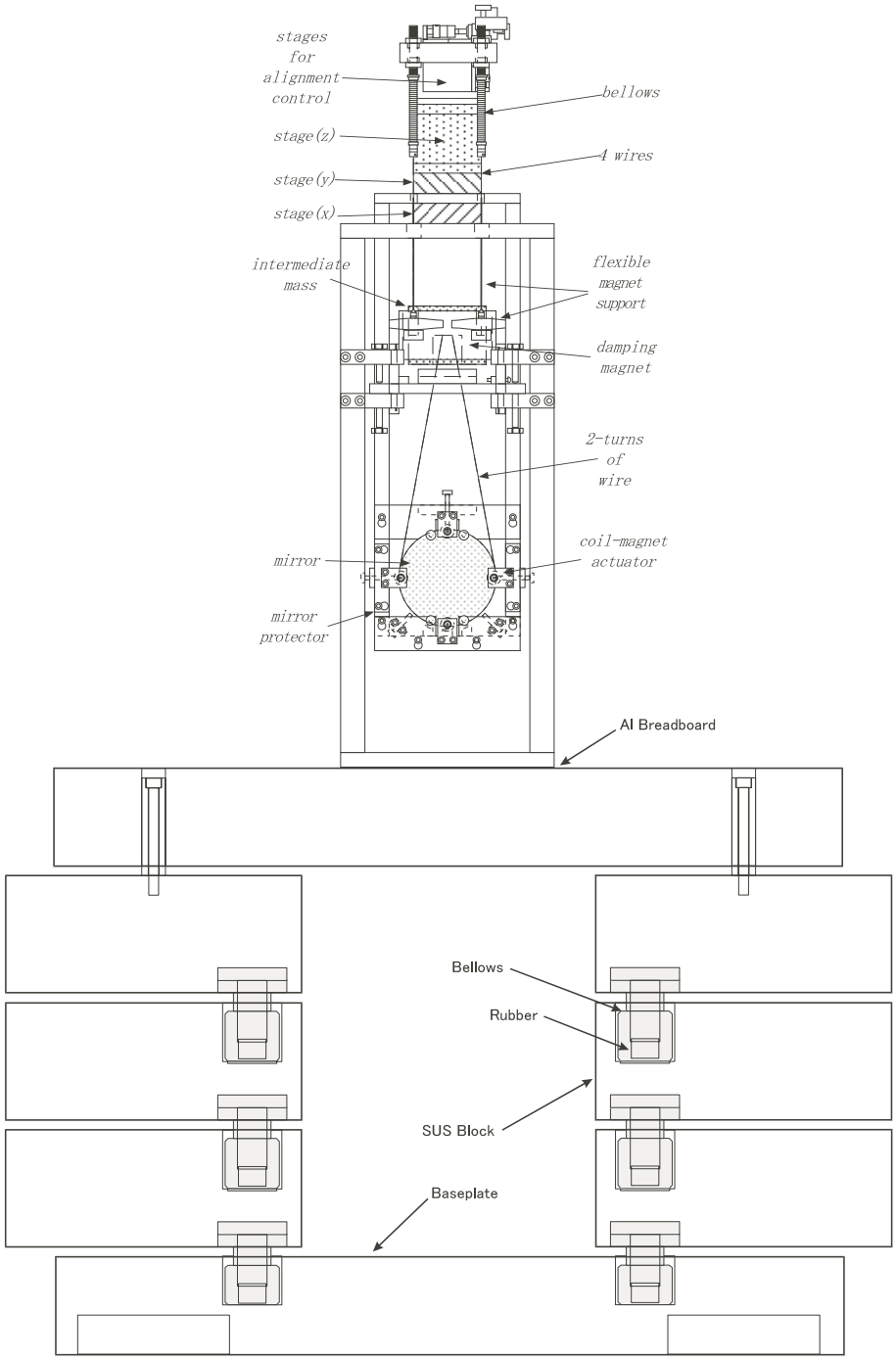

Figure 4.1: The original seismic isolation system for the TAMA300. The double pendulum suspension is located on the breadboard, which is supported by three stack legs.

Although the new system adopts the same topology as the original double pendulum, we introduced additional improvements:

- Refined matching of the resonant frequencies of the normal modes for better use of the passive damping,
- Low frequency vertical springs at the suspension points realized with mini-MGAS for better vertical attenuation and lower pitch frequency i.e. lower pitch control forces in the mirror.
- Mirror actuation from a suspended recoil mass.
- Use of the magnetic damper also for the recoil mass.
- Support of the entire SUS from a mass suspended and controlled from the preceding filter to provide hierarchical controls and reduce the actuation forces (and noise) on the mirror.

The details of these improvements will be discussed later in this section.

4.1.3 Eddy Current Damping

A passive damping technique is applied on the intermediate stage to suppress the residual motion of the mirror. Permanent magnets are located close to the intermediate mass. Eddy currents are induced on the surface of the mass, depending on its relative motion with respect to the magnets. Energy is dissipated due to the resistance of the material. The induced current is written as

$$I = \int \gamma \frac{\mathrm{d}B}{\mathrm{dt}} \mathrm{d}s, \tag{4.1}$$

where B is the magnetic field across the small region $\mathrm{d}s$ on the surface of the mass, and γ is a geometric factor. The integration is performed over the entire surface. If the field is static with respect to the damping mass, the above equation is simplified as

$$I = \gamma' \left(\dot{x}_{\mathrm{IM}} - \dot{x}_{\mathrm{DM}} \right), \tag{4.2}$$

where $\dot{x}_{\mathrm{IM}}$ and $\dot{x}_{\mathrm{DM}}$ are the velocity of the intermediate stage and the damper respectively. The coefficient γ' is a function of the magnetic field

and of the geometry of the system. The energy dissipation is expressed as $-rI^2$, where r is the resistance of the mass. Therefore, the equivalent force corresponding to the energy dissipation is written as

$$f_{\rm eq} = \frac{-rI^2}{\dot{x}_{\rm IM} - \dot{x}_{\rm DM}} = -\Gamma\left(\dot{x}_{\rm IM} - \dot{x}_{\rm DM}\right), \tag{4.3}$$

$$\Gamma = r\gamma'^2. \tag{4.4}$$

As the damping force is proportional to the relative velocity of the mass and the damper, this damping is called viscous damping. From the equation (4.3), the damper velocity as well needs to be suppressed and isolated and d at the same level and in the same frequency range of the intermediate stage. Failing this, the motion of the damper would be injected onto the mass through the damping force [54]. For this reason the damper in the SUS is also suspended by flex rods and springs from the same isolation stage as the intermediate mass.

Thermal Noise The advantage of the passive damper is the robustness of operation of a well damped SUS. Once the system is set up, it works without tuning or maintenance. However, there is the concern about the thermal noise caused by the large dissipation in the stage close to the mirror. The thermal noise is a potential reason to reject the use of the Eddy current damper, but the damping fluctuating force acts on the intermediate mass, instead than on the mirror itself, which is isolated by a single pendulum between two stages. To make a judgment, we need to compare the attenuated motion of the mirror due to the induced thermal noise with the aimed sensitivity of the detector. We will study this issue for the TAMA SAS later in this section.

4.1.4 Parameter Tuning

Fixed Parameters

Some mechanical parameters in the new suspension system were fixed by design constraints.

The new system has to use the same fused silica mirrors as the original TAMA fused silica mirror. The mechanical properties of the mirror are listed

diameter	100 mm
thickness	60 mm
mass	1.034 kg
momentum of inertia	I_x: 1.29×10^{-3} kg $\cdot$ m^2
	I_z, I_y: 9.56×10^{-4} kg $\cdot$ m^2

Table 4.1: Mechanical properties of the TAMA300 mirror.

in table 4.1. In our prototype SUS, the mirror is replaced with a dummy mass made of aluminum. The dummy mass has the same outer dimension, the same mass, and the same momentum of inertia as the real mirror.

To provide the same level of horizontal isolation as the original TAMA suspension, the length of the suspension wires in the new SUS is kept the same as the original system. The nominal length of the wires in every stage of the original suspension system was 250 mm, which corresponds to 1.0 Hz pendulum.

Point Mass Model

We started from the optimization of the horizontal isolation, using a unidimensional model. Point masses and massless wires compose this model, thus it does not include rotational motions. Here we only present the description of the model and some examples of its application.

Each stage of the SUS is represented as a point mass connected with springs. In this model, the equations of motion is written as:

$$M\ddot{\vec{x}} = -K\vec{x} + C\dot{\vec{x}}, \tag{4.5}$$

where

$$\vec{x} = \begin{bmatrix} x_0 \\ x_1 \\ x_2 \\ x_3 \\ x_4 \\ x_5 \end{bmatrix} \tag{4.6}$$

is a vector, which represent the position of each stage, and M, K, and C are the mass matrix, the stiffness matrix, and the damping matrix, respec-

tively. These matrices are the subject of optimization. If one assumes no cross talk in different degrees of freedom, the equations of motion in every degree of freedom have the same form as the above equations. For instance, in the optimization of the horizontal isolation, M describes the distribution of the mass at each stage, and K corresponds to the stiffness of the pendulum, while C has the damping coefficients as its components.

The procedure for the optimization was as follows:

1. Assume a nominal value for every parameter. Most initial values are taken from the design of the original TAMA suspension.

2. Evaluate the parameter by computing the motion of the mirror with different values for the parameter to be optimized, and then replace the assumed parameter with the optimal value.

3. Optimize all the parameters by repeating step 2.

The different design of the SUS does not have significant impact on in the r.m.s. motion and velocity of the mirror because, thanks to the magnetic damping, they are dominated by the contribution from the overall SAS motion at low frequencies, below 1 Hz. Therefore each tentative design was evaluated mainly from a point of view of attenuation performance in the GW detection band (above few tens of Hz), and of the quality factor of the rigid body modes of the SUS.

While executing the process, we found some empirical rules for optimization.

Mass Assuming that the mirror and the recoil mass are suspended by identical pendulums, only their in-phase mode will be excited by the seismic motion. Under this assumption, the optimal recoil mass is automatically defined to be equal to the mirror's mass. Then the optimization has been done for the intermediate mass only. The horizontal transfer function between the motion of the suspension platform and the mirror is plotted in figure 4.2. The isolation performance is not sensitive to the mass of the intermediate stage.

Stiffness The horizontal isolation performance at the mirror, computed by changing the independent resonant frequency of the intermediate stage

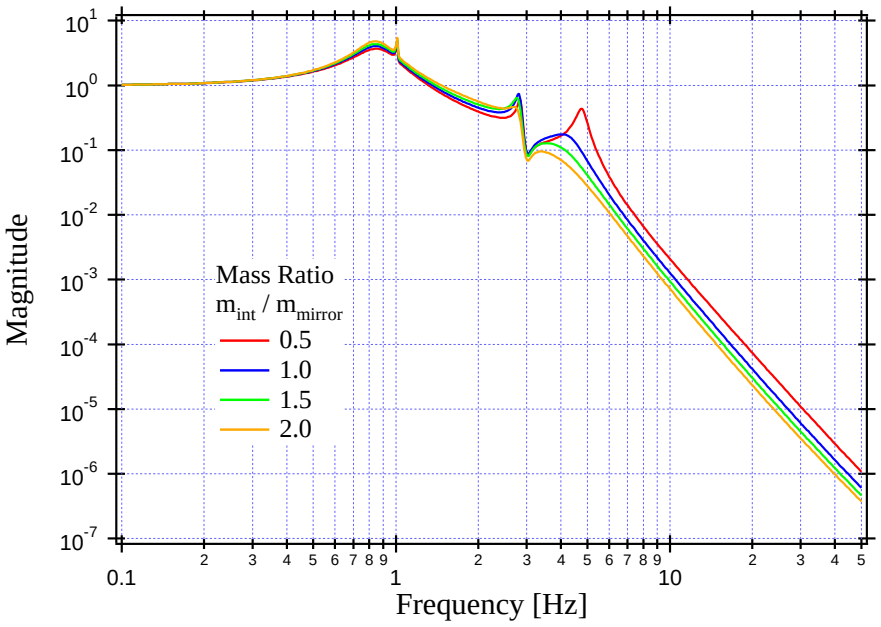

Figure 4.2: Horizontal transfer function between the suspension platform and the mirror, with different mass of the intermediate stage.

is shown in figure 4.3. The fundamental mode, in which the mirror and the intermediate mass move in phase, is damped more if the intermediate stage is softer. This trend can be understood as follows. The mirror motion recoils more effectively against the intermediate mass pendulum if its suspension is softer, and the relative velocity between the intermediate mass and the damper becomes larger, obtaining more damping force. This implies that the coupling of the intermediate and the lower pendulum motion is vital for the damping. When the intermediate pendulum is softer than the mirror pendulum (ratio <1), there is not much more to gain.

The resonant frequency of the damper of the intermediate mass is also important. From the isolation performance plotted in figure 4.4, when the frequency of the damper for the intermediate mass is too low, it injects the seismic motion to the intermediate stage around its own resonant frequency. The isolation performance at higher frequencies is spoiled when the damper is tuned at too high frequency.

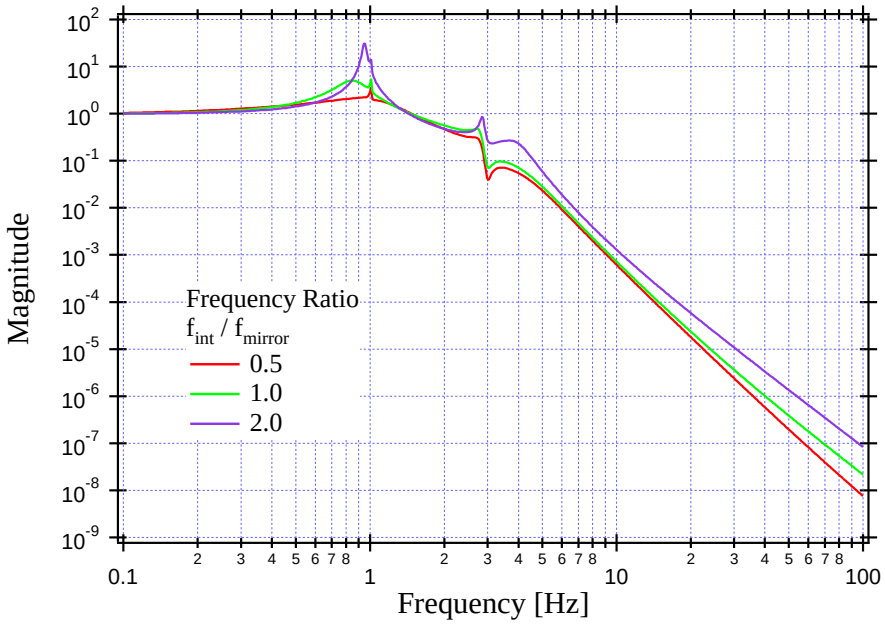

Figure 4.3: Horizontal transfer function between the suspension platform and the mirror, with different resonant frequency of the intermediate stage. The lower resonant frequency improves attenuation, the length of the intermediate pendulum was kept equal to that of the original TAMA suspension (ratio =1).

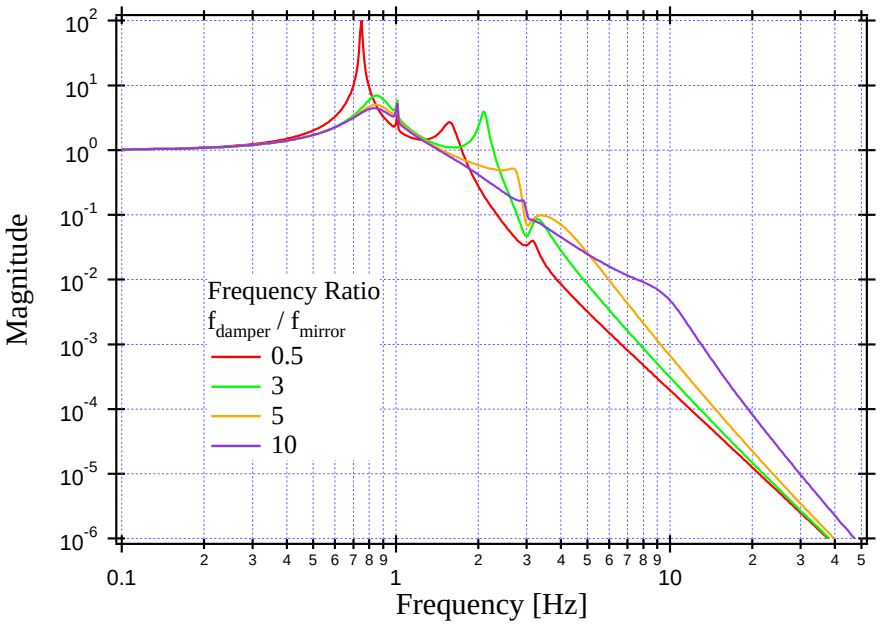

Figure 4.4: Horizontal transfer function between the suspension platform and the mirror, with different resonant frequency of the damper acting on the intermediate mass. The optimal ratio is 5.

Rigid Body Model

The point mass model is intrinsically uni-dimensional, and is not capable of dealing with cross-talk between different degrees of freedom. While the translational motions of the SUS are not affected by the geometry, the rotational motion is very sensitive to the geometric information of the system. This is because the rotational motion is determined by the torque on each mass and depends on the relative distance between the CM and the point where the external force is exerted. Therefore we used a 3-dimensional model to design the geometric parameters of the system.

The 3-dimensional model is implemented using homemade software, Mechanical Simulation Engine (MSE). The MSE is a component for the LIGO End-to-End (E2E) model. E2E describes virtual LIGO detectors, including detailed information of the mechanics, the optics, and the electronics, to simulate the behavior of the detectors essentially in the time domain. MSE is written in C++, to cover the mechanical part of E2E. In MSE the fundamental mechanical elements such as rigid bodies, springs, etc. are implemented as C++ objects. Each object is defined with the physical parameters like

vertical stiffness of spring	355 N/m
length / diameter of upper wire	250 mm / 100 μm
longitudinal stiffness of upper wire	1.3×10^4 N/m
length / diameter of lower wire1	250 mm / 50 μm
longitudinal stiffness of lower wire1	3100 N/m
length / diameter of lower wire2	250 mm / 100 μm
longitudinal stiffness of lower wire2	1.3×10^4 N/m

Table 4.2: Design parameters for the vertical spring and the wires in SUS. The lower wire1 and the lower wire2 are used to suspend the test mass and the recoil mass respectively. The soft spring at the suspension point is realized with a mini-MGAS.

mass, momentum of inertia around three axes, stiffness, and length etc.. The user can specify the connection between the objects, specifying geometric information. Then the software calculates the equilibrium status of the virtual system.

As the E2E is essentially a simulator in the time domain, the MSE computes the motion of the mechanics in time domain by solving the equations of motion, with standard numerical technique. The user can give arbitrary input to the system by using actuator objects.

The software is also used to compute the frequency response of the system by taking virtual lock-in measurements. In the virtual lock-in measurement, the excitation to the system is given with a swept frequency while sensor objects detect the amplitude and the phase of the displacement of any object. By scanning the excitation frequency, we can obtain the frequency response of all objects.

We used the MSE to optimize the geometry of the system, like the momentum of inertia of each stage, the positions of wire attachment, etc.. The optimization process for these geometric parameters is the same applied to the point mass model.

Parameters of SUS

The optimization process described in the previous sections was applied, in every degree of freedom, thus determining the mechanical and geometrical parameters for the new SUS listed in table 4.2 to 4.4, and shown in figure 4.5 and 4.6.

mass of intermediate mass	2.7 kg
momentum of inertia of i.m.	I_x : 4.4×10^{-3} kg $\cdot$ m^2
	I_y : 5.6×10^{-3} kg $\cdot$ m^2
	I_z : 6.5×10^{-3} kg $\cdot$ m^2
mass of recoil mass	1.034 kg
momentum of inertia of r.m.	I_x, : 5.6×10^{-3} kg $\cdot$ m^2
	I_y : 4.4×10^{-3}kg $\cdot$ m^2
	I_z : 6.5×10^{-3}kg $\cdot$ m^2
mass of upper damper	1.5 kg
momentum of intertia of u.d.	I_x : 6.0×10^{-3} kg $\cdot$ m^2
	I_y : 3.8×10^{-3} kg $\cdot$ m^2
	I_z : 9.1×10^{-3} kg $\cdot$ m^2

Table 4.3: Design parameters for the intermediate mass and the recoil mass.

mass of upper damper	1.5 kg
momentum of intertia of u.d.	I_x : 6.0×10^{-3} kg $\cdot$ m^2
	I_y : 3.8×10^{-3} kg $\cdot$ m^2
	I_z : 9.1×10^{-3} kg $\cdot$ m^2
damping coefficient of u. d.	γ_1: 40 kg/s
mass of lower damper	0.2 kg each
damping coefficient of l. d.	γ_2: 0.1 kg/s each

Table 4.4: Design parameters for the dampers.

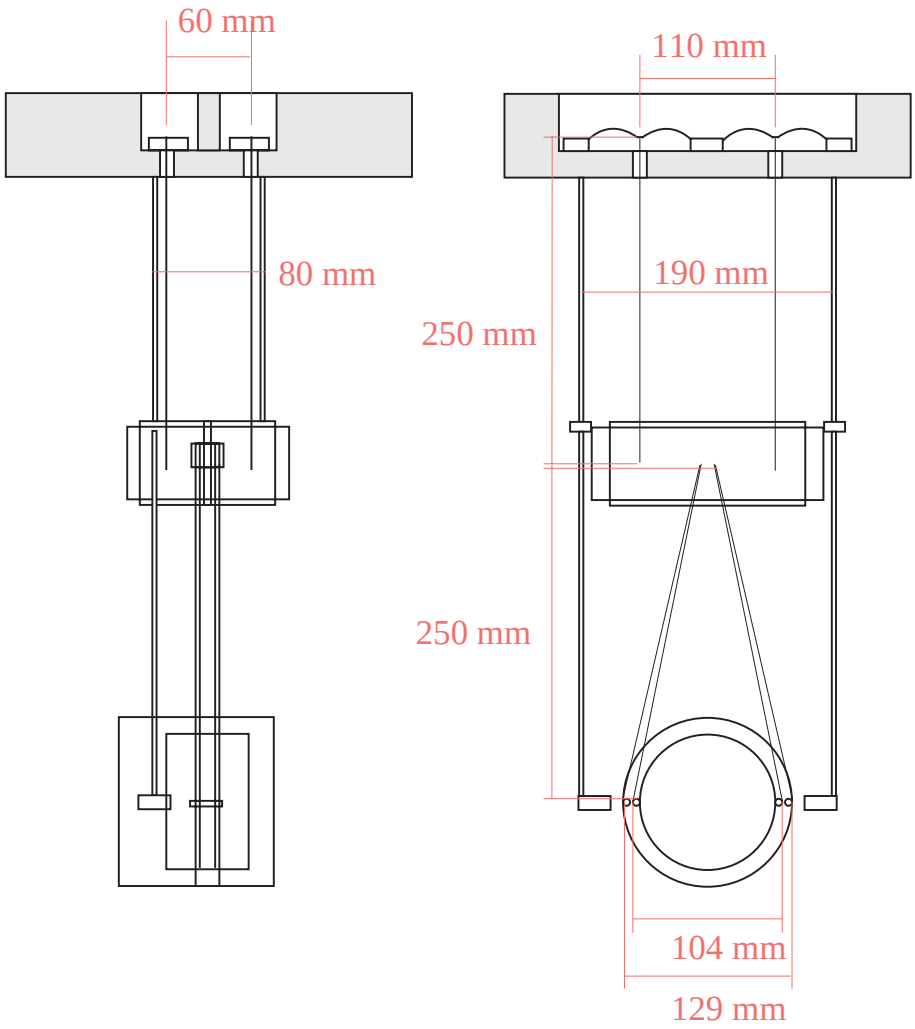

Figure 4.5: Geometry of the SUS.

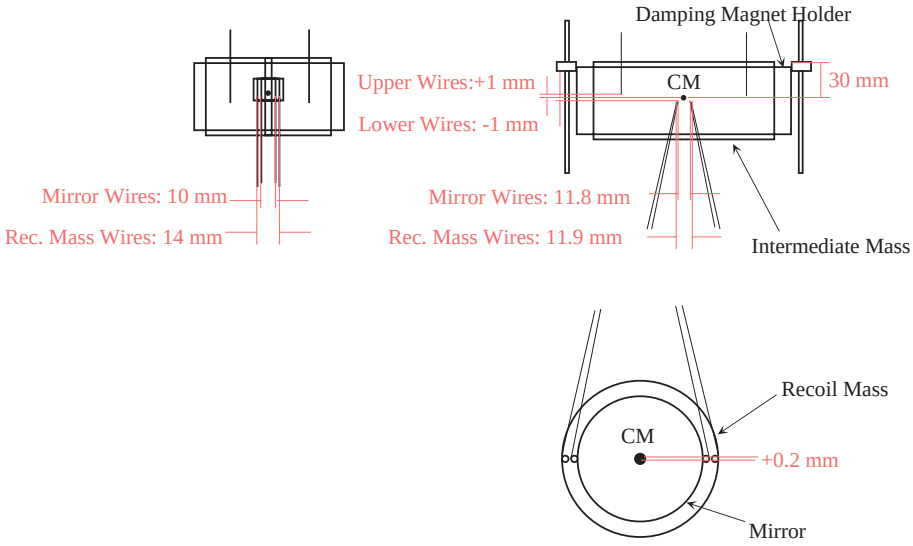

Figure 4.6: Geometry of SUS wires.

4.1.5 Recoil Mass

Motivation: Mirror Actuation

The test mass and the recoil mass are suspended from the common intermediate stage, and their mass and the length of pendulum are tuned to be identical. This topology has the following technical advantages [44, 30]:

- The actuator is isolated from the seismic disturbances, fluctuation of standing forces applied on the mirror due to the change of relative position between the mirror and the actuation mass will be suppressed. This is important for use of non-linear actuators.
- Even with linear actuators like the coil-magnet actuator, the distance between the magnet and the coil is more stable. Therefore the actuation efficiency is highly stable.
- The actuation on the mirror is isolated and independent from the upper stages, because the reaction from the mirror and the recoil mass compensate each other at the intermediate stage.

The third point is particularly important to simplify the servo design for the mirror actuation. If the mechanical impedances of the mirror pendulum and that of the actuator stage are different, they recoil on the upper stage

asymmetrically, and the motion of the upper stage induces spurious cross couplings and complex frequency response of the mirror actuation. The example of a highly asymmetric system and the frequency response of the mirror actuation are shown in figure 4.7.

On the contrary, when the mirror and the actuator stage are suspended by identical pendulums, the frequency response becomes as simple as that of a single pendulum, because of the recoil cancellation effect (figure 4.8).

Effect of Asymmetry

As shown in figure 4.8, when the bottom stage (the mirror and the recoil mass pendulum) is symmetrical, the back action induced by the mirror actuation does not interfere with the upper structure. However any mismatch in the mechanical impedance f the two pendulums makes that the back actions would not compensate perfectly. Here we study the mechanical tolerances of the system by using a simple model illustrated in figure 4.9 (a). In this point mass model, the intermediate mass of the double pendulum holds wires to suspend both the mirror and the recoil mass. Eddy current damping is applied from the platform to the intermediate mass. The nominal resonant frequency of each pendulum and the magnet support, of mass of each stage are those of the TAMA SAS prototype.

Mass imbalance The transfer from the suspension point to the mirror in the longitudinal direction is plotted in figure 4.10 with different masses for the mirror and the recoil mass, while keeping their resonant frequency identical. Also the frequency response of the mirror actuation is shown in figure 4.11. It is clear that the imbalance of the mass does not cause significant change in the behavior of the system, and the attenuation curve is smooth and the mirror can in all cases be actuated as a single pendulum.

Length imbalance In contrast of the case of mass imbalance, the different length of the suspension wires makes substantial change in the frequency response of the system. In this case the frequencies of two pendulums are non-identical and their motion separates into the common and the differential modes. In the attenuation performance of the double pendulum plotted in figure 4.12, the differential mode of the mirror and the recoil mass appears sharply at 1 Hz. The sharper peak at 1 Hz in the frequency response of the

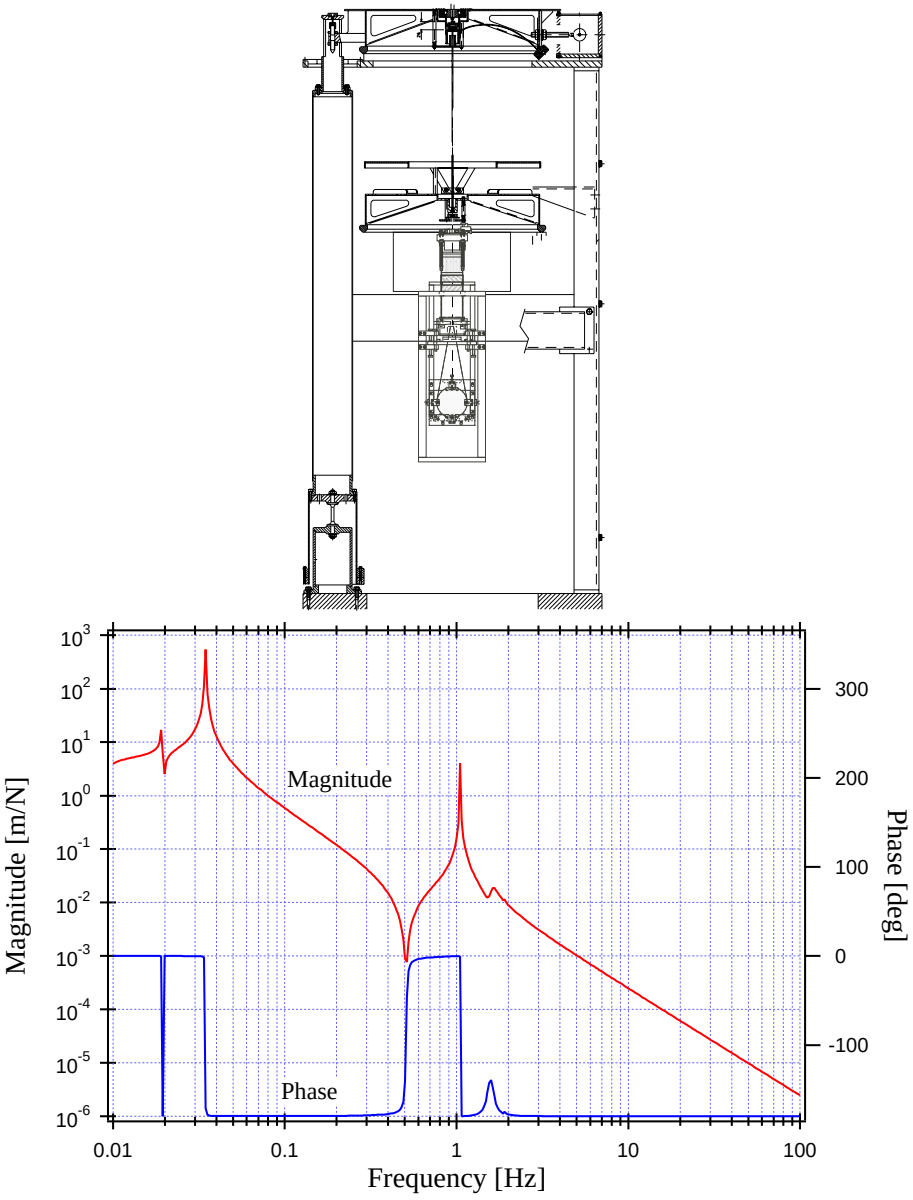

Figure 4.7: Frequency response of the mirror in the longitudinal direction, to the force exerted by the mirror actuator (bottom graph). In this simulation (top scheme) the rigid frame of the original TAMA mirror suspension system is directly suspended from the filter1, and the coils for the mirror actuation are mounted on the frame. The peak at 1 Hz corresponds to the resonance of the mirror pendulum. Complicated structures appear at lower frequencies. These structures are related to the resonance of the IP, MGAS, and the tilt of the filter etc..

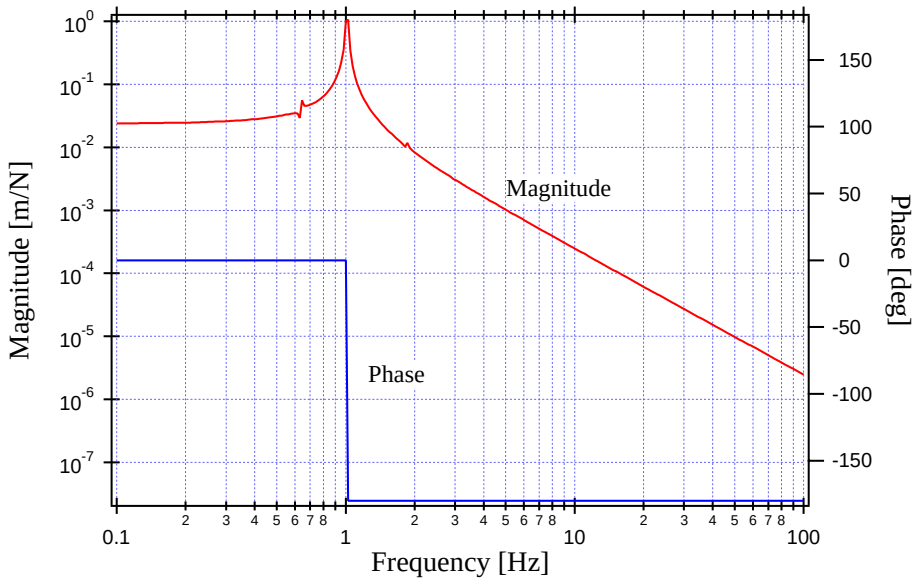

Figure 4.8: Frequency response of the mirror in the longitudinal direction, to the force exerted by the mirror actuator. The computation is based on the actual SAS prototype. There is negligible coupling between the longitudinal and the pitch motion of the mirror around 600 mHz.

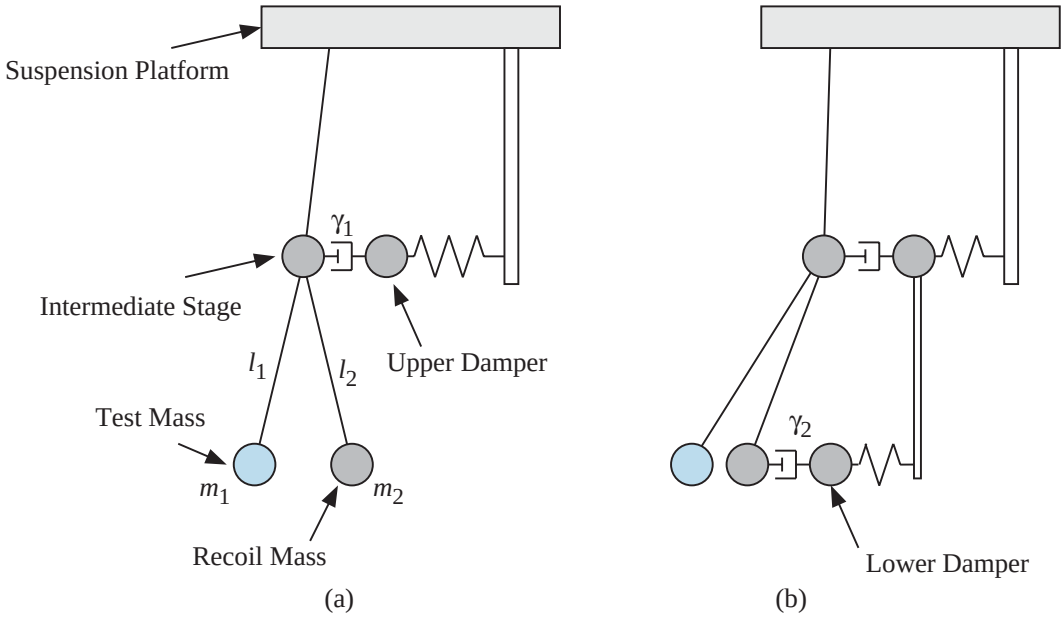

Figure 4.9: Point mass model of SUS. Flexible rods support the dampers. The upper rod is tuned at 5.2 Hz and the lower is 3 Hz. The intrinsic quality factor of 10^4 is assumed for each pendulum.

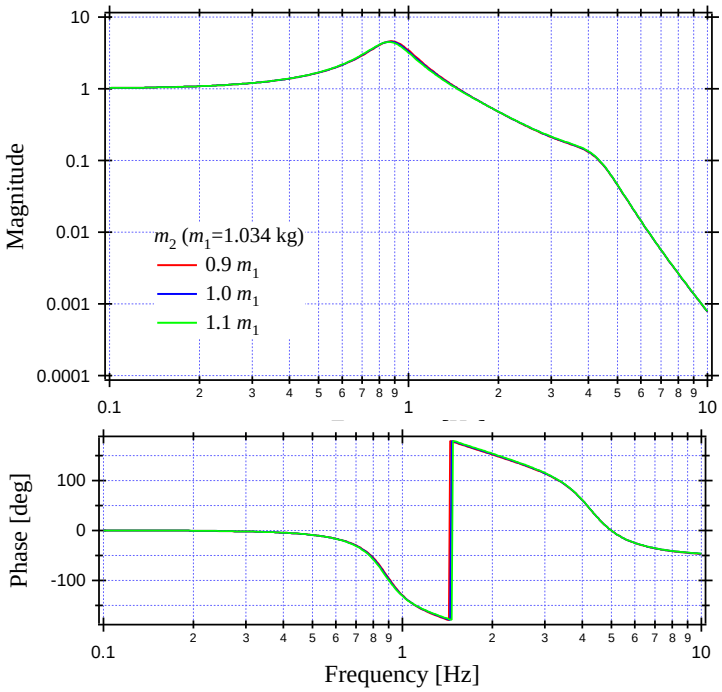

Figure 4.10: Isolation Performance of double pendulum with different lower masses. The three curves are practically indistinguishable.

mirror actuation is also the differential mode (figure 4.13, cfr. figure 4.11). This mode does not couple to the motion of the intermediate mass, because the compensation of the back actions partially works for slight differences of the wire length. For that reason, the damper on the intermediate mass is not able to suppress the peak of the mode efficiently. These sharp resonances are particularly noxious to the control system. This problem is solved with an additional passive, differential mode damper.

Damping on the Differential Mode

The differential motion of the mirror and its recoil mass remains high quality factor and, since it does not couple to the upper stages, it can not be damped by the active damping system described later. Therefore the SUS is equipped with additional Eddy current damper dedicated to this mode (figure 4.9 (b)). The permanent magnets for the damper are suspended from the damper of the intermediate stage and they are located next to the lateral surface of the recoil mass. As the damping works directly on the recoil mass, the strength

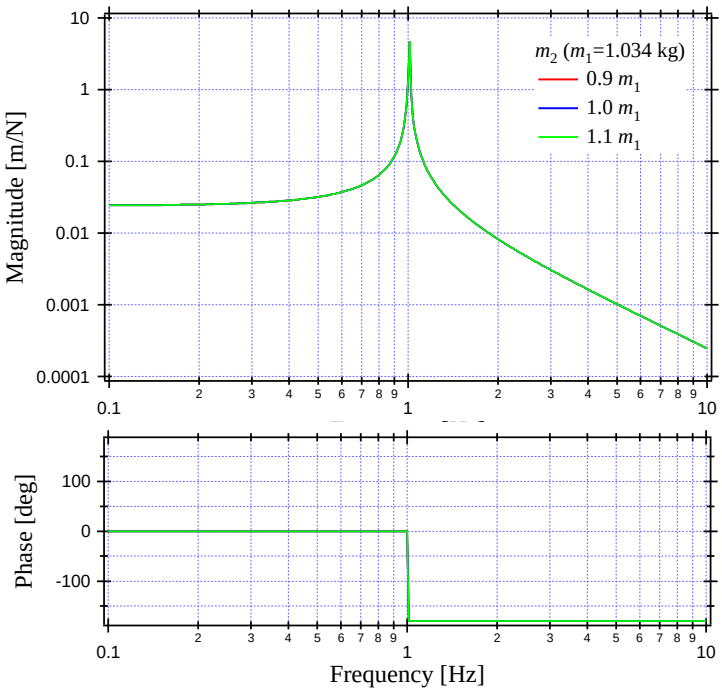

Figure 4.11: Frequency response of mirror actuation with different lower masses.

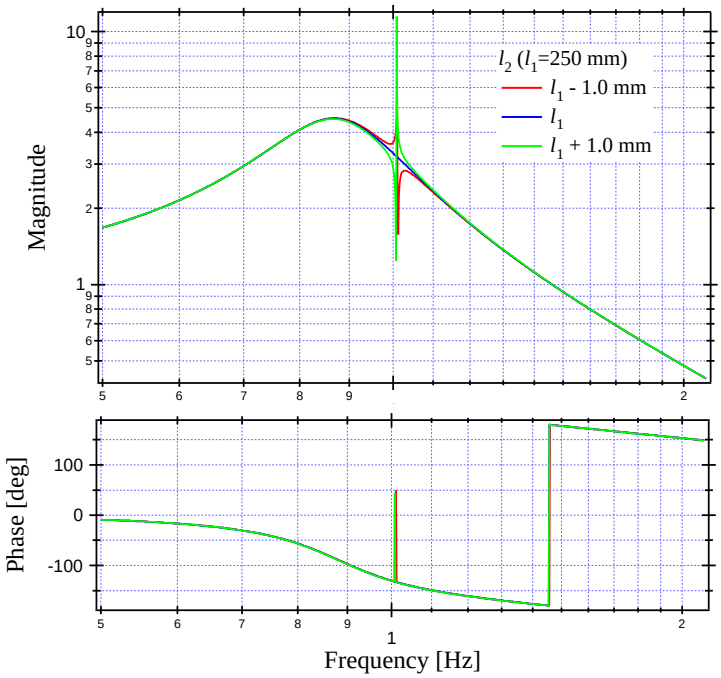

Figure 4.12: Isolation performance of the double pendulum with different length of wire for the mirror and the recoil mass. The narrow peak at 1 Hz is the differential mode of the lower masses.

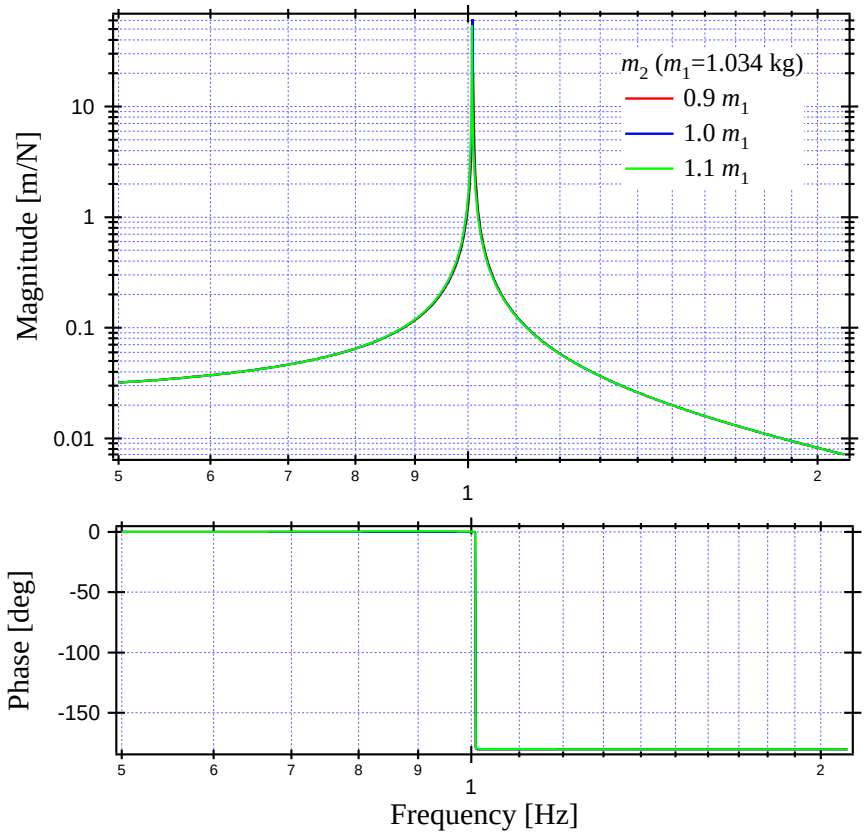

Figure 4.13: Frequency response of the mirror actuation with different length of wire for the mirror and the recoil mass.

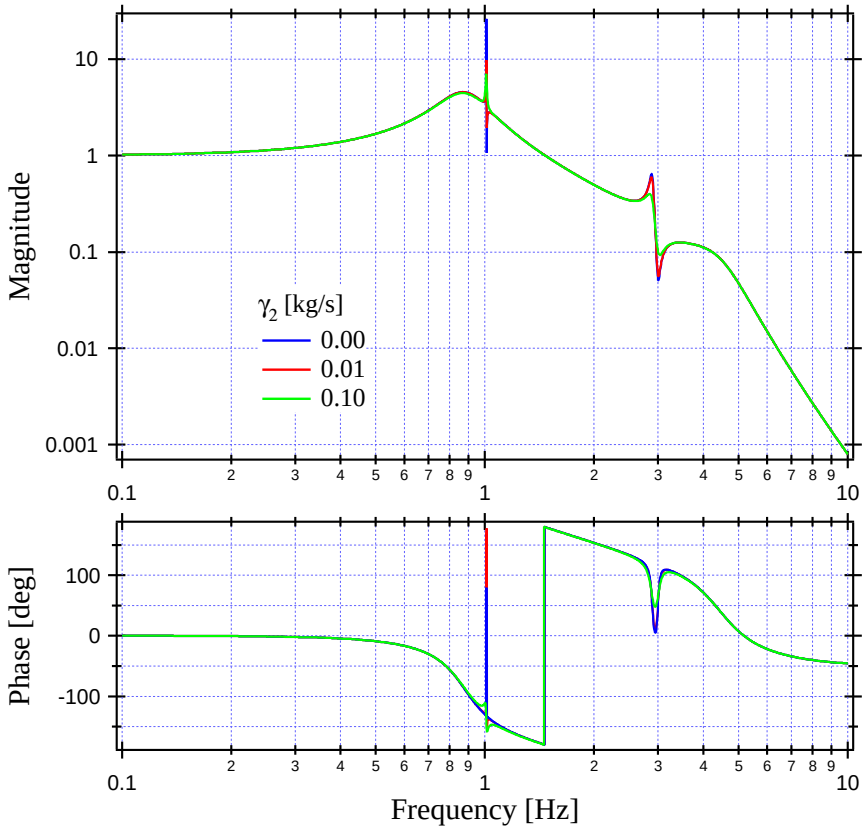

Figure 4.14: Isolation performance of the double pendulum, assuming 1.0 mm shorter wires for the recoil mass suspension. The differential mode of the mirror and the recoil mass is sufficiently suppressed by the additional differential mode damper close to the recoil mass. While the coefficient of the upper damper is $\gamma_1 = 20$ kg/s, the additional damper requires only $\gamma_2 = 0.01$ to reduce the quality factor of the mode to less than 10.

of the magnetic field can be reduced by few orders of magnitude from that of the intermediate mass damper to achieve the desired quality factor (smaller than 10) (figure 4.14). The thermal fluctuations induced by the dissipation in the recoil mass are doubly isolated from the mirror and, also because of the smaller amount of dissipation, the thermal noise cause by the lower magnets do not degrade the performance of entire system.

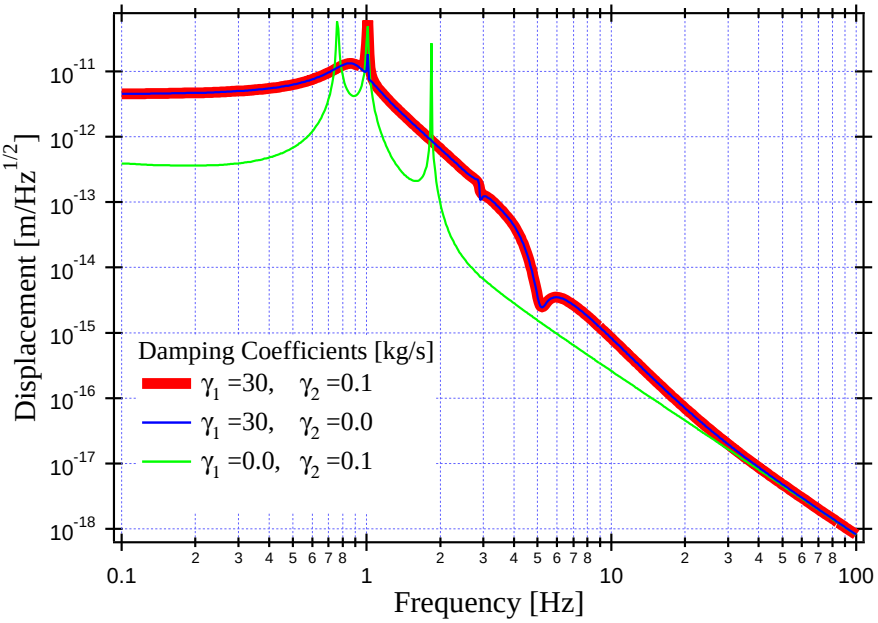

Figure 4.15: Thermal fluctuation of the mirror in the longitudinal direction for different damping configurations. The damping is applied both on the intermediate stage and the recoil mass (red), only on the intermediate stage (blue), and only on the recoil mass (green).

4.1.6 Thermal Noise in SUS

To compute the thermal noise of the SUS, we used the point mass model constructed to study the recoil mass suspension (figure 4.9-b), and applied the fluctuation-dissipation theorem. The obtained thermal motion of the SUS mirror is shown in figure 4.15. The thermal motion of the mirror is totally dominated by the fluctuation caused by the upper damper, except for 1 Hz, the frequency of the differential mirror to recoil mass mode.

4.1.7 Cross-Coupling

Coupling between Translational Modes

With the 3-dimensional simulation in MSE, it is possible to implement asymmetries in the system and to compute the relative cross-coupling transfer functions. However, the asymmetry in the actual system is in general unpredictable because it is caused by random errors in machining, assembly, etc.. In the references [55, 71], the cross-coupling functions in the original mirror

suspension for TAMA300 were computed by assuming some statistic distribution of the asymmetry. Strong frequency dependency and large variations in the amplitude of the cross-coupling functions were observed, particularly around the resonant frequencies of the rigid body modes. However, off the resonances the cross-coupling functions have amplitude of the order of 1 %. Therefore we simply assume 1 % cross-coupling in any combination of two independent translational modes as it has been routinely assumed in the most studies on mechanical filters [32]. Under this assumption, the transfer function between the suspension point to the n-th stage of a pendulum in the longitudinal direction is written recursively as

$$H_n^{\mathrm{x}} = \sum_{j=\mathrm{x,y,z}} H_{n-1}^j H_0^k \alpha_{jk}. \tag{4.7}$$

Here H_n^j $(j = \mathrm{x, y, z})$ is the amplitude of the transfer function between the suspension point (ground) to the n-th stage in a translational direction, H_0^j is the amplitude of the normal transfer function between $(n-1)$-th and n-th stage, and α_{jk} $(j, k = \mathrm{x, y, z})$ is the coupling coefficient which satisfies

$$\alpha_{jk} = \begin{cases} 1 & j = k \\ 0.01 & j \neq k \end{cases}. \tag{4.8}$$

To complete computation of the transfer function of the mirror in the longitudinal direction would require $3^5 = 243$ paths in the case of the SAS with 5 stages. To avoid this complication, we select the most critical paths and neglect the others. Since the transversal direction has practically the same level of isolation as the longitudinal direction, its contribution to the motion of the stage below is negligible. Therefore it is reasonable to drop the contributions from the transversal mode. Even with this simplification, the computation t still requires computations on $2^5 = 32$ paths. For further simplification, we approximate the equation (4.7) as

$$H^x_{\mathrm{mirror}} = H^x_{0\mathrm{mirror}} + 0.01 \times H^z_{0\mathrm{mirror}}. \tag{4.9}$$

Here $H^x_{0\mathrm{mirror}}$ is the amplitude of the normal transfer function from the ground to the mirror. In this approximation the computation becomes much simpler, but we omit all z-x coupling in the intermediate stage. The result, though, is still useful to understand the experimental results presented later.

Coupling between Rotational and Translational Modes

In general, there are two ways in which the rotational motion of the suspension stage can affect the sensitivity of the GW detectors. First, the rotational motion of a stage in the suspension directly excites the longitudinal motion of the lower stage, through the asymmetry in the mechanics. Second, the rotational motion of the test mass directly results in longitudinal motion perturbation because of mis-centering of the interferometer beam.

We neglect the first effect, because of the same reason that allows us to drop most components in the cross-coupling of translational motions.

About the second effect, when the test mass rotates by angle of θ rad, it is sensed by the interferometer as the longitudinal displacement of

$$\Delta x = a\theta, \tag{4.10}$$

where a is the distance between the center of rotation and the beam spot on the surface of the mirror. Although it is tough to evaluate the accuracy of the beam centering in the large scale interferometers, we assume that the beam can be off centered by no more than 1 mm [57]. With this assumption, we can simply add its contribution to the displacement computed by using the transfer function in equation (4.9).

4.1.8 Normal Mode Transfer Functions

The computed normal mode transfer functions between the excitation on the suspension platform to the motion of each stage are shown in figure 4.16 and 4.17. These are the results of the optimization with the rigid body model. The above transfer functions will be compared with the experimental data to validate the prototype SUS later in section 4.3.

4.2 Prototype SUS

4.2.1 General Description

The prototype SUS consists of 6 moving parts: the suspension platform, the intermediate mass, the test mass, the recoil mass, and the upper and the lower dampers. The design of the prototype SUS is shown in 4.18.

A single wire from the filter1 suspends the suspension platform. The

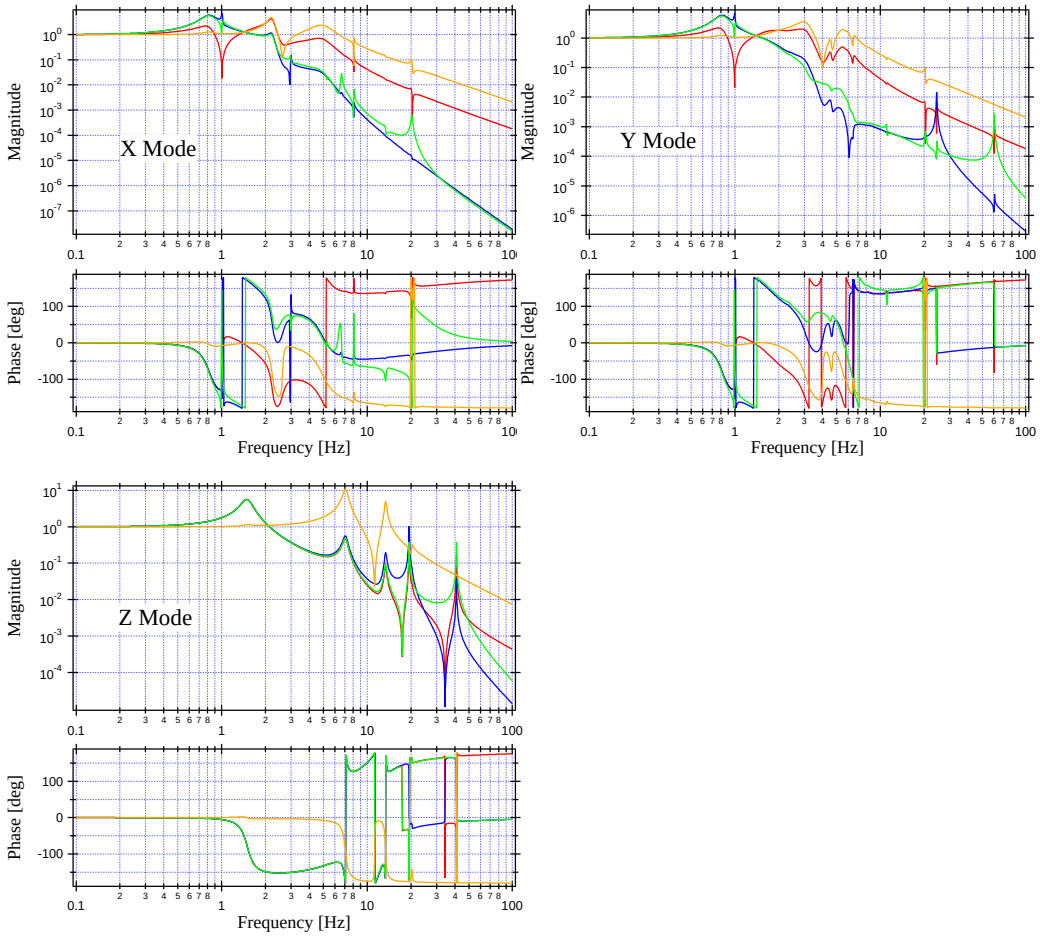

Figure 4.16: Simulated transfer function of SUS, in translational modes relative to suspension platform motion. The intermediate mass (red), the mirror (blue), the recoil mass (green), the upper damper (orange).

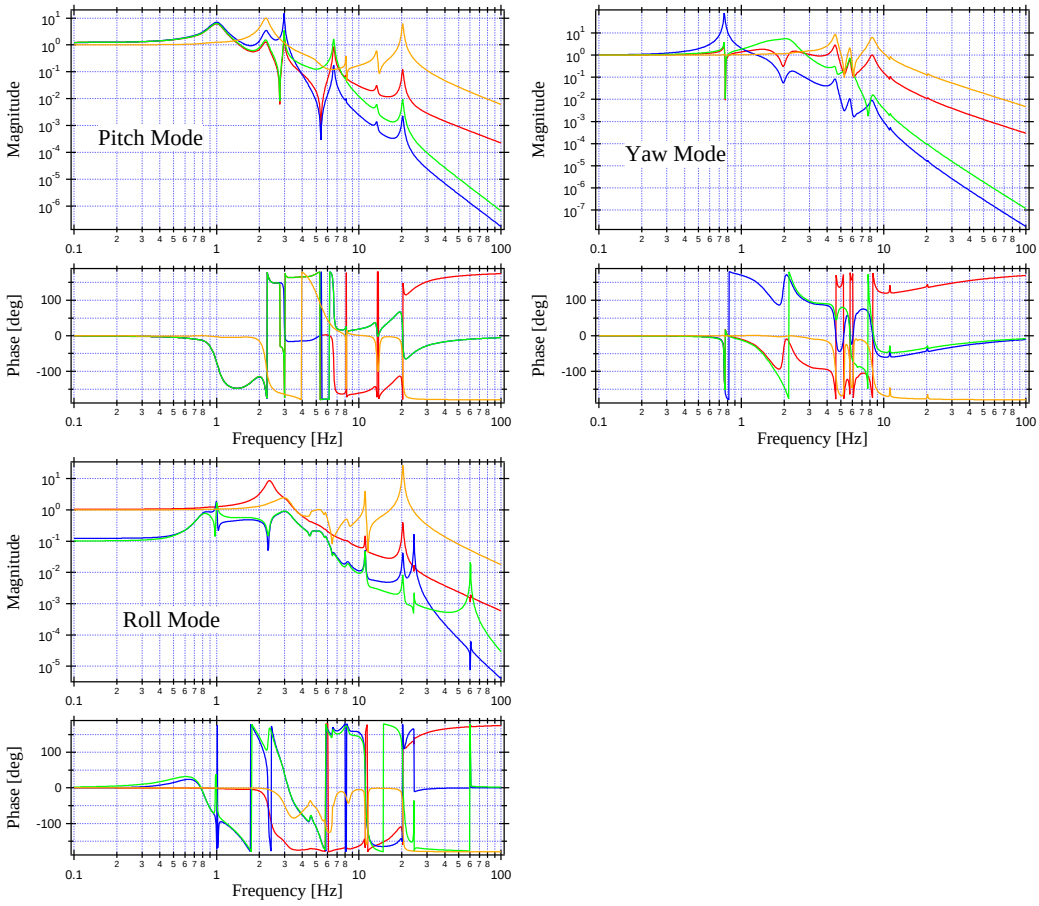

Figure 4.17: Simulated transfer function of SUS, in the rotational modes. The intermediate mass (red), the mirror (blue), the recoil mass (green), the upper damper (orange).

platform houses four mini-MGAS for the low frequency vertical isolation of the SUS. The suspension platform is contained inside a rectangular box (open in its lower face) called coil box. The coil box is rigidly connected to the lower MGASF and is equipped with eight coils, each coupled with a small magnet mounted on the platforms' surface. The coil magnet pairs allow to control the attitude of the suspension platform in all desired degrees of freedom and control, marionette like, the attitude of the mirror below. The platform controls are intended to minimize or null the DC force requirements on the mirror actuators.

The mMGAS is a simplified version of the MGAS used in the vertical filters, and it is composed by twin blades facing each other. By tuning the longitudinal compression of the opposing twin blades, they could be tuned as low as 500 mHz. For ease of operation, they are only tuned at 1.5 Hz in the prototype.

The intermediate mass, of parallelepipedal shape, is suspended by four wires connected to the four mMGAS on the platform. Four loops of wires hang down from the intermediate mass. The inner pair of loops suspends the test mass and the outer loops suspend the recoil mass. The recoil mass is co-located with, and envelops, the mirror.

Next we consider the dampers for the intermediate mass and for the recoil mass. The upper damper, for the intermediate mass, is a ferromagnetic box open at the top and the bottom, suspended from the suspension platform by means of four rods. The box is called magnet box. The dimensions of the rods are designed to obtain the desired stiffness in the horizontal direction. Each rod is connected to the damper via cross bow springs for vertical isolation. There are 16 rare metal 23 mm diameter 4 mm thick permanent magnets attached inside the Eddy current damping box. A 1 mm clearance is left between the magnets and the intermediate mass. The lower (recoil mass) dampers are suspended from both sides of the upper damper via stainless steel rods. The lower damper is a bob on which four (4 mm $\times$ 8 mm, 3 mm thick) small magnets are attached to face the lateral surface of the recoil mass.

The SUS is assembled separately from the rest of the SAS components on a custom assembly and alignment jig, then it is installed under the filter1.

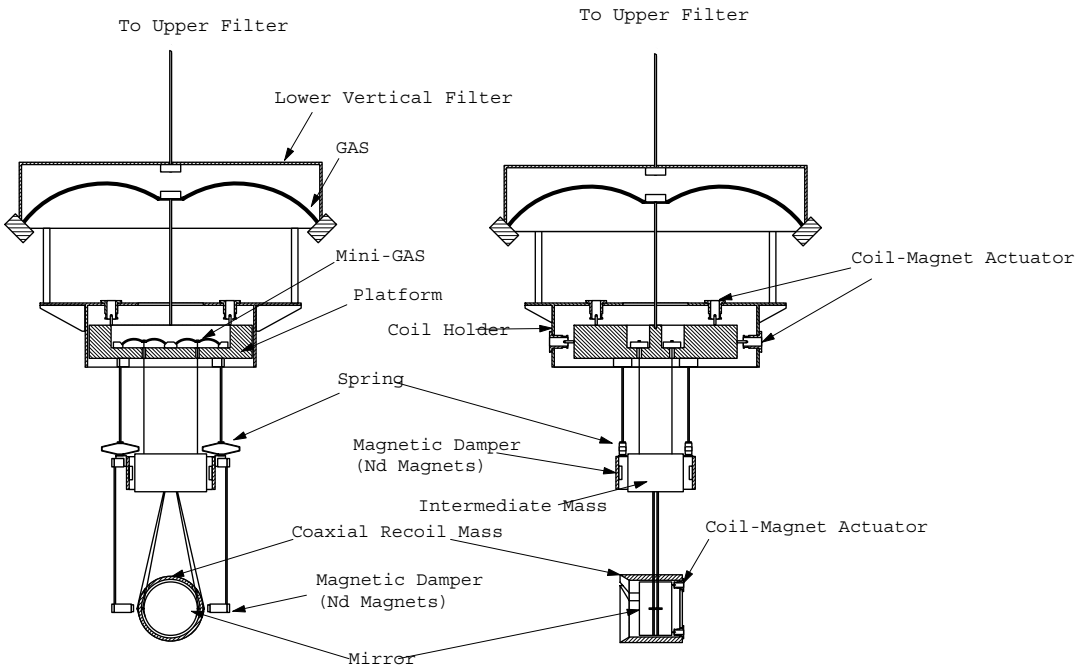

Figure 4.18: Prototype SUS.

4.2.2 Choice of Materials

Masses

To implement the Eddy current damping which requires strong permanent magnets, the intermediate mass needs to be made of nonmagnetic material and should be highly conductive to increase the damping efficiency. The possible choices were aluminum and copper. Copper is a heavier material ($\rho_{\mathrm{Cu}} = 8.96$ g/cm^3), while aluminum has similar density as fused silica, the material for the test masses ($\rho_{\mathrm{Al}} = 2.70$ g/cm^3, $\rho_{\mathrm{SiO_2}} = 2.20$ g/cm^3). To achieve similar dimensions and similar masses in all bobs of the SUS, we used aluminum to fabricate every metallic stage in the SUS. The material is also compatible with UHV.

Wires

There are not so many choices for the material and the dimension of the wires used in the SUS. Each mass needs to be suspended by four wires, in order to control the tilt of the test mass through the tilt of the above stage.

Density	19.3 g/cm^3
Poisson Ratio	0.28
Young's Modulus	400 GPa
Tensile/Yielding Strength	several GPa (highly dependent on treatment)
Shear Strength	175 GPa

Table 4.5: Mechanical properties of drawn tungsten wire.

Also nonmagnetic materials are preferable, to avoid interferences with the Eddy current damping magnets. To push the resonant frequency of the first violin mode of the lowest pendulum away from the GW detection band, the wires need to be light: i.e. small diameter and high tensile strength. Like in the old TAMA, we adopted tungsten wires. The mechanical properties of drawn tungsten wire are listed in table 4.5. In first approximation, the first violin mode frequency of the tungsten wire with length l, diameter d and tension P is written as [34]

$$\frac{1}{2l}\sqrt{\frac{P}{\rho_W}}, \tag{4.11}$$

where ρ_W is density of tungsten. When $m = 1.034$ kg, and the mass is suspended by four wires with dimension of $l = 250$ mm, $d = 50$ μm, the resonant frequency is 508 Hz. Also this diameter corresponds to the tension of 1.3 GPa in each wire, less than half of the tensile strength of the material.

Other Components

The main concern in selecting the material for the other components are magnetic properties and vacuum compatibility. For those reasons, we used aluminum, stainless steel, and maraging steel for all metallic parts, and Peek, a plastic bakeable at 250 degrees, for the parts which require insulation in the prototype SUS.

Wiring is made with copper mono-filament, kaption insulated twisted pairs.

Nickel plated Neodymium (Nd) magnets used in the force actuators in the system. They are plated with nickel for vacuum compatibility and protection. To avoid the leakage of the magnetic field, holders of the magnets are made of nickel plated transformer iron.

4.2.3 Actuators

Mirror Actuator

Four pin shaped Nd magnets (1 mm diameter and 10 mm length) are attached on the back surface of the mirror with alternated polarization. The head of the magnet is positioned to float inside a small coil mounted on the back side of the recoil mass, to form a voice coil actuator. The relative position of the magnet and the coil is selected to obtain the best actuation linearity. These actuators are able to control the longitudinal position and the orientation of the mirror. In the prototype Eddy currents on the aluminum "mirror" body was supposed to complicate the control. However, this problem was not observed in our experiments, and it will not be present with the real TAMA fused silica mirrors.

Suspension Platform Actuators

The suspension platform is suspended from the filter1, support four pin shape Nd magnets are mounted on its top surface, two on the front and two on the back surface. Eight coils mounted on the coil box face these magnets.

The actuators composed by the coil magnet pairs are used to control the orientation of the platform. Particularly this is the only point where the DC tilt of the platform can be corrected.

4.3 Experiments on the Prototype SUS

To validate the prototype SUS, we took a series of measurements of its isolation performance. The measurements were performed with a pre-assembled SUS prototype before mating it with the rest of the SAS tower.

4.3.1 Experimental Setup for Isolation Performance Measurements

To measure the isolation performance, i.e. transfer functions between the suspension point to the each stage of the SUS, we used a commercial vibration test system (E·DES-452 from Akashi). The system is composed by a voice coil actuator acting on a low friction sled with travel of 10 mm with the maximum output force of 4 kN. The table is lubricated by an oil film, like

the oil bearing we developed for the IP prototype tests, and it moves, with low friction, in the horizontal direction. The voice coil can be connected to the table for horizontal excitation, or rotated vertically for vertical excitation (see figure 4.19). In the vertical configuration, the motion of the voice coil is aligned by a cross bearing system inside it.

The detection of the motion was done with commercial accelerometers (8628B5 from Kistler), and homemade optical position sensors. 8628B5 is a light weight passive accelerometer utilizing a standard PZT beam and test mass arrangement. It has relatively high sensitivity of 1000 mV/g with transversal coupling of 1.0 %. The frequency band of the device is 1 Hz to 2 kHz with a typical resolution of 120 μg r.m.s.. [58].

The homemade position sensor is sketched in figure 4.20. It consists of an LED (L2656 from Hamamatsu), and two PDs (S1190 from Hamamatsu). The output light emitted from the LED is reflected by a mirror attached on the object of measurement, and the returned light is detected by the PDs. The output signal of the sensor is proportional to the sum of the photo current induced in the PDs. Two PDs are used to reduce the spurious sensitivity to the tilt of the mirror. The position sensor was used to take measurement below few Hz, where the commercial accelerometer becomes insensitive. The calibration curve of the sensor is shown in figure 4.20. The sensor signals were recorded by an FFT servo analyzer (R9211C from Advantest).

The SUS used for the prototype test was not equipped with the recoil mass damper, because the differential mode of the mirror and the recoil mass do not appear in the measurements presented in the next section. We compare the calculated transfer functions of the SUS without the damper to the measurements.

4.3.2 Longitudinal Isolation Performance

The transfer functions in the longitudinal direction were measured with the vibration test system described in the previous section. The assembly frame for the SUS was rigidly fixed onto the sliding table with the suspension platform attached on it. The measured longitudinal isolation performance is plotted in figure 4.21 together with the simulated curves.

The measurements were limited by acoustic noise and by the resolution of the accelerometer at higher frequencies, typically above few tens of Hz. As the acoustic excitation, part of which comes directly from the voice coil,

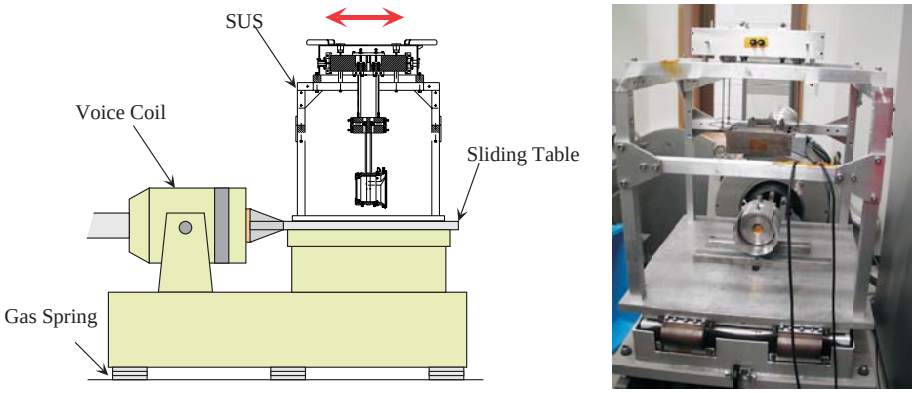

Figure 4.19: Setup for longitudinal isolation performance measurement.

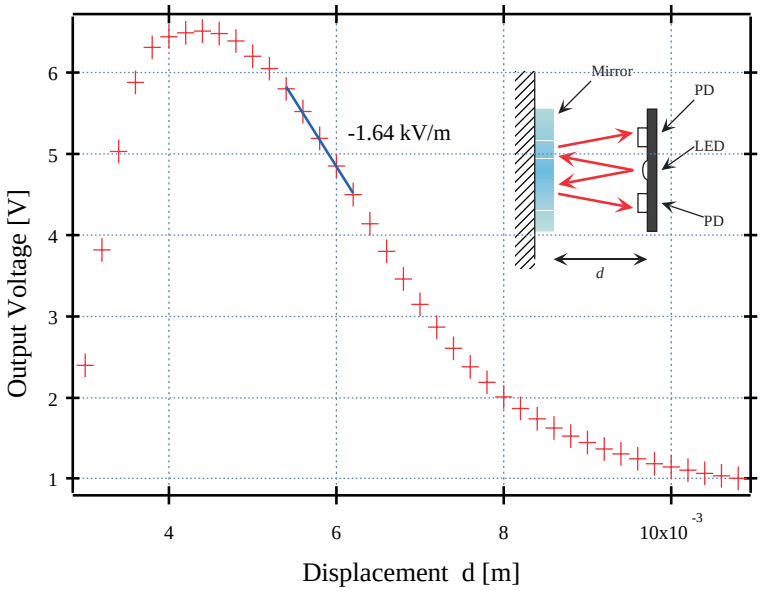

Figure 4.20: Schematic view of the reflective photo position sensor, and its calibration curve. We used the sensor in the range marked with the blue line.

is hard to distinguish from the acceleration of the objects, we evaluated the sensor noise by exciting the ratio of the acceleration of the sliding table and measuring the output signal of the accelerometer sitting on a nearby mass at rest. The noise in the measurement on the recoil mass is plotted in bottom right plot of figure 4.21, for the other measurements, we only show the results at the frequencies where the measurement is clearly dominated by the true acceleration.

The measured results mostly agree with the simulated curves, except for few peaks. In the transfer function of the mirror, the spurious peaks are located at 3, 6, 9, and 20 Hz. These peaks are identified and associated to various resonances of the system: the first two peaks the pitch resonances of the double pendulum, and the 9 Hz is the resonance of the damping magnet pitch mode, and the 20 Hz peak is the 2nd vertical resonance of the double pendulum. It is not possible to distinguish if these resonances appeared due to cross couplings in the SUS, or to the cross coupling of the exciter itself. The attenuation factor can be degraded by the internal resonances of both the assembly frame or SUS mechanics, the c.o.p. effect of the wire at higher frequencies, and other effects. However, we can regard the measured results as the lower limit of the attenuation performance. The transfer function of the mirror above few Hz is compatible with the typical $1/f^2$ asymptotic behavior. The best measured attenuation factor was 2.7×10^{-5} (-91 dB) at 28 Hz.

4.3.3 Vertical Isolation Performance

The mini-MGAS used for the vertical isolation at the suspension points of the SUS is shown in figure 4.22. The lowest resonant frequency observed was about 500 mHz. However, the achievable lowest frequency varies depending on blades, and the tuning to such a low frequency was highly delicate. To avoid these complications, we tuned all the blades to 1.5 Hz by tuning their compression.

The vertical isolation performance was measured by the same manner as the longitudinal transfer functions (figure 4.23). The peaks at 1.5, 20, and 40 Hz correspond to the vertical resonances of the double pendulum, and the 8 Hz is the resonance of the damping magnets. Only the peak at 75 Hz that appearing in the transfer function of the intermediate stage was not identified. It may be the roll mode of the recoil mass, as its frequency was

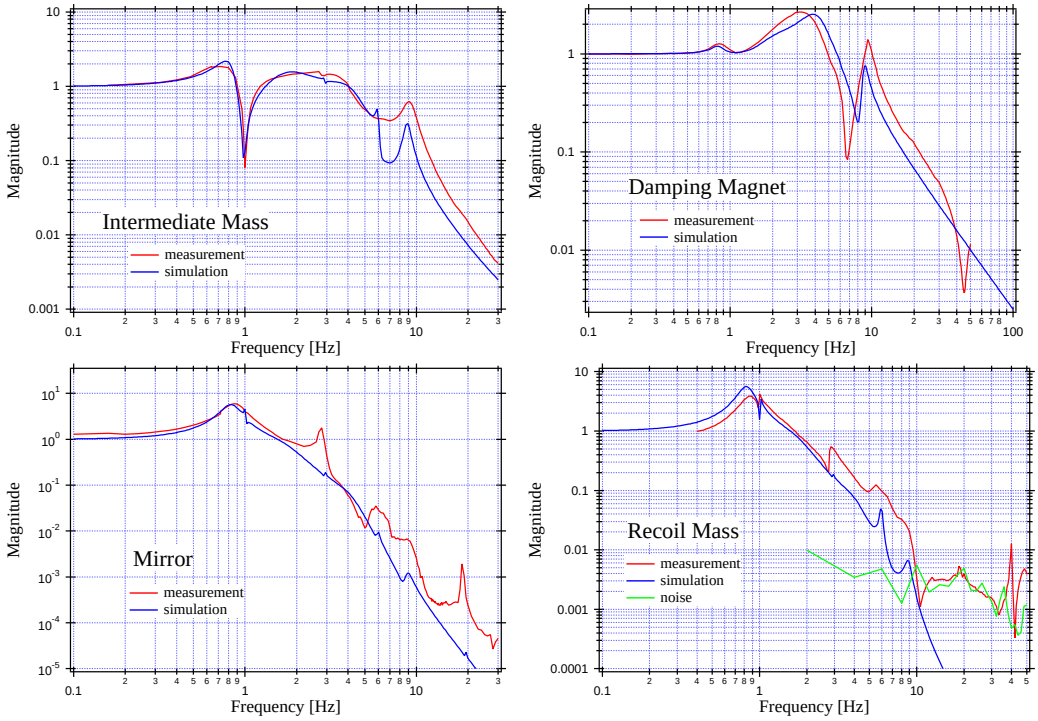

Figure 4.21: Longitudinal isolation performance of each component of the SUS.

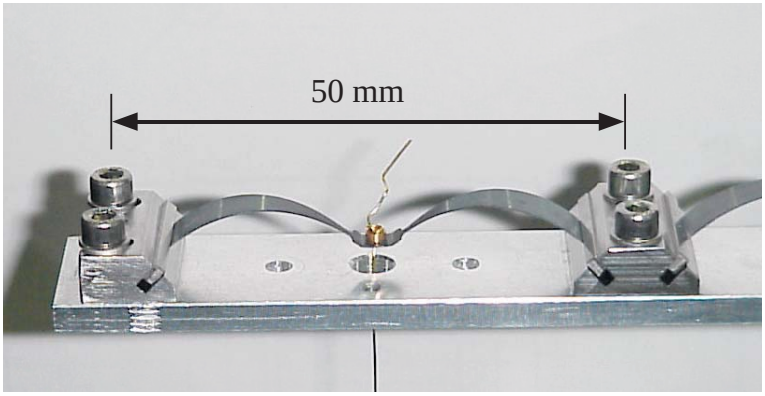

Figure 4.22: mMGAS. This is the pre-prototype mMGAS. In the prototype SUS, the wire for the intermediate mass suspension are brazed to a brass cup attached on the spring. Partially visible on the right is a second mMGAS that supports a second intermediate mass suspension wire. Two mMGAS pairs like this one are housed inside the SUS platform

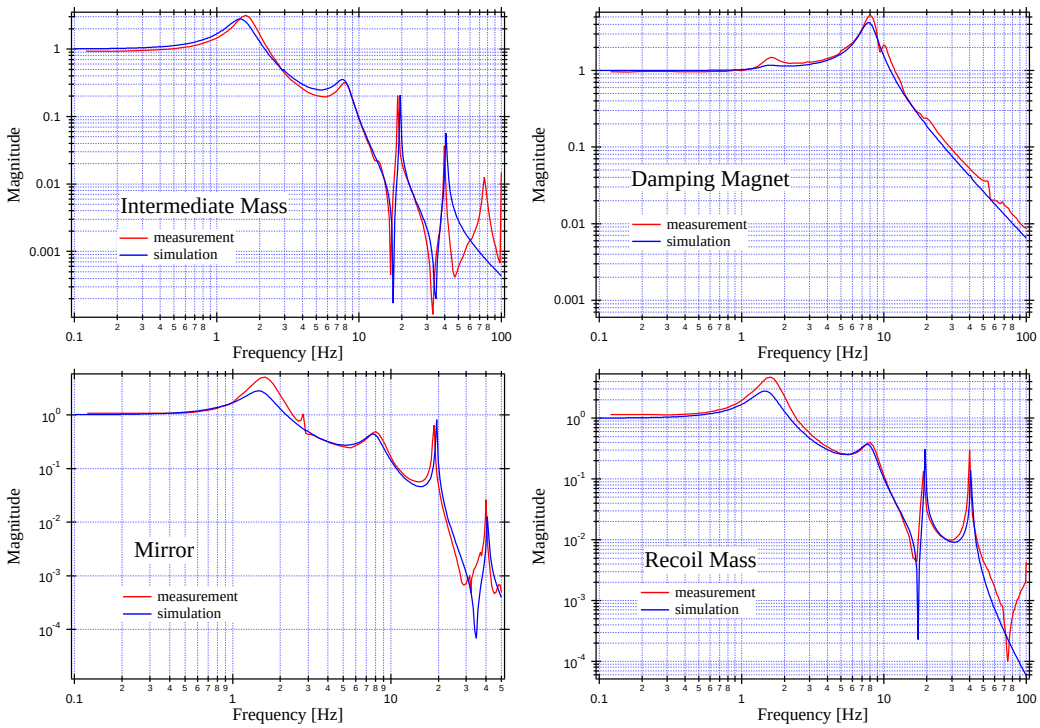

Figure 4.23: Vertical isolation performance of each component of the SUS.

computed as 60 Hz.

Like the horizontal transfer functions, the measured functions gives the lower limit of the attenuation factors. For the mirror, the measured curve agrees with the simulation up to 50 Hz, with the sensitivity limitation of -67 dB.

4.3.4 Rotational Isolation Performance

For the measurements of the rotational isolation performance, the SUS was installed into the SAS chain, with the filter1 rigidly clamped to the safety frame. The force to excite the suspension platform was generated by the coil-magnet actuators designed to control the tilt of the SUS. Therefore, the measured results would be also useful to understand the controllability of the mirror orientation from the suspension platform. However, in the operation of the prototype SAS, we only applied DC force to the platform to align the mirrors to form an interferometer.

The rotational angles of the suspension platform and the mirror were

detected by a couple of reflective position sensors. Their differential signal is the product of the angle by the distance between two detection points. Since there was not enough space to mount the accelerometers, we used only the position sensors and the bandwidth of the measurement was limited to low frequency (below 10 Hz).

The measured transfer functions from the platform to the mirror are shown in figure 4.24. The measured transfer functions were similar to the simulated ones, with some little mismatch in frequency. Some peaks have relatively high quality factor, but these will not be excited very much thanks to the excess of low frequency attenuation from the SAS chain.

4.3.5 Controllability of the Mirror

The transfer function from the current in the coil of the mirror actuator to the motion of the mirror was measured by using the reflective photo position sensor. The SUS was suspended from the filter1 in fully operational condition. As shown in the result (figure 4.25), the response of the mirror is very similar to that of the single pendulum, thanks to the actuation from the recoil mass. This would simplify the control of the mirror position.

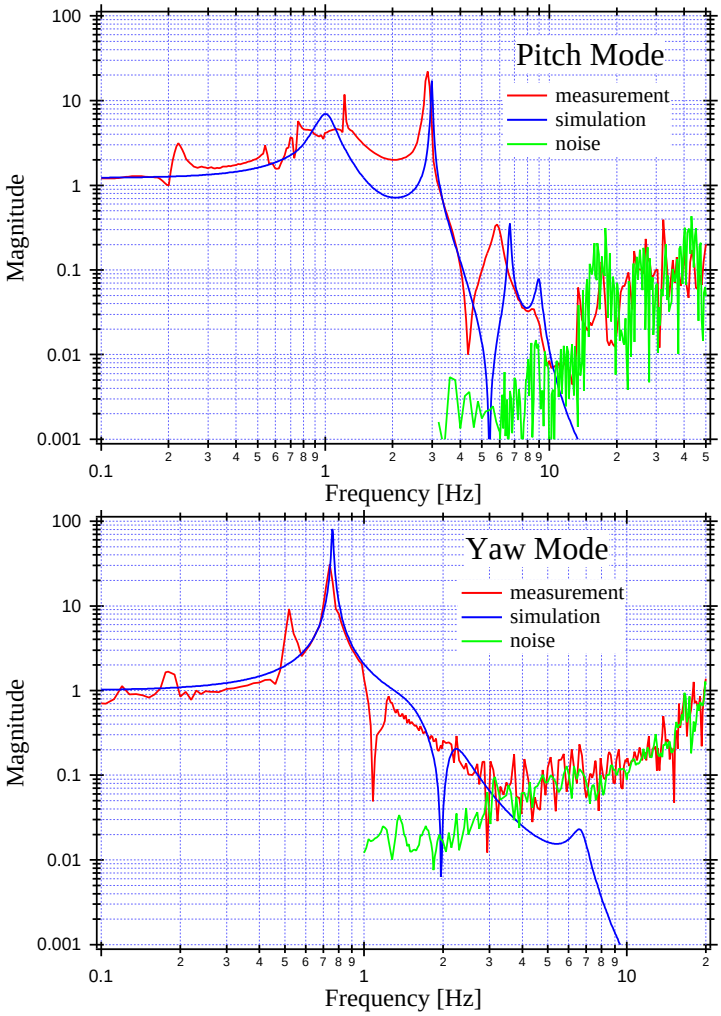

Figure 4.24: Rotational isolation performance of the SUS.

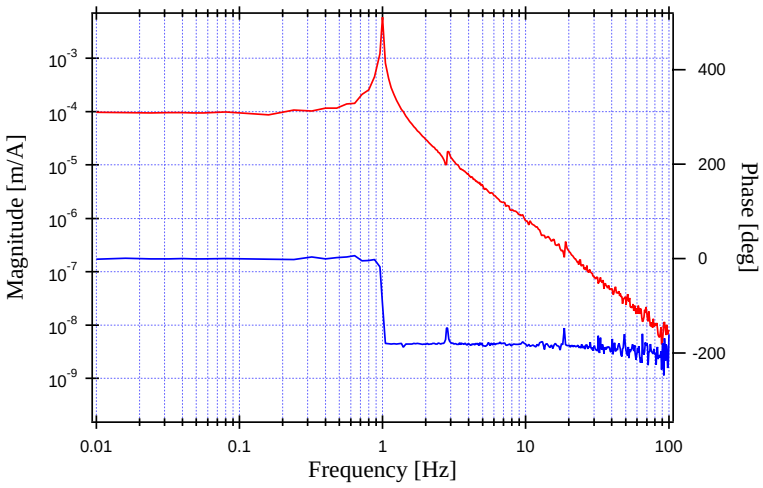

Figure 4.25: Motion transfer function of the SUS mirror from the current in the actuator coil. Magnitude (red) and phase (blue)

Chapter 5

SAS Passive Isolation Performance

5.1 Design Performance

5.1.1 3-Dimensional Model

To estimate the attenuation performance of the SAS, including the IP, two MGASFs, and the SUS, we constructed the 3-dimensional model written in MSE. The IP, the MGAS blades in each filter, and the wires between the filters and the suspension platform are represented as springs, each with assigned stiffness and mass parameters in six degrees of freedom to realize the right resonant frequencies and the measured saturation in attenuation performance. Internal resonances are not implemented in the model due to limitations of the software, and to reduce the computation time. Except for this approximation, the full system is described with all known physical components.

The IP is tuned to 35 mHz and its translational modes are degenerate. The independent vertical frequencies of the MGASFs are 500 mHz in the model.

5.1.2 Performance Estimation

Seismic Noise

The transfer functions from ground to the main stages of the SAS are shown in figure 5.1 and 5.2. The longitudinal transfer function from the ground

to the mirror are plotted in figure 5.3 together with the vertical transfer function weighted by the nominal cross-coupling factor of 1%. The sum of the two contributions is the overall attenuation performance of the SAS in the longitudinal direction. The overall performance is dominated by the cross-coupling from the vertical direction above a few Hz. The common and the differential modes of two MGASFs may or may not appear in the horizontal motion around 200 mHz and 600 mHz. The main modes that appear in the mirror's longitudinal transfer function are shown in figure 5.4. The higher modes do not appear sharply in the amplitude of the transfer function because of the passive damping system in the SUS.

Using the standard seismic model and the transfer function described above, we estimated the horizontal motion of the mirror at the TAMA site and plotted it in figure 5.5. The motion at low frequency (below 10 Hz) strongly depends on the IP resonant frequency. If the IP is tuned to 100 mHz instead of 35 mHz, the motion at 10 Hz becomes 10 times larger.

In the figure, the thermal noise design of TAMA300 is compared with the estimated seismic noise. The seismic noise is expected to reach the level of their pendulum thermal motion at a few Hz, and to the thermal motion of the mirror internal modes at 10 Hz. The safety factor at 10 Hz is estimated to be over 100.

Alignment Noise

By using the transfer functions shown in figure 5.2 and the standard seismic model described in chapter 1, we can estimate the angular fluctuation of the SAS mirrors. The result of the estimation (shown in figure 5.6) is much smaller than the angular motion of the present TAMA300, in the order of 10^{-6} rad/$\sqrt{\text{Hz}}$ around 1 Hz in both directions [56]. This is due to the superior attenuation performance of SAS in the angular degrees of freedom. As the filters are suspended by a single wire, the resonant frequencies of the angular modes are below 100 mHz. From the view point of controls, this low frequency nature is also an advantage, because one can use a lower UGF for the alignment control.

In figure 5.7, the fake longitudinal motions of the mirror caused by the coupling of the angular motion and the beam mis-centering are compared with the mirror motion estimated above. The influence of the this coupling is expected to be negligible.

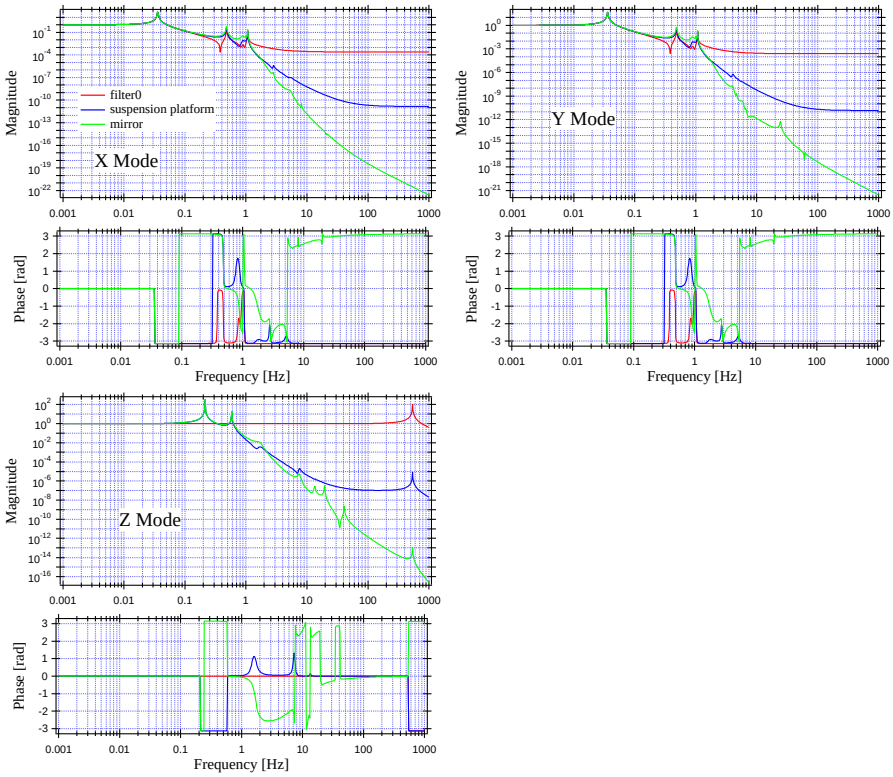

Figure 5.1: Transfer functions from ground to the main stages in the SAS, in the translational directions. Computed with the 3-dimensional model in MSE.

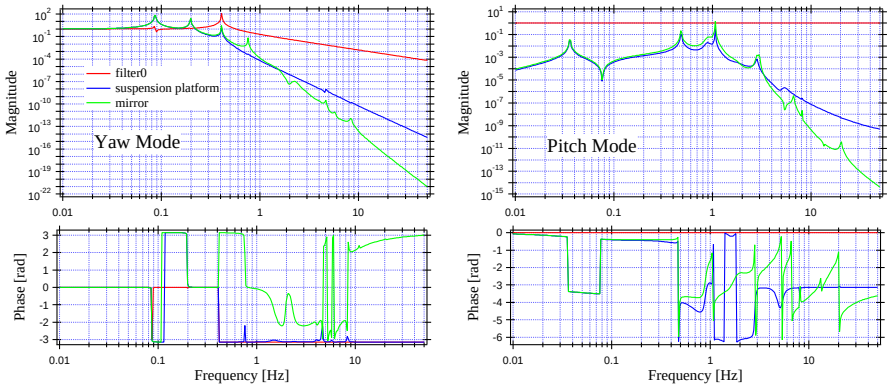

Figure 5.2: Transfer functions from ground to the main stages in the SAS, in the rotational directions. Generated by the 3-dimensional model in MSE.

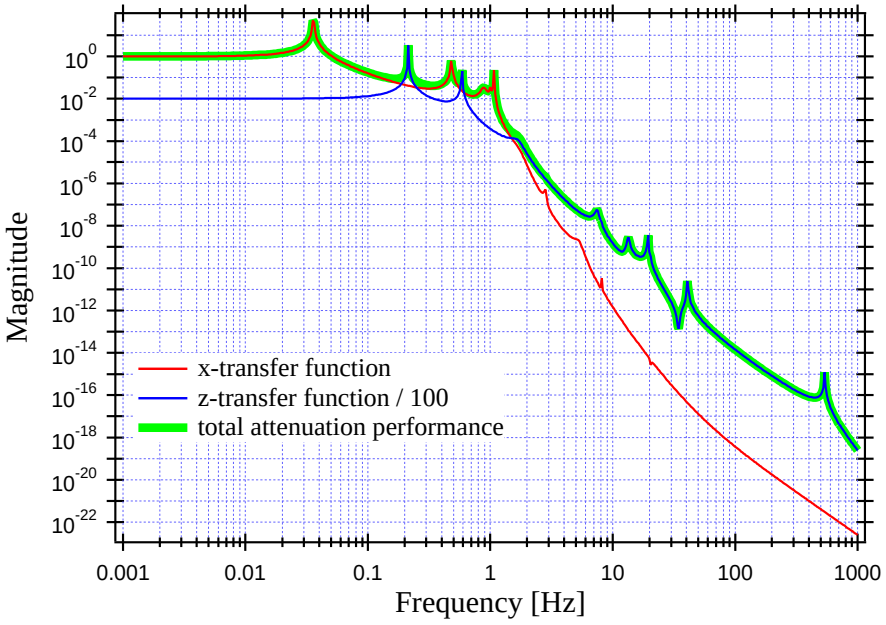

Figure 5.3: Comprehensive isolation performance at the mirror stage.

5.2 Prototype Test

In order to evaluate the total attenuation performance of the SAS, we measured the motion transfer function from the filter0 to the mirror, in addition to the measurement of the IP attenuation function describe in chapter 2. The measurement was performed by exciting the filter0 in the longitudinal direction, and by measuring the mirror motion with a small Michelson interferometer. A similar approach has been attempted by the Virgo group [44].

5.2.1 Experimental Setup

Two loudspeakers were mounted on the safety frame and their diagraphs were connected to the filter0 via rigid steel rods (figure 5.8). The speakers were driven with a homemade high power coil driver to inject the motion of the filter0. The excitation signal was supplied by an FFT servo analyzer. The movement of the filter0 was constrained in the longitudinal direction by linear sliders with cross roller bearings.

The motion of the filter0 was monitored by a commercial accelerometer, while the motion of the mirror was detected by the small Michelson

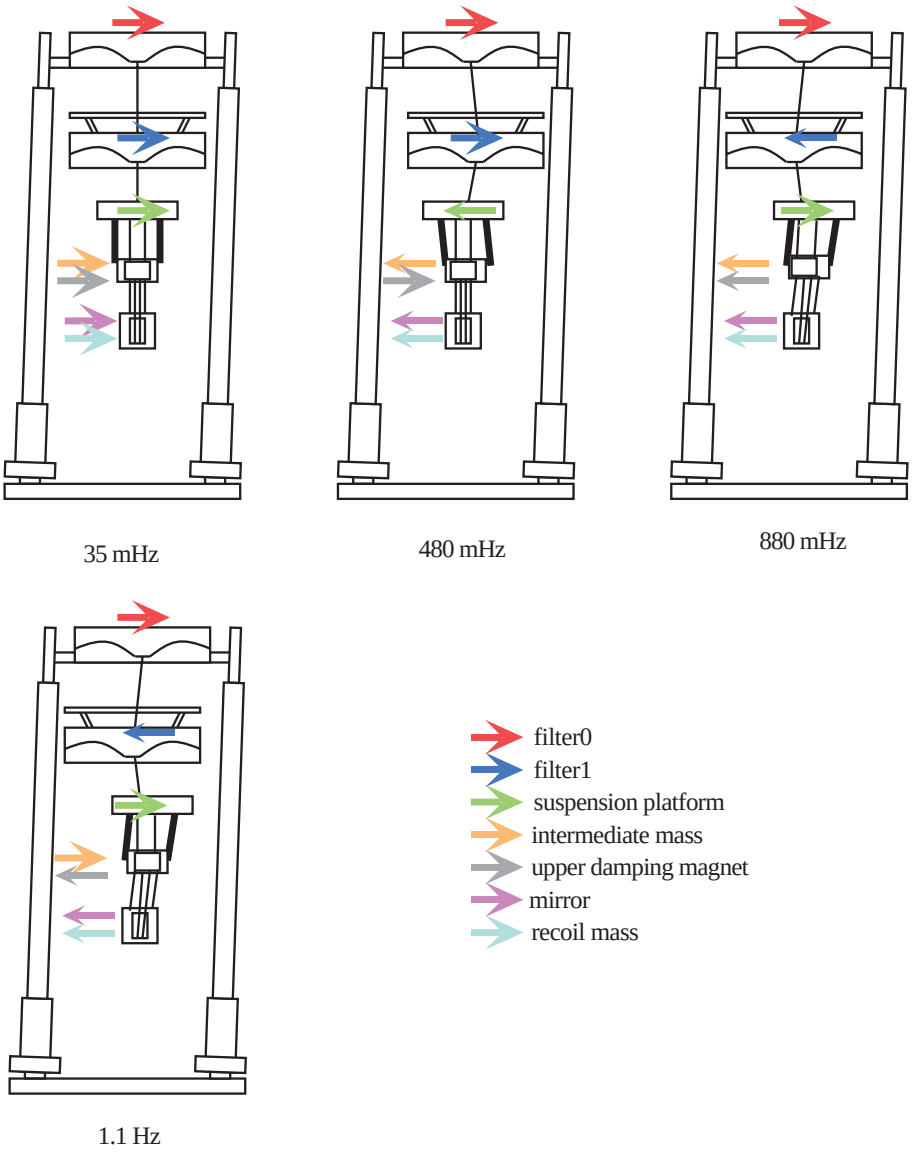

Figure 5.4: Main modes of the SAS, that contribute to the mirror motion in the longitudinal direction.

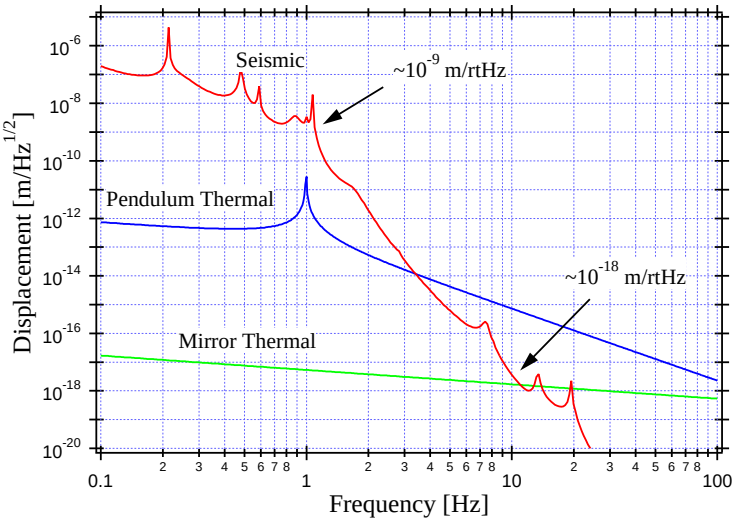

Figure 5.5: Estimated displacement of the SAS mirror in the longitudinal direction (red), thermal noise design of TAMA300 (blue and green).

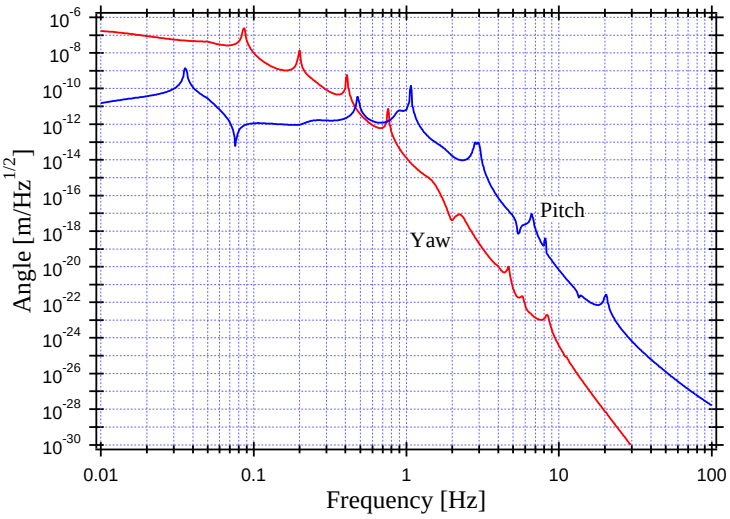

Figure 5.6: Estimated angular fluctuations of the SAS mirror in the yaw (red), and in the pitch (blue).

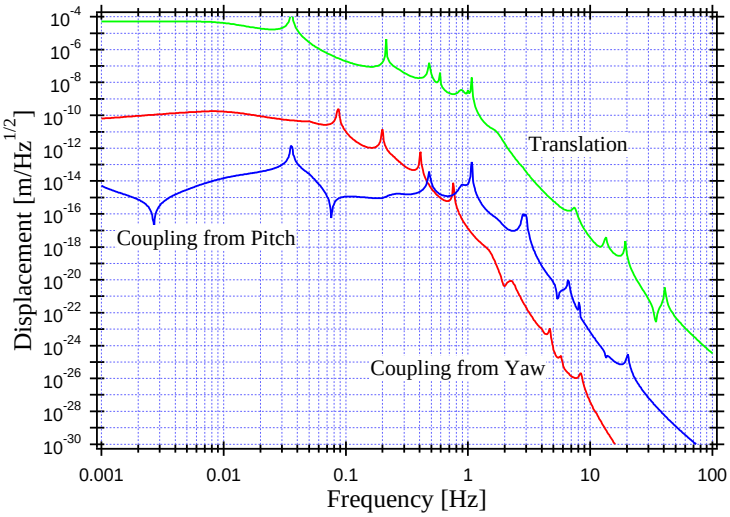

Figure 5.7: Estimated fake displacement of the SAS mirror caused by the coupling of the angular motions and beam mis-centering (red, blue), compared with the estimated longitudinal motion (green).

interferometer with the arm length of 7 cm.

The interferometer is illustrated in figure 5.9. It was locked at the working position by the differential operation technique described in chapter 1. The lock of the interferometer was achieved only by controlling the position of the mirror via coil-magnet actuators. The component of the interferometer was mounted on a small bread board attached to the safety frame. The beam splitter and the reference mirror were placed on the same platform. The platform was suspended by a single pendulum, equipped with vertical isolation springs and damping magnets to isolate the optics from the seismic disturbance. We used a commercial Nd:YAG laser as the light source.

The block diagram of the experiment is sketched in figure 5.10. Notation for the physical quantities is listed in table 5.1.

There are three contributions to the error signal recorded by the FFT servo analyzer: the SAS mirror motion caused by the filter0 excitation, by the feedback force, and the motion of the beam splitter.

From the diagram, the motion transfer function of the passive chain is written as

$$H_{\rm ch} = \frac{-1}{H_{\rm MI} x_{\rm f0}} \left\{ (1 + H_{\rm mr} G)\, x_{\rm er} + H_{\rm bs} x_{\rm sf} \right\}. \tag{5.1}$$

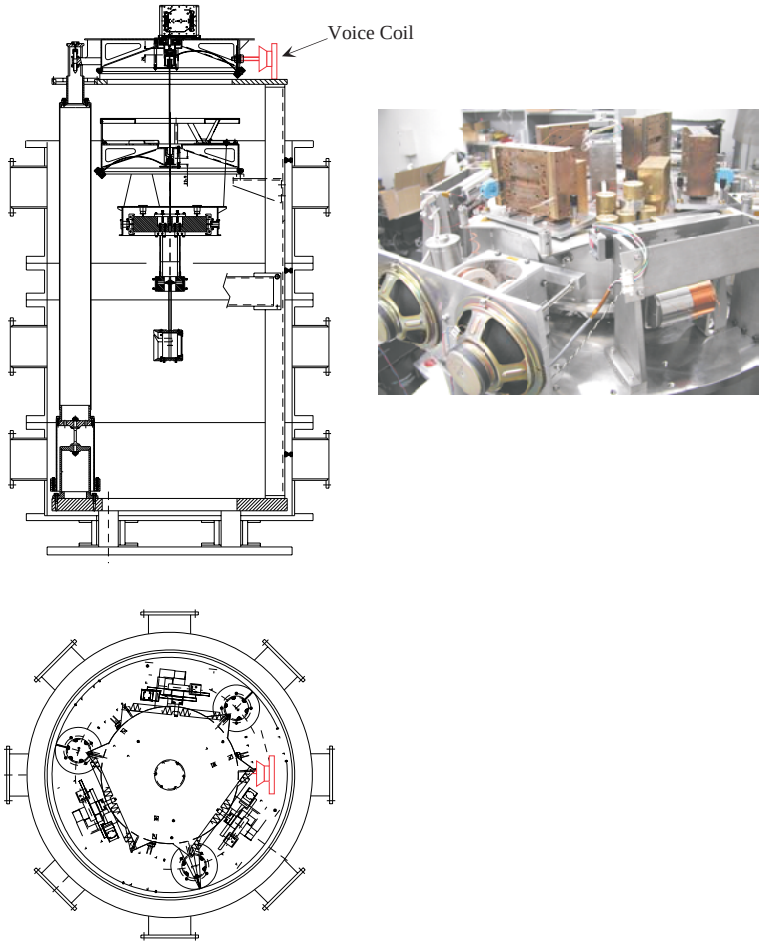

Figure 5.8: Schematic view of the setup for the passive chain isolation performance measurement. Picture in the right shows the assembly of the exciter.

x_{f0}	motion of filter0
x_{sf}	motion of safety frame
x_{bs}	motion of BS
x_{mr}	motion of mirror caused by the excitation
x_{er}	error signal
f_{fb}	feedback signal
H_{ch}	transfer function of passive isolation chain
H_{mr}	frequency response of mirror actuation
H_{bs}	transfer function of BS suspension
H_{MI}	frequency response of Michelson interferometer
G	transfer function of feedback filter

Table 5.1: Notation for the diagram shown in figure 5.10.

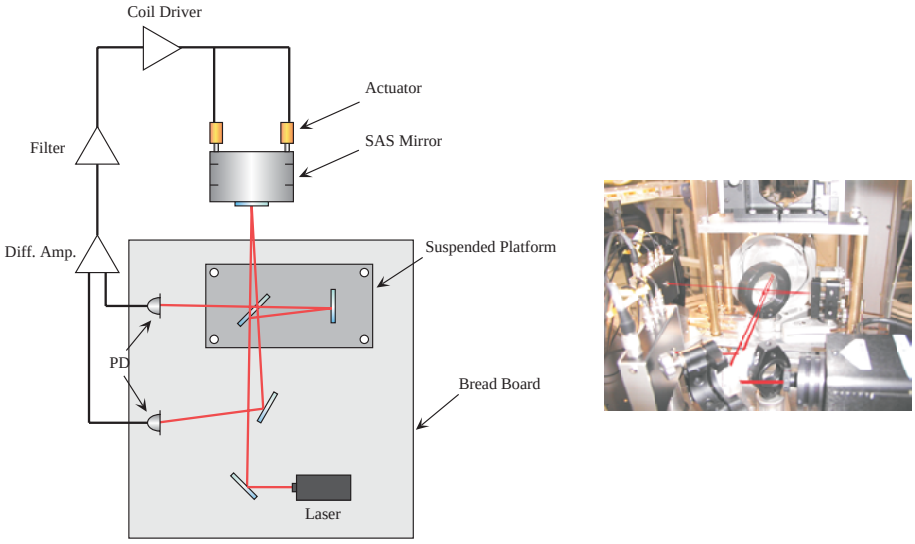

Figure 5.9: Small Michelson interferometer for the passive chain isolation performance measurement.

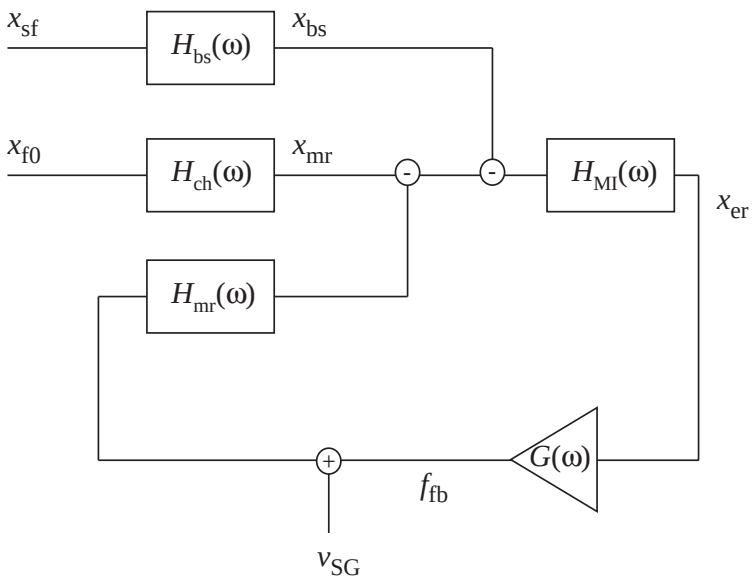

Figure 5.10: Block diagram of the small Michelson measurement.

As the critical frequency of the interferometer is higher than 2 GHz, H_{MI} is approximated as a constant which converts the displacement to the output signal. The calibration of the interferometer was done observing the freerun output signal whose amplitude corresponds to the wave length of the laser. Where the motion of the SAS mirror dominates the output signal of the interferometer ($(1 + H_{\mathrm{mr}}G)\, x_{\mathrm{er}} \gg H_{\mathrm{bs}} x_{\mathrm{sf}}$), the motion transfer function is obtained by measuring the error signal and the motion of the filter0 as

$$H_{\mathrm{ch}} = \frac{-\left(1 + H_{\mathrm{mr}}G\right) x_{\mathrm{er}}}{H_{\mathrm{MI}} x_{\mathrm{f0}}}. \tag{5.2}$$

The open loop transfer function of the feedback system $H_{\mathrm{mr}}G$ is measured by adding the excitation v_{SG} to the feedback signal while keeping the lock of the interferometer. We can measure the sum and the output signal of the compensator and these quantities are related as:

$$-\frac{f_{\mathrm{fb}}}{f_{\mathrm{fb}} + v_{\mathrm{SG}}} = H_{\mathrm{mr}}G. \tag{5.3}$$

5.2.2 Results

We measured the transfer function from the excitation signal generated by the FFT analyzer to the error signal of the interferometer. The measured error signal of the was converted to the displacement of the SAS mirror, by using the equation (5.2). The open loop transfer function of the interferometer control ($H_{\mathrm{mr}}G$) is plotted in figure 5.11. The extrapolated curve was obtained from the measured transfer function of the feedback filter and the motion transfer function of the mirror described in the previous chapter.

We also measured the transfer function between the excitation signal and the motion of the filter0 detected by the accelerometer. Then, by taking the ratio of two transfer functions, we can obtain H_{ch}, the isolation performance of the entire SAS except for the IP. It is shown in figure 5.12 with the simulated curve computed with MSE. The measured curve shows good agreement with the simulation, except for some mismatch in the low frequency structures. The mismatch of the notch at 600 mHz is practically unavoidable because it is created by the cross coupling from the yaw mode of the mirror and it is hard to distinguish if the cross coupling really caused the longitudinal motion of the mirror, or the beam of the interferometer pointed off center of the mirror. The asymptotic behavior of $1/f^8$ is clearly visible up to 3 Hz,

and the measurement has large discrepancy from the simulation above this frequency. The structures above 3 Hz were repetitively observed with high coherence. Therefore the structures are related to the excitation and they are identified as the resonances of the safety frame.

We measured the transfer function from the excitation signal to the longitudinal acceleration of the small bread board mounted on the safety frame with the commercial accelerometer. The safety frame moves slightly due to the recoil of the excitation on the filter0. We estimated the motion of the beam splitter in the longitudinal direction by taking the product of the displacement of the bread board and the isolation ratio of the single pendulum. Then normalizing it with the motion of the filter0, we evaluated the influence of the beam splitter motion to the measurement of the SAS transfer function (see equation (5.1)). The result is plotted in figure 5.12 with the black curve. The estimated noise shows good agreement with the measured transfer function above 3 Hz. Due to this limitation, we could confirm the attenuation performance of the suspended chain up to 3 Hz only. However this implies superior attenuation performance, because the measurement was limited by the motion of the beam splitter indeed in spite of the large excitation at the filter0.

Since the attenuation performance of the IP is validated up to 10 Hz. This result insures that the design attenuation performance is achieved at least up to 3 Hz. From the expected thermal noise of TAMA300, it is foreseen that the sensitivity of the detector will be limited by the thermal noise of the mirror suspension rather than by the seismic noise above few Hz, if the cross-coupling from the vertical direction does not degrade the performance significantly.

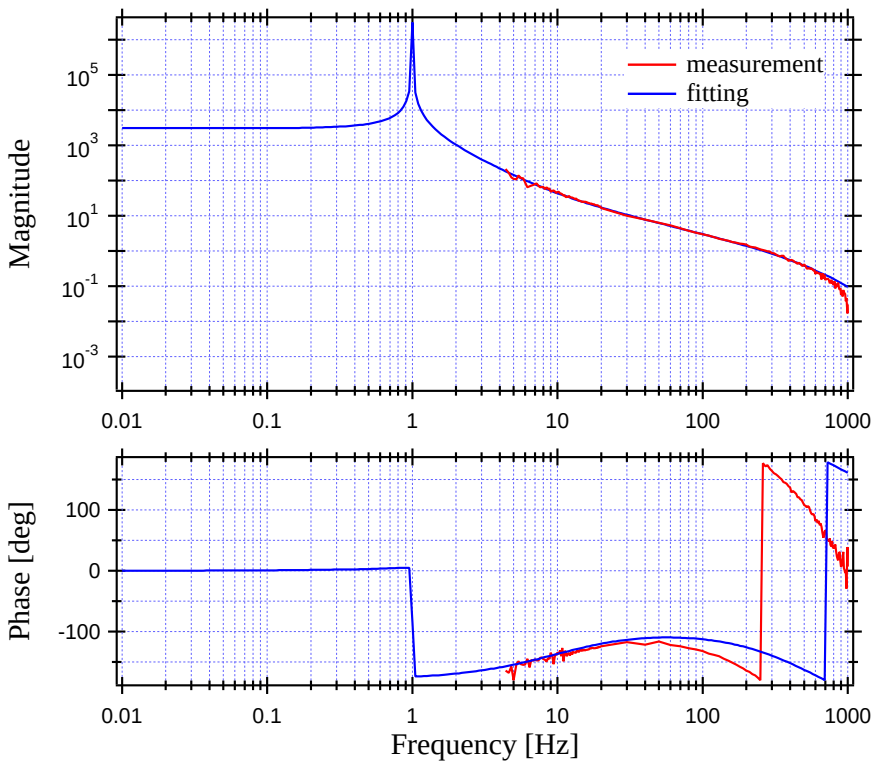

Figure 5.11: Open loop transfer function of the small Michelson interferometer control. The UGF was placed at 30 Hz.

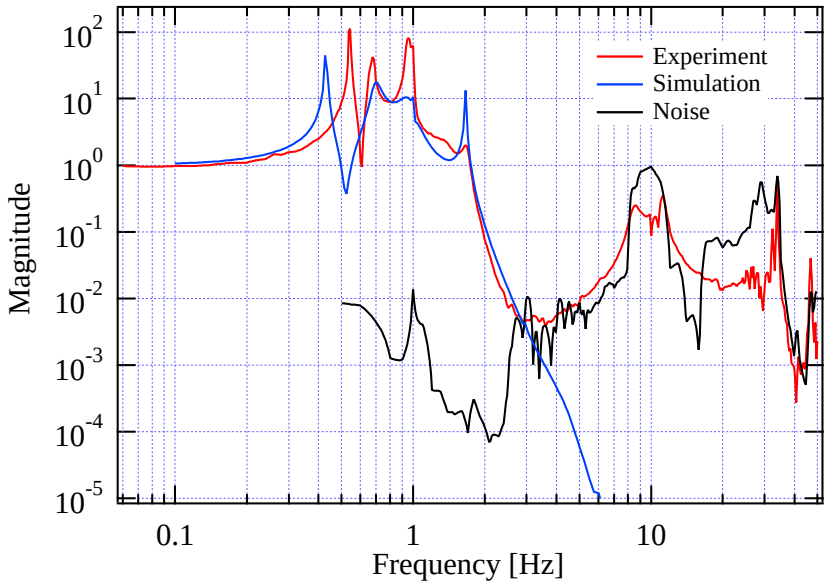

Figure 5.12: Motion transfer function from the filter0 to the mirror, in the longitudinal direction.

Chapter 6

SAS Local Controls

6.1 Purpose

The mechanics in SAS, the IP, the MGASFs, and the SUS passively provide sufficient attenuation in the frequency band of interest for GW detection. However the resonances of these mechanics enhance the motion of the mirror at lower frequencies and they need to be damped. Particularly the mechanics used in GW detectors have relatively high quality factor to allow for the thermal noise issue, and the amplification at the resonances makes substantial contributions to the residual displacement and velocity of the optical components. Assuming a typical set of parameters of a FP cavity control in GW detectors, the residual velocity of the test masses of the order of micron/second is the maximum acceptable limit for a reasonable lock acquisition time[1], and still keep the control noise below all other noise contributions. The high pendulums quality factors necessary to keep the therml noise under control may break this condition.

Additionally, the drift of the upper stages of the SAS may result into a large low frequency displacement of the test masses that needs to be suppressed.

Briefly, the suppression of the residual motions of the SAS components produces the following main advantages:

- Improves the robustness of the interferometer operation. This is an

[1]The threshold velocity is naively estimated by using an equation $v_{\rm th} = \lambda f/F$, where λ, F, and f are the laser wavelength, the finesse of the FP cavity, and the length control bandwidth, respectively. The typical values are: $\lambda \sim 1\,\mu$, $F \sim 100$, $f \sim 100$ Hz.

essential factor to insure continuous GW observation.

- Reduces the required range of the mirror actuator, thus improving its noise performance.

There have been two approaches for the suppression of the motion of the mechanics: i.e. the passive and the active approaches.

Most of the passive techniques utilize a viscous force proportional to the (relative) velocity of the object to be damped (and its reference). This force is generated through variety of physical effect, like the fluid viscosity or the induced currents like in the Eddy current damper implemented in the SUS. The active systems consist in feedback loops between sensing and actuation stages. It suppresses the motion of the object detected by the sensor, with an actuator.

Both passive and active techniques have advantages and disadvantages. The advantage of the passive system is its robustness and simplicity, a passive system always works and is immune to saturation effects even for large transients. Since it is based on simple physical process, there is no technological limitation to its performance while active systems tend to be limited by the technologies employed in the sensing and actuation components. For instance, to detect and control the motion of a test mass in the GW observation band, one would need an instrument as sensitive as the GW detector itself. The passive damping systems are more suitable to be used at the lower stages of the seismic isolator and at higher frequencies, where damping forces proportional to velocity are more effective. On the contrary, the active systems are more appropriate at lower frequencies and for the upper stages, where the larger disturbances appear. For these reasons, we applied active techniques to damp the low frequency mechanical resonances on the IP, while using the passive magnetic dampers for the relatively high frequency resonances in SUS.

6.2 Control with Local Sensors

Most rigid body modes of the SAS attenuation chain appear as the recoil motion of the filter0. By counter-acting the motion of the excited resonances, one can effectively drain the energy stored in the resonant modes. Therefore, the local control of SAS is instrumented with the sensors and actuators

mounted on the filter0 body, the top part of the IP. Positioning the sensors and actuators far from the test mass has an important technical advantage: i.e. the noise injected by the control cannot transmits through, and is attenuated by the passive isolation chain between the IP and the test mass at the bottom.

The local control of the SAS is instrumented with both position sensors and accelerometers. As the ultimate purpose of the seismic isolation is to freeze the motion of the optical component to the inertial frame, the use of the accelerometer is a natural choice. However, a control performed only with the accelerometer ends up with a fundamental uncertainty at DC. Therefore the signal of the position sensor will be used to correct the DC uncertainty of the accelerometer control.

Since the purpose of the active control of SAS is simply to suppress the residual motion of the mechanics with respect to the inertial frame, it is named 'inertial damping'[42]. The feedback system for the inertial damping is described in this section. Although it is possible to design a feedback system which directly utilizes the accelerometer signal, we implemented the inertial damping as an active *viscous* damping, mainly because it is fundamentally stable (to be discussed later in this section).

Since the inertial damping is implemented only to damp the rigid body resonances of the SAS, its control bandwidth bandwidth should be limited below 10 Hz.

Let's consider only one degree of freedom for simplicity. The schematic diagram of the local control of the SAS is illustrated in figure 6.1. The IP has two inputs per degree of freedom, the ground motion x_0 and the force exerted by the force actuator used in the local control $f_{\rm fb}$, and responds to them with different transfer functions $H_{xIP}(\omega)$ and $H_{fIP}(\omega)$, respectively. These functions are not proportional to each other because of the center of percussion effect. The motion of the IP x is the sum of these two responses. x_0 and x represent the absolute position of the ground and of the IP top in the inertial coordinate.

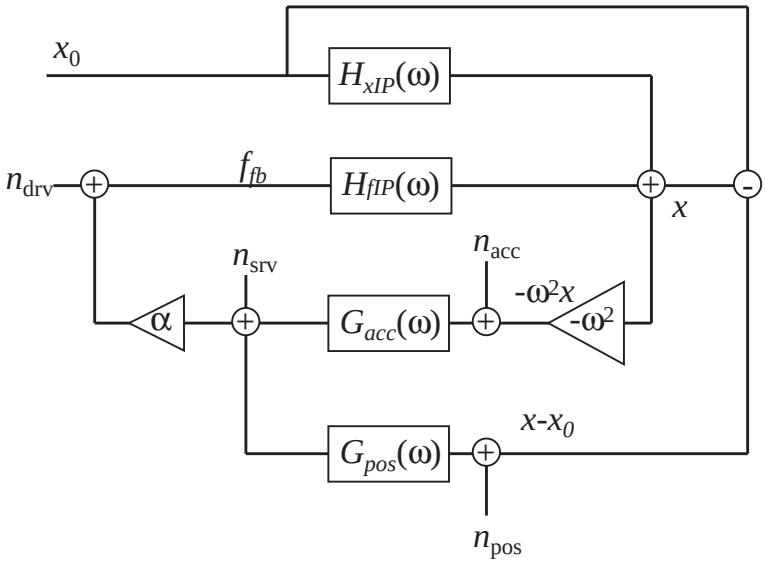

Figure 6.1: Block diagram of the perfect IP control.

6.2.1 Control of the Ideal IP

Accelerometer Feedback

The accelerometer is the instrument which detects the acceleration of the object with respect to the local inertial frame. When the IP moves by x in Fourier domain, its acceleration is expressed as $-\omega^2 x$. The response of the accelerometer mounted on the top of the IP to the force exerted onto the top of the IP is shown in figure 6.2. The magnitude of the transfer function flattens above the fundamental resonance of the IP up to the resonance of the small flex joint to link the IP leg and the filter0 at 50 Hz, thus at least one stage of low pass filtering is necessary to limit the bandwidth of the control.

Also a first order low pass filter is required to integrate the accelerometer signal and transform it to a velocity signal of the IP. The velocity information is essential for the viscous damping. Therefore the compensator for the control with accelerometer is a simple pole as,

$$G_{acc}(\omega) = \frac{\omega_1}{\omega_1 + i\omega}, \tag{6.1}$$

with the cut-off frequency ω_1 much below than the resonant frequency of the IP. Ideally, the compensator should be a complete integrator with null

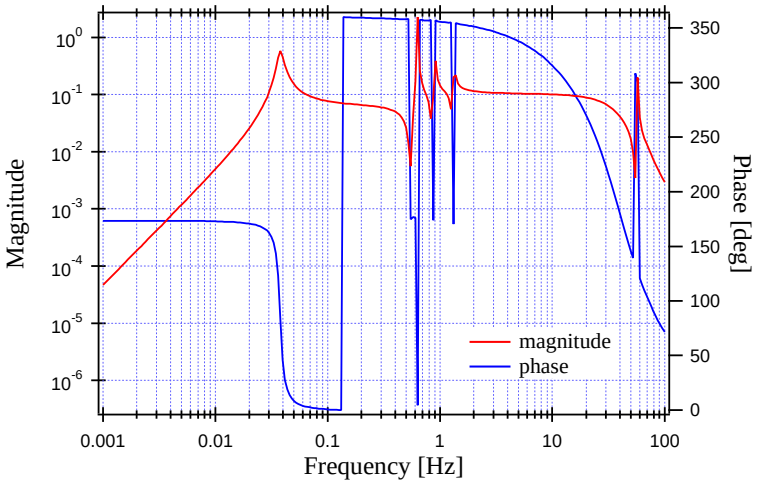

Figure 6.2: Frequency response to the actuation of the accelerometer on the IP.

cut-off frequency, but this is not possible in practice, as it would result a divergence of the signal at zero frequency.

The open loop transfer function of the accelerometer feedback becomes $G_{open1}(\omega) = \alpha H_{fIP}(\omega) G_{acc}(\omega)$, where α is the efficiency of the actuator. The open loop transfer function with the above compensator is shown in figure 6.3. The system has two unity gain frequencies (UGFs), one below and one above the IP resonance. Above the IP resonant frequency, the phase of the transfer function stays at -90 degree up to several Hz and the phase gradually grows from +90 to +180 degrees as the frequency diminishes from the resonance to zero. Therefore the system can be made stable by putting the UGFs appropriately (before it gets too close to 180 degrees in either directions). In the example, the phase margins at the lower and the higher UGF are 30 degrees and 90 degrees respectively. If one could apply the complete integrator as the compensator, the feedback system would realize pure viscous damping which is fundamentally stable as the phase lays only between +90 degrees and -90 degrees.

Neglecting the noise of the components in the system, the closed loop transfer function of the IP to the ground motion with the accelerometer control is expressed as

$$H_{close1}(\omega) = \frac{H_{xIP}(\omega)}{1 + G_{open1}(\omega)}. \tag{6.2}$$

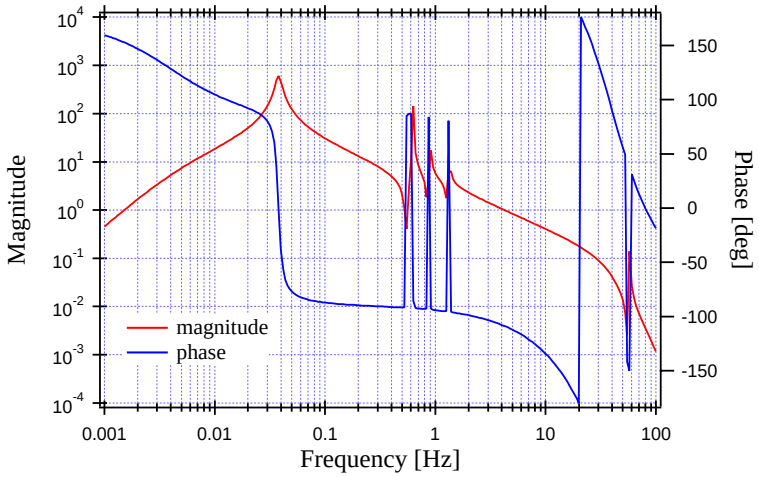

Figure 6.3: Open loop transfer function of the accelerometer feedback.

Where the open loop gain is high

$$\left|-\alpha\omega^2 G_{acc}(\omega) H_{fIP}(\omega)\right| \gg 1, \tag{6.3}$$

therefore

$$H_{close1}(\omega) \sim H_{xIP}(\omega)/G_{open1}(\omega), \tag{6.4}$$

and the amplitude of the IP motion is suppressed by the factor of the open loop gain.

The frequency response of the IP to the ground motion with and without closing the feedback with the accelerometer is plotted in figure 6.4. The peaks of the rigid body modes are clearly damped without injecting noise due to lack of phase or gain margin at any frequency.

Position Sensor Feedback

As the accelerometer is insensitive to the drift with constant velocity and at the low frequency, it is necessary to implement a complementary feedback using the position sensor signal. In the ideal IP, the position control can be simply implemented by applying a single pole filter sufficiently below the resonant frequency of the IP. In this simple approach the blending of the accelerometer feedback signal to that of the position sensor feedback is also trivial. It is sufficient to impose that the UGF of the position feedback is low enough (lower than the lower UGF of the accelerometer feedback), to insure

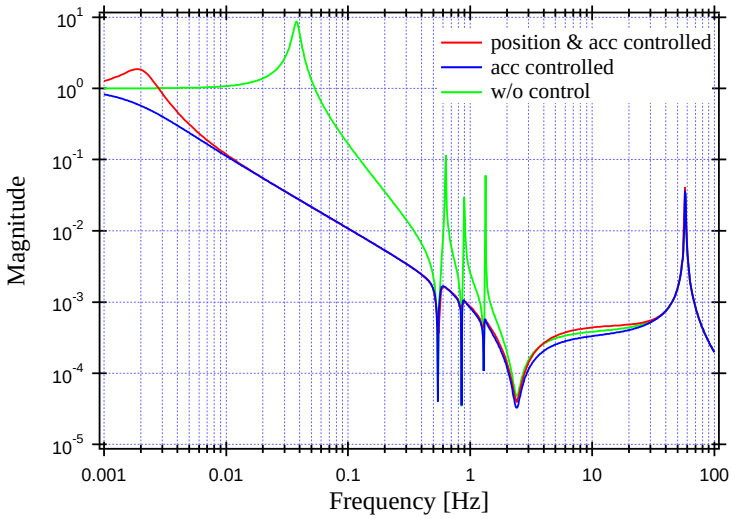

Figure 6.4: Frequency response of the IP to the ground motion: without any control (green), with only accelerometer feedback (blue), and with both accelerometer and position feedback (red)

that the two loops work almost independently. This approach has the disadvantage of loosing DC gain. The response of the IP with the accelerometer and position sensor feedback implemented together is formulated as

$$H_{close2}(\omega) = \frac{H_{xIP}(\omega) + H_{fIP}(\omega)\alpha G_{pos}(\omega)}{1 + G_{open2}(\omega)}, \tag{6.5}$$

where the open loop transfer function of the combined servo loop is $G_{open2} = \alpha H_{fIP}(G_{pos} - \omega^2 G_{acc})$. The second term in the numerator of the above equation represents the seismic noise introduced through the position sensor servo. The example of the closed loop transfer function is plotted in figure 6.4. In the case of both loops closed, the broad peak below the IP resonance is induced due to inadequate phase margin, while the amplification between few Hz and few tens of Hz is caused by the position sensor control loop. At these frequencies, the residual amplitude of the open loop transfer function of the position sensor feedback is very small (of the order of 10^{-10}), but it still injects non-negligible amount of seismic motion because the position sensor signal at these frequencies are dominated by the ground motion itself. Introducing a few poles to the position signal feedback above the IP resonance will solve this problem without spoiling the stability of the control.

6.2.2 Control Noise

Let's consider the noise of the control system sketched in figure 6.1. The noise here means that of incoherent to the IP motion. n_{acc}, n_{pos} are the noise of the accelerometer and the position sensor respectively. n_{srv} and n_{drv} are the electronic noise of the servo system, and the force noise from the driver, including the change of actuation efficiency etc..

Solving the diagram, the IP motion becomes

$$x_e = \frac{1}{G}\left[\left\{H_{xIP} + \alpha H_{fIP} G_{pos}\right\} x_0 - \alpha H_{fIP}\left\{G_{acc} n_{acc} + G_{pos} n_{pos} + n_{srv}\right\} + H_{fIP} n_{drv}\right], \tag{6.6}$$

where

$$G = 1 + H_{fIP}\left(-\omega^2 G_{acc} + G_{pos}\right). \tag{6.7}$$

Equation (6.6) includes an important information. Where the servo gain is high enough, i.e. under the condition of

$$G_X H_X \gg 1, \tag{6.8}$$

the actual mirror motion ${x_e}^2$ is simply expressed as,

$$x_e \sim \frac{\alpha H_{fIP} G_{pos}}{G} x_0 - \frac{\alpha H_{fIP} G_{acc}}{G} n_{acc} - \frac{\alpha H_{fIP} G_{pos}}{G} n_{pos}. \tag{6.9}$$

While the other noises are suppressed by the servo, the noise from the sensor is not always suppressed. Particularly at the frequencies where the accelerometer control dominates (this is true over most of the band of inertial damping), the noise of the accelerometer will dominate the performance of the system. The first term of the above equation corresponds to the seismic noise injection from the position sensor, and it is negligible if the accelerometer feedback gain is much higher than that of the position sensor servo gain ($|G_{acc}| \gg |G_{pos}|$).

[2]Note that x_e is *not* the error signal any more. The error signal detectable by the sensors is the sum of x_e and the noise contributions.

6.2.3 Controlling an IP with Asymmetric Legs

The naive servo described in the previous section provides a stable and sufficient damping under the ideal condition. However, as we saw in chapter 2, the cross coupling between the horizontal motion and the tilt of the IP is sensitive to the asymmetry of the mechanics, and every real IP has a certain level of asymmetry. When there is the coupling, the response of the accelerometer has an additional term corresponding to the projection of the gravity to the main axis of the accelerometer as,

$$a_{\text{output}} = -\omega^2 x + \gamma x, \tag{6.10}$$

$$\gamma = \alpha \frac{g}{l}, \tag{6.11}$$

and it is plotted in figure 6.5. As the cross coupling term has $1/f^2$ behavior and decreases rapidly above the IP resonant frequency, it dominates the response of the sensor at lower frequencies. The naive servo is still a good solution when the cross coupling coefficient is small and there is enough phase margin at the lower UGF of the accelerometer control loop. However, it is irrelevant any more when there is a substantial cross coupling, particularly when the cross coupling factor is positive and the projection of gravity and the normal response to the horizontal acceleration result double zeros and the phase rotates sharply at that frequency.

One of the solutions we adopted is extend the bandwidth of the position signal feedback and set the merging frequency of the two loops above the resonance of the IP. As the position sensor is insensitive to the tilt of the filter0, the cross coupling does not bother the new servo design. This point is practically useful because the even the sign of the cross coupling coefficient γ is usually unpredictable.The block diagram of the control system of the asymmetric IP is shown in figure 6.6.

Accelerometer Feedback

The concept of the feedback with the accelerometer described in the previous section basically remains in the new servo system. In other words, a single pole dominates the compensator at the frequencies of the rigid body modes except the fundamental IP mode so that they will be damped with the

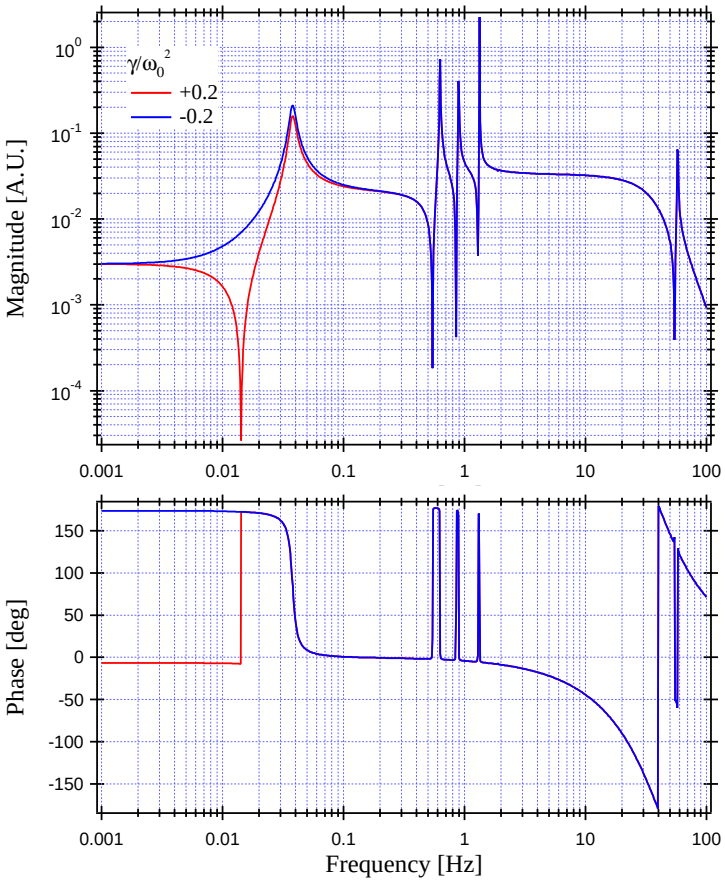

Figure 6.5: Frequency response of the accelerometer mounted on the IP with the translation-tilt coupling, for the different geometry of the IP.

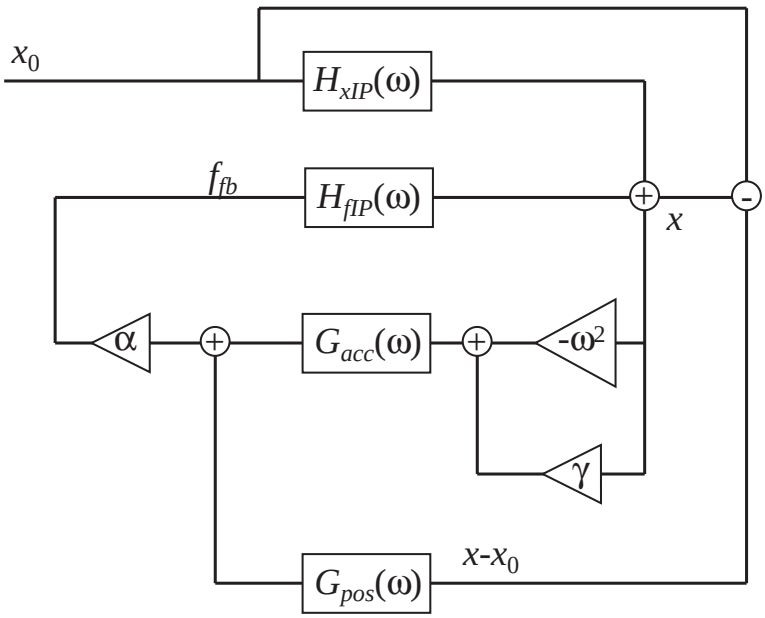

Figure 6.6: Block diagram of the asymmetric IP control.

accelerometer control.

The new compensator for the accelerometer control is

$$G_{acc2}(\omega) = \frac{\omega_1 + i\omega}{\omega_1} \frac{\omega_2}{\omega_2 + i\omega} \frac{\omega_3}{\omega_3 + i\omega}, \tag{6.12}$$

with the conditions $\omega_1 \ll \omega_2 \ll \omega_0 \sim \omega_3$. The zero-pole pair is inserted to raise the phase to match with that of the position sensor control, while the third pole is for integration of the acceleration. The example of the compensator is shown in figure 6.7.

Position Sensor Feedback

The compensator for the position sensor feedback is rather complicated than that in the naive case. The typical filter is described as

$$G_{pos2}(\omega) = \frac{\omega_1}{\omega_1 + i\omega} \frac{\omega_2 + i\omega}{\omega_2} \frac{\omega_3 + i\omega}{\omega_3} \frac{\omega_4}{\omega_4 + i\omega} \frac{\omega_5}{\omega_5 + i\omega}. \tag{6.13}$$

The first pole ($\omega_1, \omega_2 \ll \omega_0$) and zero are used to increase DC gain for the drift suppression, and the third zero ($\omega_3 \ll \omega_0$) differentiates the position signal to convert it to the relative velocity of the IP and the ground, and it also raises the phase for matching with the accelerometer control. The

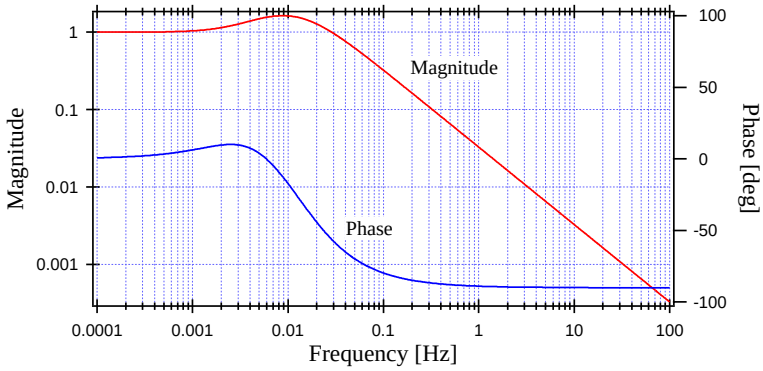

Figure 6.7: The compensator for the accelerometer control on the asymmetric IP. The IP resonant frequency is assumed as 50 mHz.

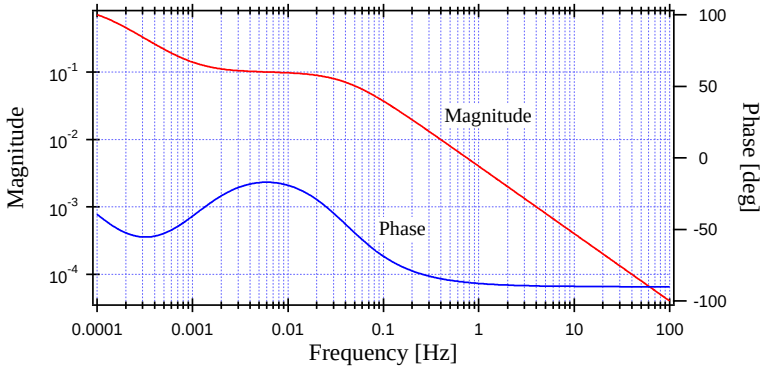

Figure 6.8: The compensator for the position sensor control on the asymmetric IP. The IP resonant frequency is assumed as 50 mHz.

other poles at higher frequencies ($\omega_4, \omega_5 \sim \omega_0$) roll off the gain to avoid seismic noise re-injection through this feedback. The compensator is plotted in figure 6.8.

Overall Control Loop

Figure 6.9 shows the open loop transfer function of the two servoes merged together. Also the IP transfer function with the loop closed is shown in figure 6.10. Modifying equation (6.5), the closed loop transfer function is formulated as

$$H_{close3}(\omega) = \frac{H_{xIP}(\omega) + H_{fIP}(\omega)\alpha G_{pos}(\omega)}{1 + G_{open3}(\omega)}, \tag{6.14}$$

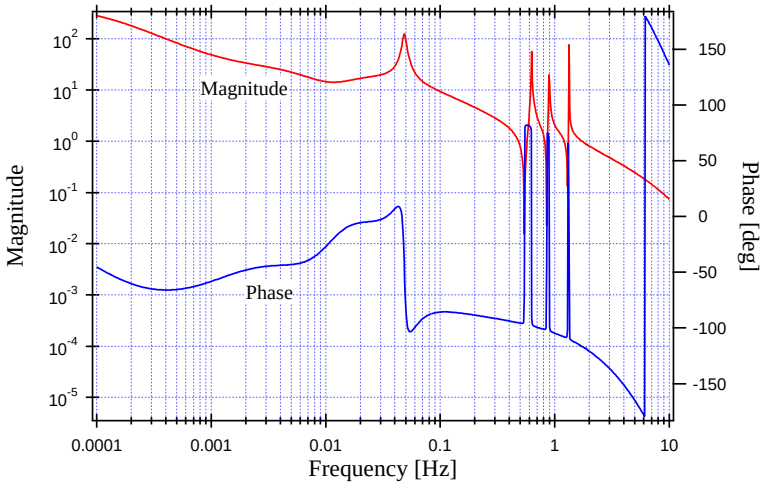

Figure 6.9: Open loop transfer function of overall feedback.

where the total open loop transfer function follows

$$G_{open3}(\omega) = \alpha H_{fIP}\left[\left(-\omega^2+\gamma\right)G_{acc2}(\omega) + G_{pos2}(\omega)\right]. \tag{6.15}$$

The seismic noise is re-injected to the IP in a wide band between 10 mHz to 10 Hz because the suppression of the gain contribution from the position sensor loop is not enough. However, imposing more poles for that purpose makes the servo unstable. Also there is a broad peak below the resonant frequency of the two loops, due to lack of phase margin. However, the rigid body modes between 100 mHz to 1 Hz are sufficiently damped.

6.3 Virtual Sensing/Actuation

As we discussed earlier, the IP has three normal modes in the horizontal plane: i.e. two translational modes and one rotational mode. The translational modes are ideally degenerate but in practice they are separated because of asymmetry of the mechanics or ununiformity of the payload. Detection and control system for the three modes essentially needs to be instrumented with three sensors and actuators. However, it is not guaranteed that each sensor or actuator is dedicated to only one mode. Although the rotational mode is obviously determined, the direction of two translational modes are usually unpredictable. Thence just by implementing it with

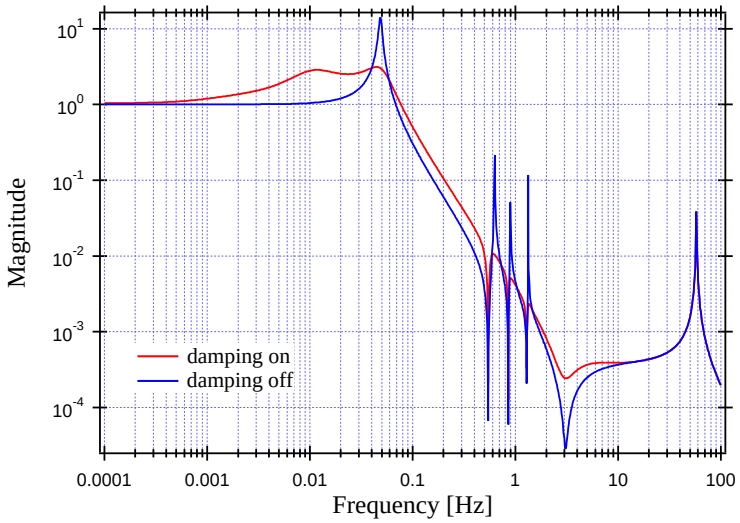

Figure 6.10: Frequency response of the asymmetric IP, with and without the inertial damping.

the sensors and actuators arbitrarily distributed, the control of the IP is in nature a MIMO (Multi-Input Multi-Output) process. It is still possible to design the servo for the MIMO system, however it is more preferable to separate each degree of freedom, because the MIMO system is then resolved to simple SISO (Single-Input Single-Output) systems.

The idea of virtual sensing (actuation) is to construct a synthetic signal (force) by using linear combinations of the actual sensors (actuators), and each virtual sensor (actuator) detects (exerts force to) only one normal mode, as illustrated in figure 6.11. The basis and the implementation of the virtual sensing and actuation is described in this section.

The model used here is illustrated in figure 6.12. In the model, the two translational modes (X and Y) of the IP corresponds the axes of the normal Cartesian coordinate $X-Y$, and the principal axis of the yaw mode coincide with the vertical axis of the coordinates. There are sets of three sensors and actuators distributed as shown in the figure.

6.3.1 Virtual Sensors

When the system is excited by one of the actuators, the injected force excites all the normal unless the force vector is normal to one of the translational mode axis. Then each sensor detects the projection of every mode to its

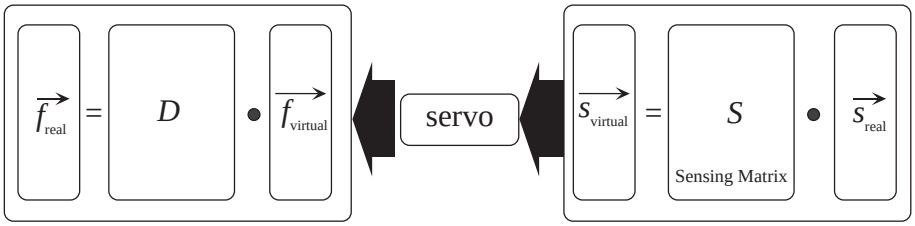

Figure 6.11: Concept of virtual sensing / actuation.

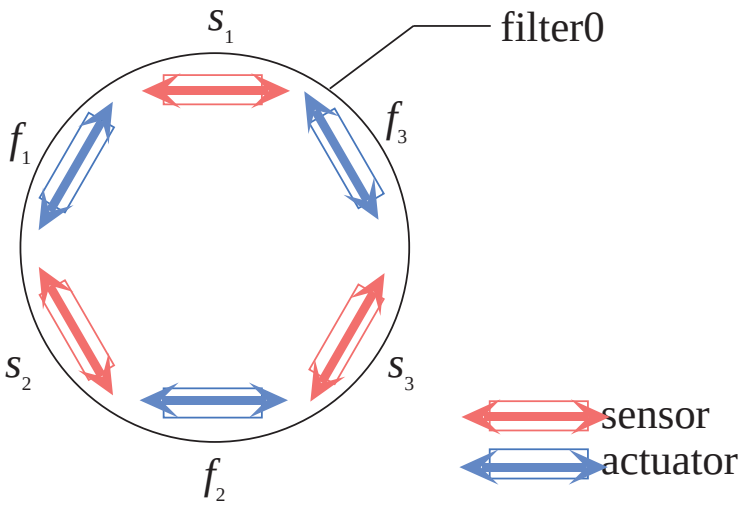

Figure 6.12: Top view of the IP. Three sensors and three actuators are located in a pinwheel configuration, with relative angle of $\pi/3$.

principal axis, unless it is normal to a translational mode. Therefore the vector of the output signal of three sensors $\overrightarrow{s_{\rm real}} = (s_1, s_2, s_3)$ is related to the input force vector of the actuators $\overrightarrow{f_{\rm real}} = (f_1, f_2, f_3)$ as,

$$\overrightarrow{s_{\rm real}} = H\overrightarrow{f_{\rm real}}. \tag{6.16}$$

Here the component of the H matrix, H_{ij} is the transfer function between j-th excitation to i-th sensor, and it is a linear combination of the normal mode response with weighting factors defined by the geometry, the load and the stiffness of the system.

$$H_{ij}(\omega) \equiv \frac{s_{{\rm real}i}}{f_{{\rm real}j}}, \tag{6.17}$$

The example of the frequency response of three sensors to one of the actuator is plotted in figure 6.14. When the quality factor of each mode is high enough (practically more than 10), measured signal $\overrightarrow{s_{\rm real}}$ at the resonance of the mode is dominated by the contribution from that normal mode. It becomes clearer by replotting the bode plots in figure 6.14, taking the real and imaginary parts separated as shown in figure 6.14. Also, the resonant frequency of each mode is more visibly determined because the real part of the transfer function is nulled and the imaginary part takes the local maximum or minima at the resonance. Assuming this and white spectrum of the injected excitation, the following approximation will be true at the resonant frequency of the i-th mode (ω_i).

$$\overrightarrow{s_{\rm real}(\omega_i)} = \begin{bmatrix} H_{i1}(\omega_i) \\ H_{i2}(\omega_i) \\ H_{i3}(\omega_i) \end{bmatrix}. \tag{6.18}$$

Here $H_{ij}(\omega_i)$ gives the projection factor of the i-th mode transfer function to the j-th sensor.

Each virtual sensor is defined to be sensitive only to one of the normal modes, and it is composed by a linear combination of three real sensor signals. The vector of the virtual sensors outputs is defined as,

$$\overrightarrow{s_{\rm virtual}} \equiv \begin{bmatrix} x \\ y \\ \theta \end{bmatrix} = S\overrightarrow{s_{\rm real}}.$$

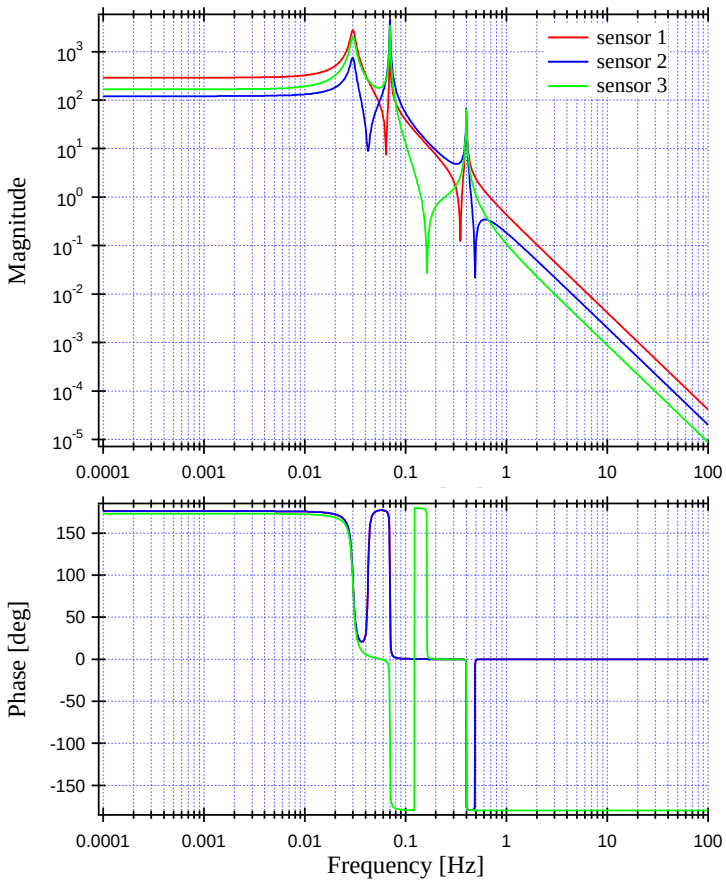

Figure 6.13: Frequency response of the real position sensors mounted on the IP to the excitation by a single actuator. Two translational modes are independent and their resonant frequencies are 30 mHz and 70 mHz, while the yaw mode is located at 400 mHz.

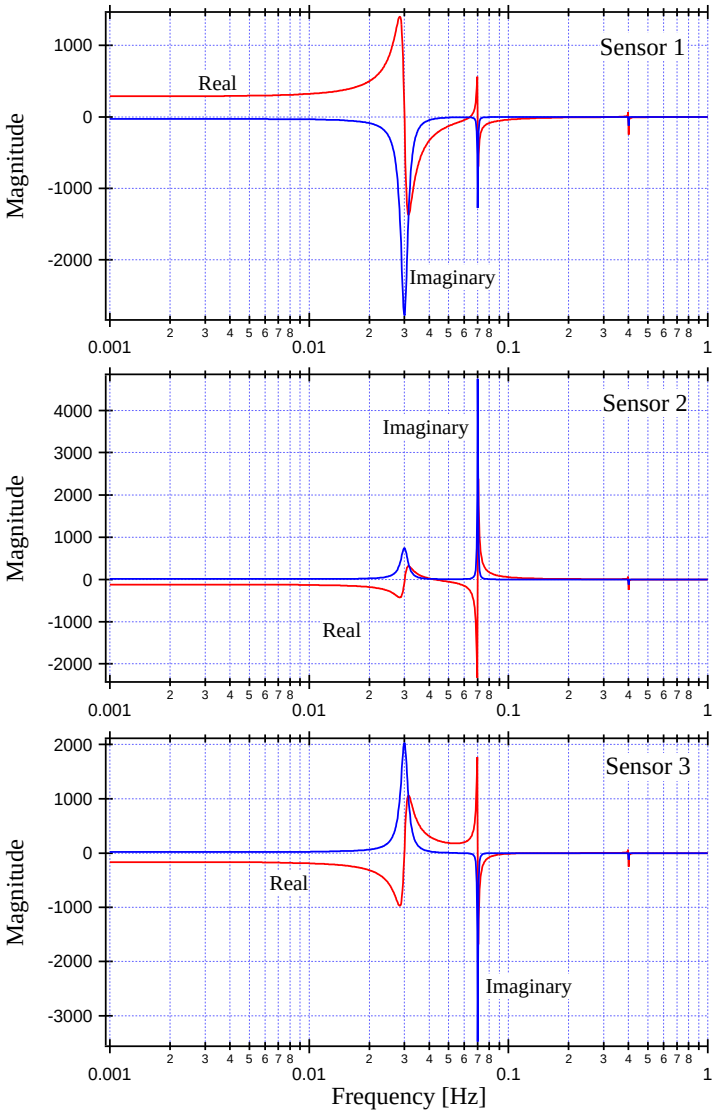

Figure 6.14: Real-Imaginary part of the transfer function of the real sensors shown in figure .

Here the matrix S, which gives the constant coefficients in the linear combinations to construct the virtual sensors is named as *sensing matrix*. From the definition of the virtual sensor, the following relation holds true.

$$\overrightarrow{s_{\text{virtual}}(\omega_i)} = \begin{bmatrix} \delta_{1i} \\ \delta_{2i} \\ \delta_{3i} \end{bmatrix}, \tag{6.19}$$

where δij is the Kronicker's delta, with normalizing by the DC response. From equation (6.18) and (6.19), the following equations are true.

$$E = S \begin{bmatrix} H_{11}(\omega_1) & H_{21}(\omega_2) & H_{31}(\omega_3) \\ H_{12}(\omega_1) & \ddots & \\ H_{13}(\omega_1) & & \ddots \end{bmatrix} \equiv SH', \tag{6.20}$$

and

$$H' = S^{-1}. \tag{6.21}$$

Since the matrix H' is obtained by the measurements, the sensing matrix S can also be defined by the measurements.

By executing above procedure, the sensing matrix for the model system is obtained and the transfer functions from one of the real actuators to the virtual sensors are plotted in figure 6.15. The example is shown for the position sensor, but the same procedure will derive the virtual accelerometers as well.

If the sensors are located perfectly symmetrically and the calibration coefficiency of each sensor is tuned to be equal, the calibration coefficiencies for the virtual sensors will be comparable to the ones for the real sensors, by normalizing each row of the sensing matrix as:

$$\sqrt{\sum_{j=1}^{3} S_{ij}^2} = 1. \ (i = 1, 2, 3) \tag{6.22}$$

6.3.2 Virtual Actuators

Like the sensing matrix, we define the *driving matrix* D which transforms a vector of virtual actuators $\overrightarrow{f_{\text{virtual}}}$ to the vector of real actuators $\overrightarrow{f_{\text{real}}}$, as

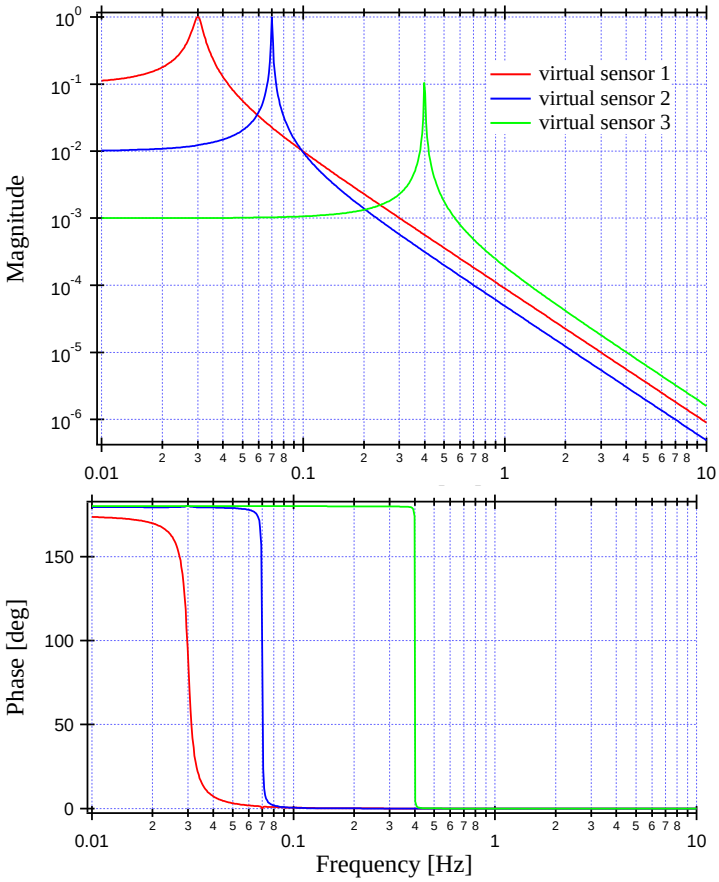

Figure 6.15: Frequency response of the virtual position sensors to the excitation by a single actuator.

$$\overrightarrow{f_{\rm real}} = D\overrightarrow{f_{\rm virtual}}. \tag{6.23}$$

Each virtual actuator exerts force only into the corresponding mode. Therefore the virtual system is described by the following equation, using a diagonal matrix composed by the normal mode transfer functions,

$$\overrightarrow{s_{\rm virtual}} = \begin{bmatrix} H_x(\omega) & 0 & 0 \\ 0 & H_y(\omega) & 0 \\ 0 & 0 & H_\theta(\omega) \end{bmatrix} \overrightarrow{f_{\rm virtual}} \equiv H_0\overrightarrow{f_{\rm virtual}}, \tag{6.24}$$

and

$$\overrightarrow{s_{\rm virtual}} = H_0 D^{-1}\overrightarrow{f_{\rm real}}, \tag{6.25}$$

$$\Leftrightarrow \overrightarrow{s_{\rm real}} = S^{-1}H_0 D^{-1}\overrightarrow{f_{\rm real}}. \tag{6.26}$$

From equation (6.16) and (6.26), one could obtain the driving matrix. Particularly by exerting force with each real actuator separately below the resonant frequency and normalizing the normal mode transfer function with the DC value this problem can be solved trivially.

6.4 Implementation in TAMA SAS Prototype

6.4.1 Accelerometer

The horizontal accelerometers used for the inertial damping in SAS are homemade device with the peculiar discrimination of the sensitive axis [36]. The mechanics of the device consists of a folded-pendulum, made of a monolithic piece of high quality beryllium copper, shown in figure 6.16. Both the positive and inverted pendulum of the folded pendulum are supported by a set of flex menbrain machined with electroerosion and electropolishing for fine adjustment of its thickness of 50 μm. Since the machining of these menbrains and pendulum legs are done in ones hot, the system is highly symmetric and results very small much cross-coupling, with coefficient of 10^{-4}. The folded pendulum is tuned at about 500 mHz.

On each end of the folded pendulum, the electrostatic position sensor

or the coil-magnet actuator is mounted. The working principle is that of the standard seismometer. The relative position of the folded pendulum and the frame is detected by the transducer and locked with the actuator through PID servo filters. The RF electronics for the capacitive transducer is mounted on the accelerometer body, and located in vacuum. There are few active components on the board, but the heat dissipation is very small and the system works stably for the long period.

The feedback signal used to freeze the reference mass is proportional to the acceleration of the frame. The control bandwidth is between DC to 40 Hz, and the phase delay at 10 Hz is about -10 degrees. Since the UGF for the inertial damping servo is limited around 2 Hz and the servo design is rather conservative as to have more than 50 degrees of phase margin at the UGF, the phase delay of the accelerometer doesn't affect the stability of the IP control.

The accelerometer has sensitivity to detect the motion of the IP below a few Hz, the band of the inertial damping. The sensitivity is shown in figure 6.17, together with the expected IP acceleration. The noise source of the sensor is the stability of the frequency of the local oscillator used for the modulation of the electrostatic sensor.

The calibration of the accelerometer is executed by tilting its platform. As the device has sensitivity at DC, the earth gravity is used as the reference. Typical calibration factor is measured as 50 mV/μg.

6.4.2 Position Sensor

The position sensor used in the IP control is the one developed for Virgo SA. It is composed with three coils: two for the Maxwell pair and one in between the other two as sketched in figure 6.18. It is know as LVDT (Linear Variable Differential Transducer). The detail of the device is described in references [59]. Briefly, the magnetic field induced by the current in the primary coil at center generates the current in the outer secondary coils. Then the current is differentially detected by a line receiver and converted to the output voltage of the sensor. The current in the central coil is modulated at 10 kHz in our case, and the detection is done with homodyne technique. Due to the modulation, the sensor is sensitive at DC, and the output of the sensor is proportional to the relative position between the primary and the secondary coils. The primary coil is mounted on the lateral side of the filter0 and

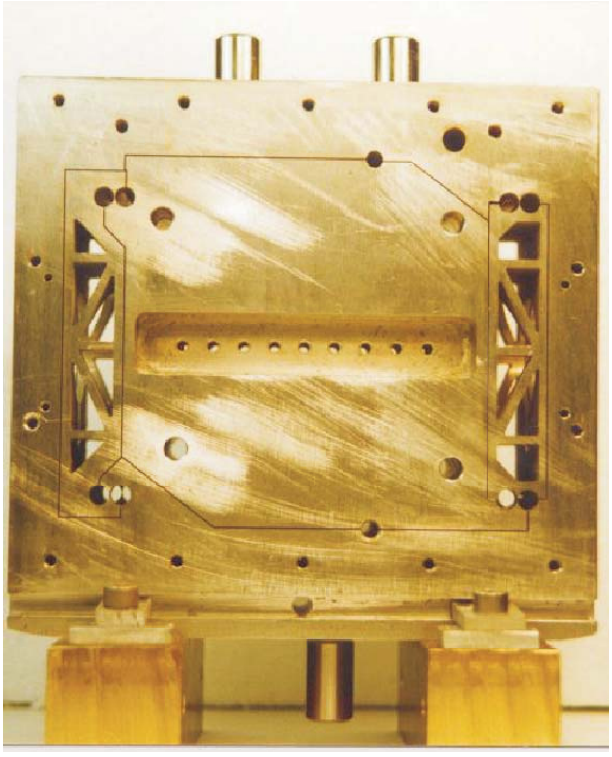

Figure 6.16: Body of the horizontal accelerometer. The normal pendulum in the right, the inverted pendulum in the left. All the flex menbrains are under tension.

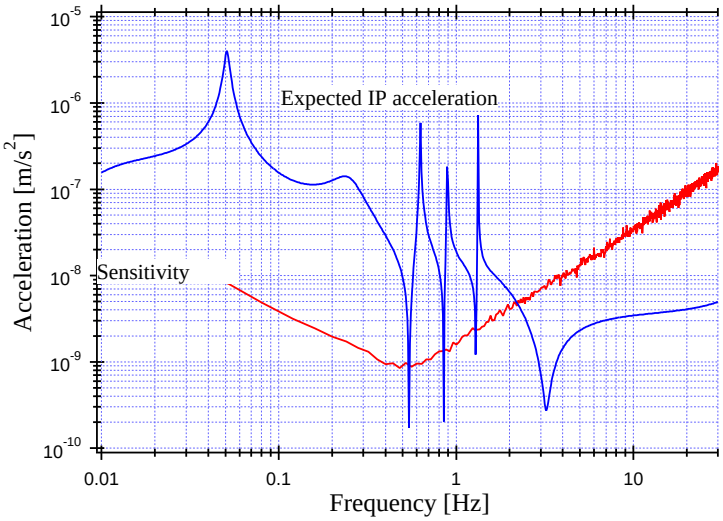

Figure 6.17: Sensitivity of the horizontal accelerometer, and the expected acceleration of the IP. The sensitivity is computed with a measured electronic noise.

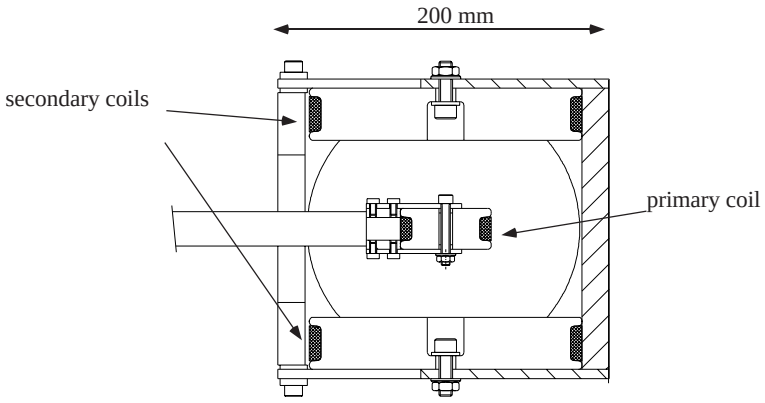

Figure 6.18: Top view of the horizontal LVDT position sensor.

the secondary coils are fixed to the safety frame. So the device detects the position of the IP with respect to the ground.

The main characteristic of the device is its large linear range. In the geometry given in the figure 6.18, the linear region is more than 20 mm, and it is much larger than the range of the IP (fig 6.19). The sensitivity of the horizontal LVDT is of the order of 10 nm/$\sqrt{\text{Hz}}$ (figure 6.20).

There is also the small version of the LVDT mounted on the filter0 to monitor the relative vertical position between the filter0 and the filter1. This version has linear region of several mm and the sensitivity is about 100 times worse than that of the horizontal version.

6.4.3 Actuators

The IP is instrumented with two types of actuators, coil-magnet actuators and stepper motors for different purposes.

Coil-Magnet Actuator

The coil-magnet actuator is a conventional voice coil, and it provides force for the inertial damping. The instrumentation of the actuator is shown in figure 6.21 [60]. It consists of the coil which has a track-shaped cross section, and the yoke that leads magnetic field of the permanent magnets. As the coil is flattened at the center, its magnetic field there is approximately same as that of parallel two planes with current in opposite direction (constant field at given distance from the surface). Therefore, by integrating the magnetic field of the yoke concentrated at the narrowest gap (figure 6.22) for the different

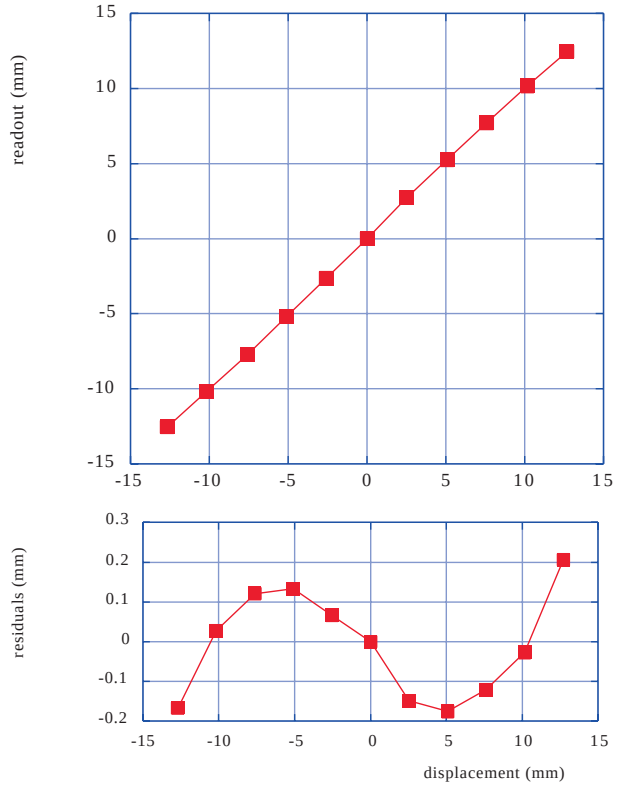

Figure 6.19: Linearity of the horizontal LVDT position sensor. The linear range is about 20 mm, within 1 % of deviation.

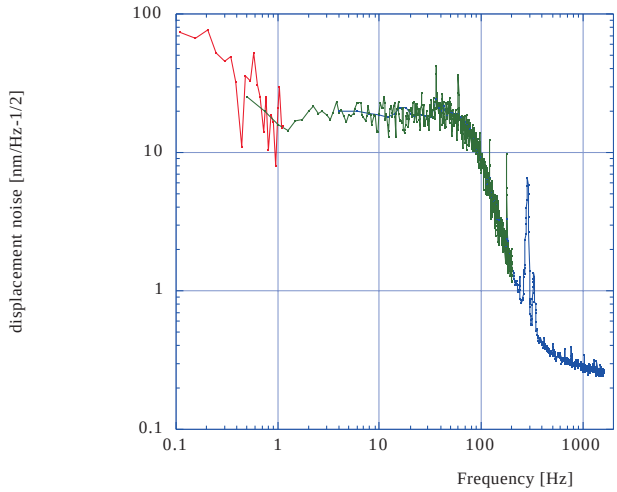

Figure 6.20: Sensitivity of the horizontal LVDT position sensor, filtered at 100 Hz.

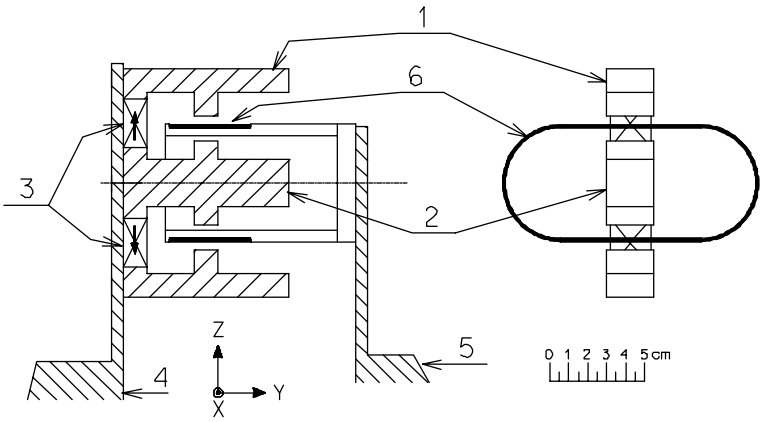

Figure 6.21: Schematic view of the coil-magnet actuator. Side view (left) and front view (right).
1. Yoke jaws, 2. Yoke central bar, 3. Permanent magnets (the arrows in the magnets indicate the field direction), 4. Mechanical support on the safety frame. 5. Mechanical support on the filter0. 6. Racetrack coil. For simplicity the mechanical supports are only sketched on the side view.

range, the force induced by the interaction of the magnetic field of the yoke and that of the coil can be estimated for different position of the coil, and one can optimize the width of the coil (figure 6.23), and the actuator has the linear range. Also one can optimize the gap of the yoke to improve the linearity. The actuator used in the control of IP of SAS has very wide linear range over 20 mm (figure 6.24), which is plenty comparing with the range of IP. The calibration of the actuator is about 0.01 N/A.

Stepper Motor

There are three stepper motors mounted on the safety frame around the SAS tower. Each motor drives a horizontal slider and the slider is connected to the filter0 via soft helical spring. The helical springs make parasitic contribution to the stiffness of the IP. The stepper motor is used for manual positioning of the IP in the current configuration. However its driver is equipped with a PIC microcomputer and can be included in the automatic control at DC.

The MGAS in the filter zero is connected to a stepper motor via soft spring, for the height positioning. It also affects the stiffness of the MGAS.

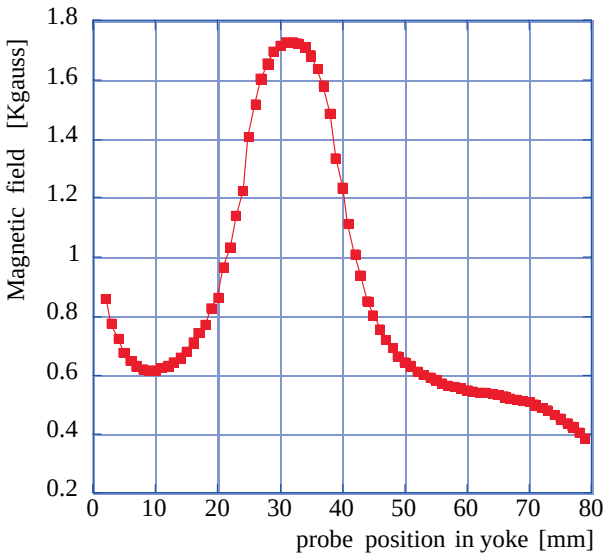

Figure 6.22: Magnetic field of the yoke, along y axis.

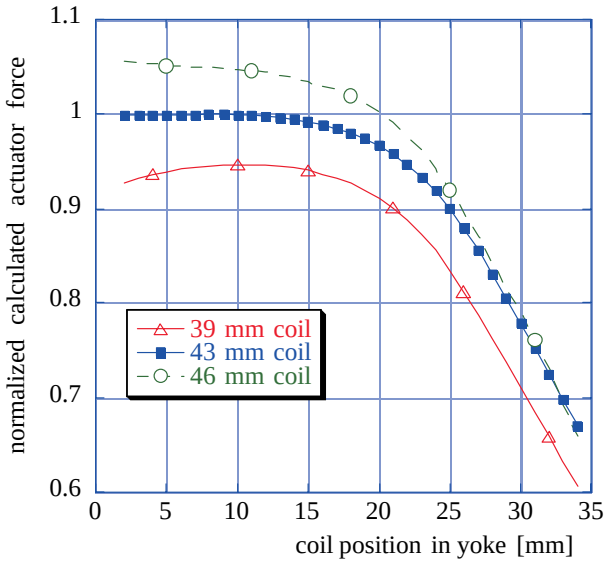

Figure 6.23: Estimation of the position dependency of the coil-magnet actuator, for different width of the coil.

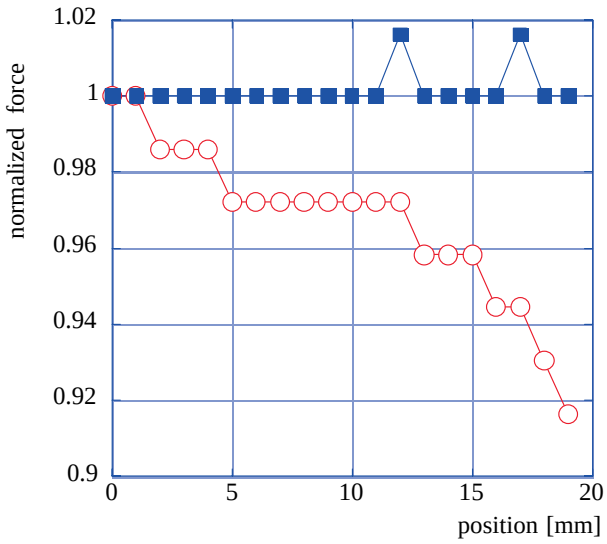

Figure 6.24: Measured actuator force with constant current in the coil before (red) and after (blue) the optimization of the yoke geometry. The measurement is quantized due to the resolution of the scale to measure the force.

6.4.4 Geometry

The apparatuses for the local control are concentrated on the filter0, the top of the IP as shown in figure 6.25. The coil-magnet actuator and the stepper motor are co-located, while the accelerometer and the LVDT are slightly off aligned. Each type of component is allocated in a pinwheel configuration.

6.4.5 Digital Control System

The compensators and the diagonalization matrices of the active damping of the IP are achieved by a digital control system developed by the Virgo team, while the drivers of the sensors and actuators are all composed by analog electronics [42].

The digital control has advantages to be used in the low frequency control like the inertial damping as

- STABILITY: If one intended to realize the low frequency filters with time constant of the order of 10000 seconds, practically high quality electronic components are hard to find. The components (particularly capacitance) for such large time constant tend to have substantial tem-

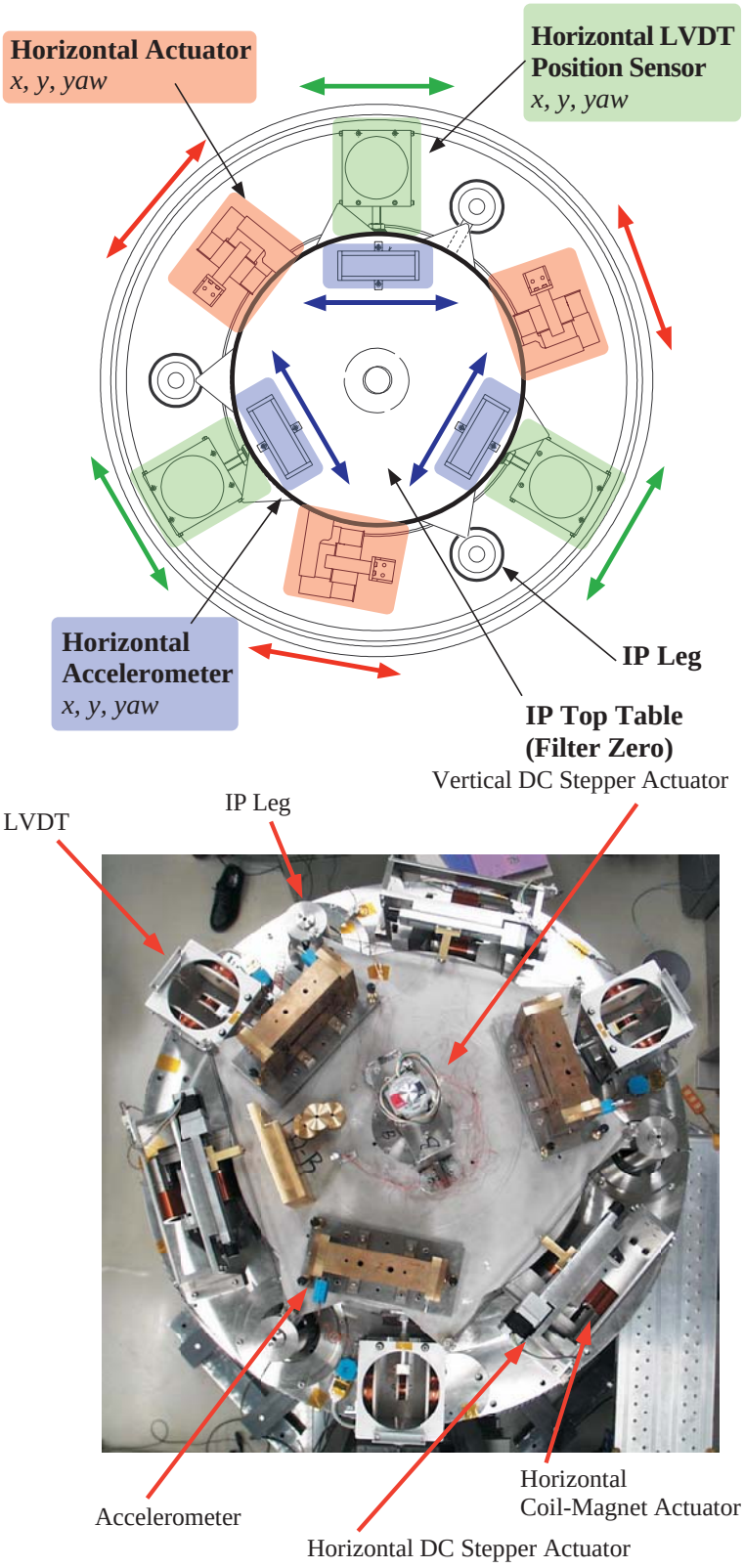

Figure 6.25: Top view of the filter0.

perature sensitivity. Digital system is in practice free from this problem.

- FLEXIBILITY: Once the digital filter is coded, it is easy to change its characteristics, while the analog electronics require physical work. Also programmability of the digital system is very useful at the R&D stage, when different filtering need to be tested.

DSP Unit

The main concerns to design the digital control system are the speed and the digitalization noise. The digital signal processing system used in the SAS control is based on DSP96002 from Motorola driven at 40 MHz, with the arithmetic precision of 32 bit. The high arithmetic resolution is essential to realize very low frequency filtering. In our test, the single pole or zero at the frequency of the order of 10 μHz worked like the theoretical one. For the speed, the system has the sampling frequency of 10 kHz and it introduces negligible amount of phase rotation at the frequencies of the inertial damping. The anti-aliasing filters used in front of ADC and at the output of DAC has the cut-off frequency of 4 kHz, and it introduces the phase delay less than 5 degrees at 10 Hz. This effect was practically negligible in the band of inertial damping.

ADC

The ADC board utilizes AD7885 from Analog Devices and it is capable to sample the input signal at 200 kHz at maximum. The noise of the circuit is dominated by that of other electronic component than the noise given by the limited number of resolution of the ADC chip, 16 bits. The nominal oversampling factor is 20. As the result, the system becomes equivalent to an ideal 15 bit ADC and the input noise level is 2.4 $\mu\mathrm{V}/\sqrt{\mathrm{Hz}}$ as shown in figure 6.26. The input range of the ADC is 10 $\mathrm{V_{pk}}$.

DAC

The DAC unit is based on the 20 bit DAC AD1862 from Analog Devices. The measured noise level is 0.2 $\mu\mathrm{V}/\sqrt{\mathrm{Hz}}$.

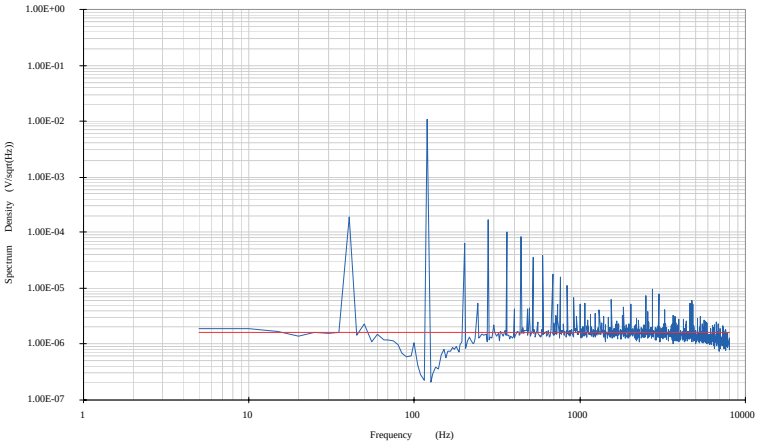

Figure 6.26: Input noise spectrum of the ADC.

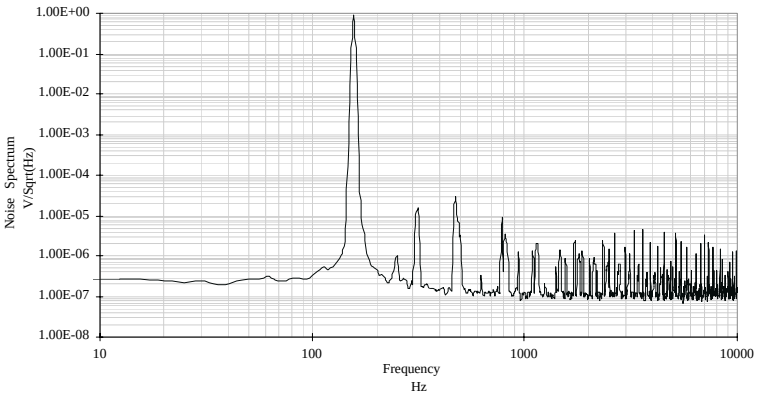

Figure 6.27: Output noise spectrum of the DAC.

6.5 Experiments of SAS Local Controls

We implemented and tested the active damping in the prototype SAS towers. The tests have been done by using the local sensors mounted on the filter0 in each tower.

6.5.1 Diagonalization of the Prototype SAS

At the beginning of the diagonalization process, we measured the motion transfer function to the accelerometers and the position sensors mounted on the filter0, by exciting the IP with a single coil magnet actuator. We injected white noise limited below 1 Hz to the actuator, and recorded both the excitation signal and the output of the real sensors with a PC based data acquisition system. The measured transfer functions are plotted in figure 6.28. The prototype towers were to tuned to have the translational mode frequency below 100 mHz, and the yaw resonance around 400 mHz (see table 6.1)[3]. By picking up the amplitude of the imaginary part of the transfer function (figure 6.29), we determined the inverse sensing matrix, thence obtained the sensing matrix itself. The response of the virtual sensors to one of the actuators is shown in figure 6.30. Also the output signal of the virtual LVDTs in time domain is plotted in figure 6.31. Three normal modes are well separated.

To obtain the inverse driving matrix, we excited the IP with each actuator by the sinusoidal input signal at the frequency lower than the translational mode frequencies. The response of the virtual LVDT was obtained by the lock-in detection technique. The amplitude, including the signal of the LVDTs' response are the components of the inverse driving matrix.

The transfer functions from the virtual actuators to the virtual sensors are shown in figure 6.32. Although there are residual cross-couplings due to the imperfection of the sensing and driving matrices, the amplitude of the normal transfer function overcomes the cross-coupling function, therefore and the noise injection due to the cross-coupling would be suppressed by the control in the normal path.

[3]We define the translational modes as X and Y, the rotational mode as Θ. X has the lower resonant frequency than Y. We separated the resonant frequencies of the translational modes by installing the parasitic positioning springs with different stiffness, for better diagonalization. Without this asymmetry, the translational modes were almost degenerate and the separation in frequency was within a few mHz.

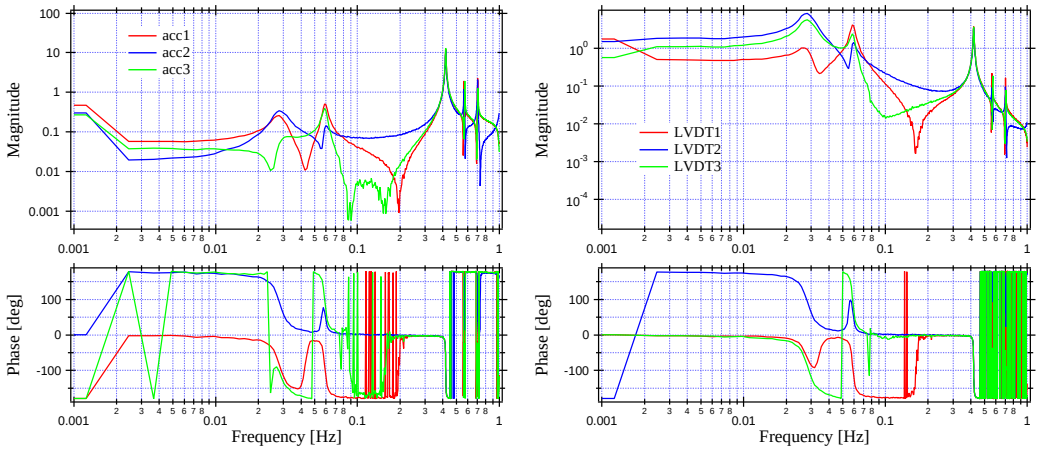

Figure 6.28: Transfer functions to the real sensors from a real actuator.

mode	Front Tower [mHz]	End Tower [mHz]
X	34.2 ± 0.6	37.2 ± 1.2
Y	41.5 ± 0.6	66.2 ± 1.2
Θ	408.3 ± 0.6	419.0 ± 1.2

Table 6.1: Resonant frequencies of the IP normal modes in the TAMA SAS prototypes..

Non-Linear Effect

During the measurements to define the driving matrix, we observed non-linear behavior of the IP. Figure 6.33 is the output signals of the virtual LVDTs and the input signal to the actuator driver both in the time domain and in the power spectrum. The resonant frequencies of the x mode and the y mode were 25 mHz and 50 mHz, respectively, and the IP was excited at 3 mHz. As shown in the plots, there was large distortion in the x mode output signal. The ratio of the power of the fundamental frequency (3 mHz) and its third harmonics (P_3/P_1) in the x mode signal reduced when the IP was re-tuned to the higher frequency. Also we observed that when we tilted the IP intentionally, it did not return to the starting position, if it was tuned below 30 mHz. The friction has non-linear effect sufficiently to the IP tuned to very low frequency.

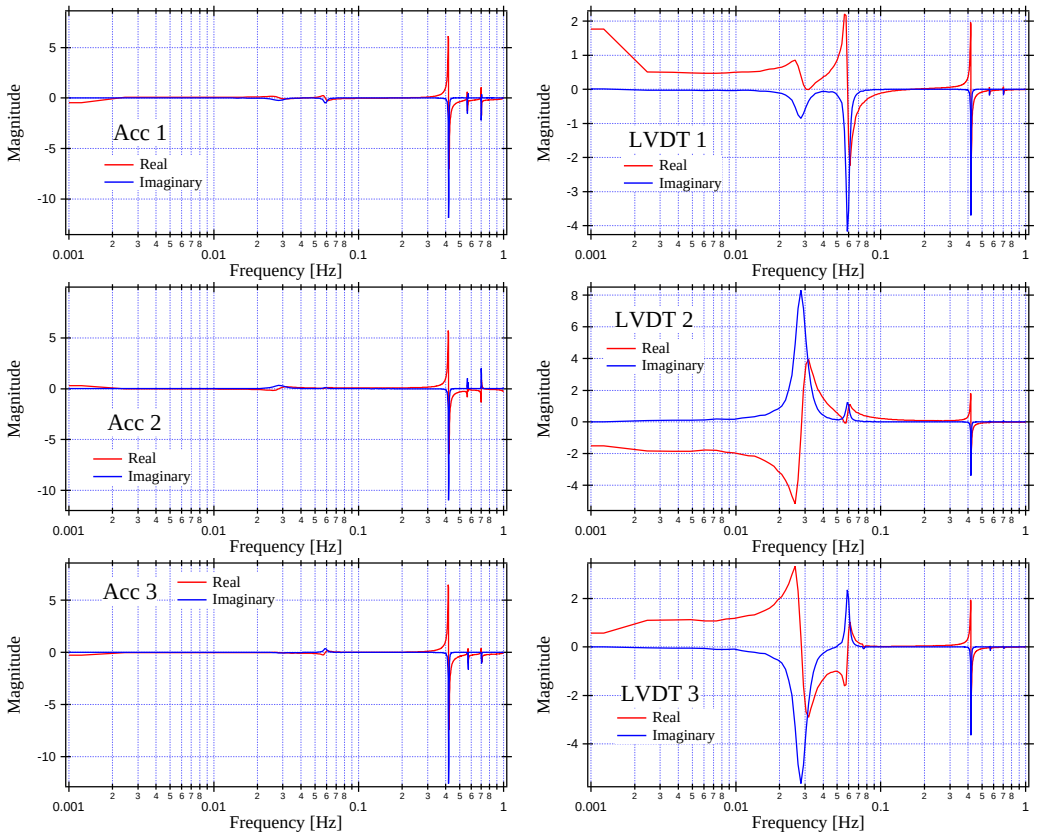

Figure 6.29: Transfer functions to the real sensors from a real actuator, the real part and the imaginary part plotted separately. In the first resonance detected by the LVDT 1, the real part does not cross zero because of the residual contribution from the second mode. However, the imaginary part of the two peaks is well separated.

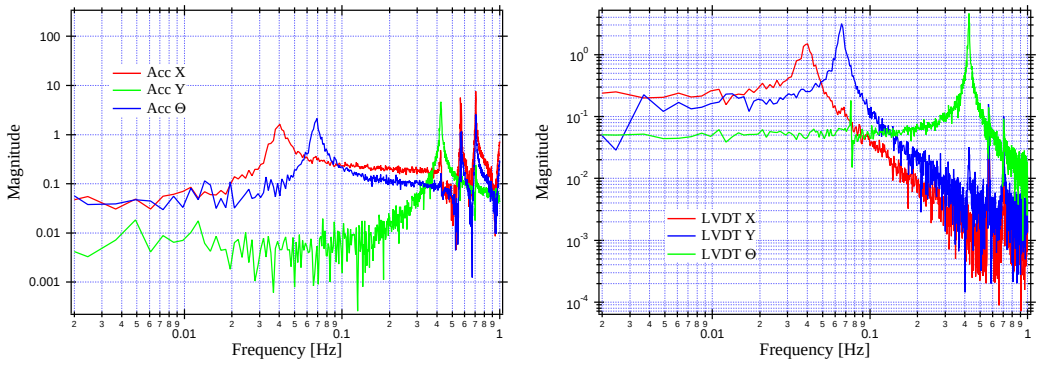

Figure 6.30: Transfer functions to the virtual sensors from a real actuator.

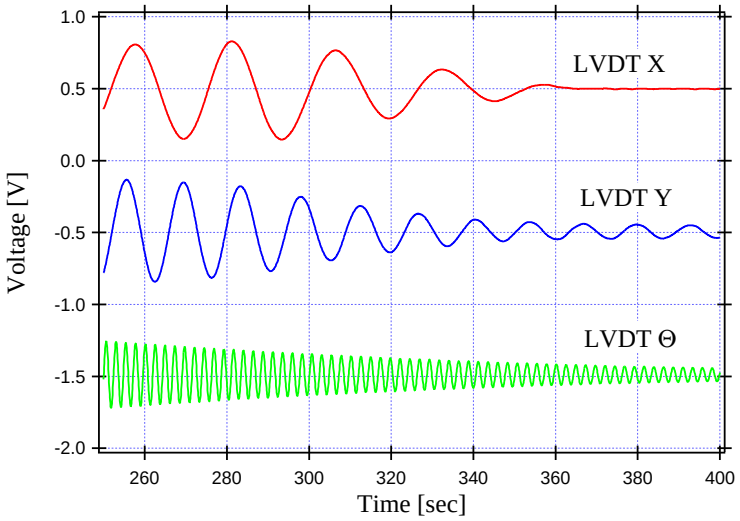

Figure 6.31: Output signal of the virtual LVDTs. An impact force is exerted to the IP to excite all the normal modes at the same time. The higher the resonant frequency of an IP mode, the higher its quality factor is.

6.5.2 Implementation of the Inertial Damping

Once the diagonalization is performed successfully, the obtained virtual system is regarded as three independent SISO, and we are able to apply the servo described in section 6.2 for the inertial damping in each mode.

The transfer functions from the virtual actuator to the corresponding virtual sensors are plotted in figure 6.34 and 6.35, for the front tower and the end tower, respectively. The ratio of the flat part A (above the resonance), and B (below the resonance) gives the measure of the symmetry of the IP. While the end tower has the ratio larger than 10 in all degrees of freedom, the ratio for the front tower is close to 1: i.e. the front tower is highly asymmetric. Although we used the filter0 itself as the jig to position the IP legs when assembling the IP, the measured transfer functions correspond to the error in the leg position of the order of a mm, and the legs diverge at the top.

Inertial Damping on the End Tower: Control of an Ideal IP

As shown in figure 6.35, the end tower responds to the actuation almost ideally. Therefore we could simply apply the feedback filter designed in section 6.2. The blending frequency of the LVDT servo and the accelerometer

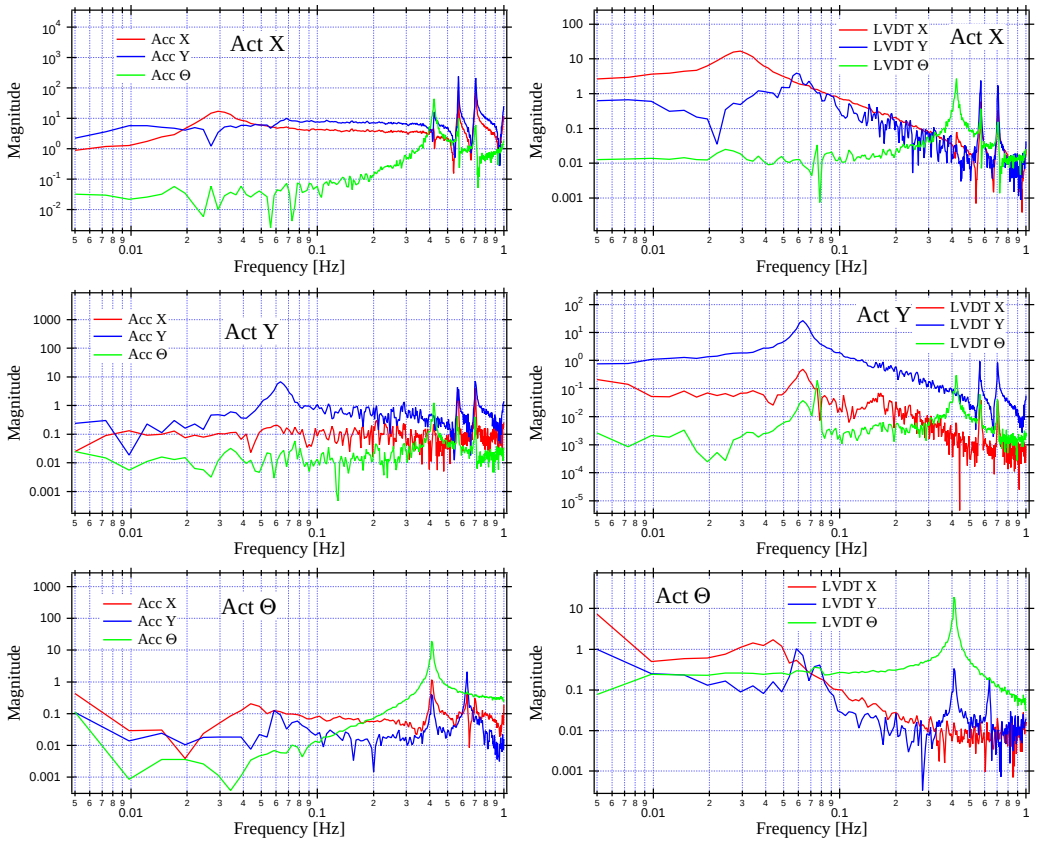

Figure 6.32: Typical transfer functions to the virtual system.

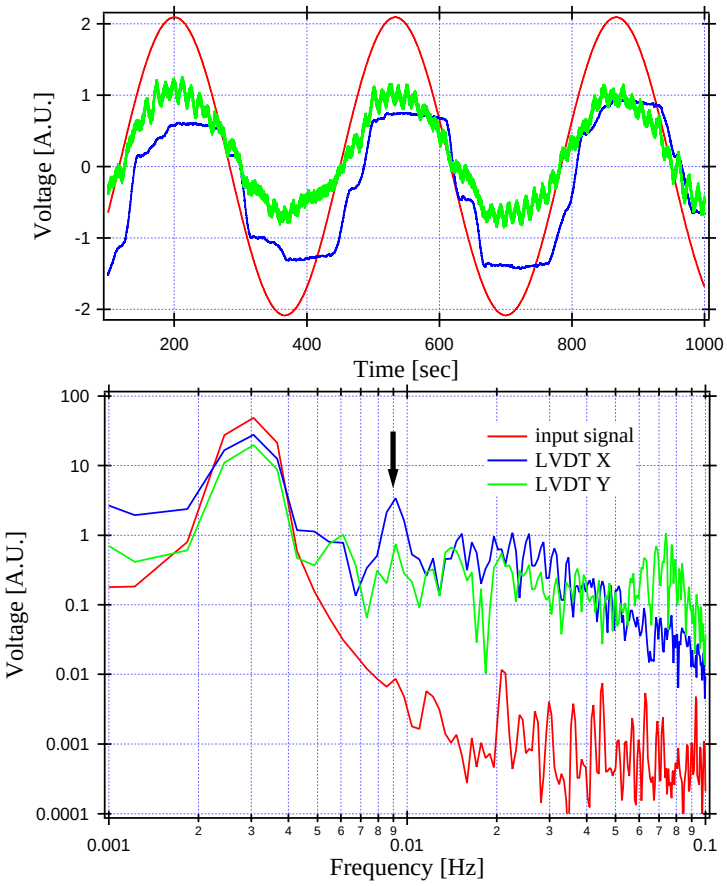

Figure 6.33: Non-linear effect observed in the diagonalization measurements. The output signal of the virtual LVDT for the x mode is strongly distorted.

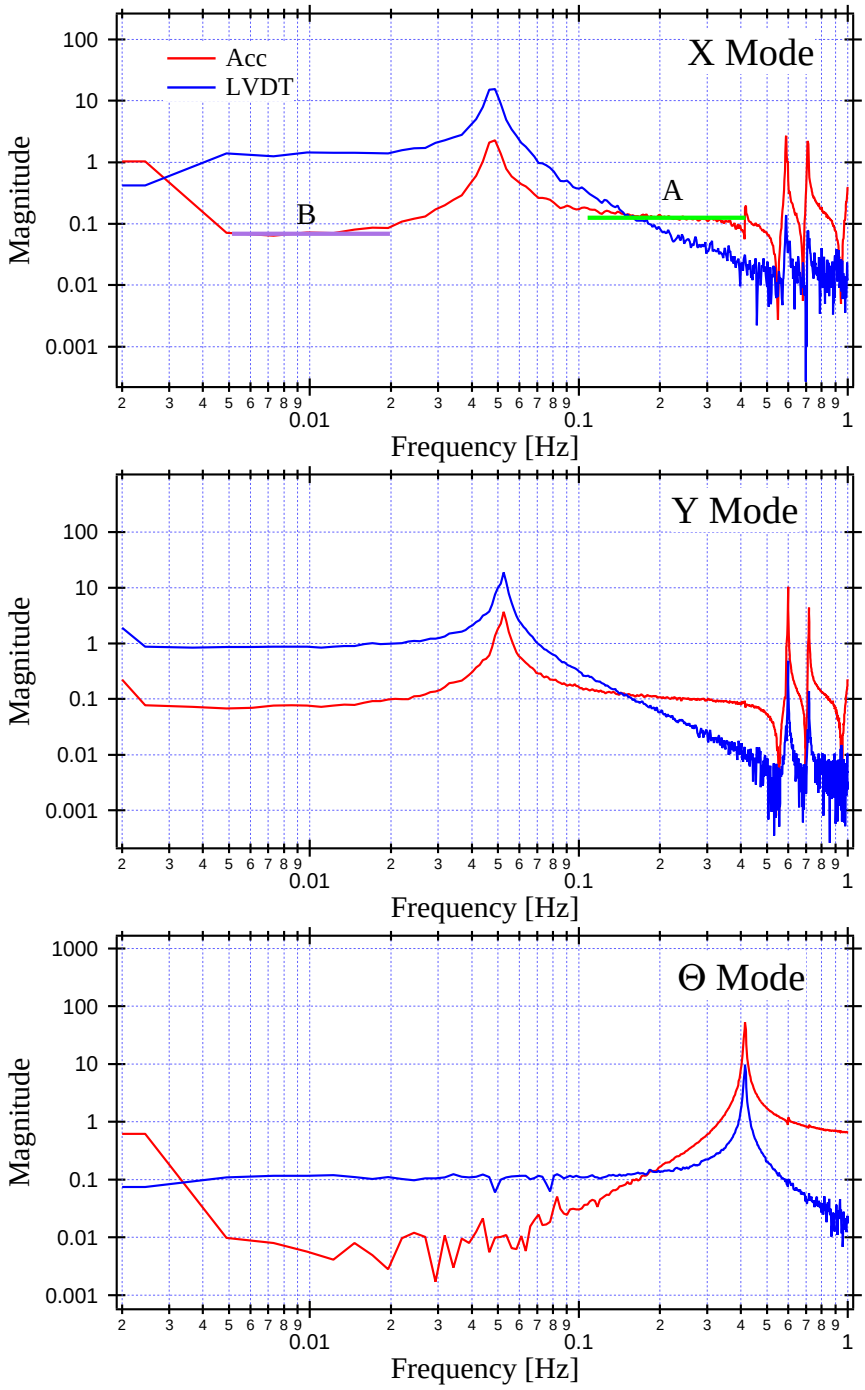

Figure 6.34: Normal transfer functions in the front tower.

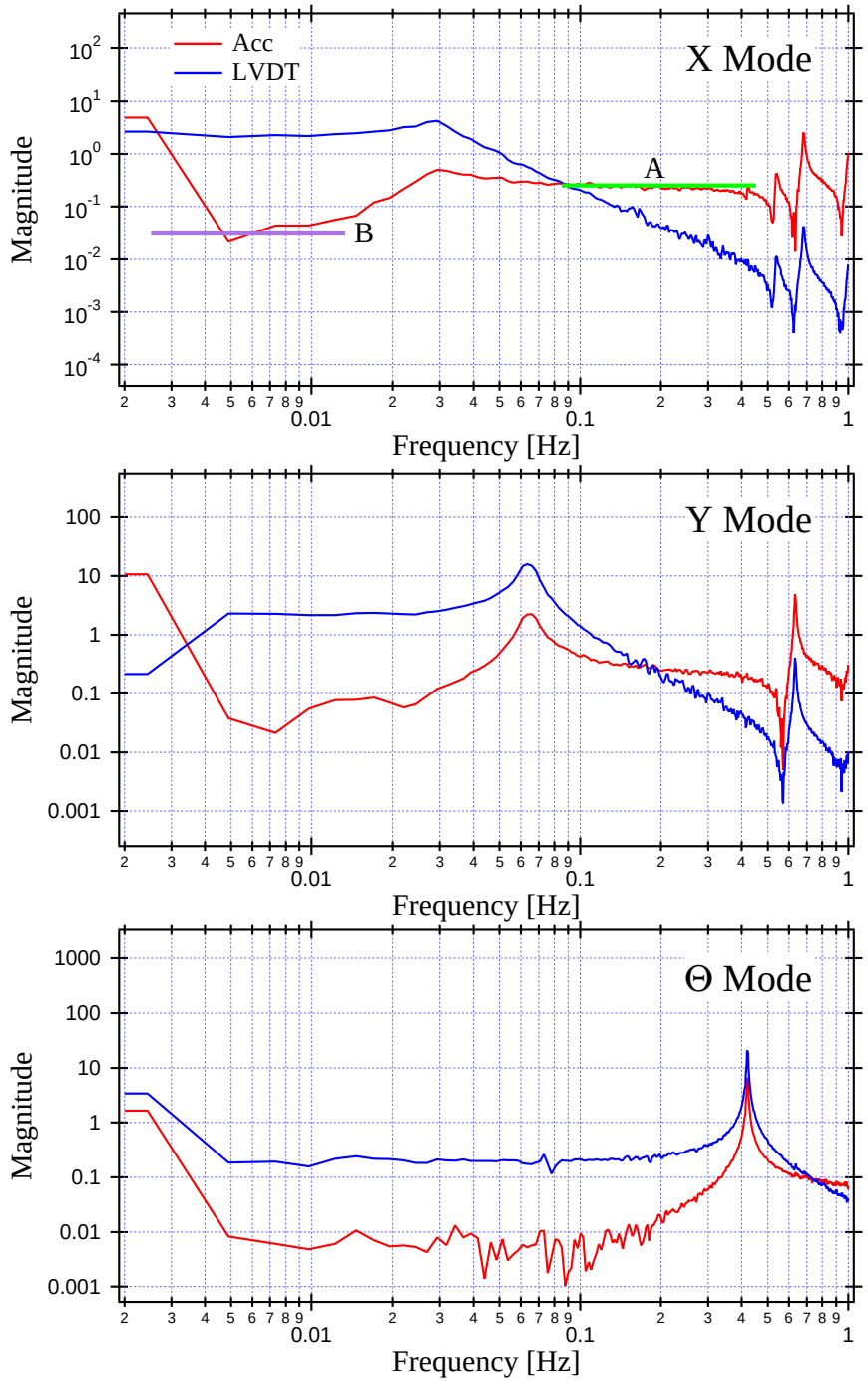

Figure 6.35: Normal transfer functions in the end tower.

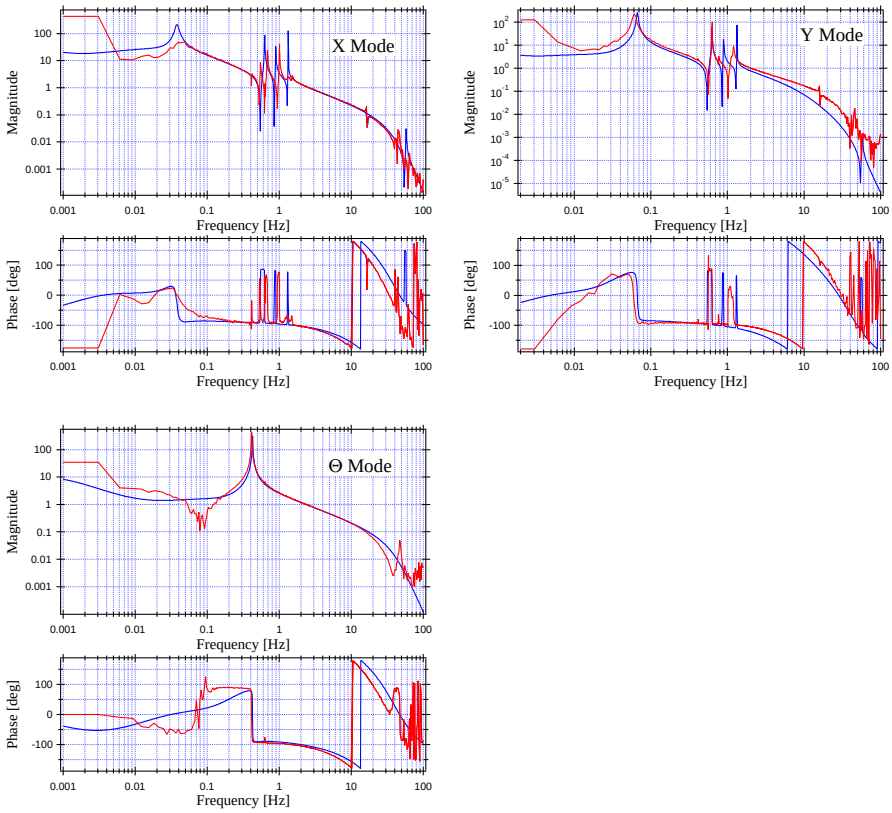

Figure 6.36: Open loop transfer function of the inertial damping for the end tower.

control loop is slightly lower than the resonant frequency of the IP in all d.o.f., and the gain of the LVDT control loop is reduced above that frequency with the higher order low pass filter.

The open loop transfer functions in the inertial damping of the end tower are plotted in figure 6.36. The UGF for each mode is limited to a few Hz with the sufficient phase margin of about 80 degrees to reduce the control noise injection in the GW detection band. Reduction of the error signal for the inertial damping was clearly observed (figure 6.37). All the peaks of the rigid body modes of the SAS were sufficiently suppressed. The r.m.s. motion of the IP was suppressed by factor of 9 thanks to the active damping, without injecting noise above the UGF.

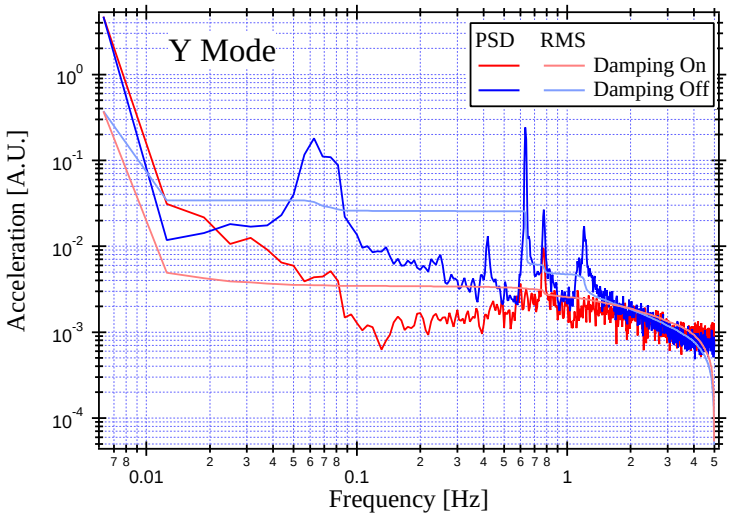

Figure 6.37: Output signal of the virtual accelerometer on the end SAS. The IP was naturally excited by the seismic motion. The power spectra were integrated above 0.1 Hz to obtain the r.m.s. acceleration. The reduction factor of the r.m.s. motion was suppressed by factor of 9.

Inertial Damping on the Front Tower: Control of an Asymmetric IP

Since the IP of the front tower is highly asymmetric, the accelerometer signal will be blinded by the translation-tilt coupling at the frequencies lower than the IP resonance. This coupling has serious effect in the translational modes, while it was not observed in the yaw mode, because the resonant frequency of the rotational mode was much higher than that of the translational modes. Therefore the servo filter for the rotational mode was designed like the end tower.

For the translational modes, we applied the compromised servo described in section . The IP resonances are damped by using the signal from the virtual LVDT. The open loop transfer function for each translational mode is plotted in figure 6.38. As the overall loop gain is lower than the LVDT loop gain just above and below the modal frequency, seismic noise will be re-injected at these frequencies.

We mounted the forth accelerometer on the filter0, aligned to the longitudinal direction. This additional accelerometer is identical to the ones used for the damping, but it is out of the control loops. The output signal of the

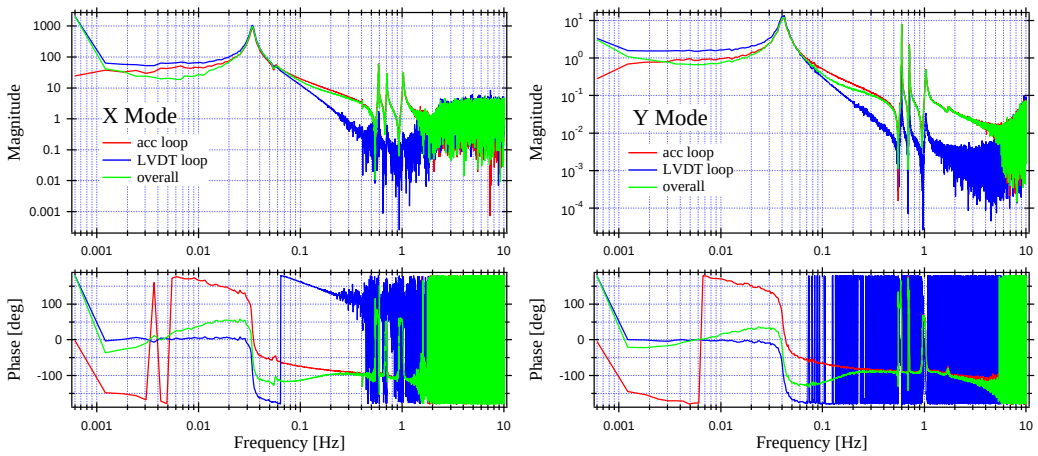

Figure 6.38: Open loop transfer functions of the inertial damping on the translational modes of the front tower.

accelerometer was used to evaluate the effect of the inertial damping (figure 6.39). Despite the compromised servo, the motion in the main axis of the interferometer was suppressed by the damping in the most frequencies. A possible explanation is that the output signal of the accelerometer was dominated by the contribution of the yaw motion of the IP, and the mode was damped significantly because it was not affected by the asymmetry of the IP. The peak around 400 mHz corresponds to the yaw mode and it disappeared when the system is damped.

The measured reduction factor of the r.m.s. motion above 100 mHz was about 4. The main contribution to the r.m.s. motion was from the micro seismic activity observed around 150 mHz. The motion in the lower frequency band may increase, but we did not observe the self oscillation of the tower.

6.5.3 Control Noise

The noise of the electronics used in the control results the displacement noise of the IP. Figure 6.40 shows the comparison of the actual displacement of the IP and the main control noise. The contribution of the digital electronics is comparable to that of the actuator noise. The actuator noise is measured by using the current monitor implemented in its driver. As shown in the plot, while limiting the bandwidth of the inertial damping below a few Hz, the electronic noise does not spoil the IP performance.

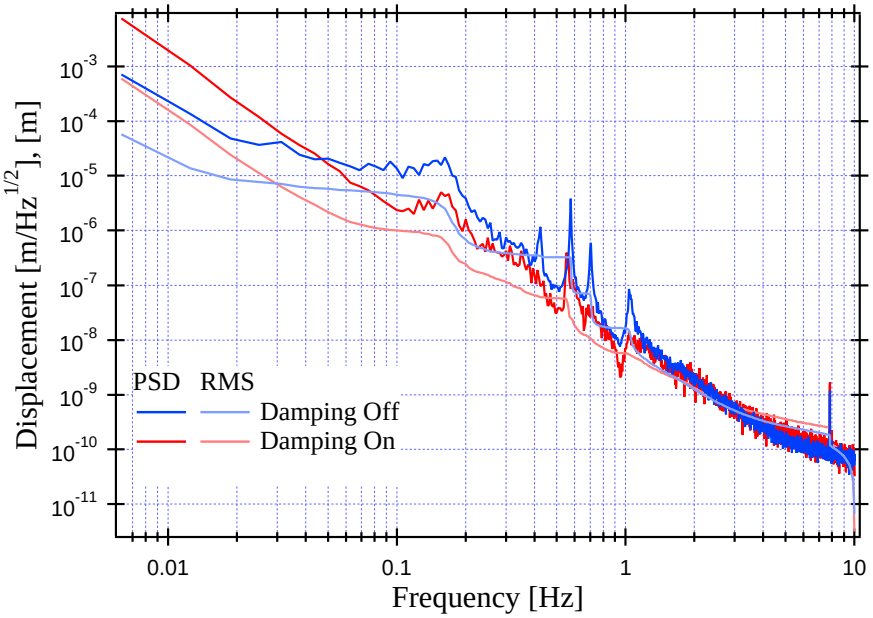

Figure 6.39: Motion of the front IP with and without the inertial damping. Detected by the monitor accelerometer.

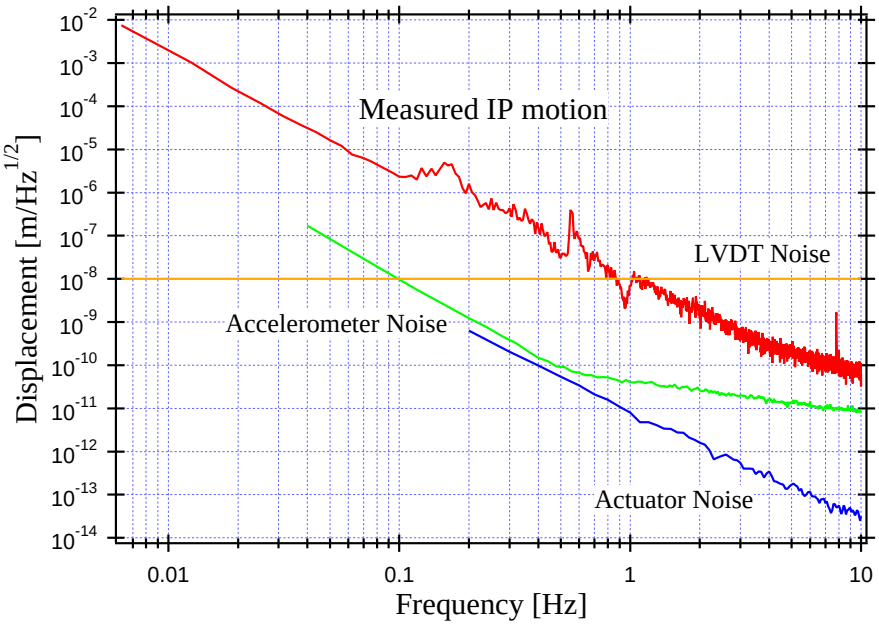

Figure 6.40: Control noise.

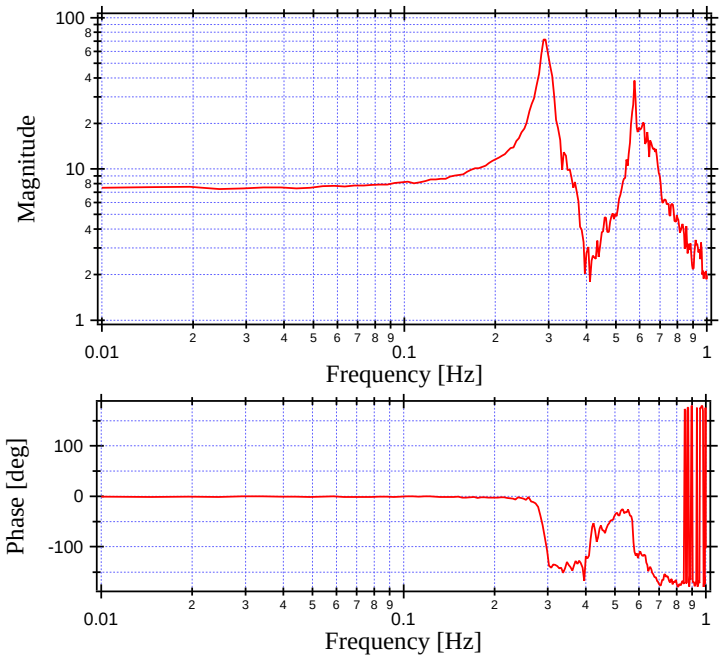

Figure 6.41: Transfer function from the vertical actuator to the vertical LVDT.

6.5.4 Vertical Resonances of the MGASFs

The vertical resonances of the MGASFs potentially couple to the horizontal motion of the IP. However, they may be damped actively by using the vertical LVDT and the vertical coil-magnet actuator mounted between the filter0 and the filter1. The vertical transfer function from the actuation to the LVDT output is plotted in figure 6.41. As it has the same structure of double poles and double zeroes, the same algorithm as the inertial damping (viscous damping) can be applied to it.

6.5.5 Summary

From the results presented above, we can conclude the following things on the SAS local control.

- The inertial damping was implemented successfully in the two prototype towers, in spite of the large asymmetry in the front tower which mimic the accelerometer signal in ultra-low frequency band.

- The actual system of the TAMA SAS, including the mechanics, electronics, and the software for the digital control was proven to work as it was designed.
- The rigid body modes of the SAS chain were damped by the inertial damping system almost critically.
- The suppression of the IP r.m.s. motion integrated above 100 mHz was observed by the accelerometer out of the control loops. The reduction factor was between a few to 10, depending on perfection of the IP assembly.

Chapter 7

3m Fabry-Perot Experiment

7.1 Scope

Two TAMA SAS prototypes designed for the main test masses of TAMA300 were fabricated to evaluate their performance. The test consisted in the operation of a Fabry-Perot cavity formed by mirrors housed in the prototype towers. The test was expected to:

- Demonstrate the SAS compatibility with the operation of Fabry-Perot cavities.
- Measure the motion of the mirrors suspended by the SAS. Due to the superior attenuation performance of the SAS, devices like accelerometers commercially available are not able to evaluate the actual SAS mirror motion. In the Fabry-Perot cavity composed by two identical suspension, one mirror can be used as a reference to detect the motion of the other mirror with respect to it.
- Evaluate the robustness of the SAS operation.

7.2 Setup

7.2.1 Overview

The prototype SAS towers were identical and fully instrumented. The mechanical plant is the one described in this article: i.e. the IP, the MGASFs, the SUS, and the electronics for the local control. They are located in the

Figure 7.1: 3m Fabry-Perot cavity in the laboratory. Each vacuum tank contains one prototype SAS tower. The racks between the tanks house the electronics for the local control.

laboratory on the sub basement floor in University of Tokyo (figure 7.1). The level of the seismic activity at the laboratory is shown in figure 1.9 (labeled as Hongo), and the standard seismic model used in our simulations is defined to match it.

The prototype towers were installed in the vacuum vessels 3m apart (center to center) to form the Fabry-Perot cavity with 3m arm length.

7.2.2 Optical System

The layout of the optical system is illustrated in figure 7.3. A commercial Nd:YAG laser (Mephisto500NE from Innolight GbmH) is located on the optical bench. Part of its beam is sampled and fed into the electro-optic modulator (EOM) for the phase modulation. Faraday isolators are used to eliminate the optical feedback by the returned light to the laser source. The spatial mode of the laser is matched to that of the 3m Fabry-Perot cavity by using appropriate cylindrical lenses [15]. After the isolators, the beam enters a first vacuum vessel which houses the setup for the laser frequency stabilization described in the reference [38]. The frequency stabilized light then enters the front vacuum vessel of the 3m Fabry-Perot cavity, through

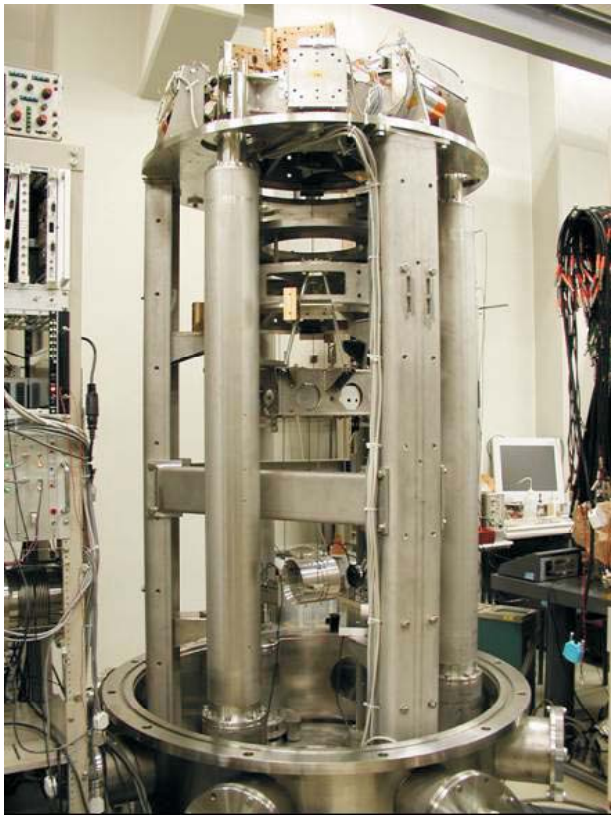

Figure 7.2: TAMA SAS prototype tower, located in the vacuum tank.

	Front Mirror	End Mirror
Diameter	30 mm	30 mm
Thickness	5 mm	5 mm
Radius of Curvature	∞ (flat)	4.5 m
Intensity Reflectivity	97.1 %	99.6 %

Table 7.1: Optical properties of the mirrors in the 3m Fabry-Perot cavity. The reflectivities are measured values [14, 13]..

Length	2.94 m
FSR	51.0 MHz
Finesse	188
Cavity Pole Frequency	136 kHz

Table 7.2: Optical properties of the 3m Fabry-Perot cavity.

an acrylic tube. The acrylic tube covers the beam while it propagates in air to reduce the influence of air currents which cause fluctuation of the refraction index and degrade the stability of the laser beam. The input beam is vertically polarized and reflected by the polarized beam splitter (PBS) in front of the input test mass suspended by the front SAS. There is a quarter-wave plate (QWP) between the input test mass and the PBS, so that the light reflected from the 3m cavity is horizontally polarized and is transmitted by the PBS and is detected by the main PD. The required input power to the cavity is a few tens of mW[1].

The mirrors that form the Fabry-Perot cavity were 30 mm diameter mirrors mounted in a bored hole in the front surface of each dummy mass (figure 7.4). They were attached with a few drops of cyanoacrylate glue on the lateral surface. The mirrors were made of glass with dielectric coating and anti-reflective coating on the front and the back surface, respectively. The measured optical properties of the mirrors used in this setup is listed in table 7.1. The properties of the Fabry-Perot cavity is shown in table 7.2. The finesse of the cavity is degraded about 10 % under atmospheric pressure [13], however this does not affect significantly the measurements at low frequency.

[1] As it turned out that our measurements were not shot-noise limited, we did not take accurate measurement of the laser power.

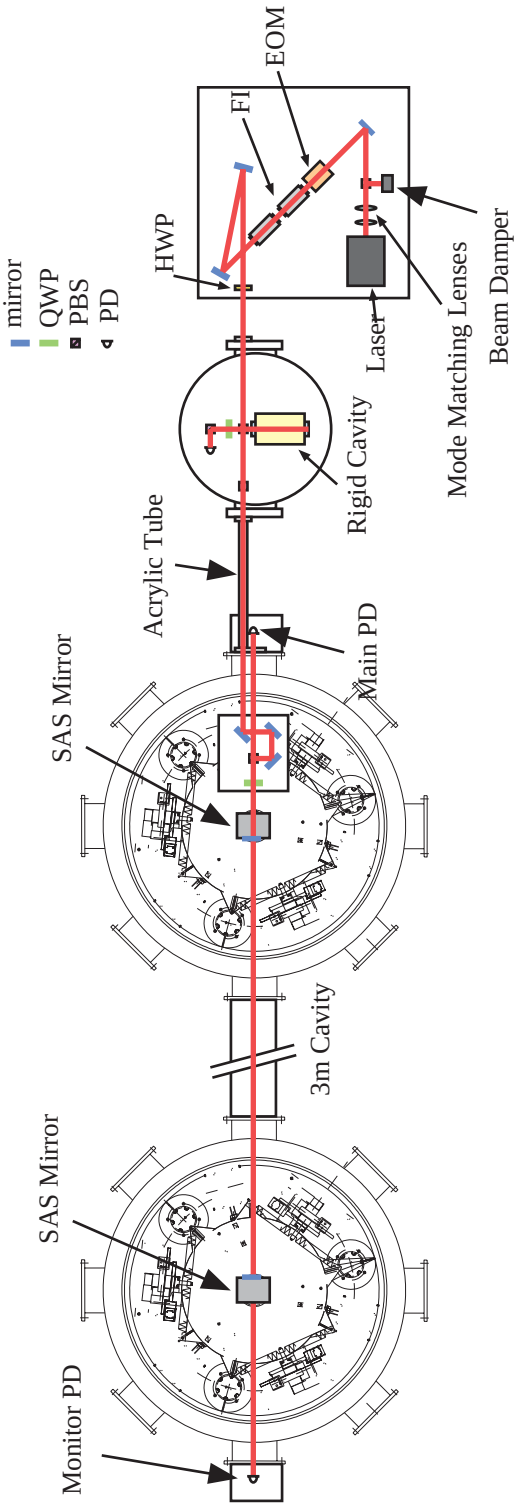

Figure 7.3: Layout of the optics.

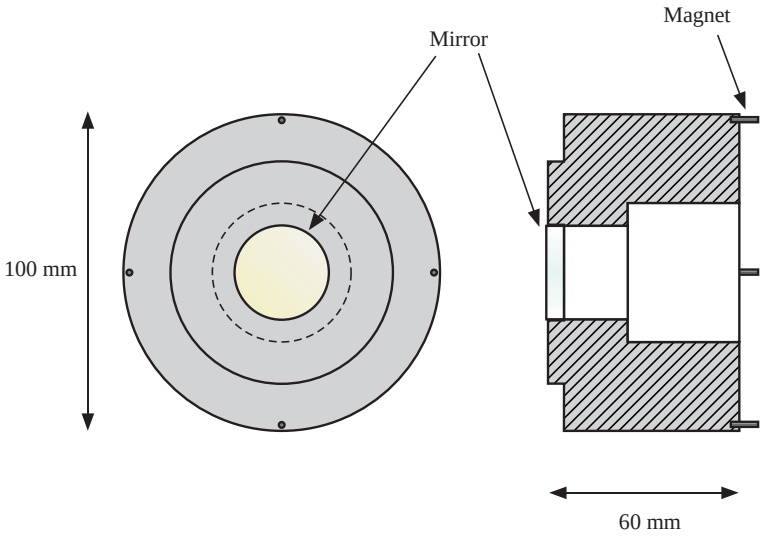

Figure 7.4: Dummy mass used in the SAS prototype.

7.2.3 Control System

We applied the PDH technique to sense the cavity length fluctuation. The phase modulation frequency was set to 40 MHz. The signal to drive the EOM was generated by a function generator (AFG2020, from Sony-Tektronix Inc.). This signal was also supplied to the demodulator to extract the error signal of the length control as a local oscillator. The demodulation phase was optimized to maximize the amplitude of the error signal.

The lock of the cavity was achieved by actuating only on the end test mass (figure 7.5). For this control loop, we used fully analog electronics because the frequency band of the control was of the order of hundred Hz, and the digital system was not able to realize the necessary compensators at such high frequency.

The alignment of the cavity was achieved only by tilting and rotating the suspension platform with the coil-magnet actuators at DC. There was no automatic alignment control.

The block diagram of the control system is sketched in figure 7.6. The parameters in the control loop are denoted as shown in table 7.3. Each noise is defined as output noise of the corresponding component. We recorded the error signal $x'_{\rm er}$ and the feedback signal $x_{\rm fb}$ with the FFT servo analyzer to obtain the length fluctuation of the cavity ΔL. These quantities are related as:

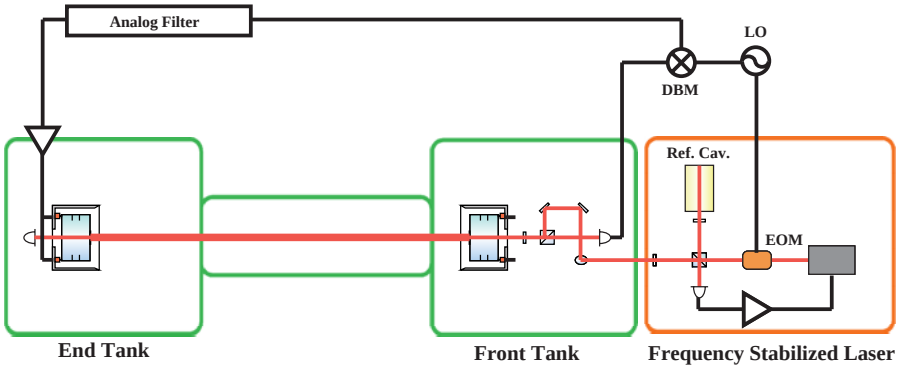

Figure 7.5: Schematic view of the cavity control.

$$\begin{array}{ccc} x'_{er} = x_{\mathrm{er}} & +\frac{H_{\mathrm{ol}}}{1+H_{\mathrm{ol}}} n_{\mathrm{det}} = & \frac{H^{\mathrm{L}}_{\mathrm{FP}}}{1+H_{\mathrm{ol}}} \Delta L - \frac{H^{\mathrm{L}}_{\mathrm{FP}}}{1+H_{\mathrm{ol}}} \left[H_{\mathrm{mr}} n_{\mathrm{drv}} + H_{\mathrm{mr}} \alpha n_{\mathrm{fb}} \right], \\ f_{\mathrm{fb}} & = & G x'_{\mathrm{er}}. \end{array} \tag{7.1}$$

Here H_{ol} is the open loop transfer function defined as:

$$H_{\mathrm{ol}} = \alpha H^{\mathrm{L}}_{\mathrm{FP}} H_{\mathrm{mr}} G. \tag{7.2}$$

By multiplying the measured error and feedback signals with the correction function $(1 + H_{\mathrm{ol}})/H^{\mathrm{L}}_{\mathrm{FP}}$ and $(1 + H_{\mathrm{ol}})/(GH^{\mathrm{L}}_{\mathrm{FP}})$, respectively, we can obtain the natural length fluctuation ΔL.

As the cavity pole is much higher than the frequency of our interest, $H^{\mathrm{L}}_{\mathrm{FP}}$ can be replaced with a constant conversion factor from the displacement to the electric signal. The open loop function was measured in the same manner used for the small Michelson interferometer. The obtained open loop transfer function is shown in figure 7.7. We also measured the frequency response of the mirror actuation and of the compensators, therefore we can construct a model to describe the open loop transfer function, which is also plotted in the graph.

7.2.4 Vacuum System

To reduce the effect of air flow and the acoustic noise, the 3m cavity was placed in a vacuum system. The vacuum chambers which house the SAS prototypes were spaced 3m center to center. They are connected by a tube with 150 mm inner diameter. A scroll pump was connected to the end

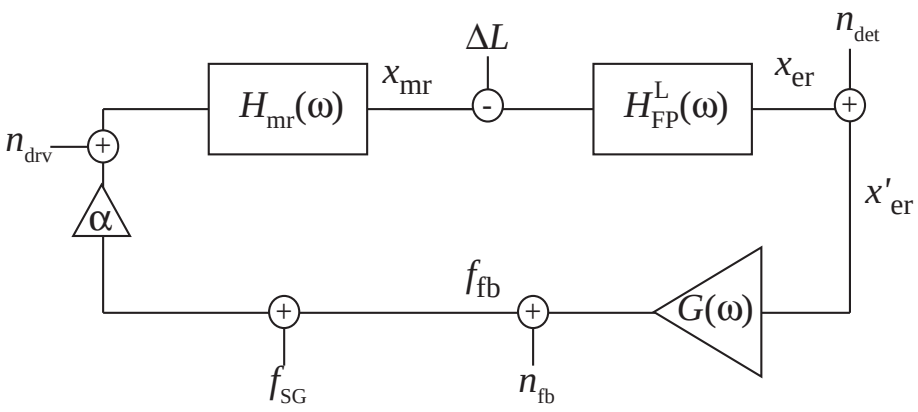

Figure 7.6: Block diagram of the cavity control.

fluctuation of cavity length	ΔL
error singnal sensed by PDH	x_{er}
feedback signal (coil driver input)	f_{fb}
driver effiency	α
readout noise of PDH	n_{det}
electric noise of feedback filter	n_{fb}
driver noise	n_{drv}
frequency response of cavity	$H^{\mathrm{L}}_{\mathrm{FP}}$
frequency response of mirror actuation	H_{mr}
frequency response of compensator	G

Table 7.3: Parameter list of the cavity control. n_{det} includes the shot noise and the output noise of the electronics used to extract the PDH error signal.

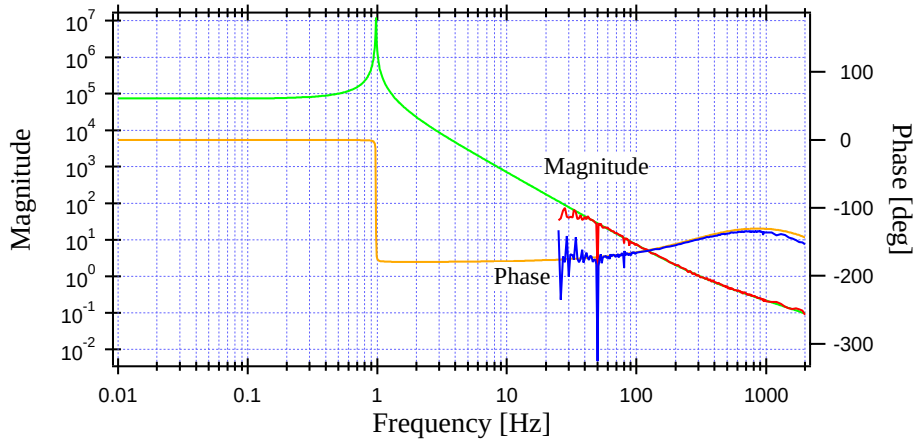

Figure 7.7: Open loop transfer function of the cavity control. Measured (Red, Blue) and Fitted (Green, Yellow)

chamber through a molecular sieve. The best vacuum level achieved was about 10^{-3} Torr, and the system maintains the vacuum level of better than 1 Torr for a week. All in vacuum measurements were performed with the pump stopped.

7.3 Results

7.3.1 Calibration

In order to calibrate the measured error signal and the feedback signal, we excited the front mirror at certain frequencies. As we have independently measured the actuator efficiency with a calibrated position sensor (see chapter on the mirror suspension), we know the amount of displacement applied to the front mirror. Since the height of the peaks at the excitation frequency in the corrected signal corresponding to the displacement of the front mirror, we can obtain the calibration factor.

We excited the front mirror at 30 Hz and 60 Hz, where there is no structure in the measured frequency response of the mirror actuation.

7.3.2 Estimation of the Mirror Motion

One can estimate the motion of the SAS mirror by using the seismic motion measured at the laboratory, and folding it with the attenuation performance generated by the point mass model. However, there is still uncertainty of the relative angle between the IP translational modes and the cavity axis.

The real LVDT #2 of the front tower, and #3 of the end tower are geometrically aligned transversally to the cavity (figure 7.8). Since the sensing matrix are normalized, the component of the sensing matrices expressing the contribution of these transversal LVDTs to the IP translational modes gives us a rough idea of the relative angle between the optical axis and the natural modes. From the measured sensing matrix of each tower, the angle between the X mode and the optical axis are obtained as $\theta_1 = \pi/6$ and $\theta_2 = \pi/4$ for the front and end tower, respectively. We estimated the motion of the SAS mirror in the longitudinal direction x_i ($i = 1$ for the front tower, $i = 2$ for the end tower)by using the following formula.

$$\langle x_i \rangle = \sqrt{(H_{\mathrm{x}} \cos\theta_i)^2 + (H_{\mathrm{y}} \sin\theta_i)^2} \times \langle x_{\mathrm{seism}} \rangle \,. \tag{7.3}$$

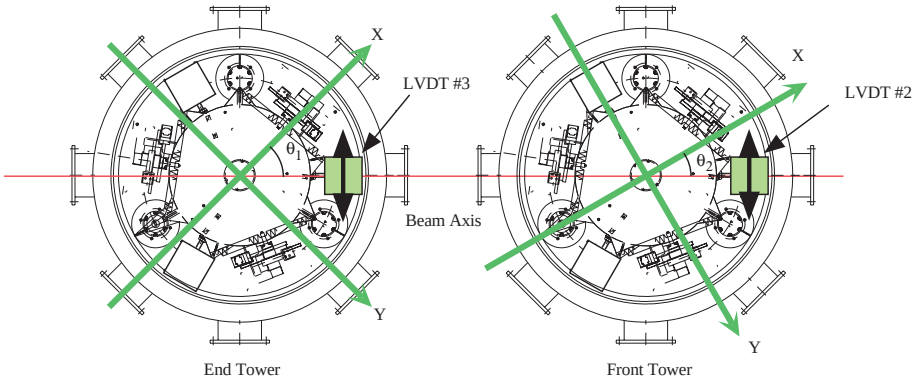

Figure 7.8: Layout of the LVDTs used to identify the angle between the X mode and the optical axis.

Here H_x and H_y are the transfer functions from the ground to the mirror in the X and Y direction[2], and x_{seism} is the ground motion measured by a commercial seismometer (LA 50 from RION). We assumed isotropy of ground motion and no correlation[3] between two towers' position. The cavity length fluctuation is then estimated as

$$\Delta L_{est} = \sqrt{x_1^2 + x_2^2}. \tag{7.4}$$

7.3.3 Displacement of the SAS Mirror without Inertial Damping

Figure 7.9 shows the length fluctuation of the 3m Fabry-Perot cavity extracted from the measured feedback signal. This measurement was taken in vacuum without inertial damping. The laser frequency was stabilized using the rigid cavity as the reference. The estimated curve from equation (7.4) is plotted as well in figure 7.9. Some comments are needed:

- The peaks of the SAS rigid body modes below 1 Hz were higher than estimated. However the floor level of the measured spectrum agrees with the estimation below a few Hz. The measured displacement floor at 1 Hz was of the order of 10 nm/$\sqrt{\text{Hz}}$. It can be improved down to

[2]These transfer functions are purely passive ones when the inertial damping is not applied.

[3]Usually, the ground motion correlates strongly between two points only 3m far each other. Therefore, this assumption will result the upper limit of the cavity length variation.

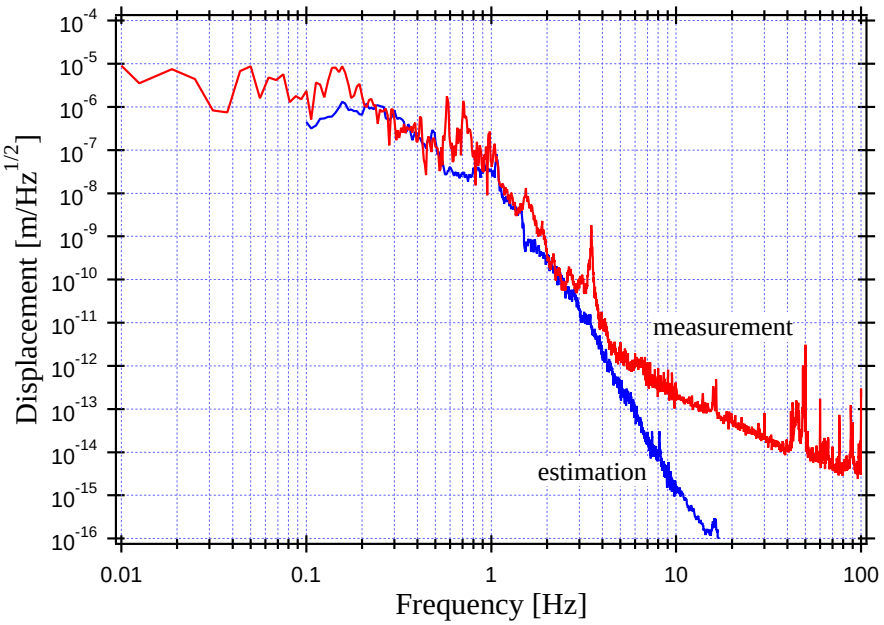

Figure 7.9: Length fluctuation of the 3m Fabry-Perot cavity. Measured (red) and Estimated (blue).

the order of 1 nm by lowering the IP resonant frequency.

- There were two significant peaks at 1.5 Hz and 3.5 Hz. These are supposed to be the cross-coupling from the vertical and the pitch motion of the mirror, because the observed frequencies are close to the vertical resonant frequency of the mMGAS at the suspension point of the double pendulum, and to the common pitch mode of the double pendulum suspension, respectively.

- A large discrepancy between the measured data and the estimation was observed above the peak at 3.5 Hz. This is due to the electric noise (discussed in section 7.3.5), and the mirror motion was properly measured below this frequency.

7.3.4 Measurements in Air

Although the effect of the inertial damping was clearly observed using the accelerometer on the IP (chapter 6), we performed a set of measurements under atmospheric pressure to evaluate the effect of the damping to the cavity

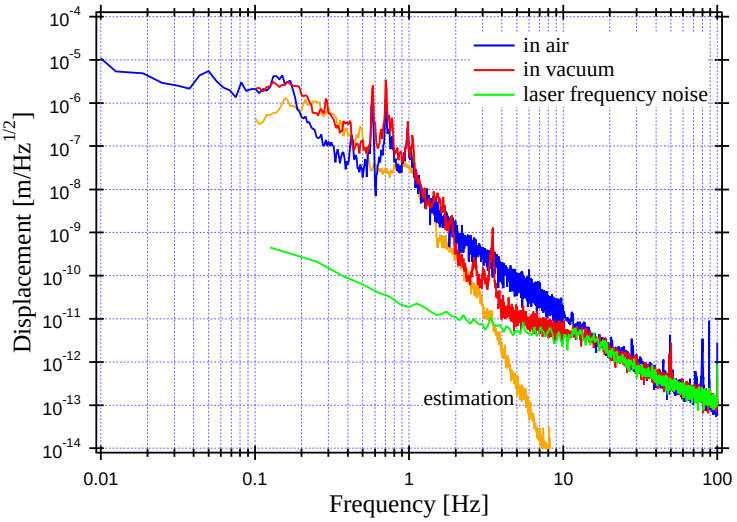

Figure 7.10: Comparison of the measurements in air (blue) and in vacuum (red). The green curve indicates the laser frequency noise without the stabilization. The yellow curve shows the estimated length fluctuation from the simulation.

length fluctuation[4] to confirm the effect. Figure 7.10 shows the comparison of the measurements taken in vacuum and in air without damping. The laser frequency stabilization was turned off in both measurements. The measured displacement in air is larger than the one in vacuum between 2 Hz and 10 Hz. This is supposed to be due to the increased laser frequency instability caused by the air in the cavity. The two curves match each other above this band and both the measurements were obviously limited by the laser frequency noise.

As the two measurements and the estimation agrees below 2 Hz, we conclude that the mirror motion was measured properly below this frequency.

With the cavity locked in air, we applied the inertial damping on both SAS towers. The result is shown in figure 7.11 with and without the damping. The mirror displacement was successfully suppressed by the damping without injecting control noise. The (limited) effect of the damping was clearly observed in spite of the compromised damping performance in the front tower, as measured by the accelerometer on it (chapter 6).

The vertical resonance peak between 500 mHz and 600 mHz was not

[4] Due to the delay of delivery of the vacuum vessels, we could not take the measurements of inertial damping in vacuum.

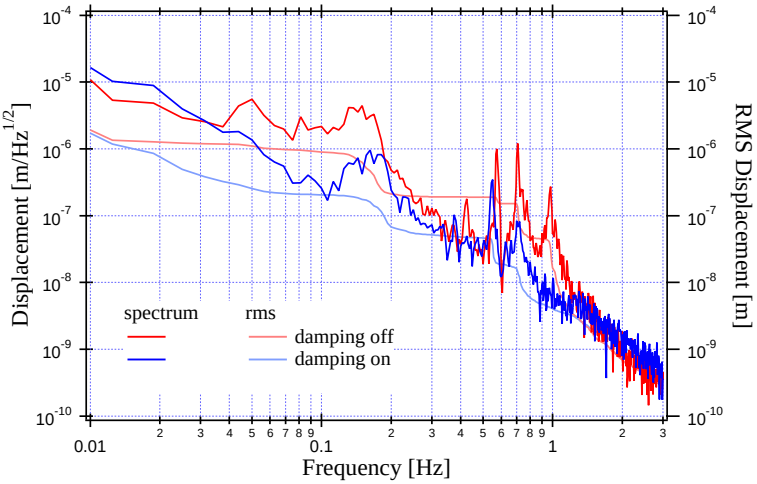

Figure 7.11: Comparison of the cavity length fluctuation with (blue) and without (red) inertial damping.

damping	r.m.s. displacement	r.m.s. velocity
off	0.9 μm	1.2 μm/s
on	0.2 μm	0.3 μm/s
ground motion	1.2 μm	2.6 μm/s

Table 7.4: R.m.s. motion and velocity of the SAS mirror, integrated between 100 mHz and 10 Hz, with corresponding ground motion.

damped as significantly as the other peaks just as observed by the local sensor. The horizontal inertial damping is ineffective in the vertical direction, that can be damped by the vertical LVDT and actuator pair in the IP MGAS filter. The mirror motion integrated from 100 mHz to 10 Hz, listed in table 7.4 was dominated by the contribution from the micro seismic peak around 150 mHz. The reduction factor of 4.5 was the same as observed by the accelerometer. The observed residual velocity with inertial damping, of the order of submicron/sec insures easy lock acquisition of the interferometer.

7.3.5 Noise Analysis

By substituting the independently measured electronic noise functions of the different circuits used in the experiment into equation (7.1), one can estimate their influence on the measurement. The result is shown in figure 7.12. As one can see, the measurement was severely limited by the electronic noise of the feedback filter between 3 Hz and 40 Hz, and by the photo detector noise

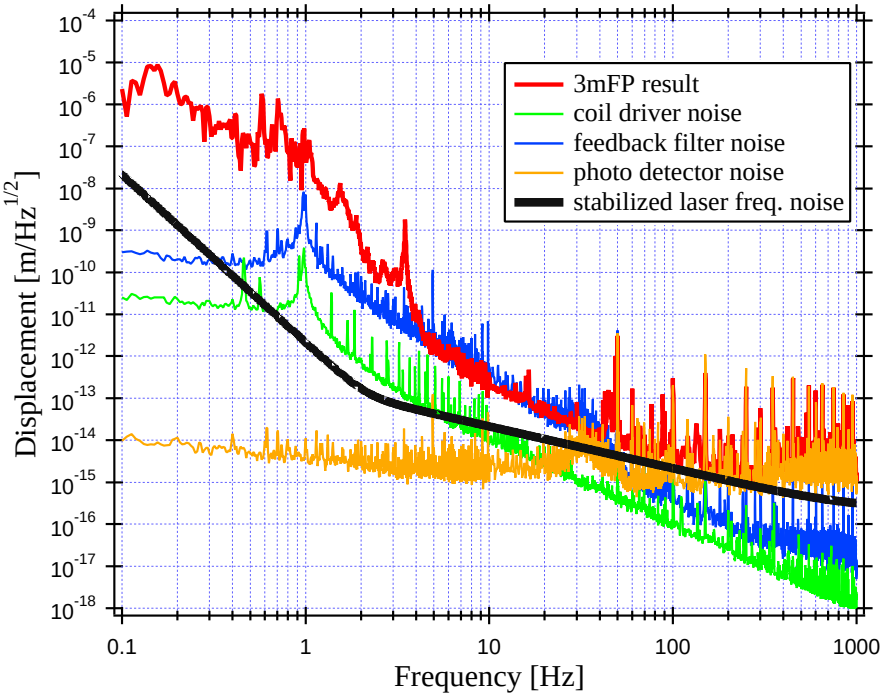

Figure 7.12: Noise budget of the 3m Fabry-Perot cavity. The stabilized laser frequency noise was supplied by its developper. [38]

above 100 Hz, while the laser frequency noise contributed in between. Of course these three main noise sources need to be improved for the further investigation of the SAS performances, but even the other noise sources, like the coil driver noise must be significantly improved as well.

7.3.6 Stability

Thanks to the good low frequency seismic isolation, the Fabry-Perot cavity proved to stay stably in lock even without inertial damping, or automatic alignment control. The longest stretch of the cavity lock was about four hours and we intentionally broke it for a different measurement. The intensity of the transmitted light is a measure of the stability of the cavity. Figure 7.13 is the typical data on the transmitted light intensity and its power spectrum. The cavity was locked without the inertial damping, and the nominal fluctuation of the intensity was about 7 %. The major component of the intensity fluctuation was caused at 80 mHz, 300 mHz, and 400 mHz. The peaks at 80 mHz and 400 mHz are the yaw resonance of the suspended

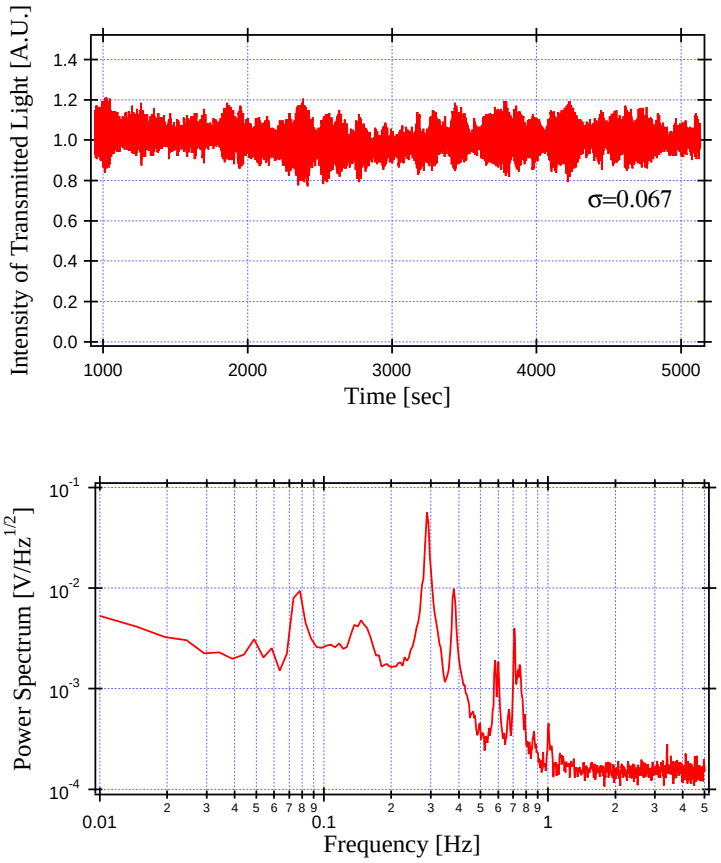

Figure 7.13: Intensity of the transmitted light (normalized) and its spectrum. The peaks above 400 mHz correspond to the longitudinal resonances of the SAS chain.

filters and the IP, respectively.The peak at 300 mHz did not appear in the length fluctuation, and it is supposed to be the common vertical mode of the MGASFs. Presumably the vertical resonance coupled to the pitch motion and caused the misalignment of the cavity.

The angular fluctuations of the SAS mirrors need to be studied in detail because longer cavities in GW detectors are less tolerant to it. All the identified peaks can be damped by the inertial damping, vertical damping and wavefront sensing controls.

7.4 Summary and Discussion

From the results of the 3m Fabry-Perot experiment, the following results are obtained.

- The SAS demonstrated its compatibility with the operation of Fabry-Perot cavity. The cavity was locked stably simply by actuating on the mirror in the longitudinal direction, even without inertial damping.
- The SAS mirror displacement was directly measured below a few Hz. To increase the bandwidth of the measurement, substantially we need to improve the frequency stability of the laser.
- The measured performance of the SAS agreed with the design below 3 Hz where the measurements were not limited by the sensitivity of the setup.
- The effect of the inertial damping was also observed by the Fabry-Perot cavity. The reduction factor of the r.m.s. motion of the mirror, limited by the misaligned front SAS tower, agreed with that of the IP, measured by the accelerometer. The reduced r.m.s. will allow lower mirror actuator force requirements. Fully hierarchical controls from the IP, the suspension platform, and the recoil mass will further reduce the mirror actuator force requirements.

Chapter 8

Discussion and Conclusion

8.1 Results and Discussion

To improve the low frequency sensitivity of interferometric gravitational wave detectors, and to realize their stable operation, we designed and tested the mechanical components and the control technique of the Seismic Attenuation System.

Figure 8.1 gives a brief idea of what has been learned about our system. To validate the passive isolation, we performed the vibration test on the each independent component and the passive isolation chain. The figure shows the frequency band where the performance of each component was tested and validated. The measured performance always matched to the design, with few exceptions as in some the peak height and the peak frequencies. In general the limitation of the bandwidth in which each component is verified is imposed by the limited sensitivity of the sensors used in our experiment. This is an inevitable problem for this kind of work because the device is specially designed to attenuate vibration transmission, and its very success makes the measurements difficult.

We also validated the inertial damping technique by using the local sensors and the 3m Fabry-Perot cavity. According to these measurements, the technique is able to sufficiently damp the horizontal resonances of the system. The residual motion of the Fabry-Perot mirror was suppressed down to sub-micron level by the damping, without any control noise injection out of the control band. The reduction factor of the mirror motion integrated above 100 mHz was limited to 4.5, because of imperfection of assembly of

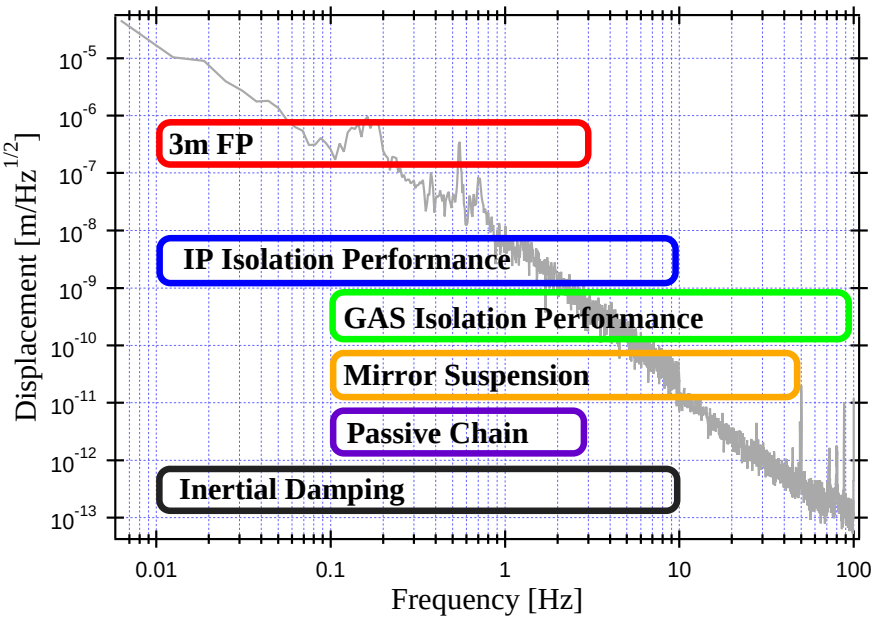

Figure 8.1: Bandwidth where each component is validated.

the front tower. The reduction factor observed by the local sensor in the end tower with better assembly symmetry was about 10.

The 3m Fabry-Perot cavity suspended from two SAS prototypes was operated with good stability. The measurement of the length fluctuation was limited by the sensing electric noise above a few Hz. Particularly, to increase the bandwidth of proper observation, we would need a significant improvement of the all noise sources. Below few Hz, the measured displacement matched well the design performance of the SAS. The length fluctuation measured in the 3m cavity is compared with the current performance of TAMA300 in figure 8.2. The displacement noise was significantly improved at least by factor of 100 below 10 Hz. This improvement is supposed to have been realized thanks to the low frequency isolators and their simple construction. From the measured passive isolation performance of the IP and the suspended chain, we expect that the seismic noise will be attenuated down to the thermal noise level of TAMA300 around few Hz, when the IP is tuned to lower frequency.

The measurement of the transmitted light showed that the vertical resonance of the MGASF and the angular fluctuations are potentially hazardous for the reliability of the interferometer operation. However, the SAS

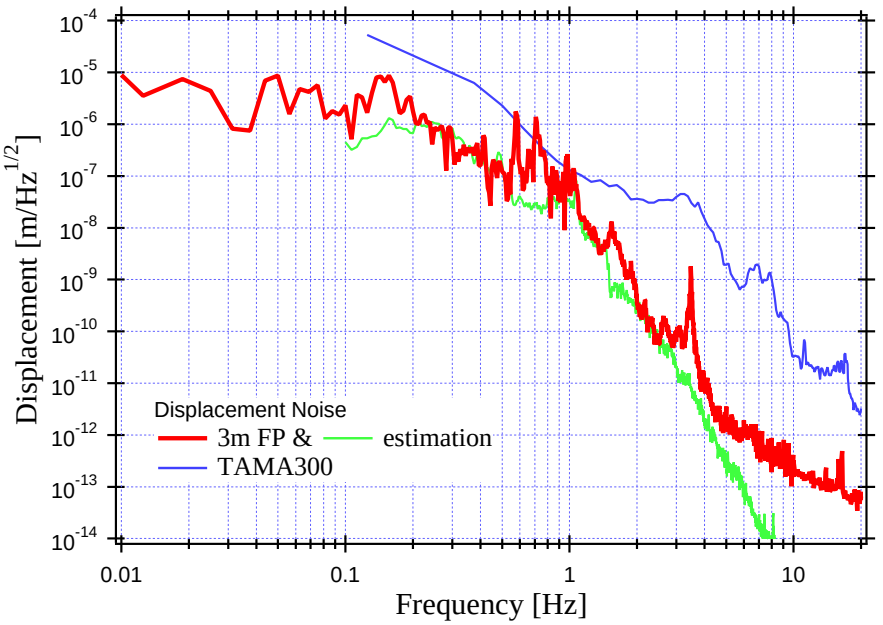

Figure 8.2: Displacement noise of the 3m Fabry-Perot cavity and TAMA300 at low frequency.

is equipped with the necessary component to actively damp the vertical resonance peaks, and the alignment noise can be suppressed by feedback from the wavefront sensors. This issue may need further study.

8.2 Perspectives

8.2.1 Further Improvements

We have learned some lessons through the assembly and operation of the SAS, and we have already started to improve the quality of the instrument.

In the 3m prototype we applied electromagnetic DC force to the suspension platform to align the test cavity. Although our measurements were not limited by the noise from this actuation, it is better to eliminate large DC force from the system. Figure 8.3 shows the improved mechanical tuning system designed to tune the DC pitch of the test mass. Parasitic springs are attached to the mMGAS that suspend the intermediate mass. These springs are connected to a beam supported by two picomotors. By moving the beam up and down via the picomotors, one can make remote tuning of the mirror tilt. The mMGAS themselves will be tuned slightly unstable (negative stiff-

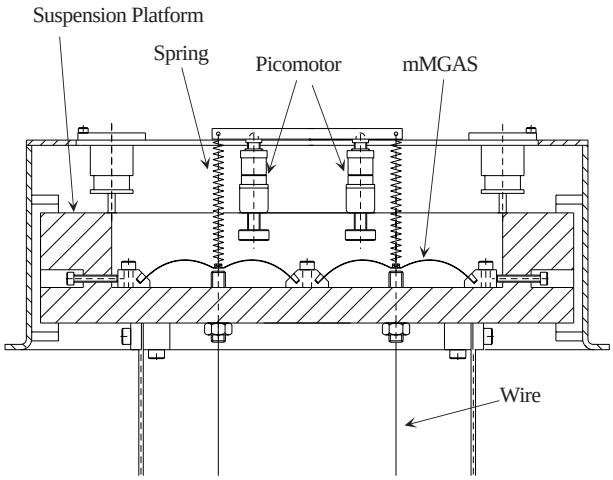

Figure 8.3: New mechanics for DC pitch tuning.

ness). The system will return to a stable condition after the addition of the parasitic springs.

For DC yaw tuning, we will install a rotator between the body of the filter1 and the wire that suspends it (figure 8.4). This rotator is equipped with a vacuum compatible thrust bearing and, can be remotely rotated by a picomotor, to tune the yaw. The rotator is pulled against the picomotor by a retainer spring for bi-directional tuning.

By using these improved mechanics, we can eliminate the DC standing forces from the suspension point. The coil magnet actuators will remain for angular resonance damping, for automatic alignment or for low frequency interferometer length control.

8.2.2 Future Project

The SAS described in this thesis was designed for the requirements of TAMA300, and does not have sufficient performance for the advanced detectors like LCGT and advanced LIGO. We can easily improve its attenuation performance with additional MGASFs. In the preliminary design of LCGT, the seismic noise is required to achieve the radiation pressure level, 10^{-18} m/$\sqrt{\text{Hz}}$ at few Hz. Taking into account the small ground motion at the LCGT site (Kamioka mine), we need to add up to four more filters to meet the requirement with safety factor of 100. If the requirement can be moved to realize safety factor of 100 at 10 Hz (still dominated by the radiation pressure), we

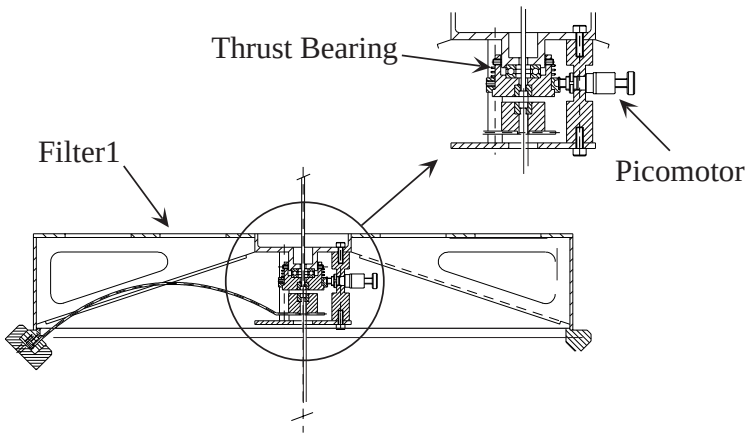

Figure 8.4: New mechanics for DC yaw tuning.

need only one more filter. Note that the performance of the SAS mechanics in the low frequency band was validated by the measurements described in this thesis.

8.3 Conclusion

We have designed a Seismic Attenuation System (SAS) to improve the low frequency sensitivity and reliability of gravitational wave detectors. We specifically designed the system for TAMA300 to provide refined isolation performance at low frequency with sufficient safety margin and to achieve reliable operation of the interferometer. The performance of the subsystems used in SAS was validated by independent tests in reasonable frequency bands. Finally we demonstrated the compatibility of the SAS with the interferometer by operating a 3m Fabry-Perot cavity suspended from the prototype SAS towers. Although further studies on the stable operation of a large scale interferometer may be needed, we did not observe any stability problem in our setup. More importantly, the operation of the 3m cavity anticipated a significant improvement in the displacement noise of TAMA300 around and above 10 Hz.

From the promising results of the independent tests and of the 3m cavity operation, the SAS is expected to realize the design performance, and its installation to TAMA300 is proceeding. Other research groups (University of Napoli, Firenze, and Pisa) have adopted the TAMA SAS towers for seismic isolation of sensors and interferometers.

Bibliography

[1] A. Einstein, *Ann. der Phys.*, **49**, 769 (1916).

[2] C. W. Misner, K. S. Thone, J. Wheeler, *Gravitation*, Freeman (1970).

[3] B. F. Schutz, *A first course in general relativity*, Cambridge University Press (1985).

[4] J. H. Taylor, J. M. Weisberg, *Astrophys. J.*, **345**, 434 (1989).

[5] R. A. Hulse, J. H. Taylor, *Rev. Mod. Phys.*, **66**, 711 (1994).

[6] P. R. Saulson, *Fundamentals of Interferometric Gravitational Wave Detectors*, World Scientific (1994).

[7] A. Abramovici, *et al., Science*, 256, 325 (1992).

[8] C. Bradaschia, *et al.*, *Nucl. Instrum. Meth. A*, **289**, 518 (1992).

[9] J. Hough, K. Dantzmann, *et al., GEO600 Proposal*, MPQ Report (1994).

[10] K. Tsubono, *Proc. 1st Edoardo Amaldi Conference on Gravitational wave experiments, Frascati, Italy*, World Scientific (1995).

[11] M. Ando *et al., Phys. Rev. Lett.*, **86**, 3950 (2001).

[12] H. Tagoshi, *et al., Phys. Rev. D*, **63**, 062001 (2001).

[13] K. Kawabe, *"Development of a 3-meter Fabry-Perot-Michelson Interferometer for Gravitational Wave Detection"*, PhD thesis, University of Tokyo (1999).

[14] M. Ando, *"Power recycling for an interferometric gravitational wave detector"*, PhD thesis, University of Tokyo (1999).

[15] K. Arai, *"Robust extraction of control signals for power-recycled interferometer gravitational-wave detectors"*, PhD thesis, University of Tokyo (2001).

[16] B. F. Schutz, *"Gravitational wave astronomy", Class. Quantum Grav.*, 16 A131 (1999).

[17] R. W. P. Drever *et al., Appl. Phys.* B, **31**, 97 (1983).

[18] D. C. Agnew, *Rev. of Geophysics*, **24**, 579 (1986).

[19] H. B. Callen, T. A. Welton, *Phys. Rev.*, **83**, 34 (1951).

[20] D. G. Blair, *et al., Appl. Opt.*, **36**, 337 (1997).

[21] P. Willems and M. Thattai, *Phys. Lett. A*, **253**, 16 (1999).

[22] M. Beccaria *et al.*, "The creep problem in the Virgo suspensions - A possible solution using maraging steel", *Nucl. Instrum. Meth. A*, **237**, 455 (1998).

[23] G. Cagnoli, *et al.*, *"Mechanical shot noise induced by creep in suspension devices", Phys. Lett. A*, **237**, 21 (1998).

[24] N. Kanda, M. Barton, K. Kuroda, *Rev. Sci. Instrum.*, **65**, 3780, (1994).

[25] D. Tatsumi, M. Barton, T. Uchiyama and K. Kuroda, *Rev. Sci. Instrum.*, **70**, 2 (1999).

[26] J. Winterflood, D. G. Blair, *Phys. Lett. A.*, **243**, 1 (1998).

[27] J. Winterflood, T. Barber and D. G. Blair, *Class. Quantum Grav.* **19**, 1639 (2002).

[28] A. N. Luiten et al., *Rev. Sci. Instrum.*, **68**, 1889 (1997).

[29] C. C. Speake, D. B. Newell, *Rev. Sci. Instrum.*, **61**, 1500 (1990).

[30] M. V. PLissi, *et. al, "GEO600 triple pendulum suspension system: Seismic isolation and control", Rev. Sci. Instrum.*, **6**, 71 (2000).

[31] M. E. Husman, PhD thesis, University of Glasgow, (2000).

[32] A. Bernardini, *et. al, "Suspension last stages for the mirrors and of the Virgo interferometric gravitational wave antenn"a, Rev. Sci. Instrum.*, **8**, 70 (1999).

[33] K. Kuroda, *et. al, "Japanese large-scale interferometers", Class. Quantum Grav.*, **19**, 1237 (2002).

[34] D. Shoemaker, *et al., Phys. Rev. D*, **38**, 423 (1988).

[35] N. Mio, *Jpn. J. Appl. Phys.*, **31**, 1243 (1992).

[36] A. Bertolini, PhD thesis, Universita' di Pisa, (2000).

[37] G. Losurdo, PhD thesis, Scuola Normale Superiore di Pisa, (1998).

[38] K. Numata, PhD thesis, University of Tokyo, (2002).

[39] R. Takahashi, *et al., Rev. Sci. Instrum.*, **73**, 2428, (2002).

[40] J. Giaime, P. Saha, D. Shoemaker, L. Sievers, *Rev. Sci. Instrum.*, **67**, 208, (1996).

[41] G. Ballardin, *et al., Rev. Sci. Instrum.*, **72**, 3643, (2001).

[42] G. Losurdo, *et al., "Inertial control of the mirror suspensions of the VIRGO interferometer for gravitational wave detection", Rev. Sci. Instrum.*, **72**, 3653, (2001).

[43] R. C. Dorf and R. H. Bishop, *Modern Control Systems (8th edition)*, Prentice Hall, (1997).

[44] E. Calloni, L. Di Fiore, A. Grado, and L. Milano, *"An interferometric device to measure the mechanical transfer function of the VIRGO mirrors suspensions", Rev. Sci. Instrum.*, **69**, 1882 (1998).

[45] S. Braccini, *et al., Rev. Sci. Instrum.*, **64**, 310, (1993).

[46] M. Beccaria, *et al., Nucl. Instrum. Meth. A*, **394**, 397, (1997).

[47] M. Beccaria, *et al., Nucl. Instrum. Meth. A*, **404**, 455, (1998).

[48] G. Cella, R. DeSalvo, V. Sannibale, H. Tariq, N. Viboud, and A. Takamori, *Nucl. Instrum. Meth. A*, **487**, 652, (2002).

[49] A. Bertolini, G. Gella, R. DeSalvo, and V. Sannibale, *Nucl. Instrum. Meth. A*, **435**, 475, (1999).

[50] Rosalia Stellacci, *LIGO Internal Document*[1], **G020466-00**, (2002).

[51] N. Viboud, thesis, INSA de Lyon, (also available as *LIGO Internal Document*, **T000007-00**), (1999).

[52] A. Araya, *et al., "Design of a Mirror Suspension System Used in the TAMA 300m Interferometer", Proc. of the TAMA International Workshop on Gravitational Wave Detection*, Universal Acad. Press., (1996).

[53] K. Arai, *et al., "Vibration Isolation of TAMA Suspension System", Proc. of the TAMA International Workshop on Gravitational Wave Detection*, Universal Acad. Press., (1996).

[54] K. Tsubono, A. Araya, K. Kawabe, S. Moriwaki, and N. Mio, *Rev. Sci. Instrum.*, **8**, 64, (1993).

[55] K. Arai, Master thesis (*in Japanese*), University of Tokyo, (1997).

[56] A. Takamori, Master thesis (*in Japanese*), University of Tokyo, (1998).

[57] Private communication with K. Yamamoto.

[58] http://www.kistler.com/

[59] H. Tariq., *et al., Nucl. Instrum. Meth. A*, **489**, 570, (2002).

[60] C. Wang, et al., Nucl. *Instrum. Meth. A*, **489**, 563, (2002).

[61] A. Takamori, *et al., "Seismic Attenuation System (SAS) for Advanced Gravitational Wave Detectors", Gravitational Wave Detection II, Proc. of the 2nd TAMA International Workshop on Gravitational Wave Detection*, Universal Acad. Press, (1999).

[62] Sz. Marka, *et al., Class. Quantum Grav.*, **19**, 1605, (2002).

[63] A. Takamori, G. Gennaro, T. Zelenova, R. DeSalvo, *"TAMA Seismic Attenuatino System (SAS) Tower Mechanical drawings", LIGO Internal Document*, **D010249-00**, (2001).

[1]LIGO Internal Documents are available from the web site: http://www.ligo.caltech.edu/.

[64] A. Takamori, G. Gennaro, T. Zelenova, R. DeSalvo, *"TAMA Seismic Attenuation System (SAS) Mirror Suspension System (SUS) Mechanical drawings", LIGO Inetrnal Document,* **D010250-00**, (2001).

[65] R. DeSalvo, *"LIGO-II Seismic Attenuation System (SAS) test tower mechanical drawings listing", LIGO Internal Document*, **T010131-00**, (2001).

[66] G. Cella, *"Mechanical Simulation Engine: physics", LIGO Internal Document*, **T990106-00**, (1999).

[67] G. Cella, *"Mechanical Simulation Engine: user's manual", LIGO Internal Document*, **T990107-00**, (1999).

[68] G. Gonzalez, *"ASC: Environmental Input to Alignment Noise", LIGO Internal Dcument*, **T960103-00**, (1996).

[69] A. Takamori, et al., *"Mirror Suspension System for the TAMA SAS", Class. Quantum Grav.*, **19**, 1615, (2002).

[70] M. Barton, *et al., "Proposal of a Seismic Attenuation System (SAS) for the LIGO Advanced Configuration (LIGO-II)", LIGO Internal Document*, **T990075-00**, (1999).

[71] A. Takamori, "Statement of Work (SOW): Evaluation of TAMA SAS at the 3m Interferometer", LIGO Internal Document, T000009-00, (2000).

[72] R. DeSalvo, K. Numata, A. Takamori, E. Ugas, and T. Yoda, *"Hysteresis Report of the Tama-SAS Filters", LIGO Internal Document*, **T010036-00**, (2000).

[73] R. J. Roark, R. G. Budynas, W. C. Young, Roark's Formulas for Stress and Strain, McGraw-Hill Professional.

[74] Cole Miller, *Talk at the ITP conference on Black Holes*, February 25-28, 2002.

Acknowledgment

Through the work described in this thesis, I shared time with many people, and learned lots from them. I would like to express my appreciation to:

Prof. Tsubono for giving me an occasion to work in this interesting and exciting field.

Riccardo DeSalvo for his infinite support for me.

Virginio Sannibale and Szabolcs Marka, for their friendship and great supports.

Alessandro Bertolini, for his friendship and strong support for me.

Hareem Tariq, Nicolas Viboud, and Chenyang Wang, for the great time in Pasadena.

Giancarlo Cella, for useful discussions on simulations.

Masaki Ando, for his advice.

Seiji Kawamura and Ryutaro Takahashi, for their support to SAS.

Kenji Numata, for his support to my work.

Tatsuo Yoda, Yukiyoshi Iida, Yuhiko Nishi, and Florian Jacquier for their support to my work.

Giovanni Losurdo, for useful discussions on mechanics and controls.

Diego Pasuello, and Roberto Taddei, for their support in the digital control.

Carlo Galli and his family, for the production of mechanics, and for the great time in Lucca.

Gianni Gennaro and his wife, for the excellent mechanical designs.

Shigemi Ohtsuka, and Yoshikatsu Nanjo, for their quick response to my outrageous requests.

Mitsuhiro Fukushima, for his help at Caltech.

The other people in the SAS collaboration.

Motorola Inc., for supplying us the digital control processors.

My friends for supporting me during hard periods.

and my family.